Politecnico di Torino

ScuDo
Scuola di Dottorato ~ Doctoral School
WHAT YOU ARE, TAKES YOU FAR

Doctoral Dissertation
Doctoral Program in Physics (38^{th} cycle)

Towards topological superconductivity in hydrogen-intercalated layered compounds

Gaia Gavello
*****

Supervisors:

Prof. Renato S. Gonnelli, Supervisor
Prof. Dario Daghero, Co-supervisor
Dr. Erik Piatti, Co-supervisor

Doctoral Examination Committee:
Prof. Gianrico Lamura, Referee, CNR-SPIN Genova
Prof. Giacomo Prando, Referee, University of Pavia
Prof. Emiliano Descrovi, Polytechnic University of Turin

Politecnico di Torino
2026

This thesis was completed at the end of the doctoral program funded by the National Recovery and Resilience Plan (PNRR), Mission 4, Component 1, "Enhancement of the education and training system: from early childhood to university" – Investment 4.1, "Expansion of the number of PhD programs and innovative PhDs for public administration and cultural heritage," under Ministerial Decree No. 351 of April 9, 2022.

I hereby declare that the contents and organisation of this dissertation constitute my own original work and do not compromise in any way the rights of third parties, including those relating to the security of personal data.

Gaia Gavello
Turin, 2026

Summary

Over the past decade, experimental breakthroughs have revealed superconductivity in hydrogen-rich compounds under high pressure at near-room temperature, renewing interest in the role of hydrogen in this phase of matter. Indeed, incorporating such an element into materials can substantially alter their electronic properties, sometimes giving rise to new superconducting phases or modifying existing ones. It can also influence with competing electronic orders, such as spin and charge density waves, providing valuable insights into the mechanisms behind superconductivity and its interplay with other ordered states.
Given this potential, hydrogen could, in principle, also serve as a promising tool in the search for topological superconductors. These materials are predicted to host exotic quasiparticles capable of encoding quantum information in a way intrinsically protected from local noise and decoherence, offering a potential route toward fault-tolerant quantum computation.
Within this perspective, this thesis ultimately aims to intercalate hydrogen into two layered materials (Bi_2Se_3 and $FeSe_{1-x}Te_x$) that are promising candidates for hosting topological superconductivity. The purpose is to investigate whether the incorporation of such an element induces effects that provide deeper insight into the actively pursued quantum state these systems are predicted to host. To achieve this, a multistep approach is employed.

The first step focuses on the technique used for hydrogen intercalation: the ionic gating-induced protonation. Although this method, based on ionic gating, has demonstrated considerable potential for modifying the electronic properties of materials, it remains relatively underexplored, leaving opportunities for optimization towards efficient and reliable hydrogen loading. Accordingly, the initial part of this thesis investigates ionic gating-induced protonation using a deep eutectic solvent, an electrolyte of a class not previously explored for this purpose. Specifically, the study examines how tuning the process parameters can maximize hydrogen loading in palladium, a material chosen for its highly suitable properties. The results reveal a clear positive correlation between the applied gate voltage and the hydrogen concentration achieved. Notably, the concentrations attained exceed those typically attained with conventional ionic liquids, which are commonly employed in

this technique. These findings demonstrate that deep eutectic solvents can outperform traditional electrolytes used in ionic gating-induced protonation and provide a potential framework for maximizing hydrogen loading in various materials, though material-specific adjustments may be required.

Next, hydrogen intercalation via ionic gating-induced protonation is performed on the layered transition metal dichalcogenide $TiSe_2$. While this material has recently been shown to exhibit superconductivity upon hydrogen intercalation, a detailed characterization of its superconducting state remains lacking. Its study is particularly compelling, as it offers insight into the interplay between superconductivity and the intrinsic charge density wave order of the pristine material. Through magnetotransport measurements, point-contact Andreev reflection spectroscopy, and tunneling spectroscopy, the superconducting phase is found to exhibit a nontrivial superconducting order parameter with two nodeless gaps. The temperature dependence of the gaps and of the upper critical magnetic field are consistent with both Bardeen-Cooper-Schrieffer theory and the Eliashberg formalism for a two-gap superconductor. This study not only clarifies the superconducting properties of H_xTiSe_2 but also provides hands-on experience with ionic gating-induced protonation and point-contact Andreev reflection spectroscopy on layered materials, offering transferable expertise for the topological candidates explored later in this thesis.

Building on this expertise, hydrogen intercalation is then performed on the layered topological superconductor candidates Bi_2Se_3 and $FeSe_{1-x}Te_x$. In Bi_2Se_3, no superconducting transition is observed in samples treated with ionic gating-induced protonation across a wide range of parameters, even when following the original protocol previously claimed to induce superconductivity. In contrast, in $FeSe_{1-x}Te_x$ with $x \approx 0.5$, ionic gating-induced protonation successfully tunes both the superconducting critical temperature and the superconducting gaps, as measured by point-contact Andreev reflection spectroscopy performed directly under gating – a measurement configuration not previously explored, since ionic gating was considered to be incompatible with such a technique. In rare cases, signatures of potential unconventional surface pairing, consistent with topological surface superconductivity, are also observed both in pristine and H-intercalated $FeSe_{0.5}Te_{0.5}$.

Acknowledgements

I would like to begin these acknowledgments by recalling the final lines of Ithaka by C. P. Cavafy:

> *"And if you find her poor, Ithaka won't have fooled you.*
> *Wise as you will have become, so full of experience,*
> *you'll have understood by then what these Ithakas mean."*

These verses beautifully capture the essence of a PhD journey, where the destination represents the goal, but the true value lies in the journey itself – the experiences, challenges, and lessons encountered along the way, whether positive or negative.

At the end of this journey – whose conclusion is anything but poor – my deepest gratitude goes to my supervisor, Prof. R. S. Gonnelli, who gave me the opportunity to embark on this path by welcoming me into his research group. His continuous guidance, encouragement, and challenges have been invaluable, providing me with experiences that shaped not only my scientific and professional growth but also my personal development. My sincere thanks also go to the members of his team: Prof. D. Daghero, for his precision and remarkable clarity in explanation, and Dr. E. Piatti, who taught me nearly everything I know about laboratory work. I am equally grateful to Mr. C. Tomaselli, who shared with me the secrets of PCARS analysis and guided me in processing the collected data.

A special thanks goes to Prof. J. Ye for welcoming me into his research group during my six-month stay abroad, and to his team at that time – in particular, Dr. P. Wan, Dr. Y. Kreminska, Dr. S. Hameed, Dr. Y. Wang, Mr. P. Hu, and Mr. J. Zoestbergen – for their support and assistance in my work, as well as for the enjoyable moments we shared outside the lab, which greatly enriched my experience.

Finally, I would like to express my gratitude to everyone I had the opportunity to share this journey with – those who laughed with me in good times and offered comfort in difficult ones – for making this experience truly special.

Contents

Introduction

Over the last decade, experimental breakthroughs showing near-room-temperature superconductivity in hydrogen-rich compounds under high pressure have renewed the interest of the scientific community in the interplay between such a light element and this phase of matter.
The hypothesis that hydrogen may unlock high-temperature superconductivity dates back to 1968, when Ashcroft suggested that its metallic state could exhibit superconductivity at elevated temperatures [1]. This prediction was based on three key points. First, the low atomic mass of hydrogen should give exceptionally high-frequency lattice vibrations. Second, the electron–phonon coupling is expected to be strong as electron-ion interaction is governed by bare Coulomb attraction. Third, once metallic, the electronic density of states at the Fermi level should be large, while the effective Coulomb repulsion between electrons remains relatively weak. However, achieving its metallic phase demands extremely high pressures that are difficult to realize experimentally. To overcome this limitation, Ashcroft proposed to address hydrogen-containing compounds, where chemical bonding between hydrogen and other elements could simulate the effects of externally applied pressure, effectively inducing a form of chemical pre-compression [2]. This mechanism is expected to enable the onset of high-temperature superconductivity at pressures lower than those necessary for pure hydrogen.
In this context, extensive computational efforts have been directed towards identifying hydrides capable of exhibiting superconductivity near room temperature under pressure. The first experimental validation of such theoretical predictions involved the sulfur hydride system, H_2S, predicted to show high-temperature superconductivity [3, 4]. Notably, at 155 GPa, H_3S – a compound formed through the pressure-induced decomposition of H_2S – was observed to exhibit superconductivity with a critical temperature T_c of approximately 203 K [5]. More recently, lanthanum hydride (LaH_{10}) demonstrated an even higher superconducting transition temperature, reaching $T_c \approx 250$ K under 170 GPa [6]. These findings have paved the way for integrating *ab-initio* simulations with experimental investigations to explore the role of hydrogen in high-temperature superconductivity and to discover materials that can achieve such a state at near-room temperature under more accessible pressures, advancing their technological feasibility [7].

Beyond their relevance for high-temperature superconductivity, these discoveries have also sparked interest in using hydrogen as a tool to engineer new superconducting phases [8] or tune existing ones [9, 10, 11] at ambient pressure. The approach relies on the same essential ingredients: the high vibrational frequencies associated with hydrogen and the coupling of these modes to the electronic states at the Fermi level. Although the resulting phases would exhibit lower critical temperatures, they can still be of practical relevance. For instance, inducing superconductivity through hydrogen incorporation in materials that, in their pristine form, host competing orders such as spin- or charge-density waves provides valuable insight into the microscopic mechanisms of superconductivity and its interplay with other ordered states – a subject of active investigation within the scientific community [12, 13, 14]. A paradigmatic example is provided by the layered transition-metal dichalcogenide $TiSe_2$. In its undoped state, this material undergoes a commensurate charge-density-wave transition below roughly 200 K, whose origin is still debated. Upon chemical or electrostatic doping, the charge-density-wave state is progressively suppressed and a superconducting phase emerges [15, 16, 17, 18, 19]. Interestingly, in lithium-intercalated or electrostatically doped $TiSe_2$ [17, 18, 19], where the two phases coexist, experiments suggests that spatial texture in the charge-density-wave order may induce anisotropy in the superconducting pairing or even a gap with non-trivial symmetry [20, 21, 22, 23, 24]. Consequently, substantial attention has been devoted to measurements of the superconducting gap function to probe the interplay between these two orders. In this context, hydrogen also plays a crucial role. As a matter of fact, a similar level of tunability in the properties of $TiSe_2$ has been achieved through intercalation of this light element [8]. Hydrogen incorporation enables robust and non-volatile control over the charge-density-wave state across a broad doping range – suppressing it while concurrently inducing superconductivity – thereby allowing the coexistence of these two competing orders. However, an investigation of the superconducting gap function in hydrogen-intercalated $TiSe_2$ is still lacking, representing a clear opportunity for further study.

Given this potential, hydrogen could, in principle, also serve as a promising tool in the search for topological superconductors that host Majorana bound states at their boundaries [25]. Interest in topological superconductors was initially sparked by the discovery of topological insulators – materials with an insulating bulk band gap but conducting edge states at boundaries with topologically trivial phases. These edge states arise as topological singularities that reconcile differences in topological invariants across the interface [26, 27]. Inspired by this phenomenon, significant research efforts have focused on finding superconducting counterparts known as topological superconductors. These materials have garnered even greater attention due to their ability to host exotic quasiparticles that are their own antiparticles,

effectively serving as condensed matter realizations of Majorana fermions. Indeed, topological superconductors exhibiting odd-parity pairing can sustain quasiparticle excitations described as equal superpositions of electron and hole states, which are effectively spinless and satisfy the self-conjugacy condition required in the second quantization framework for Majorana fermions [28]. When these quasiparticles are localized at vortex cores, defects, or system edges at zero energy, they form Majorana bound states that exhibit non-Abelian anyonic statistics. This non-Abelian nature means that exchanging or braiding two of such quasiparticles transforms the system among degenerate ground states in a non-commutative way, where the outcome depends on the order of the exchanges [28, 27]. Such braiding operations enable quantum information, encoded in fermionic states formed by spatially separated Majorana bound states, to be intrinsically protected from local noise and decoherence, since local perturbations affecting them individually do not alter the overall quantum state. This inherent robustness makes Majorana bound states highly promising for implementing fault-tolerant quantum computation, where topological properties are leveraged to store and manipulate information in a way that is inherently resistant to noise.

Motivated by these prospects, topological superconductors are actively studied and can be broadly categorized into two classes: artificially engineered and intrinsic topological superconductors [29, 30]. Artificially engineered systems typically consist of hybrid structures, such as semiconductors with strong spin-orbit coupling interfaced with conventional s-wave superconductors under an external magnetic field. In these systems, Cooper pairs from the s-wave superconductor penetrate the adjacent semiconductor over a finite distance, inducing a proximized superconducting state in the normal material. Due to the combined effects of the magnetic field and spin-orbit coupling, this state effectively exhibits odd-parity pairing [31, 32]. In contrast, intrinsic topological superconductors are materials in which a topologically nontrivial p-wave superconducting gap emerges intrinsically [33].
Focusing on intrinsic topological superconductors, a viable strategy to realize such an exotic state involves doping topological insulators inducing a bulk superconductivity while preserving the topological surface states. This strategy echoes the theoretical proposal by Fu and Kane [34], who showed that when the surface states of a three-dimensional topological insulator are proximized by an s-wave superconductor, the resulting proximized state – due to the helical spin polarization of the surface states – effectively behaves like a two-dimensional p-wave superconductor hosting Majorana bound states. Accordingly, in doped topological insulators, the superconducting bulk itself is expected to proximize the surface states, potentially realizing a similar topological superconducting phase.
Following this paradigm, considerable effort has been devoted at inducing superconductivity in the prototypical topological insulator Bi_2Se_3, with the goal of observing

an unconventional superconducting state indicative of topological superconductivity. A significant advance towards this goal was achieved by electrochemically intercalating copper [35], which induced superconductivity with $T_c \approx 3.8\,\mathrm{K}$ for copper concentrations x between 0.2 and 0.5, corresponding to electron doping near 10^{20} cm^{-3}. Point-contact Andreev reflection spectroscopy revealed a zero-bias conductance peak, which has been interpreted as evidence of a bulk, unconventional, odd-parity superconducting state [36]. Theoretical analyses subsequently showed that an odd-parity superconductor is topological if its Fermi surface encloses an odd number of time-reversal-invariant momenta in the Brillouin zone [37] – a criterion met by $Cu_xBi_2Se_3$. As a result, the observed topological superconductivity in $Cu_xBi_2Se_3$ is proposed to arise from a bulk nematic superconducting state rather than from proximity-induced superconductivity of surface states. Similar superconducting phases have also been reported in niobium- and strontium-intercalated Bi_2Se_3 [38, 39, 40, 41].
Within this context, very preliminary studies have claimed that hydrogen intercalation through ionic gating-induced protonation may induce superconductivity in Bi_2Se_3, with a T_c of approximately 3.8 K, as determined only by DC susceptibility measurements [42]. These initial results highlight the need for further investigation to confirm the reproducibility of hydrogen-induced superconductivity in this compound. If confirmed, subsequent research should focus on identifying the concentration range where the superconducting phase appears and examining the gap symmetry to assess whether hydrogen-intercalated Bi_2Se_3 exhibits a superconducting phase comparable to copper- [43, 44], strontium- [38, 45, 46], or niobium-doped variants [40].

Concurrently, topological superconductivity driven by the proximity effect has been proposed in iron-based superconductors, especially in $FeSe_{1-x}Te_x$ with $x \approx 0.5$. This material fulfills the conditions for Fu-Kane type topological superconductivity [34]: (i) substituting selenium with tellurium increases spin-orbit coupling, causing notable changes in the electronic structure [47]. In particular, spin-resolved angle-resolved photoemission spectroscopy experiments have observed Dirac-cone-like spin-helical surface states at the Fermi level, effectively turning the system into a topological material [48]. (ii) $FeSe_{1-x}Te_x$ exhibits s-wave superconductivity below its critical temperature [49]. However, alternative theoretical frameworks have also been proposed, which attribute the emergence of topological superconductivity in this compound to the interplay of surface ferromagnetism, Rashba spin-orbit coupling, and a $s_\pm$-wave superconducting order parameter [50].
Regardless of the underlying mechanism, sharp zero-bias conductance peaks have been experimentally detected within vortex cores of $FeSe_{1-x}Te_x$ [51, 52, 53, 54]. However, interpreting these zero-bias peaks as evidence of Majorana bound states requires ruling out other trivial explanations, such as unresolved Caroli–de Gennes–

Matricon states [55]. Specifically, these states appear in the vortex cores of conventional s-wave superconductors at energies given by $E = n\Delta^2/E_F$, where Δ is the superconducting gap, E_F the Fermi energy, and n is a half-integer quantum number [55]. When these states are not fully resolved, their lowest spectral signatures can appear as zero-energy peaks, thereby potentially mimicking the signals expected from Majorana zero modes.
To reliably distinguish Majorana bound states, increasing the superconducting gap is essential, as it increases the energy spacing between the zero mode and the first trivial excitation, making their detection easier even with limited experimental resolution. In this context, hydrogen intercalation could be advantageous. Experiments indicate that hydrogen doping in $FeSe_{1-x}Te_x$ (albeit at tellurium concentration different from 0.5) leads to an increase in the superconducting critical temperature [56], likely associated with an enhanced superconducting gap. It is thus of significant interest to explore whether doping of such a light element at tellurium substitution levels near 0.5 similarly enhances the critical temperature and the superconducting gap, thereby improving the experimental detectability of Majorana bound states in this system.

Outline of the thesis

The ultimate goal of this thesis is to intercalate hydrogen into materials that are promising candidates for hosting topological superconductivity, with the aim of inducing effects that provide deeper insight into this actively pursued quantum state. To achieve this, a multistep approach is adopted.

Specifically, the first step of this work focuses on the technique used for hydrogen intercalation. Doping of such an element can be achieved through several methods, including loading from high-temperature and high-pressure H_2 gas, low-temperature ion implantation, and electrochemical techniques [57]. While the first two approaches are technologically demanding and less accessible, electrochemical methods offer a more practical alternative. Among these, ionic gating-induced protonation – where hydrogen ions are driven into the host material thanks to the strong electric fields ($10^9 - 10^{10}$ V/m) attained at its interface with a voltage-polarized electrolyte – has shown considerable potential in modifying the electronic properties of materials [7]. Despite its promise, this technique remains relatively underexplored. As such, the initial part of this thesis is dedicated to establishing control over ionic gating-induced protonation by investigating the interplay among its tunable parameters. The goal is to determine how to effectively regulate these key factors to achieve efficient hydrogen uptake, ultimately developing a reliable and controllable guidelines that can later be applied to materials of interest.

Next, hydrogen intercalation via ionic gating-induced protonation is carried out in

$TiSe_2$, and its superconducting state is characterized to shed light on the interplay between superconductivity and the charge density wave order present in the pristine material. Beyond its fundamental scientific interest, the investigation of H_xTiSe_2 offers additional benefits within the context of this thesis. Firstly, $TiSe_2$, as a layered system, shares structural similarities with materials subsequently explored as candidate topological superconductors. Thus, developing expertise in hydrogen intercalation via ionic gating in $TiSe_2$ provides valuable methodological experience that is directly transferable to those systems. Secondly, the characterization of the superconducting phase of H_xTiSe_2 involves probing its superconducting gap, which can be achieved using point-contact Andreev reflection spectroscopy. This technique, capable of identifying signatures of unconventional superconductivity, will also be employed in the study of candidate topological superconductors. Its application to H_xTiSe_2 therefore serves as a preparatory work for the subsequent investigation of topological superconductivity.

Having established a robust intercalation protocol and acquired proficiency in point-contact Andreev reflection spectroscopy for probing superconducting gap structures, the final stage of this work focuses on the investigation of two candidate topological superconductors: doped Bi_2Se_3 and $FeSe_{1-x}Te_x$. These systems are explored using the developed methodologies to assess the influence of hydrogen intercalation on their superconducting properties and to search for potential signatures of topological superconductivity.

In line with this progression, the thesis is structured as follows:

- **Chapter 1** is dedicated to the technique employed in this study to achieve modulation of the electronic properties of materials – namely, ionic gating-induced protonation. To provide a broader context, an overview of the electric-field-assisted doping methods, within which protonation is classified, is provided. Particular emphasis is placed on elucidating the underlying physical mechanisms of these techniques, as well as highlighting the key results achieved through their application.
- **Chapter 2** offers a comprehensive overview of the experimental methods central to this thesis. It details the specific protocols adopted to perform ionic gating-induced protonation, as well as the techniques used to characterize the materials before and after the treatment. These techniques include electric transport measurements and point-contact Andreev reflection spectroscopy. Particular emphasis is placed on the latter technique, with a dedicated section introducing its underlying physics and the theoretical models used to interpret the spectra and extract information about the superconducting gap function in superconducting materials.

- **Chapter 3** presents the results of the investigation on ionic gating-induced protonation, aiming at gaining a deeper understanding of the process. By adjusting the controllable parameters of the treatment, this study identifies the optimal conditions for maximizing hydrogen incorporation into palladium – a material selected for its favorable ability to indicate hydrogen uptake through resistivity changes. Notably, ionic gating-induced protonation is conducted using a deep eutectic solvent, an electrolyte type not previously explored for this purpose but showing strong potential for hydrogen release under an applied electric field. The results obtained offer guidelines for maximizing incorporation of such a light element, though parameter adjustments may be necessary when applying the protocol to different materials. As this study focuses on the hydrogen insertion technique rather than on its use to modulate the superconducting properties via hydrogen insertion – central theme of this dissertation – only key motivations and results are summarized here, while full experimental details are provided in **Appendix A**.

- **Chapter 4** details the results of the characterization of the superconducting state in hydrogen-intercalated $TiSe_2$, obtained via ionic gating-induced protonation, through magnetotransport, point-contact Andreev reflection spectroscopy and tunneling spectroscopy measurements. All techniques consistently indicate the presence of a non-trivial superconducting order parameter, characterized by two nodeless superconducting gaps. Specifically, both the temperature dependence of the upper critical field, determined from magnetotransport measurements, and the superconducting gaps, extracted from point-contact spectroscopy and tunneling spectrocopy, are well described within the conventional Bardeen-Cooper-Schrieffer theory as well as the more comprehensive Eliashberg formalism for two-band superconductivity.

- **Chapter 5** reports the results obtained from hydrogen-intercalation via ionic gating-induced protonation performed on two candidate topological superconductors: Bi_2Se_3 and $FeSe_{1-x}Te_x$. For Bi_2Se_3, despite exploring a wide range of parameter configurations guided by the expertise gained from chapter 3, no superconducting transition was observed in protonated samples, even when following the original protocol reported in the study that first claimed superconductivity in hydrogen-intercalated Bi_2Se_3. In contrast, for $FeSe_{1-x}Te_x$ (with $x \approx 0.5$), ionic gating-induced protonation effectively tuned both its critical temperature and the superconducting gaps, as measured by point-contact Andreev reflection spectroscopy performed directly under gating – a measurement configuration that had never been explored before, as ionic gating was previously considered incompatible with this technique. In some rare cases, signatures of potential unconventional surface superconducting pairing, consistent with the presence of a topological p-wave surface state expected for a topological superconductor, were also observed.

- **Conclusions and future perspectives** summarizes the work presented in this thesis by reviewing the outcomes of this multistep process toward topological superconductivity and exploring potential directions for future research.

Chapter 1

Electrostatic and electrochemical ionic gating

The modification of the electronic properties of a material via the modulation of its charge carrier concentration is widely recognized as a powerful approach for advancing the understanding of fundamental mechanisms in condensed matter and unlocking novel functionalities with potential for technological applications. In this context, electric-field-assisted doping methods have emerged as promising alternatives to conventional chemical methods, offering a selective and continuous approach to tune carrier concentration [58, 59]. Although initially limited in their ability to achieve high carrier densities, advancements over the past decade have significantly improved their effectiveness, enabling the successful induction of high carrier concentrations. Among these approaches, ionic gating-induced protonation (IGP) – a technique where charge doping is realized through the insertion of hydrogen (H) ions into a material exploiting the strong electric field ($10^9 - 10^{10}$ V/m) attainable at a voltage-polarized electrolyte/electrode interface – stands out for its unique advantages. Beyond carrier doping, H insertion introduces high-frequency vibrational modes that can have an effect on superconductivity. This method is therefore a central focus of this thesis as a tool to induce novel superconducting states or tune existing ones.

This chapter presents an overview of this electric-field-based doping methods, culminating in IGP, with a focus on the key developments that have made high carrier densities achievable.

1.1 Electrostatic ionic gating

A prototypical example of using electric fields to control the electronic properties of materials is found in the semiconductor field-effect transistor. This device consists

of a metal-insulator-semiconductor junction, across which a gate voltage (V_G) is applied (see fig. 1.1a). In such configuration, the electric field that builds up across the insulating layer electrostatically modulates the surface charge density of the semiconductor. Specifically, depending on the polarity of the applied V_G, electrons can accumulate or be depleted at the insulator-semiconductor interface. This pure electrostatic doping alters the electronic properties of the semiconductor, enabling selective opening or closing of conductive pathways – an essential mechanism for performing logical operations.

Building on the success of field-effect transistors, electrostatic doping has been extended beyond semiconductors, with the hope that inducing surface carrier modulations will lead to the emergence of new and intriguing phenomena.
In early studies, oxide dielectrics such as SiO_2, commonly used for semiconductor transistors, were employed for this purpose. However, the induction of larger carrier densities via these solid dielectrics is inherently limited by the maximum electric field (E_{max}) they can withstand without undergoing dielectric breakdown. Typical E_{max} values are around 10^8 V/m, which correspond to maximum surface charge densities (n_{2D}) of approximately 10^{13} cm^{-2} [60].

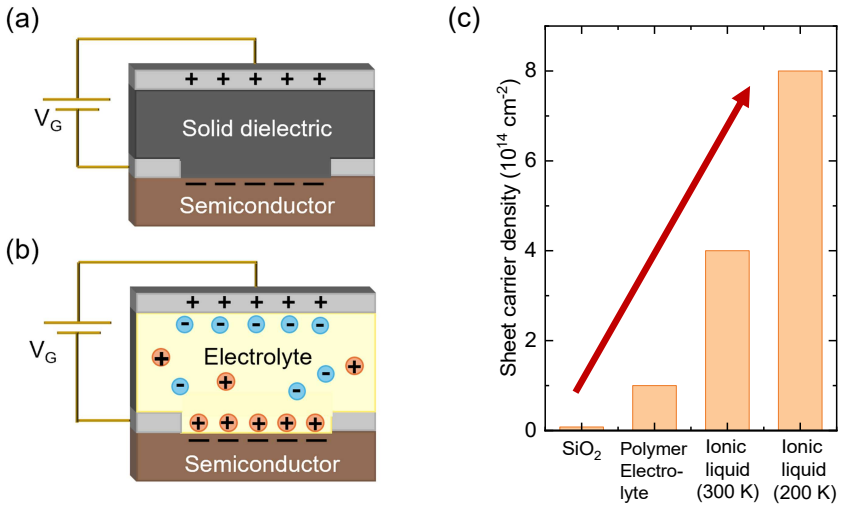

Figure 1.1: (a) Sketch of the electrostatic doping mechanism through an oxide dielectric. (b) Sketch of the electrostatic doping mechanism via ionic gating. (c) Comparison of electrostatic doping performance based on induced carrier density using an oxide dielectric, polymer electrolyte, or ionic liquid. Data reprinted from [60].

To overcome this stringent limitation, oxide dielectrics have been replaced by electrolytes, resulting in the typical configuration illustrated in fig. 1.1b. In this setup, applying a V_G across the electrolyte causes its constituent ions to migrate towards

or away from the gate electrode depending on their charges. This migration results in a net accumulation of ions at the interface with the sample, as long as V_G is not high enough to trigger electrochemical reactions within the cell. To preserve charge neutrality, an equal and opposite surface charge develops on the sample side, thereby resulting in electrostatic doping via ionic gating.

Unlike oxide dielectrics, where the electric field builds across the entire insulating layer, in this case, the electric field is confined to the effective capacitor formed at the interface between the sample and the electrolyte [61]. This effective capacitor, known as the electric double layer, extends over a distance determined primarily by the size of the accumulated ions ($\approx 1\,\mathrm{nm}$), resulting in high capacitance values typically in the range of tens of $\mu\mathrm{F/cm^2}$. In addition, electrolytes can withstand much higher electric fields (up to 10^9–$10^{10}\,\mathrm{V/m}$) compared to oxide dielectrics before undergoing chemical reactions that allow current to flow from the gate to the sample. As a result, surface charge densities as high as 10^{14}–$10^{15}\,\mathrm{cm^{-2}}$ can be attained [60].

Typical electrolytes used in ionic gating include polymer electrolytes and ionic liquids (ILs). Polymer electrolytes are composed of inorganic salts, such as $\mathrm{ACl O_4}$ (where A can be Li, K, or Cs), dissolved in a polymer matrix, such as polyethylene oxide (PEO) or polyethylene glycol (PEG). These electrolytes can exist in solid or "gel-like" states, depending on the molecular weight of the polymer [60]. In contrast, ILs are salts that remain liquid at or near room temperature, composed of organic cations and either inorganic or organic anions, such as the N,N-diethyl-N-methyl-N-(2-methoxyethyl)ammonium bis(trifluoromethylsulfonyl)imide (DEME-TFSI) or the 1-ethyl-3-methylimidazolium tetrafluoroborate (EMIM-$\mathrm{BF_4}$). Due to their liquid state and broader operational range where no electrochemical reactions occur [62], ILs provide higher ionic conductivity and usually enable greater carrier accumulation than polymer electrolytes. However, although polymer electrolytes are less efficient than ILs, their tunable physical state provides control over rigidity and mechanical stability, making them particularly suitable for applications in printed electronic devices [60].

1.1.1 Scientific impact on superconductivity

Ionic gating has significantly advanced the field of electrostatic doping, providing a powerful tool to manipulate material properties and achieve configurations that were previously unattainable.
One of the key breakthroughs enabled by ionic gating is the induction of superconductivity in layered insulators using electric fields [63, 64, 65, 66, 67, 68, 69]. Before this development, insulator-to-superconductor transitions were achieved via chemical doping methods, such as substitutional or interstitial doping, which allowed

for sufficiently high carrier concentrations [70, 71, 69]. However, chemical methods are not ideal for studying superconductivity, as they not only introduce doping but also cause structural disorder, which may be detrimental to the emergence of a superconducting state. As a result, ionic gating has emerged as a strategic alternative, offering a way to induce superconductivity in layered insulators without the drawbacks of chemical doping.

The first successful observation of a field-driven insulator-superconductor transition occurred in insulating $SrTiO_3$ single crystals using a $KClO_4$/PEO polymer electrolyte [66]. Specifically, upon gating, a superconducting state with $T_c = 0.4\,K$ emerged at relatively low sheet carrier densities: $n_{2D} \approx 10^{13}$ cm^{-2}. As V_G was increased, sheet carrier densities up to $10^{14}\,cm^{-2}$ were explored, with superconductivity persisting around 0.4 K.
The replacement of polymer electrolytes with ILs enabled the attainment of even higher carrier concentrations, further advancing the field. Notably, superconductivity was observed in both the quasi-2D layered ZrNCl [72] and the transition metal dichalcogenide MoS_2 [68] when the DEME-TFSI IL was used as the gating medium. In ZrNCl [72], increasing V_G initially triggered an insulator-to-metal transition, followed by a slight dip in resistivity, signaling the onset of superconductivity. As V_G increased further, the superconducting state fully developed, as illustrated in fig. 1.2a. This state persisted within a sheet carrier concentration

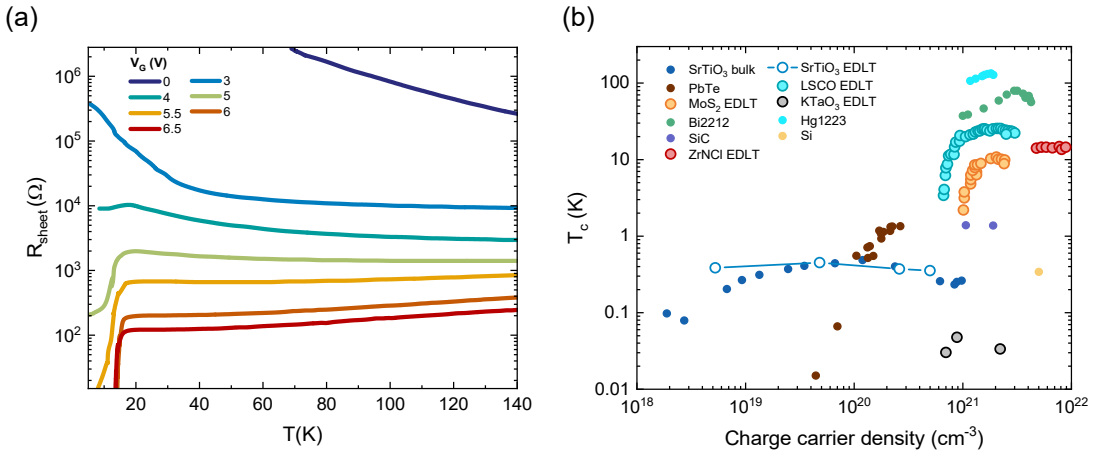

Figure 1.2: (a) Temperature dependence of the sheet resisitance of ZrNCl under ionic gating for gate voltages (V_G) ranging from 0 to 6.5 V. Data reprinted from Ref. [67]. (b) Phase diagram showing the superconducting critical temperature (T_c) as a function of volume carrier density for various field-induced superconductors obtained via ionic gating (large symbols). To highlight the effectiveness of ionic gating compared to chemical doping, relevant data for superconductivity induced by chemical doping (small circles) are also included. Data reprinted from Ref. [60].

range of $10^{14} - 10^{15}\,\mathrm{cm}^{-2}$, with T_c exhibiting a dome-like trend, peaking at 14.8 K at $n_{2D} = 5 \cdot 10^{14}\,\mathrm{cm}^{-2}$.
A similar behavior was observed in MoS_2 [68], where superconductivity emerged abruptly at $V_G = 4\,\mathrm{V}$, corresponding to a sheet carrier density of $6.8 \cdot 10^{14}\,\mathrm{cm}^{-2}$. As V_G increased, n_{2D} continued to rise, with T_c reaching a maximum of 10.8 K at $1.2 \cdot 10^{14}\,\mathrm{cm}^{-2}$, before gradually decreasing at higher densities, again forming a dome-like phase diagram.

A summary of the selected seminal findings in field-induced superconductivity is presented in fig. 1.2b, where the induced T_c is mapped as a function of the attained volume carrier doping for each material.

1.2 Electrochemical ionic gating

Electrostatic doping via ionic gating, despite its success in achieving field-induced superconductivity in layered materials, faces two significant limitations [59]. First, it only offers temporary control over material properties, as the system returns to its undoped state as soon as V_G is removed. Second, charge accumulation is confined to the surface, restricting its effectiveness in modifying bulk carrier density. As a result, this technique is not suitable for applications that require significant bulk doping.

These constraints can be overcome by transitioning to an electrochemical regime. In this regime, the application of sufficiently high voltages triggers electrochemical reactions within the electrolyte, enabling the exchange of charge carriers between the gating medium and the entire sample. This results in gate-tunable bulk doping, thereby overcoming the surface confinement typical of electrostatic doping. As a result, electrochemical doping not only outperforms electrostatic doping but also offers significant advantages over traditional chemical methods, providing a versatile, on-demand approach for continuously tuning carrier concentration.
Examples of electrochemical reactions that can be triggered include the migration of oxygen vacancies [73, 74], the intercalation of electrolyte cations [75, 76, 77], or the intercalation of ions produced from water electrolysis or direct electrolyte electrolysis [78, 79, 80, 81, 82, 74, 81, 83, 59, 84]. In the case of oxygen vacancy migration, studies on oxides have shown that the electric field that forms across the electric double layer is strong enough to promote the extraction of part of the oxygen not only from the surface layer but also from deeper regions, creating vacancies that affect bulk carrier concentration [85, 86]. In the other scenarios, instead, the electric field promotes the injection of ions from the electrolyte into the sample. These ions penetrate the top layer of the sample and diffuse deeper, driven by the concentration gradient, leading to bulk carrier doping.

Unlike electrostatic doping, the effects of electrochemical doping can be both reversible and non-volatile [81, 59]: non-volatile because the ions can remain in the material even after the voltage is removed, and reversible because reversing the voltage polarity can extract the intercalated ions, returning the material to its original state.

Given its potential, the following sections offer an overview of electrochemical doping via ion intercalation, with a particular focus on the doping technique used in this thesis, namely H^+ intercalation.

1.2.1 Ionic gating-induced intercalation

As previously mentioned, when a positive V_G is applied to an electrolyte in a configuration such as that shown in fig. 1.1b, and this voltage exceeds the stability window of the electrolyte, the cations it contains can be injected into the sample under gating, resulting in bulk doping. For instance, with the commonly used $AClO_4$/polymer electrolyte, alkali ions can be intercalated [78, 79, 80], while with IL, the injection of organic cations can take place [75, 76, 77].

In this framework, a seminal demonstration of how electrochemical doping via alkali intercalation can outperform electrostatic gating can be found in the study by Shi *et al.* [80]. In this work, ionic gating via $KClO_4$/PEG is performed on the transition metal dichalcogenide WS_2, systematically increasing V_G to probe both doping regimes. Changes in sample conductivity are evaluated by measuring the current (I_{DS}) flowing through the sample under a constant bias voltage, while the onset of electrochemical doping is monitored by tracking the gate current (I_G) flowing between the electrolyte and the sample.
For $V_G < 3\,V$, I_{DS} increases due to the electrostatic accumulation of charge, with I_G remaining negligible. Between 3 and 8 V, a rise in I_G signals the onset of K^+ ion intercalation, although its impact on I_{DS} is still limited. Beyond 8 V, both I_{DS} and I_G increase sharply, marking the transition to dominant electrochemical doping. The progression of I_{DS} across these regimes is shown in fig. 1.3a.
Hall measurements confirm that electrochemical doping outperforms electrostatic doping, achieving bulk carrier densities up to $10^{22}\,cm^{-3}$, compared to the electrostatic limit of $10^{20}\,cm^{-3}$. Within part of this concentration range, a superconducting phase emerges in K_xWS_2 characterized by a doping-independent T_c of 8 K (fig. 1.3b). Previously, such result had only been achieved using conventional chemical methods or electrostatic doping of thinner samples, where the reduced dimensionality enabled more effective tuning of electronic properties through changes in n_{2D} [87, 88].

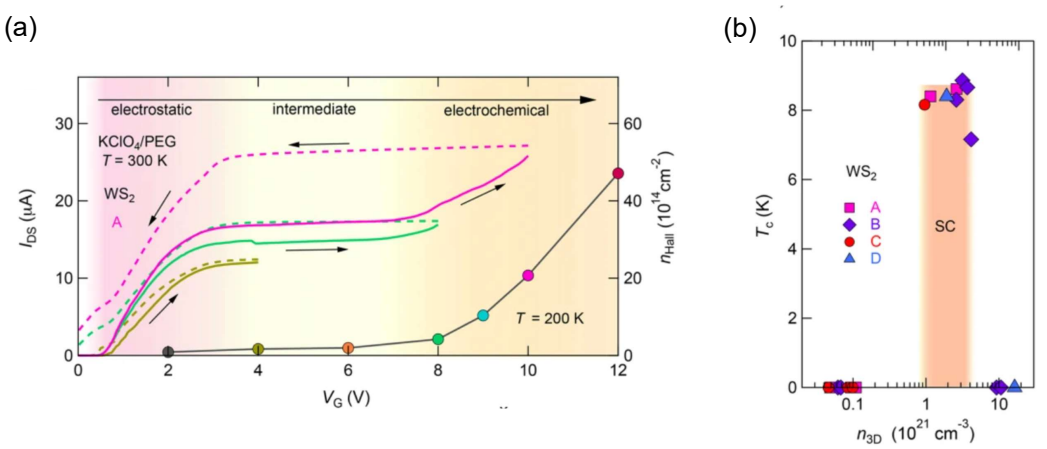

Figure 1.3: (a) Response of WS_2 to the application of a gate voltage (V_G) in an ionic gating configuration. The lines illustrate how the current (I_{DS}) flowing through the sample, under a constant bias voltage, varies with increasing (solid lines) and decreasing (dashed lines) values of V_G. Colored circles represents the Hall carrier density (n_{Hall}, right axis) measured at 200 K plotted against V_G. (b) Phase diagram of ionic gating-intercalated WS_2, showing the superconducting critical temperature (T_c) as a function of bulk carrier density (n_{3D}). The shaded region highlights the doping range in which a full superconducting transition to a zero-resistance state takes place. Adapted from Ref.[80].

A similar successful example of modifying electronic properties through ion intercalation can be found in the study by Wang *et al.* [76], where organic cations from the EMIM-BF_4 IL are intercalated into the FeSe superconductor. In their study, a voltage of 4 V is applied across EMIM-BF_4 maintained at 355 K, driving the intercalation of $EMIM^+$ cations into FeSe single crystals. X-ray diffraction analysis confirms this incorporation, revealing a pronounced expansion of the *c*-axis lattice parameter, indicative of the insertion of relatively large molecular species. Based on the applied voltage polarity, the intercalated species are identified as $EMIM^+$ ions. This intercalation significantly modifies the superconducting behavior of FeSe, raising the superconducting onset temperature from 8 K to 44.4 K, as verified by both resistivity and magnetic susceptibility measurements.

1.2.2 Ionic gating-induced protonation

Beyond simple intercalation of cations from the electrolyte, other electrochemical reactions can take place within the electrolyte beyond its stability window, leading to bulk carrier doping of the sample under gating. One of the most significant reactions is the electrolysis of water molecules, which may be naturally present or intentionally introduced into the electrolyte. Specifically, when the applied V_G

exceeds the electrolysis threshold – 1.23 V at room temperature [89] – water dissociates into protons (H^+) and superoxide ions (O^{2-}). Depending on the polarity of the applied voltage, either H^+ or O^{2-} ions can be injected into the sample, driven by the electric field across the electric double layer, and diffuse into the material due to the concentration gradient, resulting in bulk doping. A schematic representation of this process is illustrated in fig. 1.4a.

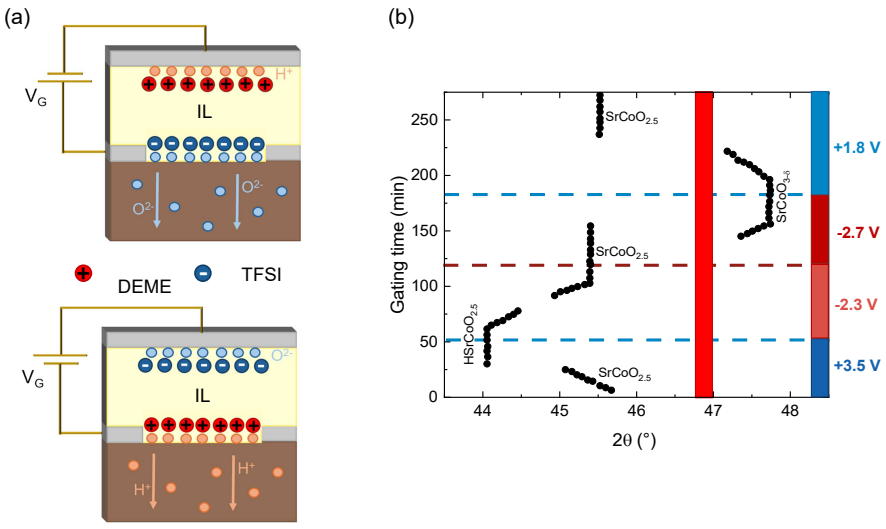

Figure 1.4: (a) Sketch of the ion loading and diffusion process that occurs when a humid ionic liquid (IL) is properly gated, leading it into the electrochemical regime where water dissociation takes place. (b) X-ray diffraction pattern of $SrCoO_{2.5}$ under electrochemical doping. Data reprinted from Ref. [81]

The first evidence of electrochemical doping through water electrolysis was observed in studies on strongly correlated transition metal oxides. In particular, gating single-crystal VO_2 nanowires with a humid ionic liquid led to a modulation of their metal-insulator transition temperature – an effect that did not occur when the same ionic liquid was used in its dry form [90]. This behavior was attributed to IGP caused by water electrolysis. Secondary ion mass spectrometry measurements confirmed bulk diffusion, showing H presence throughout the entire thickness of the sample, with a peak concentration at the surface [74]. This pattern aligns with the scenario of an initial H^+ surface penetration followed by subsequent diffusion into the entire bulk.
Further investigation of the transport properties of VO_2 after gating showed that the injection of H^+ ions led to bulk carrier doping, enabling the tuning of the metal-insulator transition. Depending on the doping level, the metal-insulator transition temperature could shift from 320 K in the undoped material to lower temperatures, eventually disappearing entirely, with the material exhibiting metallic behavior [74]. This has important implications for technological applications, as the optical

properties of VO_2 also change with the metal-insulator transition, particularly in terms of visible and infrared transmission. As a result, gate-tunable H_xVO_2 holds potential for smart window applications, where gating can adjust its transition temperature and, in turn, its transmission properties [91].

Building on this evidence, further studies on transition metal oxides have examined IGP to gain more insight on this intercalation technique. Notably, electrochemical doping of $SrCoO_{2.5}$ using a humid ionic liquid has proven to be both non-volatile and reversible. Specifically, applying a positive voltage of +3.8 V to $SrCoO_{2.5}$ induces H^+ loading leading to the formation of a new phase, $HSrCoO_{2.5}$ [81], which remains stable even after the voltage is reduced to 0 V. Conversely, applying a negative voltage of −2.3 V restores the system to its original state, demonstrating the reversibility of the process. A similar behavior is observed for O^{2-} loading: applying a voltage as low as −2.7 V results in the formation of $SrCoO_{3-\delta}$, which remains stable upon voltage removal, while the original state can be recovered by applying a voltage of 1.8 V. This phase progression is illustrated in fig. 1.4b, where X-ray diffraction results show the structural evolution of gated $SrCoO_{2.5}$ as a function of the applied V_G.
While $SrCoO_{2.5}$ retains the properties resulting from H^+/O^{2-} loading [81], VO_2 reverts to its initial state once the gate voltage is removed [74], highlighting that IGP cannot be considered universally non-volatile. Instead, its non-volatility is strongly dependent on the specific material.

Beyond water electrolysis, an alternative method to achieve IGP, which has not been explored in the literature yet, involves engineering the electrolyte to facilitate bond breaking when V_G is applied, leading to the release of H^+ ions. This approach relies on direct electrolyte electrolysis to generate ionic by-products that may load into the sample, thereby modifying its electronic properties. However, it is crucial to highlight in this preliminary discussion that operating in a regime where electrolyte electrolysis takes place increases the risk of unwanted chemical reactions with the sample, such as electrochemical etching [92], due to the high reactivity of the electrolyte. Therefore, great care must be taken to avoid irreversible damage to the sample. Controlled electrolyte electrolysis for IGP will be addressed experimentally in chapter 3.

1.2.3 Ionic gating-induced protonation: scientific impact on superconductivity

The modulation of metal-insulator transitions is just one application of IGP [82, 74, 81, 83, 59]. Another field where IGP holds immense potential is that of superconductivity, where carrier doping is achieved alongside the introduction of high-frequency vibrational modes due to the presence of H. This combination may be

crucial for discovering new materials that, when loaded with H, could exhibit HTSC at ambient pressure, or for the enhancement of the superconducting properties of materials that already display superconductivity.

Traditionally, H loading has been carried out through methods such as absorption from gases at high temperatures and pressures, ion implantation, or electrolysis of acids like HCl or H_2SO_4 [57]. However, these approaches come with challenges, including technological complexity and environmental concerns. In this context, IGP offers a simpler, more efficient, and sustainable alternative to conventional H loading techniques.
A striking example of superconductivity enhancement via proton intercalation is demonstrated by Meng *et al.* [11], who showed that the superconducting T_c of FeSe iron chalcogenide can be raised from 10 K to 44 K upon IGP. By carefully controlling the gating time, the concentration of intercalated H^+ ions was precisely adjusted, enabling fine-tuned electron doping. This process led to the appearance of multiple distinct superconducting phases in H_xFeSe, each with a specific T_c and carrier concentration (see fig. 1.5). Crucially, due to the small size of H^+ ions, structural disruption was minimal, ruling out changes in interlayer spacing as the cause for T_c enhancement. Consequently, the discrete superconducting phases observed are attributed solely to electron doping, which both suppresses the nematic ordering present in the pristine phase and significantly alters its band structure.

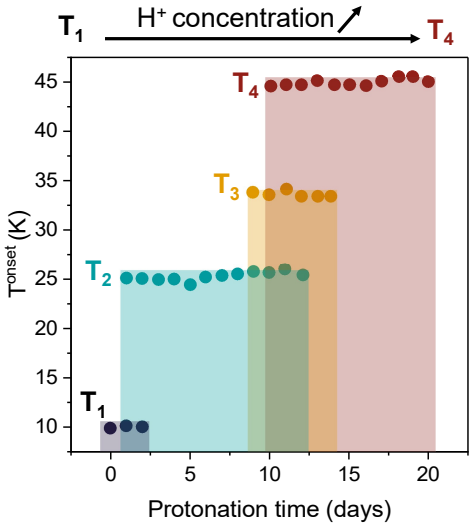

Figure 1.5: Evolution of the superconducting onset temperature (T^{onset}) of FeSe crystal as a function of the duration of ionic-gating induced protonation treatment. Data reprinted from Ref. [11]

A more modest but still notable increase in T_c was observed in Ref. [10], where

IGP was performed on the topological superconductor candidate $PdTe_2$. After proton intercalation, the T_c increased from approximately 1.6 K to 3.8 K. While the increase is less pronounced compared to FeSe, the result remains noteworthy, indicating that IGP holds promise for investigating topological superconductivity. With its ability to precisely and continuously control carrier doping, IGP proves to be a valuable tool for studying topological superconductor candidates, especially in cases where the desired phase may only emerge within a specific doping range.

Given its remarkable potential and comparatively limited investigation relative to other intercalation methods, IGP will be employed throughout this thesis to fine-tune superconductivity in a range of materials, including potential topological superconductors. This will follow an initial study aimed at optimizing IGP free parameters to achieve precise control over the intercalation process.

Chapter 2

Experimental techniques

The operative core of this experimental thesis lies in the modulation and characterization of the electronic properties of materials. The modulation, which seeks either to induce novel superconducting states or tune existing ones, is achieved via the ionic gating-induced protonation (IGP) technique, outlined in the previous chapter. The characterization, on the other hand, primarily relies on electric transport measurements, including both real-time monitoring of the room-temperature (T) resistivity during IGP and T-dependent resistivity measurements taken before and after the treatment. The continuous tracking of resistivity during IGP enables the observation of the evolution of the electric transport properties as it occurs, while T-dependent measurements are essential for identifying the emergence of new superconducting phases or modifications to existing ones resulting from the protonation process. When superconductivity is observed, the superconducting state is further analyzed using point-contact Andreev reflection spectroscopy (PCARS). This technique offers direct insights into the superconducting order parameter and its evolution under IGP, making it an invaluable tool for identifying potentially unconventional superconducting states induced by IGP.

The following sections offer a detailed discussion of these experimental techniques and their implementation, providing the experimental foundation for the investigations presented in the subsequent chapters.

2.1 Electric transport measurements

In this thesis, the changes in the electronic properties of the investigated materials are primarily tracked by using their electrical resistivity (ρ) as a proxy. For samples with known geometry, ρ is obtained from resistance measurements performed according to established protocols, which are selected based on the geometry of the sample and the required level of accuracy [93].

Since this work focuses on low-resistance materials and superconductors, whose resistance drops to zero below their critical temperature (T_c), the four-probe measurement technique is adopted to ensure high accuracy. In this method, a current (I) is injected into the sample under investigation through a pair of leads, while a separate pair measures the resulting voltage drop (V). The resistance (R) is then calculated as $R = V/I$. The four-probe setup is preferred over the two-probe method because the latter includes spurious resistive contributions from the leads and contact interfaces between the sample and the electrodes. Although such contributions are typically negligible for high-resistance samples, they can significantly distort measurements in low-resistance systems and superconductors. Thus, the four-probe method is essential for reliable resistance measurements in this work.
To further improve accuracy, a current-reversal technique is used. In this approach, I is first applied in one direction, then reversed. For each direction, the voltage drop is measured, and the voltage half-difference ΔV between the two measurements is calculated. The resistance is then determined using the formula $R = \Delta V/I$. This technique effectively cancels out common-mode offsets, such as thermoelectric voltages arising from junctions of dissimilar materials maintained at different temperatures [93].

With these precautions in place, the four-probe technique is modulated to implement the most suitable and precise configuration for measuring the resistivity of the samples, depending on their geometry. Two primary configurations are employed, based on whether the samples are bar-shaped (fig. 2.1a) or have an arbitrary planar form (fig. 2.1b).
For bar-shaped samples, the current electrodes are designed to cover the entire cross-sectional area at each end, ensuring a uniform and parallel current flow. Voltage is measured between two inner contacts along the length of the sample, which are kept small to minimize disturbance to the current path. Given the measured ΔV and injected I, the resistance is calculated and used to determine ρ through the relation:

$$\rho = R \frac{t \cdot w}{L} \tag{2.1}$$

where L is the distance between voltage contacts, t is the sample thickness, and w is the cross-sectional width (fig. 2.1a).
For samples with arbitrary shape, the van der Pauw method is employed [94]. Four small electrical contacts are thus placed around the perimeter of the sample, ensuring contact with both the surface and sides. A current is passed between each adjacent pair of contacts, and the resulting voltage drop is measured across the opposite pair. By averaging the resulting resistance values, two distinct resistances are obtained for each perpendicular direction within the sample: R_{horiz} and R_{vert} (fig. 2.1b). These resistances are related to the resistivity of the sample through the equation [94]:

$$e^{-\pi\, t\, R_{\mathrm{horiz}}/\rho} + e^{-\pi\, t\, R_{\mathrm{vert}}/\rho} = 1 \tag{2.2}$$

By entering the measured resistances and the sample thickness into this equation and solving it numerically, ρ can be determined.

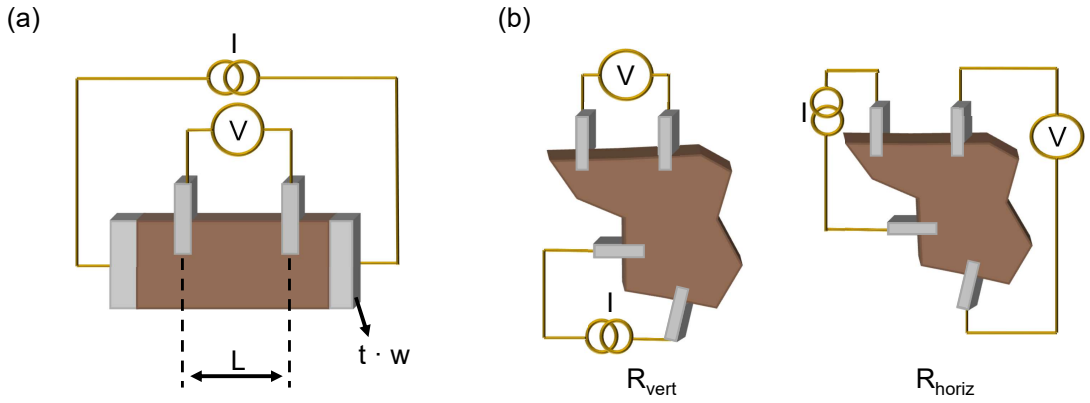

Figure 2.1: (a) Schematic representation of the measurement configuration used for resistivity characterization of a bar-shaped sample using the collinear four-probe configuration. (b) Schematic representations of the measurement configurations used for resistivity characterization of an arbitrarily shaped sample via the four-probe van der Pauw technique. Two orthogonal resistance values, R_{horiz} and R_{vert}, are obtained from the shown configurations and used in the van der Pauw equation (2.2) to determine the resistivity of the sample.

In all cases, electrical contacts are made by drop-casting conductive paste (e.g., gold or silver) on the sample. A gold or platinum wire is then embedded into the conductive paste to establish a reliable electrical connection with the rest of the circuit and instrumentation.

2.1.1 Resistivity vs. temperature characterization

The configurations outlined above are used to monitor ρ either at room T or as a function of T. These T-dependent measurements are essential for detecting the potential onset or modulation of superconducting phases induced by IGP.
To perform T sweeps, various cryogenic systems are used, each providing access to progressively lower base temperatures. Specifically, measurements down to 2.8 K are carried out using a Cryomech PT-403 pulse-tube cryocooler. For measurements below 2.8 K and/or where the application of a magnetic field is required, samples are mounted on the cold head of cryogenic inserts compatible with an Oxford Instruments ^{4}He cryostat, reaching T as low as 1.6 K and magnetic fields up to 9 T. For

ultralow-T measurements, a Cryogenic Ltd ^{3}He probe is employed in combination with the ^{4}He cryostat, allowing measurements down to 0.28 K.

2.2 Ionic gating-induced protonation

The underlying physical principles of IGP are discussed in detail in section 1.2.2. This section, instead, focuses on the experimental implementation of IGP realized in this work, highlighting the customizations made to tackle the challenges encountered in the studies presented in the following chapters.

2.2.1 Experimental configuration

The minimal experimental configuration for performing IGP consists of a metallic gate electrode in contact with an electrolyte, in which the sample to be doped is immersed. The gate voltage (V_G) is then applied between the gate electrode and a source electrode placed on the sample, with the source taken as the ground of the system [95, 81, 11]. By measuring the gate current (I_G) flowing between these two electrodes, qualitative insights into the progression of the IGP process can be obtained. This is because I_G reflects the net charge transfer from the electrolyte to the sample, resulting from water electrolysis or protonic dissociation triggered by the applied V_G [96, 90]. However, not all generated protons intercalate into the material. For instance, some may recombine and desorb as molecular H_2 [97]. Therefore, I_G serves only as a qualitative indicator of proton intercalation.

To gain better control over the IGP process, this minimal experimental setup can be enhanced by adding more components. One possible improvement is the inclusion of a reference electrode – a floating electrode placed in the region where the gated electrolyte is neutral. Measuring the voltage between this reference and the source electrode (V_{ref}) allows a more direct monitoring of the voltage drop across the electric double layer at the sample interface, which directly governs proton generation and intercalation. This V_{ref} is actually lower than the total applied V_G, as part of V_G drops across the electric double layer at the gate/electrolyte interface [98]. Increasing the contact area between the gate and the electrolyte, relative to the sample/electrolyte interface, enhances the gate capacitance, thereby reducing the voltage mismatch; however, it cannot eliminate it entirely. Therefore, the inclusion of a reference electrode is essential for accurately determining the true working voltage during IGP. A further source of voltage drop originates from the bulk resistance of the electrolyte, which becomes significant when I_G is non-negligible. This effect on V_{ref} can be minimized by positioning the reference electrode as close as possible to the source electrode (see fig. 2.2b).
Another significant enhancement involves adding electrical contacts to the sample,

as detailed in section 2.1, to enable four-probe resistivity measurements [8, 75, 99, 96]. This method provides a direct and quantitative evaluation of IGP progression through changes in the electronic properties of the sample, unlike gate-current measurements.

A schematic of the enhanced IGP experimental configuration, including voltage reference measurements and tracking of the sample resistivity, is shown in fig. 2.2a. In this thesis, the gate electrode is realized as a platinum gcoil or foil, ensuring that its surface area is significantly larger than the exposed sample surface in contact with the electrolyte. Platinum is chosen for its excellent electrochemical stability, ensuring that no reactions occur at the gate electrode during IGP [100]. For similar reasons, when silver paste is used to establish electrical contacts, given the chemical reactivity of silver, an insulating layer of GE varnish is applied over it to inhibit unwanted electrochemical interactions.

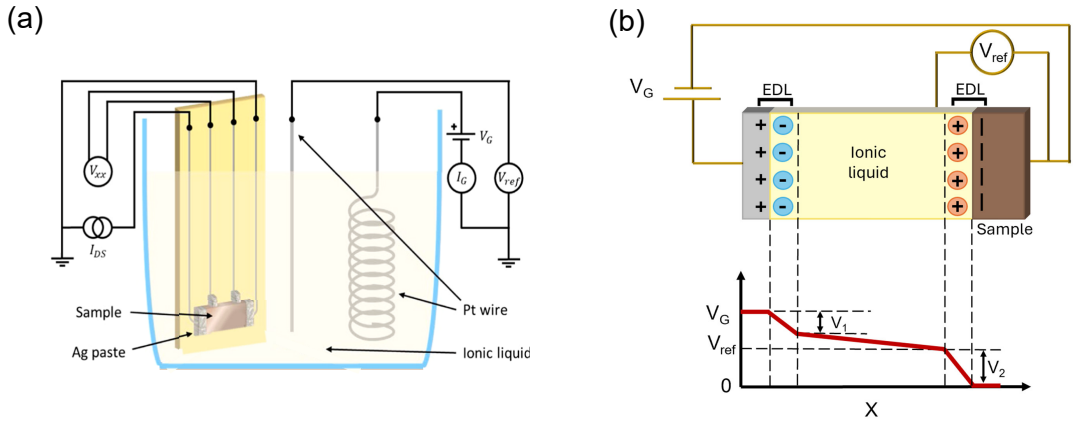

Figure 2.2: (a) Diagram illustrating the enhanced experimental configuration for ionic gating-induced protonation, which includes the electrical connection for applying the gate voltage (V_G), tracking the reference voltage drop (V_{ref}) across the electrolyte/sample interface, and measuring the four-probe resistivity. Adapted from Ref. [7]. (b) Diagram illustrating the distribution of the applied V_G across the electric double layer (EDL) capacitances at the gate/electrolyte and electrolyte/sample interfaces, highlighting that the voltage drop across the sample is smaller than the applied V_G [98].

2.2.2 Customizations

The experimental setup described above has been tailored in the following chapters to accommodate the specific requirements of the materials under investigation and

the associated measurement instrumentation. For materials prone to readily releasing intercalated protons, the setup has been integrated directly onto the cryogenic probe. This configuration allows the sample to be rapidly cooled immediately after the IGP process, minimizing hydrogen (H) desorption and enabling transport measurements at a proton concentration that would otherwise be unstable. This method is referred to as *in-situ* IGP, as the intercalation process is performed directly on the probe used for both ρ vs. T and PCARS measurements.
Conversely, for materials that are capable of retaining intercalated protons, the IGP is performed separately on a dedicated bench. After the process, the sample is rinsed in ethanol/acetone to remove any residual electrolyte, mounted onto the measurement probe, and subsequently electrically characterized. This method is therefore referred to as *ex-situ* IGP.
In the following, a brief summary of the specific customizations made for both *in-situ* and *ex-situ* IGP is presented.

Ex-situ ionic gating-induced protonation

The *ex-situ* IGP, conducted on a dedicated bench, provides significant flexibility as is not constrained by the limitations imposed by cryogenic probes. This allows for the full implementation of the enhanced configuration shown in fig. 2.2a by pouring the electrolyte into a Duran crucible where both the gate electrode and the contacted sample are fully immersed [8]. Additionally, the operating temperature of the IGP can be raised above room temperature by placing the setup on a hot plate [11, 101]. Higher temperatures are expected to enhance proton generation in the electrolyte and improve their diffusion into the sample [102, 103, 104].
However, for extended IGP treatment durations, electrical contacts for four-probe measurements are deliberately not included. This decision is based on the fact that prolonged exposure to a polarized electrolyte, which naturally degrades and becomes more reactive, increases the likelihood of interactions with the electrical contacts. This occurs regardless of the insulating GE varnish layer, leading to unreliable electrical measurements. Consequently, during extended IGP treatments, the process progression is monitored solely through V_{ref} and I_{G}. Only at the end of the IGP, the four-probe resistivity measurements are carried out as a function of temperature to assess the effects of each gating protocol.

In-situ ionic gating-induced protonation

Concerning the *in-situ* IGP, instead, the setup shown in fig. 2.2a must be adapted to fit the physical constraints of the cryogenic probes.
In the cryocooler configuration, an L-shaped holder is attached to the cold finger, supporting a compact version of the original setup shown in fig. 2.2a. Here, the electrolyte is contained within a custom-made Stycast pool, with the sample secured

at the base and a platinum foil gate electrode fixed to one of the inner walls (see fig. 2.3a). This L-shaped geometry ensures that the electrolyte remains level despite the vertical orientation of the cold finger, preventing spillage that could result in poor sample coverage or electrical shorting with surrounding components.

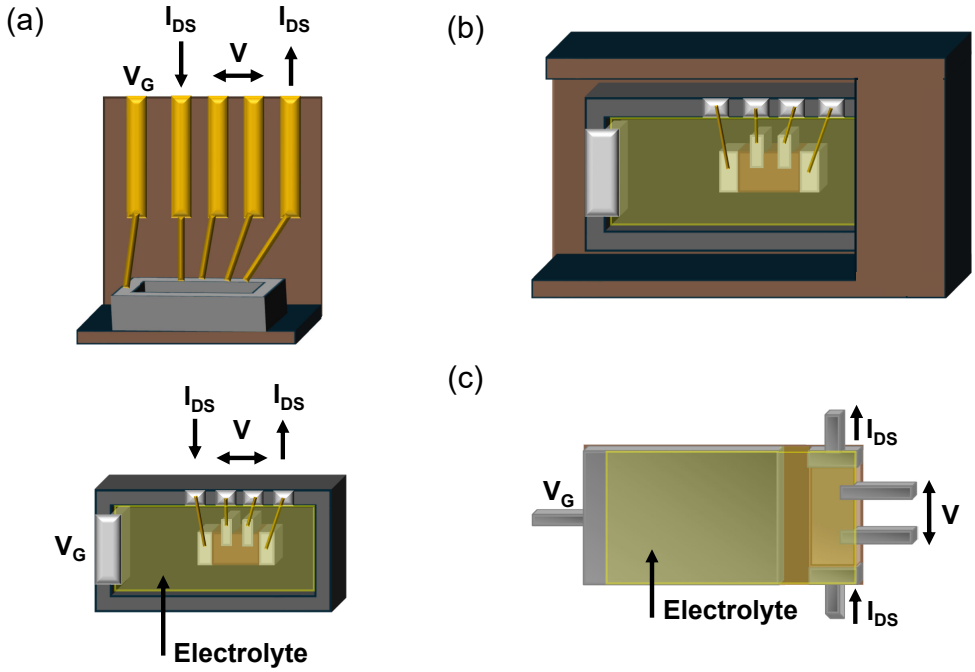

Figure 2.3: (a) Upper panel: L-shaped holder designed to house the compact experimental setup for *in situ* ionic gating-induced protonation (IGP) within the cryocooler. Electrical connections for the simultaneous application of the gate voltage (V_G) and monitoring the four-probe resistivity of the sample during gating are depicted. Lower panel: top view of the downsized experimental setup mounted on the L-shaped holder. (b) Schematic of the experimental setup, modified for mounting on ^{4}He inserts. The Stycast pool, which contains the downscaled IGP configuration, is placed into the spill-catching holder. This holder is specifically designed to reduce the impact of potential electrolyte spillage when the ^{4}He insert is vertically rotated for insertion into the ^{4}He cryostat. (c) Diagram illustrating the planar geometry implemented to enable IGP within the ^{3}He probe.

For the ^{4}He inserts, the L-shaped holder is not feasible. To address this, the insert is kept in a horizontal position during the IGP process to maintain a level electrolyte surface within the Stycast pool. Once the process is complete, the probe is rotated into its vertical operating position and quickly inserted into the cryostat to rapidly freeze the electrolyte. A Kapton foil cover is applied to prevent leakage before the electrolyte reaches the freezing point, and the entire assembly is placed in a custom

spill-catching holder to avoid shorts from potential spillage (see fig. 2.3b).
In the more space-constrained ^{3}He probe, even the full pool configuration is not viable. As a result, a planar geometry is employed, where the gate electrode is aligned parallel to the sample, and a droplet of electrolyte wets both surfaces (see fig. 2.3c). Since the sample must be mounted upside down, gravity could cause the droplet to detach and spill. To improve wettability and adhesion, a Kapton foil is placed over the droplet. For thin-film samples, this foil also helps flatten the droplet into a uniform layer, reducing mechanical stress from thermal expansion mismatch and protecting the sample during thermal cycling.
In addition to these physical constraints, the limited number of electrical contacts available on the probes makes simultaneous four-wire resistivity measurements and monitoring of V_{ref} unfeasible. Since electrical characterization is performed right after the IGP process, with the probe cooled to preserve the protonated phase while simultaneously measuring resistivity, the four-wire setup has to be configured beforehand. As a result, V_{ref} cannot be measured during the process. To compensate for the lack of this information, the gate contact area with the electrolyte is intentionally made much larger than the sample surface, minimizing the mismatch between the user-controlled V_{G} and the actual voltage drop that drives proton intercalation [105].

2.2.3 Typical voltage treatment

Ex-situ and *in-situ* IGPs differ not only in their experimental configurations but also in how V_{G} is managed throughout the process. In both methods, a V_{G} ramp is applied from 0 V up to a user-defined target voltage high enough to trigger electrochemical reactions within the electrolyte, resulting in proton generation and subsequent intercalation. The transition from a purely electrostatic to an electrochemical regime is identified by the onset of a non-negligible I_{G}, as is common practice (see 1.2) [80]. After the desired outcome is achieved, the two methods follow different procedures. In *ex-situ* IGP, the process is rapidly stopped by physically removing the sample from the electrolyte, thereby immediately opening the circuit. This abrupt termination is preferred over ramping V_{G} back to 0 V before sample extraction, as reducing the voltage can trigger the de-intercalation of the freshly intercalated protons. In contrast, in the *in-situ* IGP method, V_{G} is maintained even after the target is reached. This is because *in-situ* IGP is typically conducted on systems that are prone to easily release intercalated protons. Removing the voltage in these cases would halt proton pumping and allow proton loss to dominate. Therefore, instead of removing V_{G} to stop further intercalation, the sample is rapidly cooled to at least the freezing point of the electrolyte. This effectively suppresses any ongoing electrochemical activity, while mantaining the electric double layer polarized, thereby minimizing the potential release of protons. With the voltage still applied, the probe is then further cooled down to reduce the

likelihood of proton unloading through the formation of neutral H or H_2.

2.3 Point-contact Andreev reflection spectroscopy

As the final step in the characterization process, once superconductivity is detected, PCARS is performed. This technique consists in measuring the differential conductance of a point-like junction between a normal metal and the superconductor under investigation. Under suitable conditions, PCARS allows for the detection of the superconducting gap (Δ) and provides insights into its spatial symmetry and modulation by exploiting the phenomenon of Andreev reflection [106]. As such, PCARS can uncover spectral signatures indicative of unconventional – and potentially topological –superconductivity [36, 107].
In the subsequent sections, the fundamental principles of Andreev reflection are briefly reviewed, along with the criteria for obtaining reliable spectroscopic data. The experimental implementation of PCARS and the theoretical model employed to extract the gap information from measured spectra are then presented.

2.3.1 Andreev reflection

When a normal metal (N) is placed in contact with a superconductor (S) and a voltage bias is applied across the N/S junction, subgap electrons can contribute to transport through a mechanism known as Andreev reflection. In this process, an incident electron from the normal metal is reflected back as a hole, while a Cooper pair is simultaneously transmitted into the superconductor (fig. 2.4a). This process, solution of the Bogoliubov–de Gennes equations at the N/S interface, conserves both charge and momentum, leading to a doubling of the conductance compared to a N/N junction for sub-gap energies [108].
As a result, for applied voltages less than Δ/e and in the case of perfect barrier transparency, the current is carried entirely via Andreev reflection, producing this characteristic doubling of conductance. As the bias approaches Δ/e, the current contributed by Andreev reflection reaches a saturation point, referred to as the excess current. Beyond this voltage, two conduction channels open: Andreev reflection continues for electrons with sub-gap energies, while electrons with energies above the gap can undergo normal transmission into the superconductor. In this regime, the I–V characteristic exhibits a voltage-dependent component from normal transmission added to the constant excess current [109], causing the overall conductance to return to the N/N value (fig. 2.4b). Consequently, by measuring the normalized conductance of an ideal, barrierless N/S junction relative to an N/N equivalent case (fig. 2.4c), one can extract the value of the superconducting gap Δ, provided the energy of electrons crossing the junction is well defined. This requires the contact size to be smaller than the inelastic mean free path, ensuring

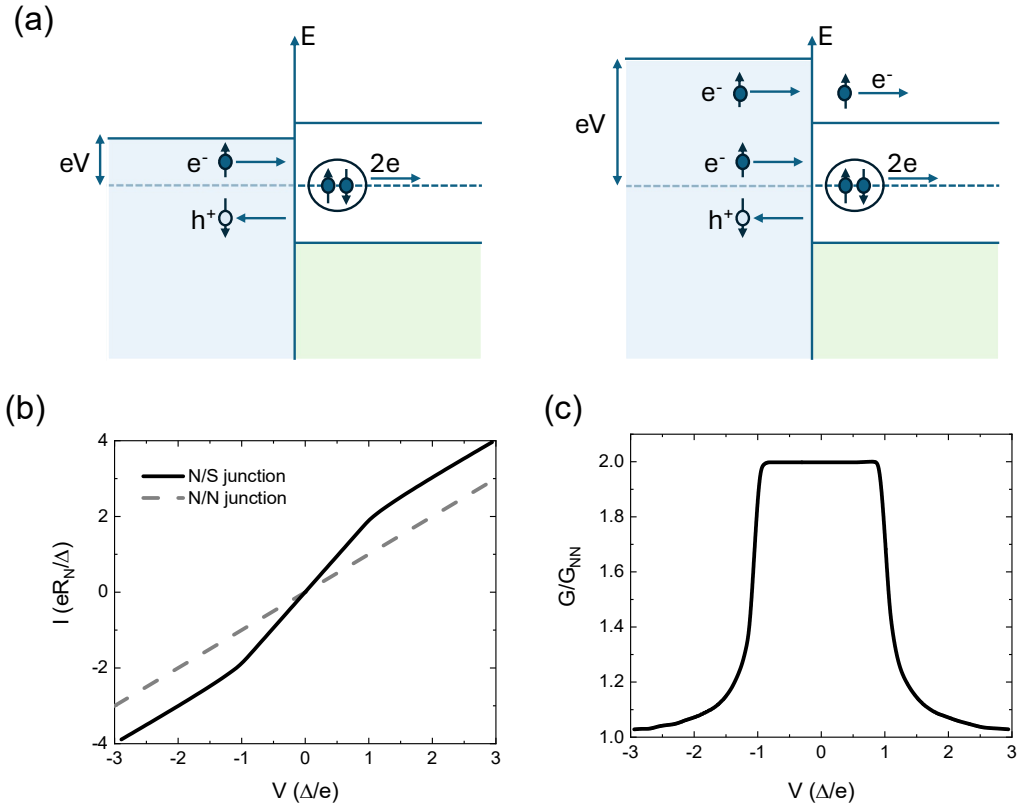

Figure 2.4: (a) Electrical transport of an ideal normal metal/superconductor (N/S) junction at 0 K, where only the Andreev reflection channel is active for voltages below Δ/e (left panel), while both the Andreev reflection and normal transmission channels are open for voltages above Δ/e (right panel). (b) I-V characteristic of an ideal N/S junction at 0 K, assuming no Andreev reflection for electrons with energy greater than Δ (solid black line), compared with the I-V characteristic of a N/N junction with the same resistance (dashed line). Both curves are normalized to the N/N current value at $V = \Delta$/e. (c) Theoretical conductance (G) of the ideal N/S junction, normalized to the equivalent N/N conductance (G_{NN}).

ballistic or diffusive transport – where electrons experience either no scattering or only elastic scattering, respectively. In addition, the contact dimensions must be smaller than the superconducting coherence length. This requirement is crucial for two reasons: first, to prevent proximity effects from suppressing superconductivity at the interface; and second, to avoid the destruction of the superconducting state around the contact due to overcritical current densities. Indeed, when the bias voltage is close to Δ/e, the current density at the contact may exceed the critical value. Although the current density decreases as it spreads away from the contact,

if the region where it remains overcritical is comparable in size to the superconducting coherence length, then the superconductivity near the contact is destroyed [110, 111].

2.3.2 Transport regimes

PCARS provides energy-resolved insight into the superconducting gap, but only under the condition that the energy of electrons crossing the junction remains well defined. This requires the absence of inelastic scattering within the contact region, since such scattering randomizes electron energies and induces local, voltage-dependent heating. The resulting local suppression of superconductivity produces a conductance spectrum that lacks spectroscopic information, appearing as a broadened peak centered at zero bias [112, 113].

To prevent these effects, the contact size (a) must be smaller than the inelastic mean free path (ℓ). When this condition is met, two distinct transport regimes can be identified:

- Ballistic regime:
  This ideal regime occurs when the contact size is much smaller than the inelastic mean free path ($a \ll \ell$) and smaller than the elastic mean free path ($a < \ell_e$). In this case, electrons travel through the contact without undergoing scattering.
  The ballistic nature of a point contact can be evaluated by measuring its resistance and estimating the contact size using the Sharvin resistance formula, which is applicable in this regime. Assuming the contact is circular with radius a, the Sharvin resistance is given by [114]:

  $$R_S = \frac{4\rho\ell}{3\pi a^2} \tag{2.3}$$

  where ρ is the residual resistivity of the material. From the measured R_S, along with known values of ρ and ℓ, the contact size a can be calculated. If the condition $a \ll \ell$ holds, the contact is confirmed to be in the ballistic regime.

- Diffusive regime:
  In this case, the contact size is still smaller than the inelastic mean free path but exceeds the elastic mean free path ($\ell_e < a < \ell$). Elastic scattering occurs within the contact region, leading to partial suppression of spectroscopic features compared to the ballistic limit. Additional complications may arise if the current exceeds the critical value, driving the superconducting region of the contact into the normal state. Indeed,the total resistance in the diffusive

regime can be expressed as [106, 115]:

$$R = R_S + \Gamma\left(\frac{\ell}{a}\right)\frac{\rho_1 + \rho_2}{4a} \tag{2.4}$$

Here, ρ_1 and ρ_2 are the resistivities of the two materials forming the contact, and Γ is a geometric factor that approaches 1 when $a \ll l$ and 0.7 when $a \gg l$. If the superconducting side becomes normal due to overcritical current, ρ_2 becomes finite, introducing an extra voltage drop across the contact. This suddenly reduces the conductance, potentially distorting the spectrum. If the transition to the normal state occurs at energies well above the gap, the extracted gap value Δ remains unaffected. However, if it occurs near Δ, it can compromise the spectroscopic signal.

2.3.3 Soft point-contact Andreev reflection spectroscopy

Experimentally, creating a small contact between N and S – narrow enough to ensure ballistic electron transport –is commonly achieved using the needle-anvil technique [116, 117, 118, 119]. In this method, a metallic tip, sharpened by electrochemical or mechanical means, is gently pressed against the sample. A current is applied across the tip-sample interface, and the resulting voltage is measured to obtain the I–V characteristic of the junction. Differentiating this curve yields the differential conductance as a function of voltage, which reflects the electron energy. This technique offers several key advantages. By adjusting the pressure applied to the tip, one can control the contact resistance, optimizing the spectroscopic conditions. Additionally, the contact can be repositioned, allowing for multiple measurements across different regions of the sample. This spatial flexibility, combined with the small contact area of the tip, facilitates local probing of superconducting properties. However, the needle-anvil method has limitations. Due to its limited mechanical stability, the contact is highly sensitive to vibrations and thermal cycling, which can be particularly problematic for superconducting gap measurements at cryogenic temperatures. Moreover, positioning the tip accurately on very small or fragile samples can be challenging.

To overcome these challenges, a "soft" point-contact approach has been adopted [120, 106, 121, 122, 36]. In this method, a thin metallic wire – typically gold, about 25 µm in diameter – is gently pressed against the sample and optionally stabilized using a small drop of conductive paste, such as silver or gold paint. The resulting contact spot is around 50 µm when paint is applied, or considerably smaller without it. In the first case, despite its larger apparent size, the contact can remain in the ballistic regime, as electrical conduction occurs only at discrete microscopic regions where the gold wire or silver grains of the paste physically touch the sample (see fig. 2.5a). Thus, the overall contact behaves as a parallel of microjunctions, which

can result in ballistic electron transport [106]. If the ballistic regime is not initially achieved, the contact can be optimized for spectroscopy by applying short voltage or current pulses (≈ 50 ms duration) [123]. These pulses can disrupt existing microjunctions or form new ones by breaking through thin oxide layers on the sample surface, thereby tuning the contact into the desired ballistic regime.

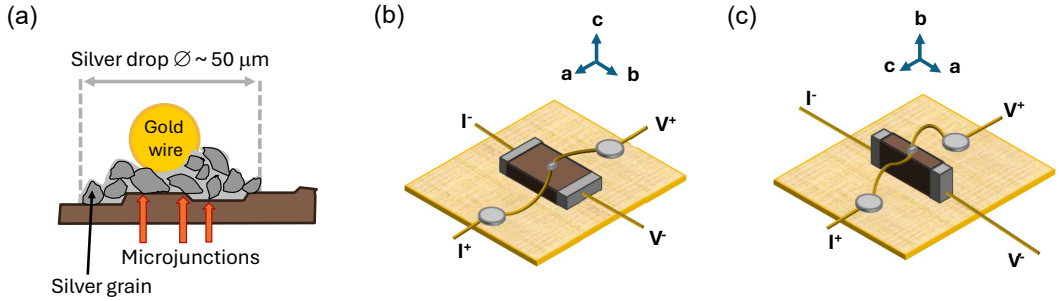

Figure 2.5: (a) Sketch of the actual soft point-contact Andreev-reflection spectroscopy (PCARS) contact, highlighting the formation of a parallel of microjunctions where silver grains in the conductive paste are in direct contact with the sample. (b, c) Electrical configurations for performing soft PCARS along different crystallographic directions: along the c axis (b) and within the ab plane (c) respectively.

Compared to the needle-anvil technique, this configuration offers enhanced mechanical and thermal stability, making it ideal for low-temperature measurements after thermal cycling, as well as for use with delicate or small crystals [124]. It allows stable electrical contacts to be made on different facets of a sample, enabling current to be injected along different crystallographic directions in anisotropic materials and enabling directional characterization of their properties. For layered materials or thin films, this allows the current to be preferentially oriented either along the c axis or within the ab plane [121, 125, 126]. The corresponding electrical connection schemes for directional soft-PCARS are shown in fig. 2.5b,c.

Soft point-contact Andreev reflection spectroscopy under gating

Remarkably, during this Ph.D. work, the soft PCARS technique has been performed even on samples under gating – that is, with the samples covered by frozen electrolyte and with V_G applied. This setup has never been explored before, since ionic gating was traditionally considered detrimental to forming reliable and tunable spectroscopic soft contacts. However, for samples that readily release H when gating is removed, a conventional preparation step from IGP to PCARS at room temperature without applied voltage would cause the intercalated state to vanish. In such cases, performing PCARS under gating became essential, so the samples

were prepared with contacts compatible with soft PCARS prior to IGP. Strikingly, tunable spectroscopic contacts were successfully attained.

2.3.4 Analysis of point-contact Andreev-reflection spectra

The actual PCAR spectra are significantly more complex than the simplified example shown in fig. 2.4c. That curve represents the theoretical conductance for an ideal case: a perfectly transparent N/S interface at 0 K, where both the normal metal and the superconductor are isotropic and have spherical Fermi surfaces. Under these conditions, the normalized conductance sharply doubles at the energy corresponding to Δ and remains constant within the energy range from $-\Delta$ to $+\Delta$ [127].
These ideal conditions are seldom realized in practice. Therefore, the model – known as the Blonder–Tinkham–Klapwijk (BTK) model – must be refined by introducing adjustable parameters that reflect deviations from ideal behavior. To extract meaningful physical information – such as the magnitude and symmetry of the superconducting gap – from PCARS measurements, a fitting procedure is employed. In this process, experimental data are compared with theoretical predictions, and the model parameters are iteratively adjusted to achieve the best agreement.

One of the first idealizations to be relaxed is the assumption of perfect interface transparency [106]. This is accounted for by introducing a dimensionless parameter Z, which characterizes the potential barrier height at the N/S interface. In this refined model, an electron incident normally on the interface may undergo four processes: Andreev reflection, normal reflection, and transmission as either an electron-like or hole-like quasiparticle [127]. At zero temperature, the total current across the N/S junction is given by [109, 106]:

$$I_{\mathrm{NS}} = \int_{-\infty}^{\infty} [f(E - eV) - f(E)]\, \sigma(E)\, dE \tag{2.5}$$

where $f(E)$ is the Fermi-Dirac distribution and $\sigma(E)$ is the differential conductance. The conductance, obtained by solving the Bogoliubov–de Gennes equations, is expressed as:

$$\sigma(E) = \tau_{\mathrm{N}} \cdot \frac{1 + \tau_{\mathrm{N}}|\gamma(E)|^2 + (\tau_{\mathrm{N}} - 1)|\gamma(E)^2|^2}{|1 + (\tau_{\mathrm{N}} - 1)\gamma(E)^2|^2} \tag{2.6}$$

where $\tau_{\mathrm{N}} = 1/(1 + Z^2)$ represents the conductance of the junction when the superconductor is in its normal state, and $\gamma(E)$ is a complex energy-dependent quantity defined as:

$$\gamma(E) = \sqrt{\frac{E - \sqrt{E^2 - \Delta^2}}{E + \sqrt{E^2 - \Delta^2}}} \tag{2.7}$$

The normalized conductance is then given by $G(E) = \sigma(E)/\tau_N$. In the ideal case ($Z = 0$), the conductance profile matches the simplified example in fig. 2.3.1c. As Z increases, the zero-bias conductance decreases, and peaks emerge near $|E| = \Delta$, signaling the onset of tunneling-like behavior (see fig. 2.6a). In the limit $Z \to \infty$, the interface behaves as a normal-insulator-superconductor junction, where Andreev reflection is suppressed and charge transport is dominated by quasiparticle tunneling. Non-zero Z values typically arise from surface roughness, interfacial disorder, or oxide layers, which enhance electron reflection at the interface.

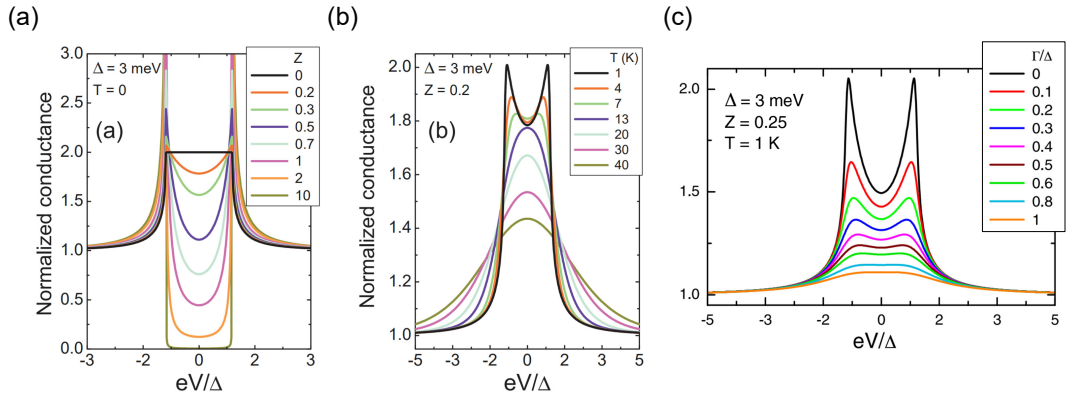

Figure 2.6: (a) Theoretical point-contact Andreev reflection (PCAR) spectra for an s-wave superconductor with an energy gap $\Delta = 3\,\text{meV}$ at 0 K, shown for various barrier transparencies Z. (b) Theoretical PCAR spectra for the same superconductor with fixed $Z = 0.2$, illustrating the effect of increasing temperature on thermal broadening. (c) Theoretical PCAR spectra at 1 K and fixed $Z = 0.25$, demonstrating the influence of different quasiparticle lifetime-induced energy broadenings. Data reprinted from Ref. [106]

Another idealization that must be relaxed is the assumption that all electrons strike the interface perpendicularly [106]. In real systems, electrons approach the interface from a distribution of angles [128]. If the Fermi velocities on the N and S sides are assumed equal [128], the directions of the reflected and transmitted particles follow that of the incident electron, as required by the conservation of transverse momentum in Andreev reflection. This angular dependence modifies the differential conductance to $\sigma(E, \theta_N)$, where θ_N is the angle between the trajectory of the incident electron and the normal to the interface. For an isotropic gap, eq. (2.6) remains valid, but the N/N transmission coefficient τ_N is now angle-dependent: $\tau_N = \cos(\theta_N)^2/(\cos(\theta_N)^2 + Z^2)$. The normalized conductance is then obtained by integrating $\sigma(E, \theta_N)$ over the entire half-plane of incidence angles and normalizing

it by the corresponding integral of τ_N over the same angular range:

$$G_{2D}(E) = \frac{\int_{-\frac{\pi}{2}}^{+\frac{\pi}{2}} \sigma(E, \theta_N) \cos(\theta_N) d\theta_N}{\int_{-\frac{\pi}{2}}^{+\frac{\pi}{2}} \tau_N \cos(\theta_N) d\theta_N} \tag{2.8}$$

In practice, the Fermi velocities are rarely identical on both sides, leading to a discrepancy between the incidence angle in the normal metal, θ_N, and the transmission angle in the superconductor, θ_S. Nevertheless, if the difference in Fermi velocities is not too large, equation (2.8) can still provide a good approximation, with the mismatch effectively incorporated into the barrier strength parameter Z, which then becomes an effective parameter Z_{eff}.

Despite these refinements, the model often struggles to accurately reproduce the shape of measured PCAR spectra, particularly the width and height of the conductance peaks. This discrepancy arises because Cooper pairs have a finite lifetime, during which they decay into quasiparticles. As a result, their energy is not sharply defined, leading to a broadening of the gap feature. Additionally, extrinsic factors can further broaden the spectra. To account for this broadening, the energy E is replaced with a complex value $E - i\Gamma$, where Γ is treated as an additional fitting parameter along with Z (see fig. 2.6c) [129, 130, 131]. Furthermore, all experimental measurements are performed at finite temperatures, as opposed to absolute zero. This introduces thermal smearing of spectral features. To model this effect, the Fermi functions in eq. (2.5), must be evaluated at the actual experimental temperature, instead of assuming ideal step functions. The differential conductance is then obtained by convolving the calculated $\sigma(E, \theta_N)$ with the derivative of the Fermi function evaluated at the working temperature, thus incorporating thermal broadening into the model (see fig. 2.6b).

Finally, the model can be generalized beyond conventional superconductors, where Cooper pairs consist of electrons with opposite spins experiencing an isotropic gap in momentum space. Other gap symmetries are also possible, though constrained by the spin configuration of the Cooper pair: the gap function must be even for singlet states and odd for triplet states to preserve the overall antisymmetry of the superconducting wavefunction under particle exchange. Adopting the terminology from atomic orbitals to describe the angular dependence of the gap function in momentum space, even-parity gap functions can be s-wave, which are isotropic with a uniform magnitude in all directions, or d-wave, which have two angular nodes and a cloverleaf-like structure. Odd-parity gap functions can be p-wave, with a single angular node and a sign change along a particular direction, or f-wave, which display more complex angular variations.

2.3.5 Point-contact Andreev reflection spectroscopy and topological superconductivity

The final generalization discussed in the previous paragraph establishes PCARS as a powerful probe for identifying signatures of potentially topological superconducting states. To illustrate this point, the paradigmatic example of a one-dimensional spin-polarized p-wave superconductor is considered [132, 28, 133]. This system is predicted to host Majorana bound states localized at its ends, or equivalently, zero-energy Majorana modes in the excitation spectrum. In practice, this theoretical model can be effectively realized in a one-dimensional semiconductor nanowire with strong Rashba spin–orbit coupling placed in proximity to an s-wave superconductor [133]. When a sufficiently large magnetic field is applied, the proximity effect generates an effective p-wave pairing, leading to the emergence of a pair of Majorana zero modes at the two ends of the nanowire. Solving the BTK model at the end of the nanowire for different barrier strengths Z at the superconductor/normal-metal (here, nanowire/normal-electrode) junction produces the spectra shown in fig. 2.7a [132]. As long as the transparency is not perfect ($Z \neq 0$), a zero-bias conductance peak emerges. This peak originates from the sign change of the effective p-wave order parameter at the interface, which generates surface Andreev bound states that, in this context, are precisely the Majorana quasiparticles. As the transparency

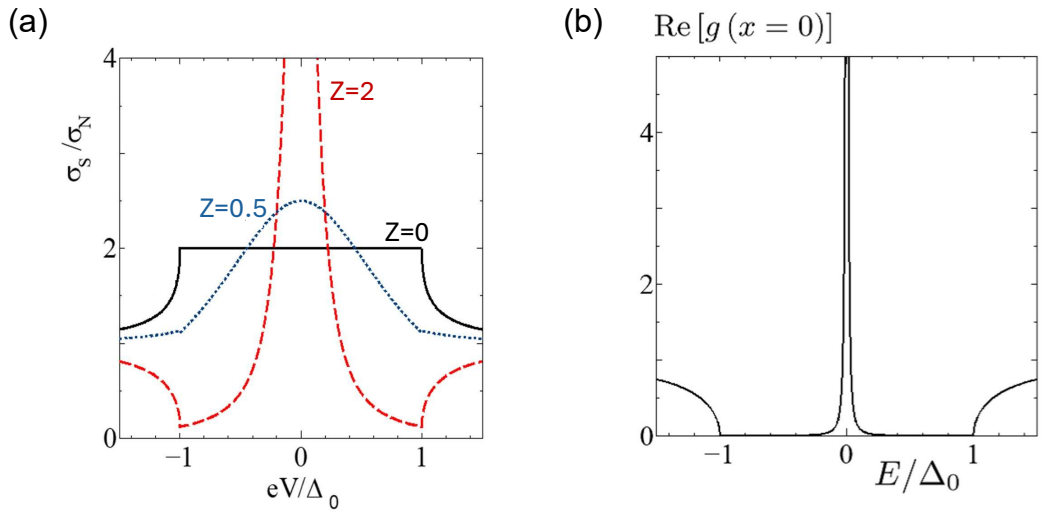

Figure 2.7: (a) Theoretical conductance of a normal metal/spin-polarized p-wave superconductor junction, normalized to its normal-state value, for different barrier strengths Z. The black, blue, and red curves correspond to $Z = 0$, $Z = 0.5$ and $Z = 2$, respectively. (b) Energy dependence of the local density of states in a one-dimensional spin-polarized p-wave superconductor. Adapted from [132].

reduces ($Z > 0$), the peak increases in amplitude and narrows in width, consistent with the expectation that for large Z, when the system crosses over from the Andreev to the tunneling regime, the conductance spectrum approaches the local density of states. In this limit, the density of states indeed exhibits a sharp peak at zero energy, as shown in fig. 2.7b [132]. This example thus demonstrate the effectiveness of PCARS in detecting topological superconductivity.

Attention is now focused on a class of topological superconductors central to this thesis, namely superconductors with a two-dimensional $p_x \pm ip_y$ pairing symmetry. Such systems can be realized experimentally through the proximity effect between a topological insulator and an s-wave superconductor, which induces an effective $p_x \pm ip_y$ pairing on the surface while retaining the bulk s-wave character [34]. These superconductors are predicted to host Majorana bound states in their vortex cores - either in vortices generated by an external magnetic field or in vortices that form even in zero applied field due to the presence of magnetic atoms within the material [134].
These vortex-core states have been extensively studied and continue to be actively investigated, primarily using tunneling spectroscopy. The dominance of this technique arises from two key advantages: its exceptional spatial and energy resolution – especially when atomically sharp tips are employed – which enables mapping of the local density of states within a vortex with nanometric precision, and its non-contact operation [135], which makes it ideally suited for experiments in which vortices (and therefore Majorana bound states) are manipulated in space. In principle, this allows braiding operations to be performed while simultaneously monitoring the electronic signatures of Majorana modes [54]. Consequently, before considering how they might be distinguished using PCARS, it is useful to briefly summarize what tunneling experiments and theory have established so far.

From tunneling theory, these states are predicted to be localized at the vortex core, with amplitudes that decay radially over a length scale set by the superconducting coherence length, while remaining pinned at zero energy. At zero temperature, the peak height is expected to reach the quantized value $2e^2/h$ [136], as in the one-dimensional case discussed above. In real experiments, however, finite temperature reduces the amplitude and broadens the peak in energy. The Majorana zero-energy peak is also expected to remain robust in both height and width under variations of magnetic field. However, at sufficiently high fields, overlap between neighboring Majorana modes can lead to hybridization and splitting of the zero-energy state [137]. At still higher fields, where superconductivity is suppressed, these states disappear entirely.
Experimentally, tunneling spectroscopy has revealed zero-bias conductance peaks consistent with Majorana zero modes confined to vortex cores [54, 135, 51, 52, 53]. Owing to its high spatial and energy resolution, the evolution of the zero-bias

peak has been mapped across individual vortices, showing a reduction in amplitude away from the core center while remaining centered at zero energy (see fig. 2.8). Nonetheless, alternative explanations for zero-bias peaks must be carefully consid-

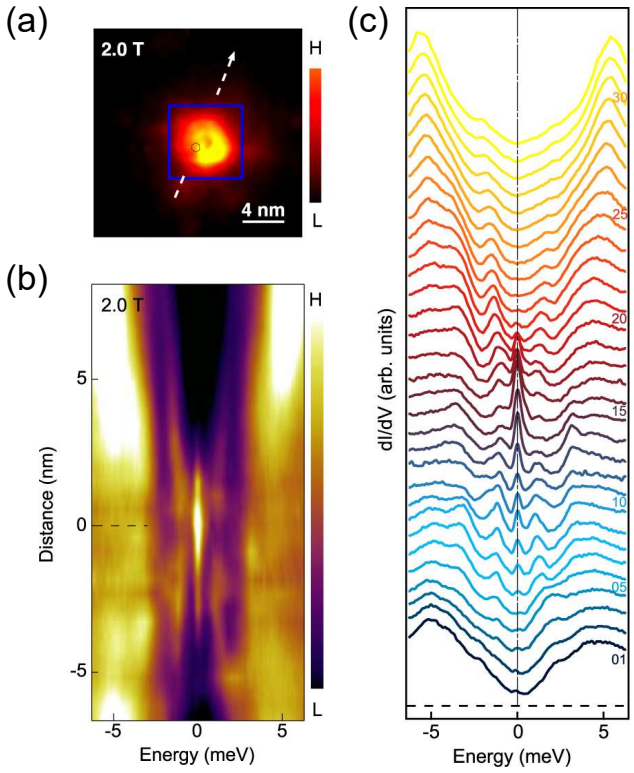

Figure 2.8: (a) Zero-bias scanning tunneling conductance map of a vortex pinned by an impurity in LiFeAs. (b) Differential conductance (dI/dV) as a function of energy, measured along the white dashed line in (a) under a 2.0 T magnetic field, highlighting the spatial resolution of scanning tunneling microscopy in resolving vortex bound states. (c) Waterfall plot stacking the spectra from (b). Adapted from [135]

ered. These include the Kondo effect from magnetic impurities [138], a Josephson supercurrent arising from an unintended superconductor–insulator–superconductor junction [139], weak antilocalization in systems with strong spin–orbit coupling [140], and trivial Caroli–de Gennes–Matricon states [141] that can merge into an apparent zero-bias peak if the energy resolution is insufficient. These possibilities can be distinguished experimentally. For instance, a Kondo-induced peak is expected to split with increasing magnetic field [142]. Caroli- de Gennes- Matricon states, by contrast, fan out and decrease in amplitude as the scanning tip is moved away from the vortex center [55, 143], allowing the lowest-order peaks to be resolved

if the experimental resolution is sufficient – or, if not, producing an apparent broadening of the zero-bias peak. Such diagnostics are essential for separating genuine Majorana signatures from other mechanisms that produce zero-bias features.

By analogy with the one-dimensional spin-polarized p-wave case, PCARS measurements on vortices are expected to show a zero-bias conductance peak whose height and width depend sensitively on the barrier strength Z. As in tunneling experiments, however, such a peak can also arise from conventional mechanisms. Applying a magnetic field helps rule out both weak antilocalization and the Kondo effect. Moreover, because a PCARS junction is formed by a direct metallic contact between a normal metal and a superconductor, the appearance of a Josephson supercurrent is highly unlikely. Turning instead to Caroli–de Gennes–Matricon states, there is no explicit theory treating the BTK model in the presence of such bound states. Nevertheless, since these states appear as peaks at half-integer multiples of Δ^2/E_F [141], it is reasonable to expect that, for finite Z, they overlap and merge into a plateau in the conductance. Consequently, in a trivial superconductor, this overlap would prevent a peak at zero bias, whereas in a topological superconductor, a signature at zero energy should persist.
Experimentally, it is also important to remember that PCARS is a contact technique whose spatial resolution is far from the atomic sharpness of tunneling spectroscopy, especially in soft-PCARS (see paragraph 2.3.3). In this case the measured signal is effectively a parallel sum over many microjunctions formed by the conductive paste grains contacting the sample. Consequently, part of the signal originates from vortex cores, while part comes from regions outside the vortices, such as the s-wave bulk. This mixing, together with the strong Z-dependence of the peak shape, makes it difficult to predict how distinguishable the vortex signal is from the background. Increasing the vortex density – via impurities or an applied magnetic field – may further be detrimental, as it can lead to wavefunction overlap and an actual splitting of the zero-bias peak. It is therefore likely that, in such systems, spectra exhibiting a zero-bias conductance peak will be relatively rare. In those spectra where such a peak is observed, however, Caroli-de Gennes-Matricon states may be safely ruled out as its origin, owing also to the aforementioned spatial averaging intrinsic to (soft) PCARS; additionally, a strong indication of a topological – rather than trivial – origin would be the lack of splitting, or broadening, under the application of a magnetic field. Overall, these considerations should still be considered speculative as a comprehensive theoretical framework for soft PCARS in this context is still lacking.

Finally, a further class of topological superconductors of interest in this thesis comprises three-dimensional systems with linearly dispersing Majorana fermions on their surfaces [27]. These modes generate surface Andreev bound states, leading to a zero-bias peak in the conductance spectrum. A PCAR spectrum measured

in $Cu_xBi_2Se_3$, interpreted as arising from dispersive Majorana fermions, is shown in fig. 2.9 [36, 144]. Because these modes are dispersive in energy and extend continuously across the surface, they do not correspond to the localized Majorana bound states with non-Abelian statistics that are of primary interest for quantum computation. Nevertheless, this case demonstrates that PCARS can yield useful information even in systems of this type.

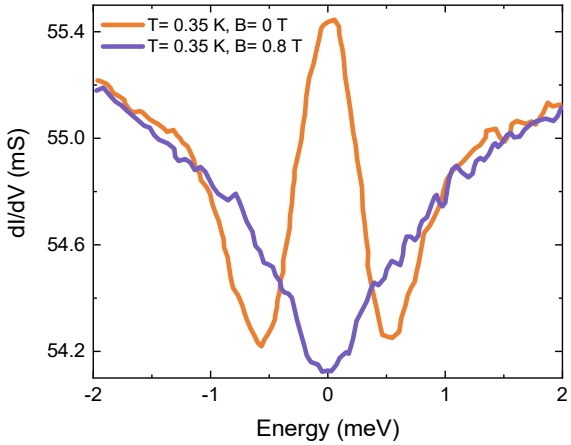

Figure 2.9: Point-contact Andreev reflection spectra (dI/dV vs. energy) of the potentially nematic spin-triplet topological superconductor $Cu_xBi_2Se_3$, which is expected to host dispersive Majorana fermions at its edge. Both spectra were measured at the base temperature of 0.35 K with the orange curve taken at zero magnetic field and the purple curve at 0.8 T. [36]

Chapter 3

Deep eutectic solvents for ionic gating-induced protonation

Despite its potential – particularly for the induction of superconductivity – ionic gating-induced protonation (IGP) remains relatively underexplored. This gap offers an opportunity to optimize IGP as an efficient and reliable approach for hydrogen (H) loading via ionic gating, with electrolyte choice playing a critical role. This study examines a previously uninvestigated class of electrolytes: deep eutectic solvents (DESs). Guidelines for performing DES-based IGP are developed and optimized to maximize H loading in palladium, selected for its high H absorption capacity and well-characterized transport properties as a function of the H content. The results demonstrate that DESs can outperform the electrolytes conventionally used in IGP and establish a potential framework for maximizing H loading in different materials, although material-specific adjustments may be required. The findings reported here will be useful in the following chapters, where IGP is employed on candidate topological superconductors to induce superconductivity or fine-tune the existing superconducting state.
As this study focuses on the H insertion technique itself rather than on modulating the superconducting properties via H insertion, only key motivations and results are summarized here; full experimental details are provided in Appendix A.

3.1 Framework

As discussed in section 1.2.2, IGP evolved as a natural extension of electrostatic gating. Consequently, the electrolytes traditionally used in IGP are those optimized for enabling substantial carrier accumulation, namely ionic liquids like DEME-TFSI and EMIM-BF_4 [145, 102, 146, 103, 147, 148, 101]. These electrolytes are commercially available, have low melting points, wide electrochemical windows, and minimal water content after prolonged heating in dry conditions [149]. The latter

two properties are particularly crucial for electrostatic gating, where preventing unwanted electrochemical reactions is essential. However, ionic liquids are not ideal for IGP: despite their hygroscopicity, they absorb insufficient water at ambient conditions to support significant H^+ injection in IGP, which relies on water dissociation. As a result, the external addition of pure water is often required, especially when IGP is carried out under dry or vacuum conditions. Moreover, fluorinated ionic liquids pose environmental and safety issues, as TFSI-based compounds are reported to be toxic [150, 151, 152] and BF_4 hydrolysis produces corrosive HF [153]. Beyond being hazardous, these corrosive byproducts can also directly compromise the integrity of samples during IGP.

To overcome these limitations, one potential strategy is to perform IGP using DESs, a distinct class of electrolytes compared to ionic liquids. Composed of a H-bond donor and acceptor, DESs – unlike ionic liquids – can generate H^+ via direct solvent dissociation, eliminating dependence on water and allowing IGP in environments that are not necessarily humid. In addition, they have melting points far below those of their individual components [154], are less toxic, biodegradable, and easily synthesized from inexpensive, widely available materials [155, 156, 157].

To date, DESs have not been explored for IGP. Thus, to validate their potential as a viable alternative to ionic liquids, it is crucial to demonstrate their ability to enable substantial H^+ injection. Accordingly, a study was conducted to evaluate the proton-loading capability of a 1:3 choline chloride:glycerol DES, hereafter referred to as 1:3 ChCl:gly DES. This composition was chosen for its high ionic conductivity, which promotes the formation of a strong electric field at the DES/sample interface, and for its ability to release protons at relatively low voltages, making it well suited for this application [158, 159, 160]. The 1:3 molar ratio further reduces viscosity compared to 1:2 or 1:4 mixtures, enhancing conductivity and ensuring more uniform H^+ uptake [161].
Palladium (Pd) was selected as the most suitable metallic material for this study due to its well-characterized response to increasing H doping levels, allowing real-time evaluation of IGP effects and estimation of injected H. Both Pd thin film and bulk foil were examined to evaluate the effectiveness of DES-based IGP across different sample thickness. Detailed information on the properties of Pd and the experimental methods employed in this study is provided in Appendix A.

3.2 Results

IGP were performed both on commercial Pd foils ($\sim 25\mu$m thick) and thermally evaporated Pd films (~ 34 nm thick). All protonation treatments were carried out *in situ* under ambient conditions. The gate voltage (V_G) was gradually increased

from 0 V to a final value ranging from 2 V to 12 V to induce H^+ uptake, while simultaneously monitoring the gate current (I_G) and resistivity (ρ). A representative example of the IGP dynamics for a Pd thin film is shown in fig. 3.1a. During the applied V_G ramp-and-hold sequence, I_G remained negligible until the onset of electrochemical reactions; once H^+ release started, it increased, reached a maximum, and subsequently declined due to DES degradation and pseudocapacitive contributions. Concurrently, the resistivity followed the characteristic non-monotonic evolution associated with H absorption in Pd. Pre- and post-gating resistivity vs. temperature ($\rho - T$) measurements confirmed successful protonation through the resulting changes in the transport properties. A summary of the ρ–T responses of Pd thin films treated at different final V_G values is shown in fig. 3.1b. The curves maintained a metallic coefficient, with their specific shape – namely, the presence or absence of the 50 K anomaly – depending on the amount of H loaded into Pd. Detailed descriptions of the measurement procedures are provided in Appendix A.

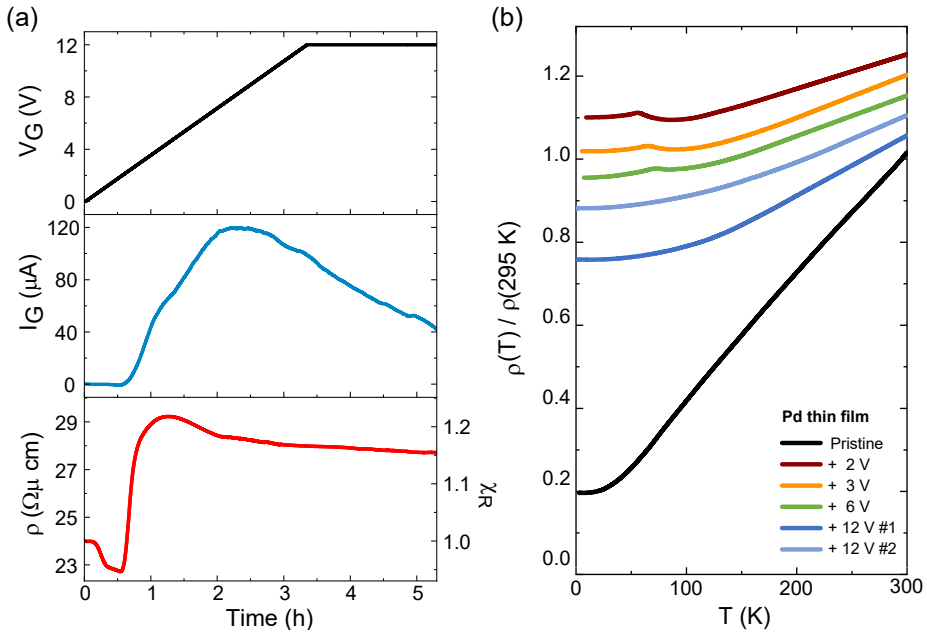

Figure 3.1: (a) Typical time evolution of ionic gating-induced protonation (IGP) of Pd thin films, presented in terms of the temporal profiles of the *in-situ* applied gate voltage V_G (top), the measured gate current I_G (middle), and the film resistivity ρ (bottom). Resistivity is presented both in absolute units (left axis) and normalized to the pristine resistivity ($\chi_R = \rho(x)/\rho(0)$) (right axis). (b) Resistivity as a function of temperature for Pd thin films measured before and after IGP. Each curve is normalized to its value at $T = 295\,K$ and labeled based on the final applied gate voltage V_G. To improve readability, curves with $V_G > 0$ are vertically shifted by 0.05. Adapted from Ref. [105].

From these measurements, the room-temperature resistivity after gating – specifically its value normalized to that of pristine Pd ($\chi_R = \rho(x)/\rho(0)$) – served as an indirect estimate of the H content (x) introduced through IGP, bypassing the inability to directly measure x (see Appendix A). This estimation was validated against systematic errors by analyzing the ρ–T response after each treatment, specifically by examining the temperature at which the resistivity anomaly occurred, when present.
Across experiments with different final V_G values, a positive correlation between H uptake and V_G emerged once the 1:3 ChCl:gly DES stability limit for electrochemical reactions ($V_G = 1.9\,V$) was exceeded (fig. 3.2). H concentration increased sharply around $V_G \sim 2$–$3\,V$, then continued to rise more gradually for $V_G > 3\,V$. Efficient H loading occurred without visible Pd damage up to $V_G = 12\,V$, reaching a maximum $x = (0.85 \pm 0.03)$ in bulk foils and an even higher H content in thin films: $x = (0.89 \pm 0.03)$, corresponding to $\sim 5.3 \times 10^{22}$ H cm^{-3} when accounting for the loading-dependent PdH_x unit cell [162]. Beyond $V_G = 12\,V$, rapid device degradation occurred.

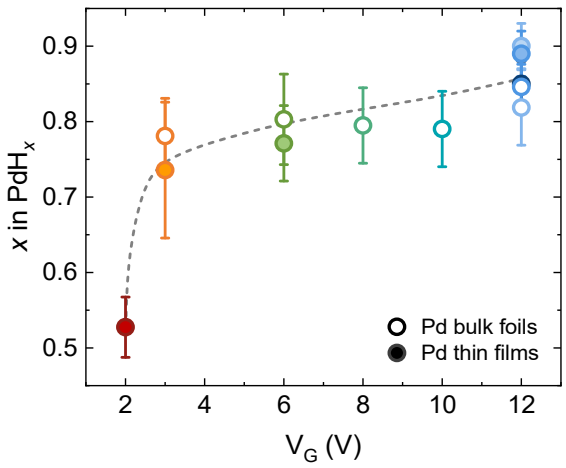

Figure 3.2: Gate voltage (V_G) dependence of the H concentrations (x) for gated bulk foils (hollow circles) and thin films (filled circles). The gray dashed line serves again solely as a visual guide. Adapted from Ref. [105].

To benchmark the performance of the 1:3 ChCl:gly DES, the experiment was repeated with EMIM-BF_4 under identical conditions, except that the final V_G was limited to $+3.5\,V$ to avoid direct intercalation of $EMIM^+$, a process known to occur above this threshold [75] (this would not be an issue in palladium, since the large $EMIM^+$ ion cannot be injected in its dense lattice; it would however be a critical issue when performing IGP on the layered materials targeted in the later chapters). Under these conditions, the maximum H concentration was achieved in

Pd thin films at a final V_G of +3.0 V, yielding $x = (0.65 \pm 0.04)$ or an H density of $\sim 3.9 \times 10^{22}$ cm^{-3}.

3.3 Discussion

Comparing the performance of 1:3 ChCl:gly DES and EMIM-BF_4, it becomes thus evident that the deep eutectic solvent outperformed the more conventional ionic liquid. As a matter of fact, at the voltage applied to EMIM-BF_4 that yielded the maximum doping (+3 V), the 1:3 ChCl:gly DES already achieved 13% greater H incorporation. This advantage is even more pronounced at the highest sustainable voltage for the 1:3 ChCl:gly DES (+12 V), where it enabled significantly higher protonation – yielding a maximum H uptake 37% greater than that of EMIM-BF_4 (see table 3.1). When compared with traditional electrochemical H loading techniques, the H concentration reached through DES-based IGP in palladium is equally impressive. Traditional approaches typically employ strong acidic electrolytes such as HCl and H_2SO_4, with HCl achieving H concentrations in Pd up to 5.3×10^{22} H cm^{-3} [163, 164] and H_2SO_4 reaching 5.8×10^{22} H cm^{-3} [165, 166]. The 1:3 ChCl:gly DES used here attained H loading comparable to HCl and approached within 9% that obtained with H_2SO_4, all without the use of corrosive or toxic substances. This underscores the potential of the relatively underexplored IGP, when combined with deep eutectic solvents, as a safe and effective alternative for H loading.

Compound	Electrolyte	Stoichiometry	Cell volume Å^3	H density 10^{22} cm^{-3}	Ref.
Pd	1:3 ChCl:gly DES	$PdH_{0.89}$	16.85 [162]	5.3	[105]
Pd	EMIM-BF_4	$PdH_{0.65}$	16.69 [162]	3.9	-
Pd	1 N HCl	$PdH_{0.89}$	16.85 [162]	5.3	[164]
Pd	0.1 N H_2SO_4	$PdH_{0.99}$	16.98 [162]	5.8	[166]

Table 3.1: Overview of the highest hydrogen (H) concentrations achieved in Pd through IGP. For studies where H densities were not explicitly reported, these values were estimated by dividing the reported stoichiometries by the corresponding unit-cell volumes. Note that all unit-cell volumes are given per formula unit.

Although this DES-based IGP method proved to enable impressively high H loading, the resulting H distribution was likely to be highly inhomogeneous (see Appendix A for supporting experimental evidence). Future work should therefore focus on designing deep eutectic solvents that enhance H uniformity within the host material, thereby advancing the synthesis of high-quality H-loaded samples

via IGP and fully realizing the potential of DES-based IGP. A promising approach involves optimizing ionic diffusivity both in the electrolyte and within the material undergoing IGP. Ionic mobility in the electrolyte can be increased by lowering its viscosity [167], while diffusivity inside the material can be enhanced by performing the IGP at higher temperatures [11, 101, 102, 103, 104]. However, it should be noted that increasing the working temperature carries risks of unwanted electrochemical side reactions such as electrolyte degradation or material etching [81], emphasizing the need to develop systems that remain stable at higher temperatures. In particular, alternative deep eutectic solvents for IGP applications should be designed with the following optimal characteristics:

- low viscosity to ensure high ionic conductivity and promote uniform H transfer [167],
- high proton availability to maximize gate-driven H injection,
- low threshold voltage for H release, allowing operation at lower gate voltages,
- a wide electrochemical window to minimize competing side reactions and permit the application of higher voltages to stabilize phases with elevated H concentrations,
- a broad liquid-phase temperature range – both above and below room temperature – to enable precise control of the IGP via temperature adjustments.

Chapter 4

Evidence for two-gap superconductivity in H_XTiSe_2

So far, this thesis has focused on understanding the mechanisms underlying the ionic gating-induced protonation (IGP) technique for inducing controlled modifications in the electronic properties of materials. These modifications have primarily been inferred through changes in their electric transport properties. However, when investigating superconductors – the main focus of this study – more detailed insights can be gained by probing the superconducting gap function via point-contact Andreev reflection spectroscopy (PCARS). This technique not only enables the detection of changes in the gap structure due to electronic modifications but also offers the potential to reveal the emergence of exotic superconducting states, including those associated with topological superconductivity.

Given the critical role of PCARS in this investigation, the focus now turns toward developing expertise in this technique for its application to candidate topological superconductors. Specifically, PCARS is employed to investigate the superconducting gap structure of the recently synthesized compound H_xTiSe_2. Due to its recent discovery, the superconducting phase of this material, obtained via hydrogen (H) intercalation of layered $TiSe_2$ [8], remains largely unexplored, with only preliminary magnetotransport measurements hinting at possible multigap superconductivity. Characterizing the superconducting gap function in this system is particularly compelling, as it may shed light on the interplay between superconductivity and the charge density wave (CDW) order present in pristine $TiSe_2$. Accordingly, directional PCARS measurements are performed on H_xTiSe_2, synthesized using the IGP expertise developed earlier, with the dual goals of directly investigating its gap function and gaining practical experience with PCARS in a layered compound structurally akin to materials subsequently explored as candidate topological superconductors.

The following sections provide a brief overview of the platform material, followed by a detailed presentation and analysis of the results of the measurements carried out to determine whether H_xTiSe_2 exhibits multiband superconductivity.

4.1 Framework for H_xTiSe_2 gap study

To appreciate the potential of assessing whether the superconducting state of recently synthesized H-intercalated $TiSe_2$, obtained via IGP, exhibits a nontrivial superconducting gap function, it is crucial to first outline the research framework that underpins this investigation. Specifically, this study is part of the broader endeavor of examining the possible interplay between CDW order and superconductivity.
$TiSe_2$ is a well-suited material for this purpose: as a layered transition metal dichalcogenides composed of $TiSe_2$ trilayers held together by van der Waals forces (fig. 4.1a) [168], it features a complex electronic structure resulting in a rich phase diagram encompassing both CDW and superconducting phases [169, 170, 171].

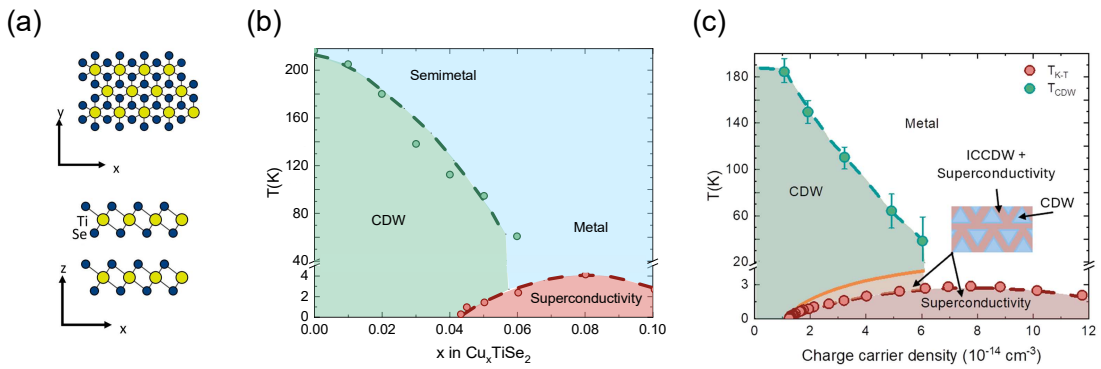

Figure 4.1: (a) Schematic crystal structure of 1T-$TiSe_2$, consisting of Se–Ti–Se trilayers stacked via van der Waals forces, shown from the top (upper panel) and side (lower panel) views. Adapted from Ref. [8]. (b) Electronic phase diagram of Cu_xTiSe_2 in the temperature–doping space. The regions of charge density wave (CDW) order and superconductivity are delimited by their respective transition temperatures. Data reprinted from Ref. [15]. (c) Electronic phase diagram of electrostatically doped $TiSe_2$ in the temperature–charge space. Regions showing CDW order and superconductivity are delimited by their characteristic transition temperatures. The inset illustrates one of the proposed mechanisms for superconductivity, arising at the incommensurate CDW domain walls between commensurate CDW islands. Data reprinted from Ref. [17]

In its pristine form, $TiSe_2$ hosts a commensurate $2\times2\times2$ CDW phase below $\approx$200 K,

whose origin remains debated. Upon Cu intercalation, this CDW order is progressively suppressed, giving rise to a superconducting dome with T_c reaching up to $\approx 4.15\,\mathrm{K}$ [15] (fig. 4.1b). Similar tunability has been observed under external pressure [172], electric-field-induced charge doping (fig. 4.1c) [17], and intercalation with Pd [16], Li [18], and diamines [173].
Within this framework, the observation of the Little-Parks effect in electrostatically gated and Li-doped $TiSe_2$ – which reveals a periodic modulation of the superconducting order parameter amplitude [17, 18, 19] – raises the intriguing possibility that the spatial texture of the CDW phase influences the superconducting state. This influence could manifest as anisotropy in the superconducting pairing or even a nontrivial symmetry of the superconducting gap.
Motivated by these prospects, several studies have explored the superconducting gap structure in $TiSe_2$. Notably, research on Cu-intercalated $TiSe_2$ has generally reported a single, isotropic superconducting gap (fig. 4.2a) [20, 21, 22]. However, in regimes where CDW order coexists with superconductivity – potentially resulting in spatial variations of the superconducting amplitude – more complex behavior has emerged. For example, muon spin rotation (μSR) experiments have suggested a two-gap state in underdoped Cu_xTiSe_2 (fig. 4.2c)[23], while PCARS on electrostatically doped $TiSe_2$ has revealed a zero-bias conductance peak inconsistent with simple isotropic s-wave pairing (fig. 4.2b) [17]. Tunneling spectroscopy measurements on Li_xTiSe_2 revealed an s-wave-like gap, but with a closing temperature exceeding the BCS prediction, suggesting the presence of strong phase fluctuations similar to those observed in superconductors in the 2D limit. Moreover, recent experiments have proposed that unconventional $s_\pm$ pairing – mediated by CDW fluctuations and triggered by a Lifshitz transition – may be responsible for superconductivity in both pressurized and electron-doped $TiSe_2$ [24].
Within this framework, the recently discovered H-intercalated $TiSe_2$ superconductor [8], synthesized through IGP, offers novel insights. Notably, ^{1}H nuclear magnetic resonance measurements reveal that CDW order persists strongly at the intercalation sites [146], implying local coexistence of CDW and superconducting orders. Simultaneously, the high doping levels attained in H_xTiSe_2 (up to $x \approx 2$) enable a complete reconstruction of the Fermi surface via orbital-selective filling of the Ti d_{z^2} band [8]. This Fermi surface reconstruction resembles that seen in other superconducting transition metal dichalcogenides such as NbS_2 and $NbSe_2$, where anisotropic superconducting gap distributions lead to well-established two-gap features [174, 175, 176, 177, 178, 179, 180, 181, 182].

Given these compelling indications of a potentially nontrivial superconducting order parameter, this study employs IGP to intercalate H into $1\,T$-$TiSe_2$, enabling the synthesis of the recently discovered superconducting H_xTiSe_2 and directly probe its yet uncharacterized gap symmetry using three complementary techniques: magneto-transport measurements, PCARS, and tunneling spectroscopy.

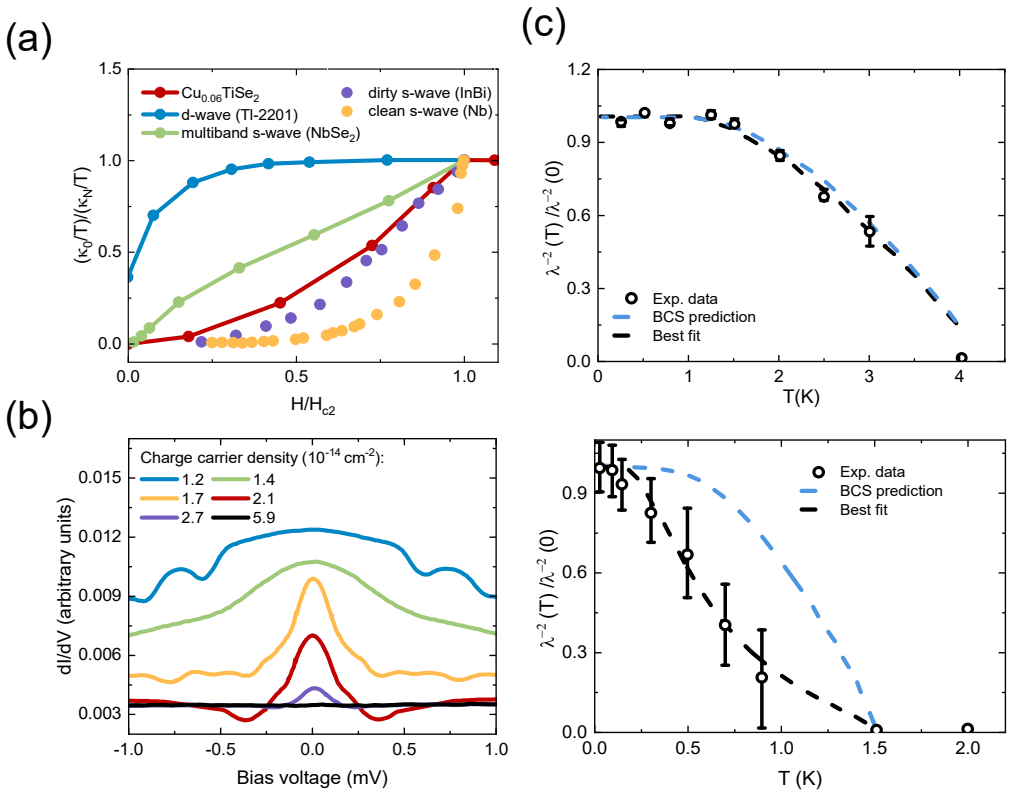

Figure 4.2: (a) Low-temperature thermal conductivity results for $Cu_{0.06}TiSe_2$, showing the normalized residual linear term κ_0/T as a function of the applied magnetic field H (in units of the upper critical field H_{c2}). For comparison, data from reference materials with well-established gap structures are included, as indicated in the legend. The close similarity between $Cu_{0.06}TiSe_2$ and the dirty s-wave superconductor InBi suggests that $Cu_{0.06}TiSe_2$ is also a dirty s-wave superconductor. Data reprinted from Ref. [20]. (b) Low-temperature point-contact Andreev reflection spectra of electrostatically doped $TiSe_2$ at various charge carrier densities (as labeled), showing a zero-bias conductance peak which might be incompatible with a conventional s-wave pairing symmetry. Data reprinted from Ref. [17]. (c) Temperature dependence of $\lambda(T)^{-2}$, where λ is the penetration depth, extracted from muon spin rotation measurements for underdoped Cu_xTiSe_2 ($x \sim 0.044$, lower panel) and optimally doped Cu_xTiSe_2 ($x \sim 0.081$, upper panel). In the optimally doped sample, the behavior follows a BCS-like trend, whereas in the underdoped sample, the fit is poor, with a gap at 0 K that is too small, suggesting the possible presence of multigap superconductivity, as $\lambda(T)$ in multiband systems primarily reflects the smaller gap. Data reprinted from Ref. [23].

4.2 Experimental methods

As anticipated, the starting point of this investigation involves inducing the superconducting phase in H_xTiSe_2 by performing IGP on pristine $TiSe_2$. According to the initial study that first reported superconductivity in this system [8], performing IGP using the conventional ionic liquid EMIM-BF_4 introduces H^+ ions into the van der Waals gaps of the layered $TiSe_2$ crystal, resulting in non-volatile H incorporation. The amount of intercalated H can be controlled by varying the duration for which the EMIM-BF_4 is maintained under a gate voltage (V_G) of +3 V, leading to different degrees of modification of electronic properties.
Transport measurements show that pristine $TiSe_2$ initially exhibits a resistivity anomaly near 160 K, associated with CDW order. After 5 minutes of gating, the CDW is suppressed and a superconducting transition appears below 4 K. Extending the gating time to 45 minutes further weakens the CDW and slightly increases the superconducting onset temperature. For longer gating times, the resistivity behavior converges to a common profile, with full superconductivity below 4 K and only a subtle CDW signature persisting below $\approx$ 200 K.

Building on these results, IGP was performed on single crystals of $TiSe_2$ obtained from HQ Graphene to induce the superconducting phase. Taking advantage of the non-volatile nature of H intercalation – unlike in palladium (see chapter 3) – the gating was carried out *ex situ* (see section 2.2.2). Crystals were immersed in a crucible containing EMIM-BF_4 (from Sigma-Aldrich), and across the electrolyte a V_G was ramped from 0 V to 3 V at an optimal rate of 1 mV/s, as determined in the previous study on PdH_x. V_G was then held constant at 3 V for approximately 2 hours. After gating, the intercalated crystals were thoroughly rinsed with acetone and ethanol before being contacted for transport measurements. Between measurements, samples were stored in a vacuum desiccator to preserve their intercalated state.
A representative T-dependent resistivity (ρ) curve of H_xTiSe_2 synthesized by the outlined IGP procedure is shown in fig. 4.3a.

The resulting superconducting samples were initially characterized by performing magneto-transport measurements up to 1 T and down to 0.3 K, employing a ^{3}He insert combined with a ^{4}He cryostat. Spectroscopic analysis was then carried out by performing soft PCARS and tunneling spectroscopy.
Soft PCARS allowed the formation of stable electrical contacts either on the sample surface or along its thin edge, allowing directional measurements by controlling the current injection to be predominantly along the c-axis or within the ab-plane, respectively. Current–voltage (I–V) characteristics were then recorded and numerically differentiated to yield differential conductance (dI/dV) spectra as a function of bias voltage V. Notably, well-defined spectroscopic features in the conductance

curves appeared only when contacts were made immediately after cleaving (for *c*-axis measurements) or breaking/cutting (for *ab*-plane measurements), minimizing exposure to air and moisture. The contact resistance corresponding to clear spectroscopic signals differed significantly between the two directions, being considerably higher for *ab*-plane contacts ($R_N \geq 500\,\Omega$) than for *c*-axis contacts ($R_N \approx 10\,\Omega$).

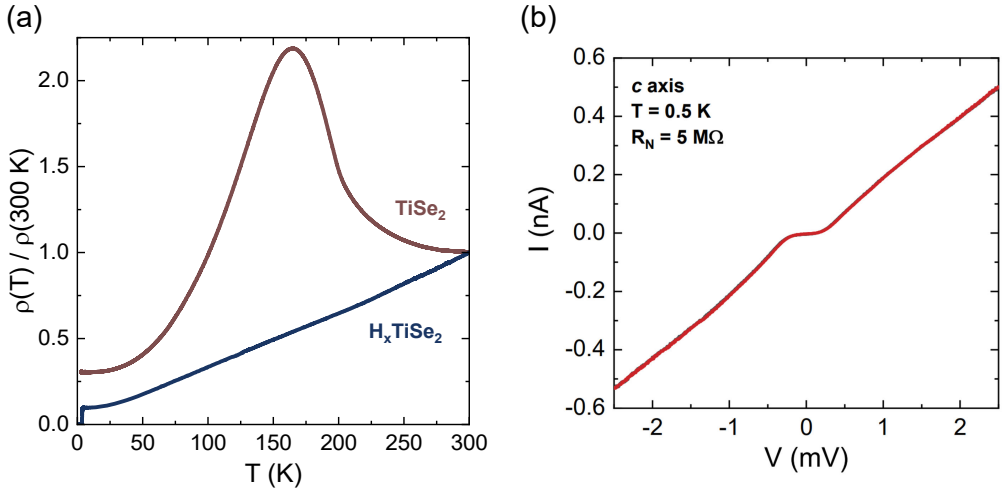

Figure 4.3: (a) Representative resistivity (ρ) versus temperature (T) curves for pristine $TiSe_2$ (red solid line) and H-intercalated $TiSe_2$, synthesized via the IGP protocol described in the text (blue solid line). (b) Example of a raw current–voltage (I–V) curve measured by biasing a sharp Au tip in a scanning tunneling microscope after breaching the surface oxide layer. Adapted from Ref. [183].

Concerning tunneling spectroscopy measurements, they were performed in Dr. P. Szabò's group at the Slovak Academy of Sciences. Here, the samples were exfoliated under ambient conditions and loaded into the scanning tunneling microscope within 20 minutes. Prior to data acquisition, the tips were prepared by mechanically sharpening of an Au needle against a bulk Au piece. Then, as for PCARS, I–V characteristics were recorded and numerically differentiated to obtain differential conductance (dI/dV) spectra as a function of V. However, conventional tunneling spectroscopy proved ineffective due to the rapid formation of a surface oxide layer during sample handling, which prevented reliable spectroscopic measurements. To overcome this, the Au tip was gently pressed into the sample surface and subsequently slightly retracted, thereby breaching the oxide layer and exposing the pristine H_xTiSe_2 surface for measurement. This configuration, exhibiting a normal-state resistance R_N around $5 \times 10^6\,\Omega$, more closely resembles a high-resistance point-contact junction rather than a standard tunneling junction. Despite this, the resulting I–V curves exhibited nearly ideal tunneling behavior, as illustrated by the representative example shown in fig. 4.3b.

4.3 Results

4.3.1 Magnetotransport characterization

As anticipated, after synthesizing the superconducting H_xTiSe_2, its magnetotransport properties were investigated by measuring temperature (T)-dependent resistivity under various magnetic fields (B) applied perpendicular to the ab-plane of the crystal. Specifically, measurements were performed in fields up to 1 T and temperatures down to 300 mK, thus enabling extension of the existing B-T phase diagram of H_xTiSe_2 to these ultra-low temperatures [8].
Magnetotransport results are presented in fig. 4.4a, where the obtained $\rho(T)$ curves – normalized to their respective values at 5 K – are displayed on a linear scale for both zero and finite magnetic fields. Notably, at $B = 0$ T, the midpoint of the superconducting transition – defined as the temperature at which $\rho(T)$ reaches 50% of its normal-state value – occurs at 3.53 K. Upon further cooling, the resistivity continues to decrease and eventually drops below the noise threshold at $T_{zrs} = (2.9 \pm 0.2)$ K, indicating the emergence of the zero-resistance state. Increasing B shifts the superconducting transition toward lower temperatures and progressively broadens it. This behavior is attributed to significant thermal phase fluctuations arising from the inhomogeneous and quasi-2D nature of the system [184, 185]. Nevertheless, a clear zero-resistance state remains observable up to 0.25 T, whereas higher magnetic fields result in finite resistivity even at the lowest measured temperature.

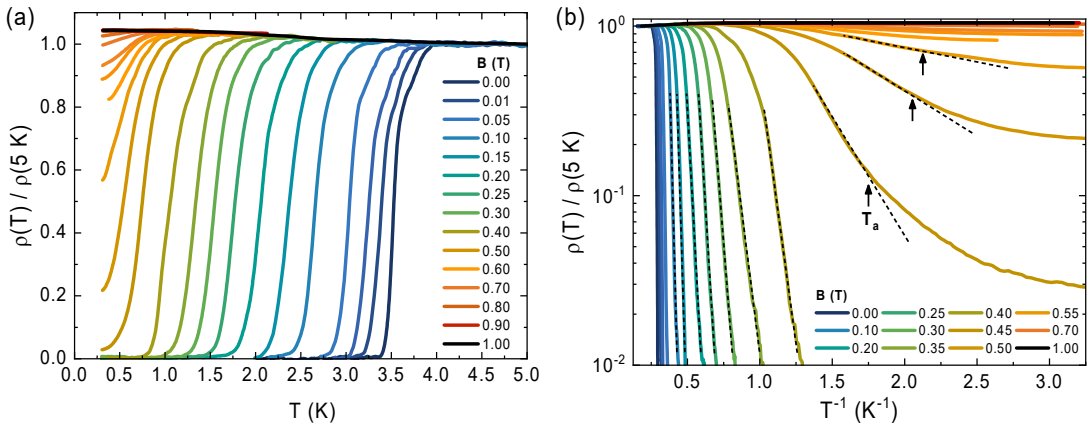

Figure 4.4: (a) Temperature-dependent resistivity $\rho(T)$ of H-intercalated $TiSe_2$ measured under increasing perpendicular magnetic fields B ranging from 0 T to 1 T. (b) Semilogarithmic plot of the data from panel (a) as a function of T^{-1}. Dashed lines represent linear fits, indicating that the dissipative regime is predominantly governed by thermally activated flux flow (TAFF) scaling. Arrows mark the characteristic temperatures T_a, where the high-field curves begin to deviate from the TAFF regime. Adapted from Ref. [183].

At $B = 1\,\mathrm{T}$, the system exhibits a normal-state $\rho(T)$ profile, with a slight upturn at low temperatures likely stemming from electronic correlations [186, 187] associated with localized Ti d orbitals [188, 189].

Additional insight into the system is gained by plotting the normalized resistivity on a semi-logarithmic scale as a function of the inverse temperature, T^{-1} (see fig. 4.4b). In this representation, the dissipative region of most curves follows the thermally activated flux flow (TAFF) model, described by $\rho(B,T) = \rho_0 \exp\left[-U(B)/(k_\mathrm{B}T)\right]$, where $U(B)$ is the energy required for vortices to overcome the pinning forces and start flowing [190]. Indeed, the model provides a good fit for most curves, as indicated by the dashed lines in fig. 4.4b. However, at higher fields, the measured resistivity at low temperatures exceeds TAFF predictions, indicating a departure from thermally activated behavior. This deviation emerges below a field-dependent temperature $T_\mathrm{a}(B)$, marked by black arrows in fig. 4.4b. Notably, this behavior was not observed in earlier studies of H_xTiSe_2, likely due to the lack of measurements below 1.6 K [8].

To accurately map the B–T phase diagram of superconducting H_xTiSe_2, it is crucial to determine not only $T_\mathrm{zrs}(B)$ and $T_\mathrm{a}(B)$, but also the T-dependence of the superconducting onset field, $B_\mathrm{on}(T)$, as well as the mean-field upper critical field, $B_\mathrm{c2}^\mathrm{mf}(T)$. The latter is essential for assessing vortex-state properties and superconducting gap symmetry, while deviations of $B_\mathrm{on}(T)$ from $B_\mathrm{c2}^\mathrm{mf}(T)$ offer insight into the influence of thermal fluctuations and spatial inhomogeneity on the superconducting phase.
$B_\mathrm{on}(T)$ data are obtained via two equivalent methods, yielding consistent results. The first extracts the complementary onset temperature $T_\mathrm{on}(B)$ from isofield $\rho(T)$ curves as the temperature where $d\rho/dT = 0$ for each applied B [184]. The second constructs isothermal $\rho(B)$ curves by interpolating the isofield $\rho(T)$ data onto a finely spaced temperature grid (ranging from 0.3 to 4 K in 0.1 K increments), thereby constructing a resistivity matrix $\rho(B,T)$ from which fixed-T slices are taken. From these isotherms (fig. 4.5a), $B_\mathrm{on}(T)$ is identified via crossing points of adjacent curves, following established protocols [191, 192] (fig. 4.5c). For each crossing, the corresponding temperature is defined as the average of the two adjacent isotherm temperatures, with the uncertainty given by their semidispersion. The magnetic field at the crossing is assigned as B_on, and its uncertainty is estimated from the local noise at the intersection.
The values of $B_\mathrm{c2}^\mathrm{mf}(T)$, or equivalently $T_\mathrm{c}^\mathrm{mf}(B)$, are determined using the empirical method introduced by Berghuis and Kes [193]. This approach involves identifying, for each resistivity curve, the intersection between the linear extrapolation of its flux-flow regime and the normal-state curve. For isofield $\rho(T)$ curves, this procedure is straightforward: the flux-flow regime is linearly extrapolated to its intersection with the normal-state curve at $B = 1\,\mathrm{T}$ (fig. 4.5b). This intersection defines the

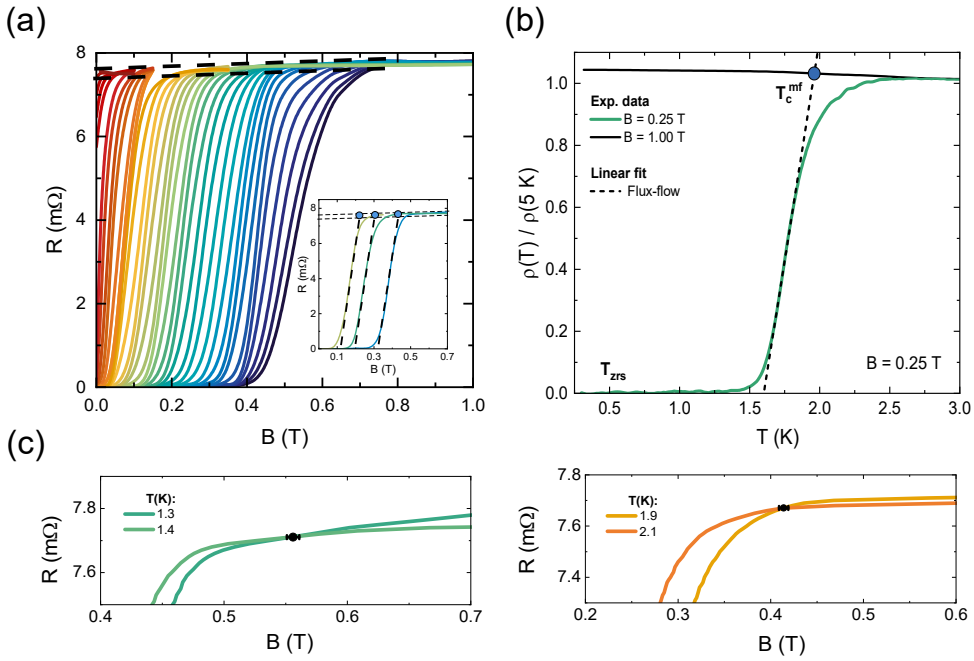

Figure 4.5: (a) $\rho(B)$ isotherms derived by matrix inversion of $\rho(T)$ isofield curves. The temperature spans from 0.3 K (black) to 4 K (dark red) in 0.1 K increments, with each curve corresponding to a specific temperature. Dashed lines define the boundaries of the normal state envelope. The inset presents representative examples illustrating the determination of the mean-field critical field, B_c^{mf} as described in the text. Midpoints for the isotherms at 1.2 K (light blue), 1.8 K (green), and 2.3 K (light green) are highlighted with blue-filled markers. (b) Representative example of the determination of the mean-field critical temperature, T_c^{mf}, determined as described in the text. The example shown corresponds to $\rho(T)$ at $B = 0.25\,\mathrm{T}$ intersecting the curve measured at $B = 1\,\mathrm{T}$, representing the normal state. The dashed line represents the linear fit to the data using the flux-flow model described in the text. (c) Representative examples of the determination of the onset field, B_{on}, defined as the crossing point of two consecutive isotherms. Adapted from Ref. [183].

corresponding $T_c^{mf}(B)$ value. For $\rho(B)$ isotherms obtained via matrix inversion, instead, the situation is more complex. Not all inverted isotherms cover the full magnetic field range, and the normal-state resistivity depends on temperature. To address this, the normal-state reference is taken as the envelope of all isotherms above B_{on} (see fig. 4.5a, dashed lines). For each isotherm, B_{c2}^{mf} at that temperature is defined as the midpoint between the extrapolated flux-flow trend and the envelope, with the associated uncertainty given by half the distance between their actual intersections (fig. 4.5a). Compared to the common method of mapping (T,

B) points where resistivity drops to 90% of the normal-state value in the $\rho(T)$ isofield and $\rho(B)$ isotherm curves, the Berghuis–Kes method is more robust – especially for 2D and anisotropic superconductors, where thermal fluctuations and inhomogeneities affect resistive transitions [184, 194]. Furthermore, it is consistent with the well-established Ullah–Dorsey scaling technique [195, 192] but avoids its limitations, such as failure below $T_c/2$ and reliance on specific fluctuation models or assumptions about dimensionality.

At this point, combining all the quantities extracted from the magnetotransport measurements results in the detailed B–T phase diagram of H_xTiSe_2 presented in fig. 4.6. Notably, the onset curve defined by $T_{on}(B)$ and $B_{on}(T)$ is found to lie signif-

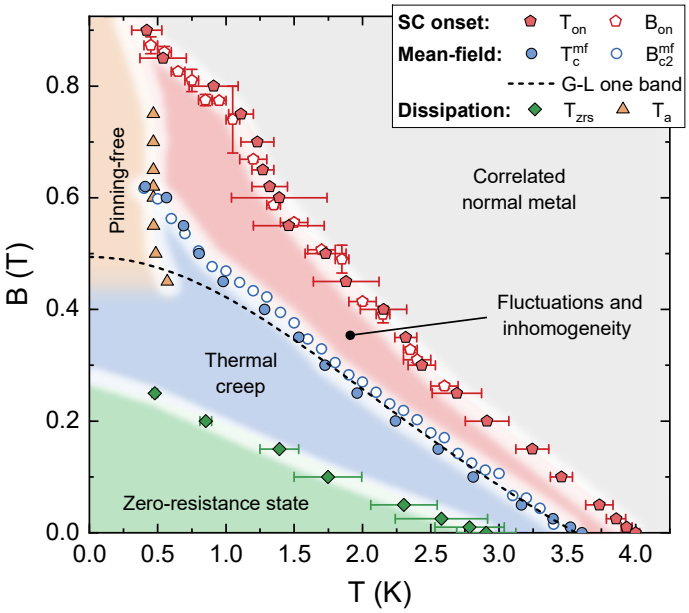

Figure 4.6: Magnetic field–temperature (B–T) phase diagram of H_xTiSe_2 as determined from magneto-transport measurements. The green region indicates the dissipationless zero-resistance state, bounded by T_{zrs} (green diamonds). Mean-field critical values, T_c^{mf} and B_{c2}^{mf}, are indicated by filled and open blue circles, respectively, delineating a blue-shaded region where dissipation emerges due to thermal creep. The onset of superconductivity is identified by T_{on} and B_{on} (filled and open red pentagons), outlining a red-shaded region between the mean-field transition and the onset, dominated by inhomogeneities and amplitude fluctuations. Orange triangles (T_a) mark the boundary of the orange region where dissipation arises from free vortex motion. The black dashed line corresponds to the theoretical mean-field critical line from the one-band Ginzburg-Landau model [196]. Reprinted from Ref. [183].

icantly above the mean-field critical line determined by $T_c^{mf}(B)$ and $B_{c2}^{mf}(T)$. This

indicates the existence of an extended region between the onset of superconducting fluctuations and the mean-field transition, as commonly observed in quasi-2D superconductors. Furthermore, the separation between onset and mean-field critical fields widens as the temperature decreases. Such a widening cannot be attributed solely to thermal fluctuations of the order parameter amplitude [194, 195]. Instead, it points to a significant role played by mesoscopic inhomogeneities [185, 197, 198], potentially enhanced by quantum fluctuations at elevated magnetic fields.
In the region bounded by the mean-field line and the zero-resistance state boundary given by $T_{\mathrm{zrs}}(B)$, the system is dominated by collective flux creep (thermal phase fluctuations) [190]. This interpretation is supported by the observed magnetic field dependence of the vortex activation barrier, which follows the logarithmic form $U(B) = U_0 \ln(B_0/B)$. Fitting the data to this model yields parameters $U_0 = (53 \pm 2)\,\mathrm{meV}$ and $B_0 = (0.48 \pm 0.06)\,\mathrm{T}$, consistent with earlier findings for both ion-gated [185] and H-doped [8] $TiSe_2$. Since $U(B)$ approaches zero for fields $B \gtrsim B_0$, the pinning potential effectively vanishes in the high-field region below $T_{\mathrm{a}}(B)$. In this region, thermal creep breaks down, leading to pinning-free vortex motion likely driven by a combination of finite excitation current, high-frequency noise, and quantum fluctuations [199].
Interestingly, the mean-field critical line consistently shows an upward curvature over the entire temperature range, mirroring the onset curve. This contrasts with observations in gated ZrNCl [184] where the onset line exhibited an upturn at low temperatures, but the mean-field critical one displayed a pronounced downward curvature in agreement with Werthamer–Helfand–Hohenberg (WHH) theory. This discrepancy indicates that, in H_xTiSe_2, the upward curvature of the superconducting onset curve arises not merely from inhomogeneities and fluctuations – as is the case in ZrNCl – but is primarily an intrinsic property of the material itself, already evident in the T-dependence of $B_{\mathrm{c2}}^{\mathrm{mf}}$. For temperatures below $T_{\mathrm{c}}/2$, this dependence markedly deviates from both WHH predictions and the standard one-band Ginzburg–Landau model: $B_{\mathrm{c2}} \propto (1 - t^2)/(1 + t^2)$, where $t = T/T_{\mathrm{c}}$ [196] (see black dashed line in fig. 4.6). Such a positive curvature in $B_{\mathrm{c2}}(T)$ typically signals the presence of multiple effective superconducting gaps on the Fermi surface [200, 201, 202].

4.3.2 Point-contact Andreev-reflection spectroscopy

Motivated by potential signs of multigap superconductivity in the B–T phase diagram, the superconducting gap structure of H_xTiSe_2 was investigated by performing directional soft-PCARS.

Initial PCARS measurements were conducted at the base temperature of 0.3 K and in zero magnetic field. Representative spectra obtained under these conditions are shown in fig. 4.7 for both c-axis (panels a and c) and ab-plane (panels b and d)

contacts, with recurring features marked by colored arrows.

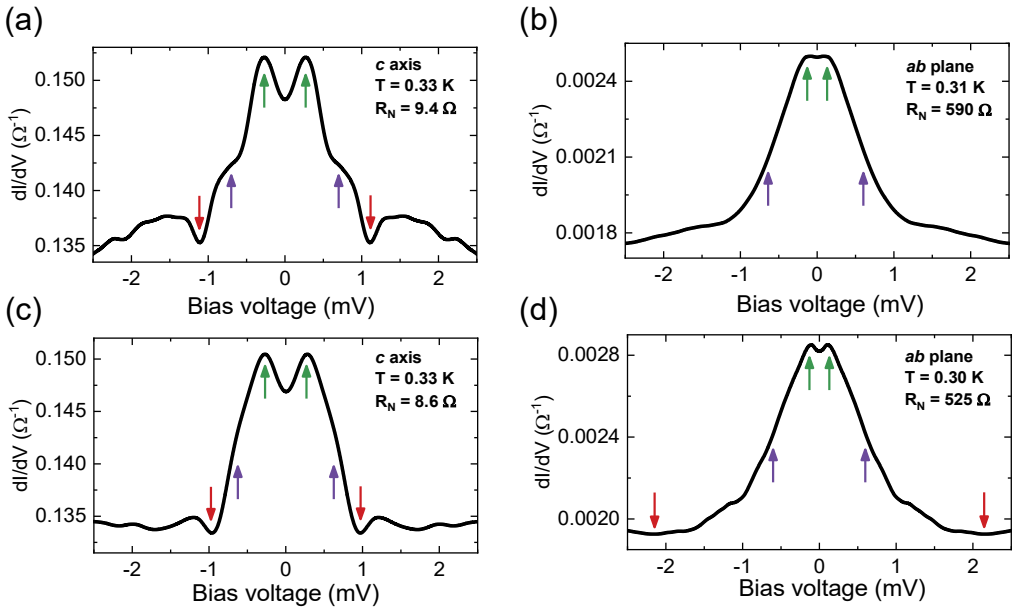

Figure 4.7: Representative point-contact Andreev reflection (PCAR) spectra (dI/dV vs. V) obtained in H_xTiSe_2 with current primarily injected along the c-axis (a, c) and the ab-plane (b, d), enabling directional PCARS analysis. Each spectrum includes labels indicating the normal-state contact resistance R_N and the measurement temperature T. Spectral features corresponding to the small gap Δ_1, large gap Δ_2, and critical current dips (due to non-purely ballistic contacts) are marked with green, violet, and red arrows, respectively. Adapted from Ref. [183].

Notably, all spectra display a conductance enhancement characteristic of the Andreev regime, featuring a pronounced zero-bias conductance dip between two symmetric maxima, indicative of a fully gapped, nodeless superconducting order parameter [106]. Two distinct low-energy conductance maxima (green arrows) are consistently observed, pointing to the presence of a first superconducting gap (Δ_1). In addition, broader features – such as shoulders or kinks marked by purple arrows – suggest the presence of a second gap (Δ_2). This interpretation is supported by the observation that these broader features occur at the same energies regardless of contact orientation or resistance, confirming their intrinsic origin. Furthermore, similar spectral characteristics have been observed in established multigap superconductors like MgB_2 [126, 203] and various iron-based superconductors [121, 204, 205]. Finally, some spectra display conductance dips marked by red arrows, which are identified as extrinsic effects stemming from non-ballistic transport at the contacts, as explained in chapter 2. These dips are more pronounced in the c-axis spectra, while in the ab-plane direction they are suppressed and shifted toward

higher voltages, sometimes extending beyond the measured voltage range (fig. 4.7b).

Based on the initial observations at 0.3 K, the spectral features were further examined through PCARS measurements conducted at different temperatures to investigate their T-dependence. Representative dI/dV spectra, obtained with current injected both within the ab plane (panel a) and along the c axis (panel b), are shown in fig. 4.8.

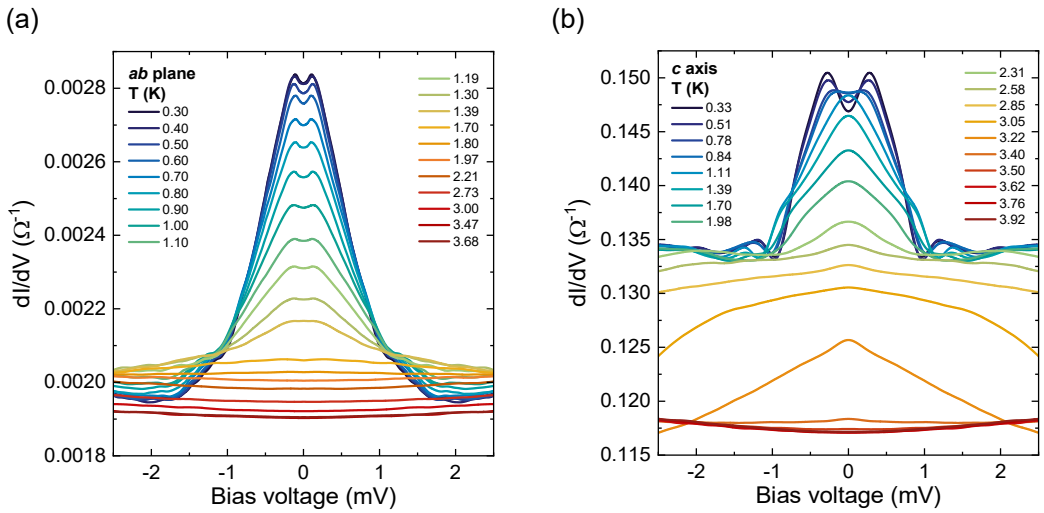

Figure 4.8: T dependence of the conductance spectra shown in panels (c,d) of fig. 4.7. Adapted from Ref. [183].

In both configurations, raising the temperature leads to a gradual decrease in the amplitude of the Andreev reflection signal. The two conductance peaks shift to lower bias voltages and eventually merge into a broad zero-bias hump, consistent with the thermal suppression of the superconducting gap. At sufficiently high temperatures, all signatures of the Andreev reflection vanish and the spectra flatten into the featureless profile typical of the normal state.
Notably, in both geometries, a T-dependent downward shift of the high-bias spectral tails is observed. This phenomenon originates from the bulk of superconducting H_xTiSe_2 transitioning to the normal state under the effect of injected current and temperature, adding a series spreading resistance. The resulting voltage drop alters the total measured voltage in the PCARS setup, affecting the conductance spectra regardless of whether the point contact is ballistic. While negligible at low temperatures, this effect grows near T_c as the critical current decreases, causing bending of the high-voltage tails and a downward shift of the conductance curves.

Following data acquisition, the experimental conductance spectra are analyzed to determine whether the observed features arise from two isotropic superconducting

gaps or from a single anisotropic one. To this end, the data are systematically compared with theoretical models representative of both scenarios. This procedure includes symmetrizing the raw conductance spectra, normalizing them to the normal-state conductance measured just above T_c, and correcting for the influence of spreading resistance [205]. The processed spectra are then fitted using the 2D BTK model introduced in chapter 2, modified to accommodate either a single anisotropic gap or two distinct isotropic gaps [126, 106].
For the anisotropic scenario, the gap function in eq. (2.8) is modeled with the angular dependence:

$$\Delta(\theta) = \Delta_{is} + \Delta_{an}\cos^4(2\theta), \tag{4.1}$$

yielding a 2D BTK model with four fitting parameters: the isotropic gap Δ_{is}, the anisotropic component Δ_{an}, the interface barrier strength Z, and the quasiparticle broadening parameter Γ.
For the two-gap case, the total conductance is modeled as a weighted sum of contributions from two distinct bands: $G = w_1 G_1 + w_2 G_2$, where each G_i follows eq. (2.8). This approach results in a 2D BTK model with seven free parameters: the gap amplitudes Δ_i, the broadening parameters Γ_i, the barrier strengths Z_i, and the spectral weights w_i, constrained by the condition $w_1 + w_2 = 1$. Despite the large number of free parameters, each one affects the spectra in a distinct and recognizable way, allowing for a reliable and unambiguous determination of their values [106, 121].
Fig. 4.9 shows a representative comparison of both models fitted to experimental data acquired at the base temperature with current injected along the *c*-axis. This

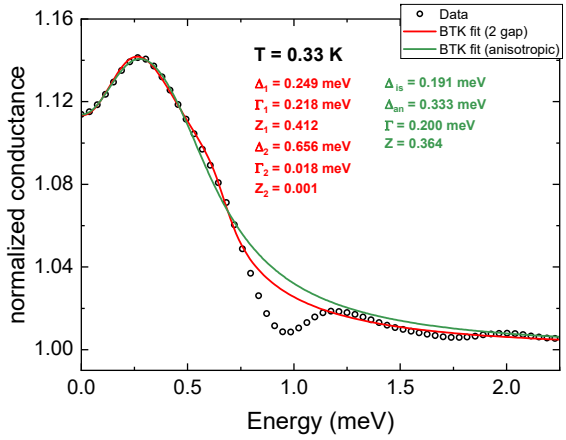

Figure 4.9: Comparison of the 2D BTK model fitted to a representative experimental point-contact Andreev reflection (PCAR) spectrum measured at base temperature (open black circles). The model is adapted for two scenarios: two isotropic gaps (solid red line) and one anisotropic gap (solid green lines). Corresponding BTK model parameters are shown in the labels. Adapted from Ref. [183].

orientation is chosen because c-axis PCAR spectra typically exhibit pronounced shoulders and kinks, which aid in distinguishing between the models and assessing their accuracy in reproducing spectral features. The two-gap model (solid red line) provides an excellent fit up to approximately 0.75 meV, beyond which conductance dips arise due to critical-current effects. This model accurately captures the zero-bias minimum, the peak at approximately 0.25 meV, and the shoulder near 0.65 meV. Conversely, the anisotropic-gap model (solid green line) reproduces the spectrum only up to roughly 0.5 meV; it fits the zero-bias minimum and the low-energy peak but fails to account for the higher-energy shoulder.

Given the better agreement with key spectral features – aside from the non-ideal dip structures – the two-gap model is adopted, and the anisotropic single-gap scenario is ruled out. Accordingly, all spectra recorded at various temperatures and for both current injection directions are fitted using the two-band BTK model. Fitting is limited to temperatures slightly above 2 K, as beyond this point (see fig. 4.8a,b), spreading resistance dominates, causing the spectra to shift downward and stretch horizontally [206, 207, 208], and thus precluding meaningful spectroscopic analysis. Representative two-band fits to spectra measured at different temperatures are presented in fig. 4.10a,b, using the same experimental data as in fig. 4.8a,b. The resulting T-dependence of the gap amplitudes is displayed in fig. 4.10c,d, respectively. Strikingly, both gaps vanish well below the transport-derived T_c, reaching zero at approximately 2.6 K for the ab-plane and 2.2 K for the c-axis. This behavior is consistently observed across all contacts, regardless of injection direction, R_N, or contact location on the crystal. Importantly, these Andreev-derived critical temperatures (T_c^A) align closely with the lower bound of the estimated T_{zrs}, suggesting a strong correlation with the onset of TAFF regime. This interpretation is corroborated by muon-spin rotation experiments on H_xTiSe_2 [8], which observed the superfluid density vanishing near 2 K. Such consistency suggests that the observed gap suppression is not a surface effect but rather a bulk property, likely related to a loss of superfluid stiffness.
Examining the T-dependence of the gaps for each current direction, Δ_2 decreases with increasing temperature in a BCS-like manner, vanishing near the suppressed T_c^A and following the relation $\Delta(T) = \Delta(0)\tanh\left(1.74\sqrt{T_c^A/T - 1}\right)$ (dashed purple line). Minor deviations from this trend are observed, including a weak maximum at low temperatures and some divergence at higher temperatures, where the spectral features associated with Δ_2 are in any case less well defined. The smaller Δ_1 exhibits a similar overall trend and vanishes at the same T_c^A. However, instead of saturating at low temperature, it displays a linear dependence below approximately 0.7 K. This behavior is reminiscent of observations in 1H-$NbSe_2$ via scanning tunneling spectroscopy [209], and in $RbCa_2Fe_4As_4F_2$ via soft PCARS [205]. Comparing the two directions, the absolute values of both Δ_1 and Δ_2 are found to be

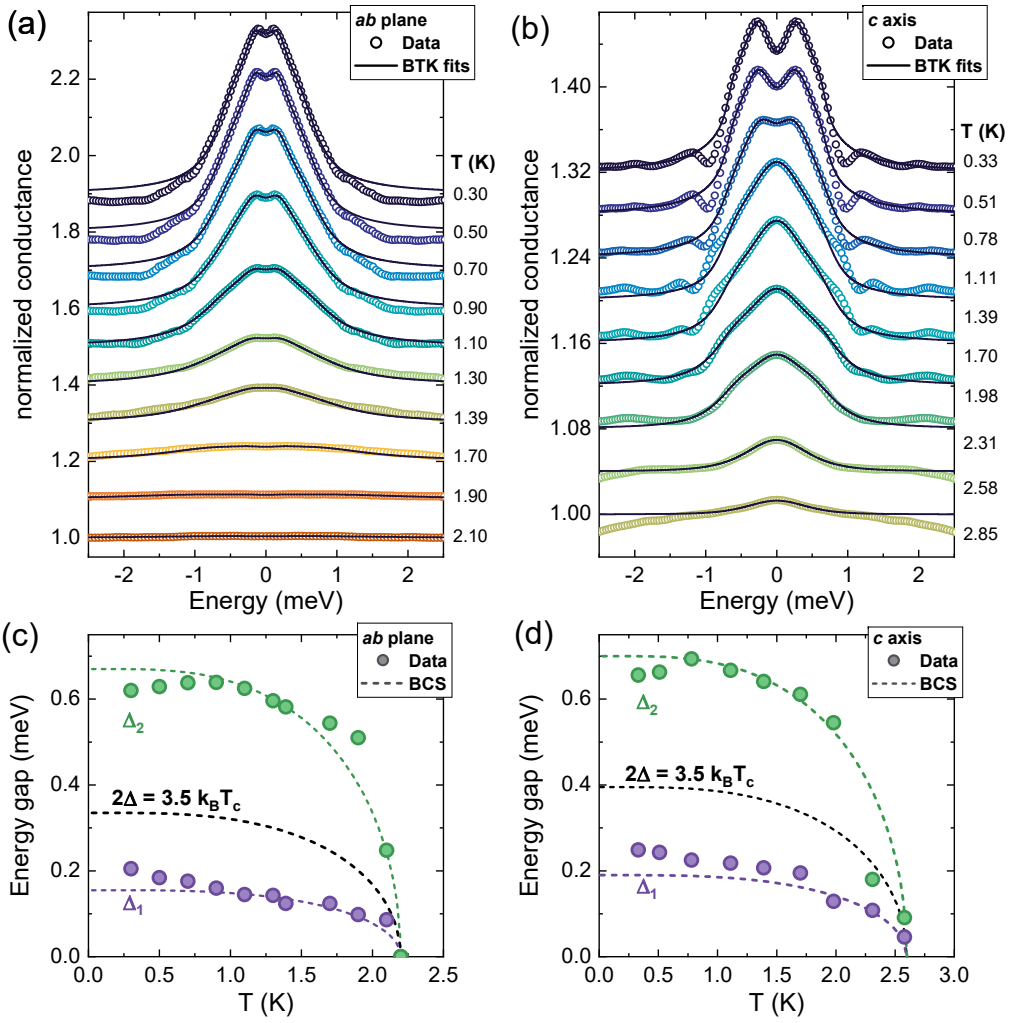

Figure 4.10: (a,b) Representative two-band BTK fits (solid lines) to symmetrized and normalized spectra measured at various temperatures and along different current directions (symbols). The original experimental data prior to symmetrization and normalization correspond to the curves displayed in fig. 4.8a,b. (c,d) T-dependence of Δ_1 (purple circles) and Δ_2 (green circles) extracted from the fits in panels a,b, respectively. Dashed lines are BCS functions of the form $\Delta_i(T) = \Delta_i(0)\tanh\left(1.74\sqrt{T_c^A/T-1}\right)$. Adapted from Ref. [183].

comparable, indicating minimal anisotropy in the superconducting order parameter between the *ab* plane and the *c* axis. Regarding the gap spectral weights, values of approximately $w_1 \approx 0.9$ for *c*-axis contacts and $w_1 \approx 0.4$ for *ab*-plane contacts are observed. This directional anisotropy is consistent with expectations for superconductors possessing a Fermi surface that cannot be approximated by a simple sphere [106, 121].

4.3.3 Tunneling spectroscopy

To validate the PCARS results, complementary spectroscopic measurements were carried out in the tunneling regime by Dr. P. Szabo's group, using a custom-built scanning tunneling microscope operating down to 0.3 K. Due to its inherently high spatial resolution, this technique provides a critical complement to the spatially averaged PCARS data, helping to discriminate whether the observed multigap superconductivity is an intrinsic feature of H_xTiSe_2 or arises from different superconducting gaps associated with spatially distinct regions.
Through this method, high-quality differential conductance spectra were obtained across various temperatures, clearly revealing a well-defined superconducting gap after correcting for the linear normal-state background. This correction involved normalizing the raw data to a linear baseline, determined by fitting the dI/dV signal within a ± 0.1 mV range centered around ± 2.5 mV using a linear function. Representative spectra recorded at different temperatures are shown in fig. 4.11.

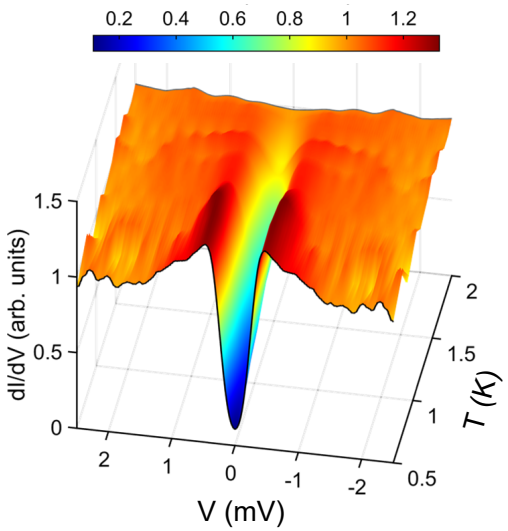

Figure 4.11: Color map of typical normalized tunneling spectra (dI/dV vs. V) measured at different temperatures T in zero magnetic field. Adapted from Ref. [183].

Notably, the tunneling spectroscopy results corroborate the PCARS findings, with both techniques observing the superconducting gap closing near 2 K. Consequently, the critical temperature extracted from tunneling spectoscopy is denoted using the same notation as for the Andreev reflection measurements: T_c^A. As for PCARS, fitting the tunneling spectra with a single-gap model (Dynes model), where the differential conductance is given by

$$\frac{dI(V)}{dV} = N \int_{-\infty}^{+\infty} \mathrm{Re}\left(\frac{E - i\Gamma}{\sqrt{(E - i\Gamma)^2 - \Delta^2}}\right)\left[\frac{\partial f(E - i\Gamma + eV)}{\partial eV}\right] dE \qquad (4.2)$$

with N the constant density of states of the metallic tip, Δ the superconducting gap, $f(E)$ the Fermi distribution, and Γ the spectral broadening parameter analogous to that in the BTK model [129], yields poor agreement. In contrast, a two-gap 2D BTK model for a superconductor–insulator–normal metal junction offers a significantly better fit across all temperatures up to 2 K. This comparison is illustrated in fig. 4.12, which shows fits of both single-gap and two-gap models to two representative spectra measured at 0.5 K and 1.1 K. At 0.5 K (fig. 4.12a), the Dynes model (solid green line) fails to accurately reproduce key spectral features, notably the depth of the zero-bias conductance minimum, as well as the position and width of the coherence peaks observed between ≈ 0.4 and 0.5 meV. In contrast, the two-gap BTK model more accurately reproduces both the position and shape of the coherence peaks, albeit with a persistent underestimation of the zero-bias dip. This discrepancy between the models becomes more pronounced with increasing temperature. Indeed, at 1.1 K (fig. 4.12b), the two-gap BTK model closely matches the full experimental spectrum, while the Dynes model continues to inaccurately represent the zero-bias minimum and poorly fits the height, position, and width of the coherence peaks. Interestingly, the two-gap BTK model captures the depth

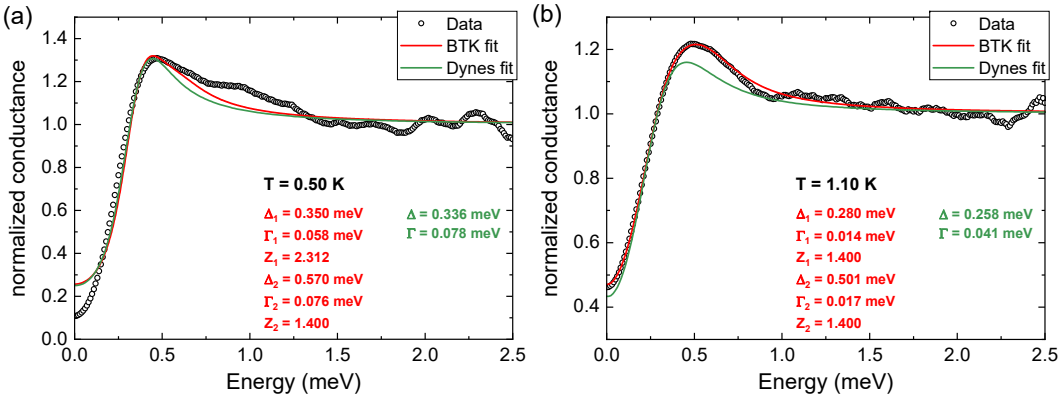

Figure 4.12: Comparison of the fits to the experimental normalized dI/dV spectra (hollow black circles) using the one-gap Dynes model (solid green lines) and the two-gap BTK model (solid red lines), demonstrating their respective agreements with the raw data. The fitting parameters for both the Dynes and BTK models are provided in the labels. Reprinted from Ref. [183].

of the zero-bias dip at 1.1 K but not at 0.5 K. This behavior can be attributed to either a smaller superconducting gap embedded within the coherence peaks or a broad distribution of gap amplitudes, as suggested by a noticeable change in the slope of the low-bias tunneling curve at 0.5 K. However, as temperature increases, thermal broadening smooths these features, enabling the fit at 1.1 K to more closely align with the experimental data.

Since tunneling spectroscopy, with its high spatial resolution, also detects two-gap superconductivity, the option of two gaps arising from distinct spatial regions is ruled out. Then, fig. 4.13a displays representative best-fit curves obtained by fitting the normalized tunneling spectra at various temperatures using the two-gap 2D BTK model. The superconducting gap amplitudes extracted from these fits are shown in fig. 4.13b.
Assuming a BCS-like T-dependence, the resulting larger gap, Δ_2, closely follows the expected behavior (green dashed line) across the entire temperature range. Conversely, the smaller gap Δ_1 gradually closes at the same T_c^A, but deviates from the BCS trend. Specifically, assuming Δ_1 to follow BCS behavior near T_c^A (purple dashed line), as similarly observed in the PCARS measurements (see fig. 4.10c,d), its deviation becomes evident around 1.4 K. Below this point, Δ_1 increases approximately linearly with decreasing temperature.
Notably, the weight of the smaller gap is found to be $w_1 \approx 0.8$, which aligns reasonably well with the value obtained from PCARS along the c-axis. However, it should be noted that the definitions of spectral weight differ between the Andreev and tunneling regimes [106, 121].

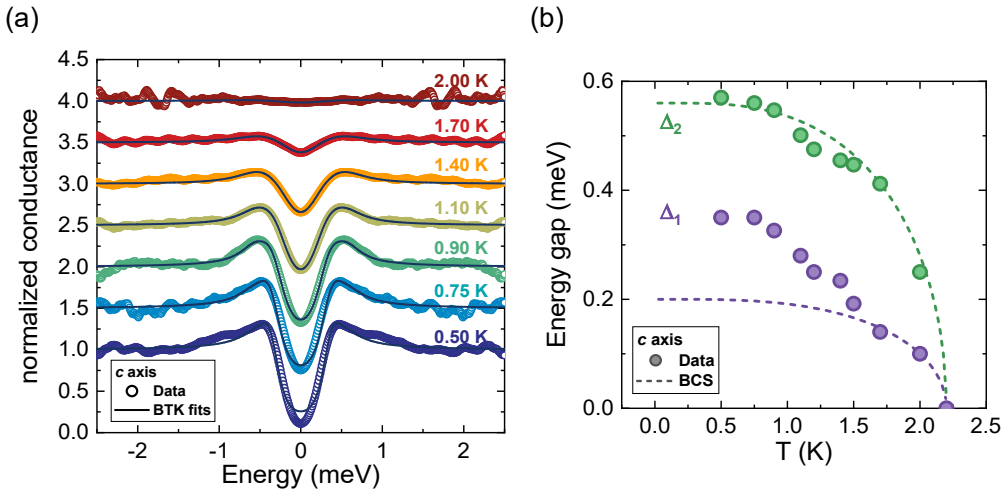

Figure 4.13: (a) Representative spectra from fig. 4.11 (symbols) together with the corresponding best-fit curves (solid lines) obtained using the two-gap BTK model. (b) Temperature dependence of the superconducting energy gaps (symbols), as extracted from the fits in panel (a). The dashed lines correspond to the expected BCS-like behavior, described by the function $\Delta_i(T) = \Delta_i(0) \tanh\left[1.74\sqrt{T_c^A/T - 1}\right]$. Adapted from Ref. [183]

4.4 Discussion

Building on the PCARS and tunneling spectroscopy results, which provide evidence for the two-gap nature of the superconducting state in H_xTiSe_2, and excluding the possibility that the two gaps originate from spatially separated regions – since highly spatially resolved tunnelling spectroscopy detects both gaps simultaneously, and the gap ratio $2\Delta_i/k_BT_c$ is larger than the BCS value for $i = 2$ and smaller for $i = 1$ (see figs. 4.10c,d), as expected in multi-gap superconductors [106, 121] – it is therefore relevant to examine whether the observed T-dependence of the gaps and of the mean-field upper critical field can be accounted for within a two-gap theoretical framework.

4.4.1 $\Delta(T)$: comparison with two-band models

To evaluate the T-dependence of the superconducting gaps, a preliminary step involves determining whether the PCARS and tunneling spectroscopy datasets can be regarded as statistically equivalent and therefore averaged. This assessment is performed at the lowest temperature, by analyzing the gap amplitudes – obtained through fitting the experimental spectra with the two-gap 2D-BTK model – as a function of the contact resistance R_N. As shown in fig. 4.14a, the data cluster into two well-defined energy intervals, highlighted by shaded regions, and exhibit negligible dependence on R_N. These findings confirm that the contacts are in the spectroscopic regime and that the measured gaps are independent of the specific contact. However, the significant spread within each energy range suggests a spatial modulation of the gap amplitudes. Consequently, the midpoint and half-width of each energy range are assigned as the respective gap values, yielding $\langle\Delta_1\rangle = (0.26 \pm 0.12)$ meV and $\langle\Delta_2\rangle = (0.62 \pm 0.18)$ meV at 0.3 K. This procedure is repeated for all other temperatures, resulting in the T-dependence of the average gap amplitudes (symbols) shown in fig. 4.14b. The average values of the larger and smaller gaps display, respectively, BCS-like and quasi-linear T-dependencies, both closing at the same T_c^A. This behavior is consistent with the observations from individual contact spectra and may account for the absence of low-T saturation in the superfluid density reported by muon spin rotation measurements [8]. In a multigap system, such a deviation from saturation can be attributed to the smaller gap(s) being thermally excited at lower energies than the larger gap, thereby contributing additional quasiparticles beyond those associated with the larger gap alone.

With the average T-dependence of the gaps established, the comparison with theoretical predictions is performed by initially calculating their expected behavior as function of temperature within a two-band BCS framework. This specifically involves solving the self-consistent gap equations for a two-band superconductor in the weak-coupling limit. In the original formulation by Suhl, Matthias, and Walker

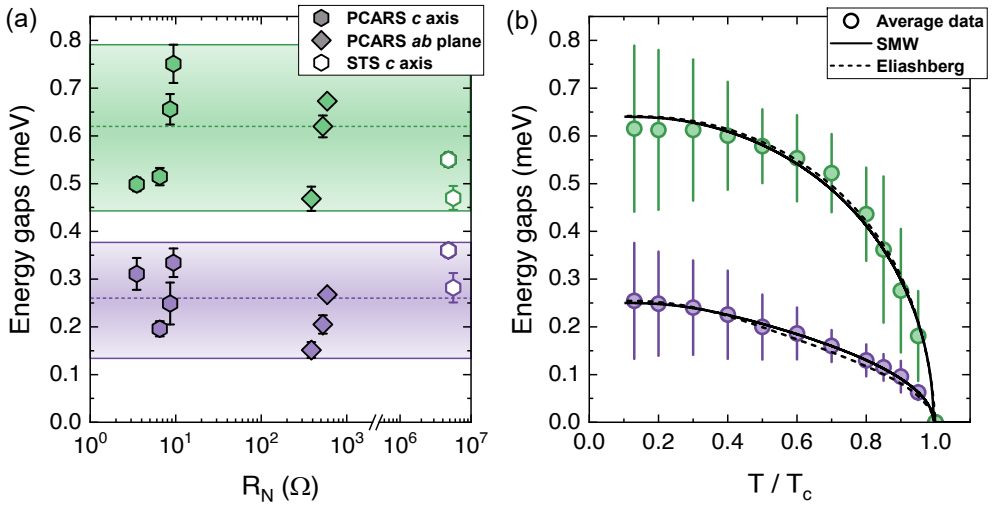

Figure 4.14: (a) Energy gaps obtained from point-contact Andreev reflection spectroscopy (PCARS, filled symbols) and tunneling spectroscopy (STS, open symbols) measurements plotted as a function of the contact resistance R_{N}. The error bars on each data point represent the variability arising from different normalization choices applied during the fitting procedure, providing an estimate of the internal uncertainty of the fitting method. (b) Dependence of the measured energy gaps on the normalized temperature T/T_{c}. At each temperature T, symbols represent the mean values obtained by averaging measurements from all contacts, with the associated error defined as half the spread among the individual measurements. Solid and dashed lines correspond to fits using the two-band SMW model [210] and the Eliashberg model [211, 212, 213], respectively. Adapted from Ref. [183]

(SMW model) [210], these equations are expressed as follows:

$$\begin{aligned} \Delta_1 \left[1 - V_{11} N_1(0) F(\Delta_1)\right] &= \Delta_2 V_{12} N_2(0) F(\Delta_2) \\ \Delta_2 \left[1 - V_{22} N_2(0) F(\Delta_2)\right] &= \Delta_1 V_{12} N_1(0) F(\Delta_1) \end{aligned} \tag{4.3}$$

Here, $N_{\mathrm{i}}(0)$ denotes the density of states at the Fermi level for the i-band, V_{ii} represent the intraband interaction energies, and $V_{12} = V_{21}$ is the interband interaction energy. The function $F(\Delta_{1,2})$ is defined as:

$$F(\Delta_{1,2}) = \int_0^{\hbar\omega} d\varepsilon \tanh\left(\frac{(\varepsilon^2 + \Delta_{1,2}^2)^{1/2}}{2\,k_B\,T}\right) \Big/ \left(\varepsilon^2 + \Delta_{1,2}\right)^2 \tag{4.4}$$

For consistency with the rest of the analysis, it is convenient to reframe these equations in terms of the dimensionless BCS coupling parameters $\lambda_{ij} = V_{ij} N_j$, following the formulation in [200]. This yields the equivalent set of equations:

$$\begin{aligned} \Delta_1 &= \Delta_1 F(\Delta_1)\,\lambda_{11} + \Delta_2 F(\Delta_2)\,\lambda_{12} \\ \Delta_2 &= \Delta_2 F(\Delta_2)\,\lambda_{22} + \Delta_1 F(\Delta_1)\,\lambda_{21} \end{aligned} \tag{4.5}$$

where the inter-band couplings λ_{21} and λ_{12} are not independent, but related through the ratio of the electronic density of states at the Fermi level for the two bands, $\nu_{21} = N_2(0)/N_1(0)$, such that $\lambda_{12} = \lambda_{21}\nu_{21}$.

To track the theoretical T-dependence of Δ_i within this model, the coupling constants λ_{ij} must first be determined. This is accomplished by solving eqs. (4.5) for λ_{ij} at a fixed temperature (e.g. 0.3 K), along with the requirement that the superconducting gaps vanish at T_c [210, 200]:

$$k_B T_c = 1.14\,\hbar\omega_D \exp\left[-\frac{\sqrt{4\lambda_{12}\lambda_{21} + (\lambda_{11} - \lambda_{22})^2} - (\lambda_{11} + \lambda_{22})}{2(\lambda_{12}\lambda_{21} - \lambda_{11}\lambda_{22})}\right] \tag{4.6}$$

The above constraint is derived by imposing $\Delta_{1,2} = 0$ at $T = T_\mathrm{c}$ into eqs. (4.5).

By substituting the experimentally measured gaps at 0.3 K and the transport-derived T_c into eqs. (4.5) and (4.6), a closed system of three equations is eventually obtained for the unknowns λ_{11}, λ_{22}, and λ_{21}. This system is then numerically solved by specifying the ratio ν_{21} and the cutoff frequency $\hbar\omega$ used in the function $F(\Delta_{1,2})$. Specifically, $\hbar\omega$ is estimated by assuming a Debye temperature of approximately 203 K [214], while ν_{21} is initially set to a guess value of 0.35.
At this stage, eqs. (4.5) are solved iteratively by applying the previously determined λ_{ij} values at progressively higher temperatures to compute the theoretical T-evolution of Δ_i. This iterative procedure involves discretizing the temperature range and, at each temperature step, updating the gap amplitudes recursively according to:

$$\begin{aligned} \Delta_1^{i+1} &= \Delta_1^i F(\Delta_1^i)\,\lambda_{11} + \Delta_2^i F(\Delta_2^i)\,\lambda_{21}\,\nu_{21} \\ \Delta_2^{i+1} &= \Delta_2^i F(\Delta_2^i)\,\lambda_{22} + \Delta_1^i F(\Delta_1^i)\,\lambda_{21} \end{aligned} \tag{4.7}$$

where i denotes the iteration index. Convergence is achieved when the difference between successive iterations falls below a threshold of 10^{-12} meV. For $i = 0$, the initial values of Δ_i are taken from the gap amplitudes obtained at the previous temperature step. Thus, the experimental values of $\Delta_{1,2}$ measured at 0.3 K serve as the starting point for the entire calculation, with the first iteration carried out at the next temperature step above 0.3 K.
This iterative method yields the T-dependence of the gaps for the trial value of $\nu_{21} = 0.35$. However, it is found that the shape of the $\Delta_1(T)$ curve – especially near T_c – depends sensitively on the choice of ν_{21}. Therefore, the entire procedure is repeated for different values of ν_{21} until the calculated gap evolution matches the experimental observations. The comparison is performed after rescaling the temperature axis of the calculated and experimental data by T_c and T_c^A, respectively, to account for the mismatch between the two quantities. The best agreement is obtained for $\nu_{21} = 0.48$ (solid lines in fig. 4.14b) and the corresponding values of

the BCS coupling constants are listed in tab. 4.1. Based on these optimized parameters, the effective total coupling constant, λ_{eff}, is also evaluated. This is done by equating the expression for T_c as predicted by the two-band BCS model (eq. (4.6)) with McMillan's empirical formula [215]:

$$k_B T_c = 1.14\,\hbar\omega_D \exp\left(-\frac{1+\lambda_{\text{eff}}}{\lambda_{\text{eff}}-\mu^*}\right) \tag{4.8}$$

where the Coulomb pseudopotential μ^* is set to zero, consistent with the two-band BCS theory, which neglects Coulomb repulsion [210, 200]. Applying this procedure yields $\lambda_{\text{eff}} = 0.34$, which represents a lower bound for the effective coupling constant of the system.

Given that the T-dependence of the gaps in H_xTiSe_2 is accurately captured by the SMW two-band model, further analysis explores whether comparable agreement is achievable using the more comprehensive Eliashberg formalism [211, 212, 213]. This approach involves solving the four coupled Eliashberg equations for the gap functions Δ_i and the renormalization functions Z_i - with i denoting the band index— in the absence of magnetic impurities [216, 211, 217, 212, 218, 213]. These computations were carried out by Prof. G. A. Ummarino at Politecnico di Torino. Due to the large number of input parameters, several simplifications were necessary to keep the problem tractable. Specifically, certain parameters were fixed based on experimental data, while others were estimated using physically motivated assumptions. A detailed account of the adopted approximations is provided in the Supplementary Information of Ref. [183].
The resulting T-dependence of $\Delta_{1,2}$ again yields excellent agreement with experimental observations (dashed lines in fig. 4.14b) for $\nu_{21} = 0.48$. The corresponding coupling constants λ_{ij} are provided in tab. 4.1. Based on these values, the total effective coupling constant, defined within the two-band Eliashberg framework as

$$\lambda_{\text{eff}} = \frac{\lambda_{11} + \lambda_{12} + \nu_{21}(\lambda_{22} + \lambda_{21})}{1 + \nu_{21}}, \tag{4.9}$$

is found to be $\lambda_{\text{eff}} = 0.34$, which coincides with the weak-coupling BCS limit.

At this stage, since both models accurately capture the data, a comparison between them can now be made based on tab. 4.1. This table reveals that both models achieve the best fit to the experimental data when the strongest coupling is the intraband interaction within the band associated with the larger gap, accompanied by a notable interband coupling. Furthermore, the density of states for the band with the larger gap should be approximately half that of the band with the smaller gap. Despite differences in the numerical values of the coupling constants – attributable to distinct model formulations – both approaches converge on an

effective coupling constant $\lambda_{\text{eff}} = 0.34$, indicative of a weak-coupling superconducting regime. These results confirm the robustness of the two-band BCS model in accurately describing the T-dependence of the superconducting gaps in H_xTiSe_2.

	λ_{11}	λ_{22}	λ_{21}	ν_{21}	λ_{eff}	η_{21}	$B_{c2}(0)$
SMW + Gurevich	0.14	0.22	0.06	0.48	0.34	12.4	0.79 T
Eliashberg	0.24	0.41	0.07	0.48	0.34	10.5	0.69 T

Table 4.1: Summary of parameters derived from calculations using either the weak-coupling SMW-Gurevich model or the strong-coupling Eliashberg model. Reported values include the electron-phonon coupling constants λ_{ij}, the density of states ratio ν_{12}, the total effective coupling constant λ_{eff}, the diffusivity ratio η_{21}, and the zero-temperature upper critical field $B_{c2}(0)$.

4.4.2 $B_{c2}^{mf}(T)$: comparison with two-band models

Given the effectiveness of two-band models in describing the non-BCS, quasi-linear T-dependence of the smaller superconducting gap, the focus now shifts to investigate whether the anomalous positive curvature in $B_{c2}^{mf}(T)$ can also be accounted for within a two-band framework. To address this, B_{c2}^{mf} is analyzed using a weak-coupling BCS model for a two-gap superconductor in the dirty limit. Originally proposed by Gurevich [200], this model incorporates intra-band scattering from non-magnetic impurities through band-specific diffusivities D_i, while neglecting inter-band scattering. Within this framework, the T-dependence of B_{c2}^{mf} is described by the following implicit equation:

$$a_0[\ln(t)+U(b/t)][\ln(t)+U(\eta_{21}b/t)]+a_1[\ln(t)+U(b/t)]+a_2[\ln(t)+U(\eta_{21}b/t)]=0 \quad (4.10)$$

where $t = T/T_c$ denotes the reduced temperature, $b(T) = B_{c2}(T)/B_{c2}(0)$ is the normalized upper critical field, and $\eta_{21} = D_2/D_1$ represents the ratio of band diffusivities. The function $U(x)$ is defined as $U(x) = \Psi(x+1/2)-\Psi(x)$, where $\Psi(x)$ is the digamma function. The coefficients a_0, a_1, and a_2 arise from combinations of the BCS coupling constants λ_{ij}, and are explicitly expressed as:

$$a_0 = \frac{2(\lambda_{11}\lambda_{22}-\lambda_{12}\lambda_{21})}{\lambda_0}, \quad a_1 = 1+\frac{\lambda_{11}-\lambda_{22}}{\lambda_0}, \quad a_2 = 1-\frac{\lambda_{11}-\lambda_{22}}{\lambda_0}$$

where $\lambda_0^2 = (\lambda_{11}-\lambda_{22})^2 - 4\,\lambda_{12}\lambda_{21}$. In this analysis, the coupling constants λ_{ij} are fixed based on values previously determined using the SMW model, while $B_{c2}(0)$ and η_{21} are treated as free fitting parameters. Eq. (4.10) is then solved through nonlinear regression, minimizing the least-squares iteratively to identify the best fit to the experimental data. This fitting process yields the optimal fit represented

by the solid black curve in fig. 4.14b, with the resulting parameters $B_{c2}(0) = 0.79\,\mathrm{T}$ and $\eta_{21} = 12.36$.

Again, since the agreement with the data is excellent, a further analysis is performed to investigate whether the same agreement level can be obtained using a two-band model based on the more comprehensive Eliashberg theory [219, 220]. This involves solving the Eliashberg equations in the presence of a magnetic field. These calculations, once again performed by Prof. G. A. Ummarino, use the same λ_{ij} values previously obtained from the T-dependence of the superconducting gaps and again actions are taken to reduce the number of free input parameters. As before, efforts are made to reduce the number of free input parameters: certain parameters are fixed based on experimental results, while others are estimated using reasonable approximations. For instance, the nonmagnetic scattering rates are estimated from the T dependence of the resistivity in the normal state, under the assumption – consistent with the BCS treatment – of negligible interband scattering. Further details on this procedure can be found in the supplementary information of Ref. [183]. The resulting curve that best fits the data is shown as a dashed line in fig. 4.15 and corresponds to a diffusivity ratio of $\eta_{21} = 10.47$.

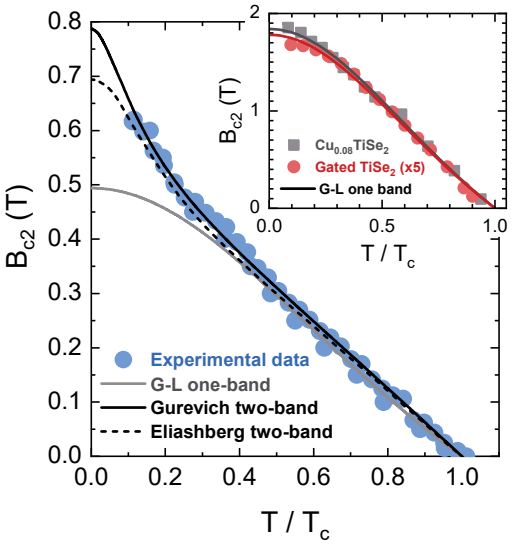

Figure 4.15: Dependence of the upper critical field B_{c2} on the reduced temperature T/T_c for H_xTiSe_2. Symbols represent mean-field values as shown in fig. 4.6. Theoretical fits are based on different models: the one-band Ginzburg-Landau model [196] (solid gray line), the two-band Gurevich model [200, 201, 202] (solid black line), and the two-band Eliashberg model [219, 220] (dashed black line). For comparison, the inset displays B_{c2} versus T/T_c for Cu_xTiSe_2 (gray squares from Ref. [15]) and ion-gated $TiSe_2$ (red circles from Ref. [17]), with corresponding one-band Ginzburg-Landau fits (solid lines). Adapted from Ref. [183]

This result demonstrates that this Eliashberg-based model also accurately reproduces the experimental $B_{c2}(T)$ across the entire temperature range.
In conclusion, both the weak- and strong-coupling models, *employing the same coupling parameters used to reproduce the T-dependence of the gaps*, demonstrate excellent agreement with the experimental data. They accurately capture the temperature trend, including the positive curvature, and yield comparable values for $B_{c2}(0)$ and η_{21}. Such findings firmly distinguish the H-induced superconducting state in H_xTiSe_2 from those induced in $TiSe_2$ by either electric-field-driven charge doping [185] or Cu intercalation [15]. In the latter cases, $B_{c2}(T)$ displays the conventional negative curvature characteristic of single-gap superconductors (red and black symbols in the inset of fig. 4.15), which is well described by the one-band Ginzburg-Landau model (solid lines).

4.5 Possible origin of two-gap superconductivity

Since quantitative analysis of all measurements performed consistently indicates the presence of two-gap superconductivity, this section eventually explores the possible origins of this phenomenon in H_xTiSe_2.

To contextualize the discussion, however, it is helpful to briefly review what is currently known about the band structure of both pristine and doped $TiSe_2$. At low temperatures and ambient pressure, undoped $TiSe_2$ is well described by a single electronic band formed by six equivalent electron pockets located at the L points of the Brillouin zone [221, 222]. Moderate electron doping – achieved, for example, via Cu intercalation – raises the Fermi level without significantly altering the band structure [223, 8]. In contrast, the application of pressure markedly modifies the Fermi surface of $TiSe_2$, inducing a Lifshitz transition characterized by the emergence of large hole pockets at the Γ point. This transition gives rise to multiband superconductivity, where electron and hole pockets contribute distinct superconducting bands. A comparable behavior has been observed in Nb-based superconducting transition metal dichalcogenides, such as NbS_2 and $NbSe_2$ [176, 177, 178, 179, 180, 181, 182]. By analogy, the emergence of two-gap superconductivity in H_xTiSe_2 could be attributed to H doping inducing a Lifshitz transition that modifies the Fermi surface. However, Hall effect measurements do not show evidence of charge compensation via hole pocket formation [8]. This observation suggests that the two bands may originate from multiple inequivalent electron pockets, resembling the behavior observed in electron-doped semiconducting transition metal dichalcogenides such as MoS_2, WS_2, $MoSe_2$, and WSe_2 [224, 225, 226, 202]. Nonetheless, this scenario appears inconsistent with *ab-initio* calculations, which predict the presence of only a single electronic band crossing the Fermi level in H_xTiSe_2 [8].

Alternatively, drawing inspiration from $2H$-$NbSe_2$ [175], the two-gap behavior observed in H_xTiSe_2 might be attributed to a strongly anisotropic distribution of the superconducting gap in reciprocal space. In this perspective, the apparent two-gap superconductivity likely originates not from multiple bands but from a multi-orbital effect triggered by H intercalation. Indeed, *ab-initio* calculations revealed that H intercalation in $TiSe_2$ results in partial filling of the d_{z^2} band, which couples strongly to phonons, and promotes hybridization with H-derived states. Thus, given that the $Ti_{d_{z^2}}$ states are mainly localized along the Γ–A direction in the Brillouin zone, this significant alteration in the orbital character at the Fermi level is expected to drive a pronounced gap anisotropy (fig. 4.16).

However, distinguishing between the different scenarios is not straightforward, but requires a direct probe of the Fermi surface, including quantum oscillation measurements or angle-resolved photoemission spectroscopy. Such experiments represent promising directions for future research.

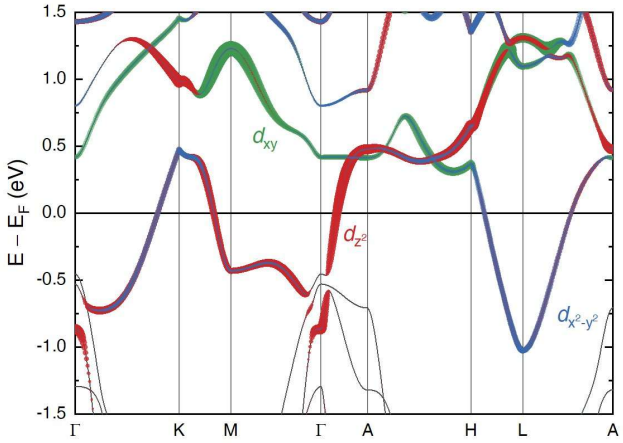

Figure 4.16: Electronic band structure of $1T$-H_1TiSe_2 obtained from *ab-initio* calculations, with the orbital character highlighted using different colors: red for the d_{z^2} contribution, green for the d_{xy} and blue for $d_{x^2-y^2}$.

4.6 Conclusions

This study exploits IGP to intercalate H into $1T$-$TiSe_2$, enabling the synthesis of the recently discovered superconducting H_xTiSe_2, which preliminary evidence suggested may host a non-trivial superconducting order parameter. The nature of this superconducting order parameter is then examined through three independent techniques: magneto-transport measurements, directional PCARS, and tunneling

spectroscopy. Among these, directional PCARS not only provides critical insights into the superconducting properties of H_xTiSe_2 but also provides valuable technical expertise for studying more exotic superconducting states, which will be explored in the following chapter.

Converging evidence from these measurements supports the presence of a non-trivial superconducting order parameter characterized by two nodeless superconducting gaps. Specifically, the temperature dependence of the superconducting gaps extracted from PCARS and tunneling spectroscopy, together with the upper critical field obtained from magneto-transport data, is well described by both BCS theory and the more comprehensive Eliashberg formalism for two-band superconductivity. The fits of these theoretical models to the experimental data yield coupling constants, densities of states, and diffusivity ratios that exhibit strong mutual agreement.

Nonetheless, variations in the gap values are observed across different PCARS contacts, indicating a possible spatial modulation in the gap amplitudes. Despite this, the highly spatially resolved tunneling spectroscopy reliably detects two distinct gaps, effectively ruling out the possibility that these arise purely from phase separation. In light of this, drawing on insights from previous *ab initio* calculations, the two-gap superconductivity observed in this system is proposed to arise from an unconventional multi-orbital, single-band electronic structure, rather than from a conventional multi-band Fermi surface scenario.

Chapter 5

Towards topological superconductivity

Having acquired proficiency in using both ionic gating-induced protonation (IGP) and point-contact Andreev reflection spectroscopy (PCARS) to induce and probe superconductivity respectively, this chapter presents the final investigation of the thesis, which focuses on two candidate topological superconductors: layered Bi_2Se_3 and $FeSe_{1-x}Te_x$. Specifically, IGP is performed on pristine Bi_2Se_3 to determine whether hydrogen (H) intercalation induces a superconducting phase, as preliminarily claimed in a previous study, and whether this hypothetical phase exhibits potential signatures of topological superconductivity detectable via PCARS. Similarly, IGP and PCARS are applied to layered $FeSe_{1-x}Te_x$ to investigate the effects of H intercalation on its intrinsic superconducting phase and to search for potential topological superconductivity.

The chapter is structured in two main sections, each dedicated to one of the candidate materials. After a brief overview of the key experimental evidence from previous studies suggesting their potential to host topological superconductivity, the results of the present investigation are presented and critically discussed.

5.1 Doped Bi_2Se_3

5.1.1 Framework for $H_xBi_2Se_3$ study

Following the Fu-Kane proposal suggesting that 2D topological superconductivity can be induced by proximizing a topological insulator with a conventional *s*-wave superconductor [34], significant efforts have been dedicated to inducing conventional bulk superconductivity in topological insulators. The rationale is that a bulk superconducting state could, in turn, induce superconductivity in the inherent topological surface states of topological insulators, thereby resulting in superficial

topological superconductivity.

Within this context, Bi_2Se_3 has emerged as a particularly promising topological insulator. This material features a favorable layered crystal structure composed of Se–Bi–Se–Bi–Se quintuple layers, which are weakly bound to adjacent layers via van der Waals forces [227]. Due to this layered architecture, various doping strategies, such as substitution or intercalation of foreign atoms, can be employed to tune its electronic properties and potentially induce superconductivity.
Thus, motivated by the successful induction of superconductivity in $TiSe_2$ via Cu intercalation [15], Cu was initially investigated as a dopant in Bi_2Se_3. Preliminary experiments demonstrated that substitutional Cu doping, yielding $Bi_{2-x}Cu_xSe_3$ with $0 \leq x \leq 0.15$, failed to induce superconductivity. In contrast, Cu intercalation, resulting in $Cu_xBi_2Se_3$ for $0.1 \leq x \leq 0.3$, gave rise to a superconducting phase with $T_c \approx 3.8\,\mathrm{K}$ (fig. 5.1a) [228, 229]. However, transport measurements showed finite resistivity below T_c, and DC magnetic susceptibility indicated that only about 20% of the sample volume exhibited full diamagnetism, questioning the bulk nature of the superconductivity and motivating the search for higher-quality samples [230].

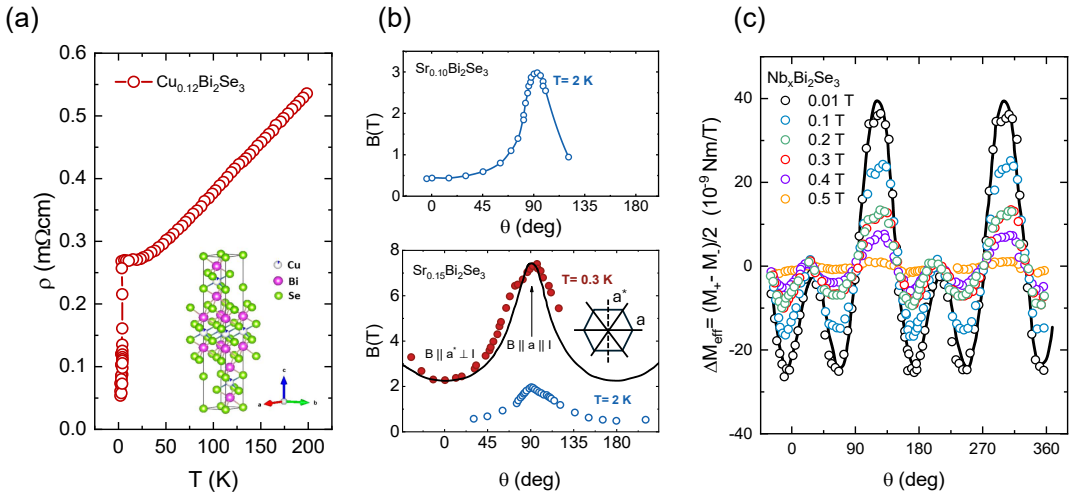

Figure 5.1: (a) Temperature-dependent resistivity of $Cu_{0.12}Bi_2Se_3$ single crystals. Reprinted from Ref. [228]. A schematic of the $Cu_{0.2}Bi_2Se_3$ crystal structure is presented in the inset. Reprinted from Ref. [231]. (b) In-plane angular dependence of H_{c2} from magnetoresistance in $Sr_xBi_2Se_3$, and (c) in-plane field-angle dependence of the irreversible magnetic torque in $Nb_xBi_2Se_3$, providing evidence for nematic superconductivity. Data reprinted from Ref. [232].

To enhance sample quality, an electrochemical technique was employed to intercalate Cu^+ ions into Bi_2Se_3 by applying a voltage across a saturated solution of CuI powder in acetonitrile [233, 234]. Although samples treated via this method

were initially non-superconducting, appropriate post-treatment annealing successfully induced superconductivity for x values between 0.09 and 0.64, yielding T_c values ranging from 2.2 K to 3.6 K and shielding fractions up to 50%.
With $Cu_xBi_2Se_3$ prepared by electrochemical intercalation showing a T_c of 3.2 K, PCARS measurements were then carried out to probe the superconducting gap symmetry [36]. Contrary to expectations for a proximity-induced 2D p-wave state, the results provided evidence for a 3D, unconventional nematic superconductivity with odd-parity, spin-triplet Cooper pairing [36, 232, 44, 43].

Cu is not the only dopant whose intercalation into Bi_2Se_3 leads to superconductivity; similar effects have been observed for Sr and Nb [232]. In early work on Sr-intercalated Bi_2Se_3 ($Sr_xBi_2Se_3$) prepared by melt growth, superconductivity emerged with $T_c = 2.5$ K and a shielding fraction of 91.5% for $x = 0.06$ [38]. Later studies reported superconductivity for $x = 0.1$–0.2, with T_c between 2.5 K and 3 K and shielding fractions remaining close to 90% [39, 235, 236]. Nb-intercalated Bi_2Se_3 ($Nb_xBi_2Se_3$), also grown by the melt method, shows $T \approx 3$ K and nearly 100% shielding for $x = 0.25$ [237, 238, 239]. In both Sr- and Nb-intercalated samples, the field–angular dependence of magnetoresistance and of the magnetic upper critical field provides strong evidence for unconventional nematic superconductivity with odd-parity, spin-triplet Cooper pairing (fig. 5.1b,c)[45, 240, 40, 41]. In this

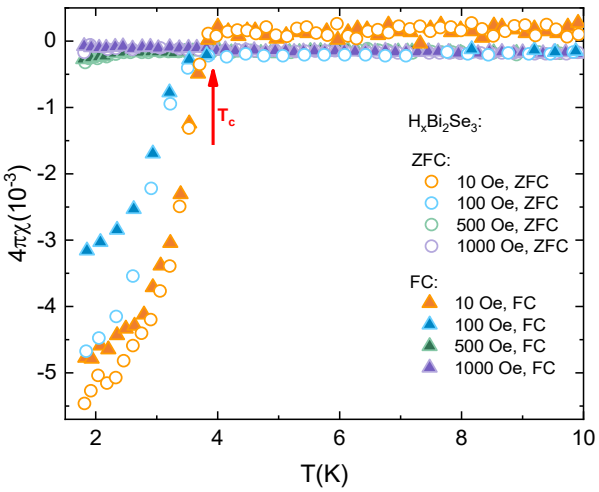

Figure 5.2: DC susceptibility of $H_xBi_2Se_3$, obtained via ionic gating-induced protonation of Bi_2Se_3 single crystals, measured under field-cooled (FC) and zero-field-cooled (ZFC) conditions at the magnetic fields indicated in the labels. The onset of the superconducting transition for the lowest-field curve is marked by a red arrow. Data reprinted from Ref. [42]

context, a preliminary incomplete investigation by Cui *et al.* [42] indicated that H

intercalation via IGP may also induce superconductivity in Bi_2Se_3, with a T_c of approximately 3.8 K, as determined from DC susceptibility measurements (fig. 5.2). These results motivate further experiments to reproduce the claimed superconducting state and, if confirmed, to investigate its superconducting gap structure to determine whether it is consistent with the behavior observed for other intercalants.

5.1.2 Experimental methods

This investigation was carried out on single crystals of Bi_2Se_3 purchased from 2D Semiconductors Inc. The study involved performing IGP and subsequently characterizing the electronic properties of the treated samples through transport measurements, with the goal of identifying any modifications induced by IGP and verifying the possible emergence of the superconducting phase previously claimed in the literature.

IGP was conducted both *ex situ* and *in situ* (see chapter 2). Initially, *ex-situ* IGP was performed to replicate the conditions under which superconductivity had previously been claimed: specifically, applying a gate voltage (V_G) of +3 V across the conventional ionic liquid (IL) EMIM-BF_4 at approximately 350 K for 15 days [42, 95]. The *ex-situ* setup was chosen because, unlike the *in-situ* configuration, it can be implemented on a hot plate, thereby allowing operation above room temperature (T). Additionally, it supports long-duration IGPs due to the use of larger electrolyte volumes compared to the *in-situ* approach. Larger volumes results in a reduction of the relative rate of electrolyte degradation under a constant applied voltage, enabling a continuous +3 V gating for the full two-week duration, provided that a drop of water is added daily to sustain the water dissociation mechanism underlying IL-based IGP [11].
After this treatment, the sample was quickly removed from the gating medium – effectively stopping intercalation by opening the gating circuit – rinsed with acetone, and electrically contacted to measure its resistivity vs. temperature (ρ–T) behavior. This preparation required approximately one hour before the sample was inserted into the ^{4}He cryostat for transport characterization.

Subsequently, IGP was carried out by varying the tunable parameters of the original gating protocol to investigate the response of the material to different levels of H^+ intercalation. As an initial step, in the *ex-situ* configuration, the same procedure described above was repeated at a reduced working temperature of 300 K. Next, the duration of the V_G application was reduced, shifting toward short-duration IGPs on the order of hours. This adjustment enabled the usage of the *in-situ* configuration, allowing real-time monitoring of the response of the material to IGP via resistivity measurements. At the same time, it eliminated the need for rinsing and contacting the sample prior to transport characterization, thereby removing

any dead time between IGP treatment and transport measurements and reducing potential sources of deintercalation.
Within this *in-situ* setup, additional parameters were adjusted, including the final applied V_G and the choice of the electrolyte, to explore the possibility of achieving higher levels of H^+ intercalation. Specifically, the 1:3 choline chloride: glycerol deep eutectic solvent (1:3 ChCl:gly DES) used in chapter 3 was employed as a substitute for the conventional EMIM-BF_4. Finally, this configuration was also used to assess the reactivity of the material to the sudden removal of V_G at different temperatures, providing insights into its deintercalation behavior.

5.1.3 Results

As anticipated, the first step in investigating $H_xBi_2Se_3$ as a potential topological superconductor involved reproducing the superconducting phase that had been preliminarily claimed in literature. To this end, the original procedure used by Cui *et al.* [42, 95] to observe superconductivity in Bi_2Se_3 was replicated. In the *ex-situ* configuration at 350 K, V_G was ramped from 0 V to 3 V at 1 mV/s – a rate previously determined (chapter 3) to allow the ion dynamics in the EMIM-BF_4 to follow the gating ramp effectively – and then held constant for 15 days. The resulting ρ–T curve, shown in fig. 5.3a (solid brown line), exhibits a behavior markedly different from that of pristine Bi_2Se_3 (solid black line). Pristine Bi_2Se_3 exhibits a metallic-like T-dependence ($d\rho/dT < 0$) arising from bulk conduction due to n-type doping from selenium vacancies [241, 242, 243, 244]. The residual resistivity ratio (RRR), defined here as $\rho(200\,K)/\rho(4\,K)$, is 1.45 and is consistent with previous reports on high-quality bulk Bi_2Se_3 crystals [245, 246, 247]. In contrast, IGP-treated Bi_2Se_3 maintains a metallic-like trend but exhibits an increased RRR of 1.96, indicating that IGP treatment effectively modifies the transport properties of Bi_2Se_3. However, no evidence of superconductivity was detected, either at the previously reported temperature of 3.8 K [42] or down to 1.7 K.

Since no superconducting transition was detected under the initial protocol, the tunable parameters of IGP were systematically adjusted to probe how the material responds to different levels of H^+ intercalation. The aim was to investigate the evolution of the ρ–T behavior of Bi_2Se_3 across varying H concentrations and determine whether and when a superconducting transition emerges. As a first step, the process temperature was adjusted: the same procedure previously applied was repeated at 300 K instead of 350 K. Temperature has two competing effects: on one hand, higher temperatures can facilitate H^+ intercalation by enhancing water dissociation in the IL and promoting ion diffusion into the sample [11, 101, 102, 103, 104]; on the other hand, elevated temperatures can accelerate electrolyte degradation, which may diminish its capacity to sustain H^+ intercalation, favor the intercalation

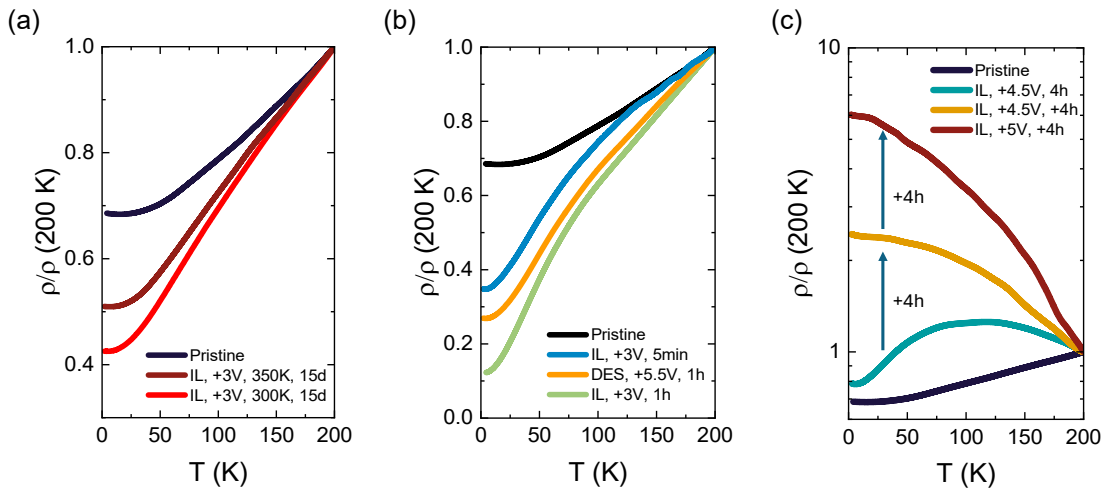

Figure 5.3: Temperature (T)-dependence of the resistivity (ρ), normalized to its value at 200 K, for Bi_2Se_3 single crystals treated with different ionic gating-induced protocol (IGP) protocols. The legend summarizes, for each curve, the corresponding IGP process in terms of electrolyte type, final applied gate voltage, and application duration. Panel (a) presents results from long-duration IGPs, panel (b) from short-duration IGPs, and panel (c) from ionic liquid (IL)-based IGPs performed at higher V_G compared to the original protocol that yielded a superconducting phase. For reference, the pristine curve (solid black line) is shown in all panels.

of organic ions [76], and increase reactivity that could potentially damage the sample [248]. The resulting ρ–T curve from this adjusted protocol, shown in fig. 5.3a as the solid red line, retains the overall shape of the 350 K-treated sample with no evidence of superconductivity, but exhibits a higher RRR of 2.35.

Although the curves obtained so far differ, their variations remain relatively modest, motivating an exploration of other parameter configurations to induce more pronounced changes. A key parameter in this regard is the duration for which the final $V_G = +3$ V is applied. Indeed, longer IGP treatments are expected to result in increased exposure to H^+ injection and, consequently, higher H concentrations, whereas shorter treatments are likely to result in samples with lower H^+ content [11]. To investigate this effect, the application time was reduced, shifting toward *in-situ* IGP treatments on the order of hours. In these procedures, the gating ramp was kept identical to that used in long-duration IGPs, but the final V_G was maintained for only 5 minutes (solid blue line, fig. 5.3b) or 1 hour (solid green line, fig. 5.3b). Since processes above room T are not feasible in the *in-situ* setup, all these IGP treatments were conducted at 300 K. In both short-duration cases, the resulting ρ-T curves differ markedly from those obtained after long-duration IGPs,

both in overall shape and in *RRR*. Below 100 K, the resistivity decreases more steeply with decreasing T, giving rise to a hump-like profile. This enhanced drop results in significantly higher *RRR* values: 2.87 for the 5-minute treatment and 8.02 for the 1-hour treatment. Nonetheless, no evidence of superconductivity is observed in both cases.

At this stage, another adjustable parameter was considered: the final applied V_G. Like temperature, this parameter can induce competing effects. Increasing the voltage enhances the reactivity of the IL, which can, on the one hand, promote more efficient water dissociation and potentially increase the degree of intercalation. On the other hand, higher voltages may also trigger undesired reactions, such as the intercalation of other ionic species (e.g., $EMIM^+$ from EMIM-BF_4 [76, 75]) or direct chemical interactions with the sample, potentially leading to structural damage [248]. To enable comparison with previously studied short-duration IGPs, experiments at gate voltages above 3 V were conducted over similar timescales (on the order of hours). Initially, V_G was ramped from 0 to 4.5 V at a rate of 1 mV/s and held for 4 h. The resulting ρ–T curve (solid blue line in fig. 5.3c) clearly exhibits a different behavior: the resistivity is larger than the pristine one in the whole temperature range, with a positive slope between $\sim$ 7 and 100 K and a negative slope between 100 and 200 K, yielding a reduced *RRR* of 1.27.
To further investigate this behavior, after measuring this ρ–T curve, the sample was brought back to room T to allow the EMIM-BF_4 to reactivate, and $V_G = +4.5$ V was applied for an additional 4 h. The resulting ρ–T curve (solid orange line, fig. 5.3c) displayed a clear insulating-like behavior, with $d\rho/dT < 0$ across the entire temperature range. Repeating the procedure with an increased voltage of +5 V once the EMIM-BF_4 was active and maintaining it for additional 4 h produced an even stronger insulating behavior (solid brown line, fig. 5.3c). This striking difference in the response of the gated Bi_2Se_3 system to the value of V_G suggests that for $V_G \leq 3$ V, H^+ ions were efficiently intercalated, whereas at $V_G > 3$ V, the larger $EMIM^+$ ions were preferentially intercalated. Such intercalation is likely to expand the spacing between the quintuple layers of Bi_2Se_3, which are held together by van der Waals interactions [76], thereby inducing a transition from a metallic-like to an insulating state [249]. Indeed, Bi_2Se_3 crystals gated at $V_G > 3$ V often exhibited an increase in thickness and a partial delamination when they were inspected at the end of the measurements.

To mitigate this effect, the conventional EMIM-BF_4 was replaced with the 1:3 ChCl:gly DES employed in the study presented in chapter 3, which had been shown to facilitate a more extensive H^+ intercalation in palladium compared to EMIM-BF_4 at the same applied V_G [105]. In addition, the 1:3 ChCl:gly DES demonstrated the capability to sustain H^+ intercalation in palladium at voltages (up to 12 V) significantly higher than the operational limit of EMIM-BF_4. On these basis, V_G was

ramped across the 1:3 ChCl:gly DES from 0 V to 5.5 V at a rate of 1 mV/s and then held constant for 1 h. Contrary to expectations, the resulting ρ-T curve (solid orange line in fig. 5.3b) was found between the 5-min and the 1-h treatment ones obtained with EMIM-BF_4, exhibiting a similar hump-like profile with an RRR of 3.96 and no indication of superconductivity. This suggests that, unlike in palladium, DES-based IGP on Bi_2Se_3 does not provide a clear advantage over IL-based IGP, as operating at higher voltages over comparable timescales yields no significant improvement relative to EMIM-BF_4.

After exploring various alternative parameter configurations, the focus ultimately shifted toward enabling a rigorous comparison between results obtained under *in-situ* and *ex-situ* conditions. Indeed, unlike *in-situ* IGP, *ex-situ* treatment requires the samples to remain at room T for at least 1 h without applied voltage during the contacting procedure – a condition that could permit partial deintercalation. Therefore, it is crucial to quantify the tendency of Bi_2Se_3 to release H^+ ions and return to its pristine state. To directly probe this effect, multiple sequential deintercalation cycles were performed under *in-situ* conditions, enabling continuous monitoring of the response of the material. The first deintercalation was conducted on the protonated sample prepared by applying a final $V_G = +3$ V for 1 h. After recording its ρ–T characteristics, the sample was held at 240 K for 1 h with V_G removed by physically opening the gating circuit, ensuring that only deintercalation could occur [11]. This temperature was chosen deliberately as an initial trial because it minimizes deintercalation, allowing the response of the material to small perturbations to be observed.
The resulting ρ–T curve after 1 hour of deintercalation is shown by the solid green line in fig. 5.4, with the left panel covering the 0–200 K range and the right panel providing a zoomed-in view of the 5–50 K subrange. Notably, the initial ρ–T characteristics were smoothed, the hump-like feature was suppressed, and the RRR decreased by 7.23%, from 8.02 to 7.44. Repeating the same procedure under identical conditions (240 K, 1 h) produced a similar curve (solid yellow line) with a slightly lower RRR of 7.15, indicating only a limited additional effect.
To promote more substantial deintercalation, the sample was then held at 270 K for 10 h. This cycle resulted in the solid orange curve, which preserved the overall shape but exhibited a further reduced RRR of 5.53. A final cycle at room T for 10 h decreased RRR to 3.96 while maintaining a similar curve profile. Throughout all cycles, no signatures of superconductivity were observed.
These results suggest that at low temperatures (240 K), deintercalation is largely suppressed; however, the observed smoothing of the curve may indicate H rearrangement within the crystal. At higher temperatures, deintercalation becomes increasingly effective, leading to a pronounced reduction in RRR.

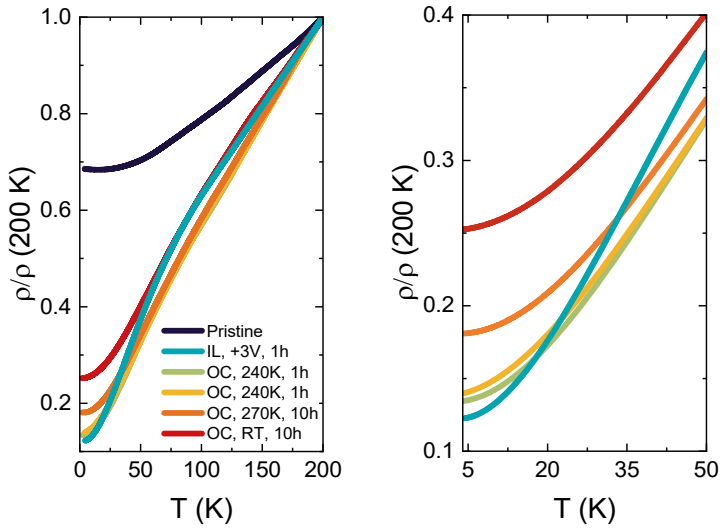

Figure 5.4: T-dependence of the resistivity, normalized to its value at 200 K, for $H_xBi_2Se_3$ undergoing successive deintercalation cycles. The initial $H_xBi_2Se_3$ sample (solid petrol blue line) was prepared by applying $V_G = +3$ V for 1 h across the EMIM-BF_4 ionic liquid (IL) on pristine Bi_2Se_3 (solid black line). Deintercalation was then induced by opening the gating circuit (OC = open circuit) at a specified temperature for a controlled duration. For each curve, the legend indicates whether the circuit was open, the temperature at which deintercalation was performed, and the duration of the process. The right panel presents a zoom of the left panel to better resolve the low-T behavior and highlight the effects of deintercalation.

5.1.4 Discussion

Analysis of the collected data indicates that the observed changes in the transport properties of Bi_2Se_3 under IGP at +3 V are primarily due to H^+ intercalation. This interpretation is supported by tests at higher gating voltages, where $EMIM^+$ intercalation takes place and produces a distinctly different material response.

In addition, deintercalation tests rule out the possibility that the ρ–T behavior observed after long-duration *ex-situ* IGP experiments is primarily governed by deintercalation during the time required for mounting the sample for resistance measurements. Indeed, although the test carried out at room-T under open-circuit (OC) conditions produced a 39% change in the RRR relative to its initial value, it is important to note that this experiment was conducted over a timescale nearly an order of magnitude longer than the time required for rinsing and contacting the *ex-situ* treated samples before transport measurements. Consequently, the influence of deintercalation on the ρ-T curves of *ex-situ* treated samples is expected to be negligible, with the observed transport trends dominated by intercalation effects.

Within this framework, the fact that the ρ–T curves from long-duration IGPs retain an overall shape resembling the deintercalation curves – without exhibiting the hump-like feature typical of short-duration IGPs – can likely be attributed to H dynamics. In long-duration IGPs, although a larger amount of H^+ is intercalated into the crystal, the ions have sufficient time to diffuse and redistribute within the lattice. This redistribution, previously proposed as the main factor responsible for smoothing the hump observed during the deintercalation cycle at 240 K, occurs in long-duration IGPs but is suppressed in short-duration IGPs, resulting in the presence of the hump in the latter.

Based on these observations, it is reasonable to infer that, under otherwise fixed IGP conditions, longer exposure to the applied V_G results in increased H^+ intercalation and, consequently, a higher overall H content in Bi_2Se_3. Within this perspective, the data suggest that the *RRR* exhibits a dome-like trend as a function of exposure time – or tentatively, as a function of increasing H content. As a matter of fact, during short-time IGPs (up to 1 h), *RRR* increases with longer exposure. In contrast, long-duration IGP (15 days at 300 K) – likely corresponding to much higher H uptake – yields a substantially lower *RRR*, implying that *RRR* first reaches a maximum and then decreases at high H content. Consistent with this picture, the long-duration curve obtained at 350 K, which displays an even lower *RRR*, can be attributed to further enhanced H incorporation, in line with the expectation that elevated working temperatures promote stronger intercalation and diffusion, and/or larger disorder, as observed in H-intercalated $TiSe_2$ [8].

Eventually, concerning superconductivity, despite testing a range of parameter configurations, no superconducting transition was observed, even when following the original protocol reported by Cui *et al.* [42, 95]. Considering the difference in characterization techniques between this study and Cui *et al.* [42, 95] – resistivity measurements versus susceptibility measurements – it is possible that, if a superconducting phase does build up, the fraction of the material exhibiting superconductivity is too small to produce a detectable signal in electric transport measurements, since they require a percolative network of the superconducting phase to be successfully established to allow clear detection. Conversely, small diamagnetic signals can be picked up in susceptibility measurements, and indeed Cui *et al.* [42] did not evaluate the superconducting fraction corresponding to their measured curves. If this is indeed the case, considerable effort would be required to identify a protocol capable of achieving a zero-resistivity state. Accordingly, future investigations on protonated Bi_2Se_3 should focus on systematically mapping (both with transport and magnetic measurements) the behavior of the material at different levels of H^+ intercalation, ideally with quantitative estimation of the H content in each treatment, to enable a more rigorous understanding of the response of the material.

5.2 $FeSe_{1-x}Te_x$

5.2.1 Framework for $FeSe_{1-x}Te_x$ study

Since no superconducting phase could be induced in Bi_2Se_3 through IGP, the focus was redirected towards alternative materials that may host 2D topological superconductivity via the proximity effect between their Dirac-cone–like surface states and a bulk *s*-wave superconductivity, as proposed by Fu and Kane [34]. Within this framework, the investigation was extended to $FeSe_{1-x}Te_x$, which, as described below, exhibits both Dirac-cone–like surface states and bulk superconductivity.

$FeSe_{1-x}Te_x$ belongs to the family of iron-based superconductors, the second class of materials discovered to exhibit high temperature superconductivity [250]. Its parent compound, FeSe, crystallizing in the tetragonal PbO-type structure, undergoes a superconducting transition at $T_c = 8\,\mathrm{K}$ [251]. Notably, this superconducting phase is highly sensitive to pressure, with T_c increasing to 36.7 K under high pressure [252]. Similarly, partial substitution of Se with Te, forming $FeSe_{1-x}Te_x$, affects T_c, increasing it to a maximum of 14.5 K around $x \approx 0.5$ in the single crystals. The complete substitution (FeTe), instead, leads to a compound with an antiferromagnetic ground state and not exhibiting a superconducting phase (fig. 5.5).

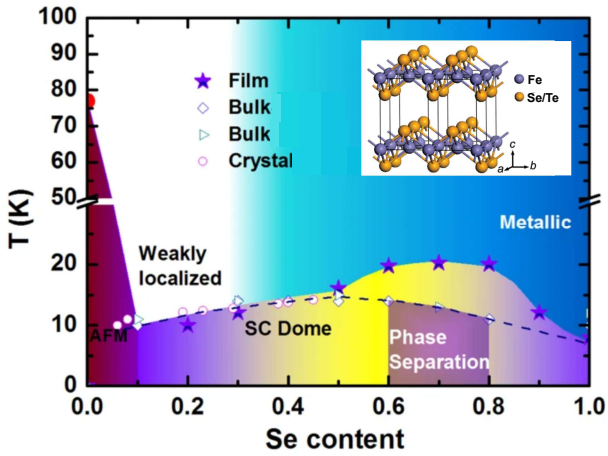

Figure 5.5: Electronic phase diagram of $FeSe_{1-x}Te_x$ plotted in the temperature–Se content plane. Adapted from Ref. [253]. The inset shows the schematic side view of the $FeSe_{1-x}Te_x$ crystal structure. Reprinted from Ref. [254]

This scenario becomes even more complex in the presence of excess Fe, yielding $Fe_{1+\delta}Se_{1-x}Te_x$. As a matter of fact, excess Fe ions are known to suppress T_c and induce local magnetic behavior [255, 256].

Beyond the enhancement of T_c, Te substitution at $x \approx 0.5$ has been proposed to drive the emergence of intrinsic topological surface states. Density functional theory calculations along the Γ–Z direction indicate that Te substitution shifts the odd-parity p_z band of FeSe downward, toward the Fermi level (E_F) [47] (fig. 5.6a). This highly dispersive band intersects the even-parity d_{xz} band, and the strong spin–orbit coupling (SOC) introduced by Te [257] opens a gap at the crossing point. When the band structure is projected onto the (001) surface, a Dirac-cone–like spin-helical surface state appears inside this SOC gap, lying close to E_F [48]. Consequently, $FeSe_{1-x}Te_x$ (with x between 0.4 and 0.7) can be regarded as a topological insulator, where superconductivity arising in the bulk may proximize the topological surface states, thereby inducing a 2D p-wave topological superconductivity [34].

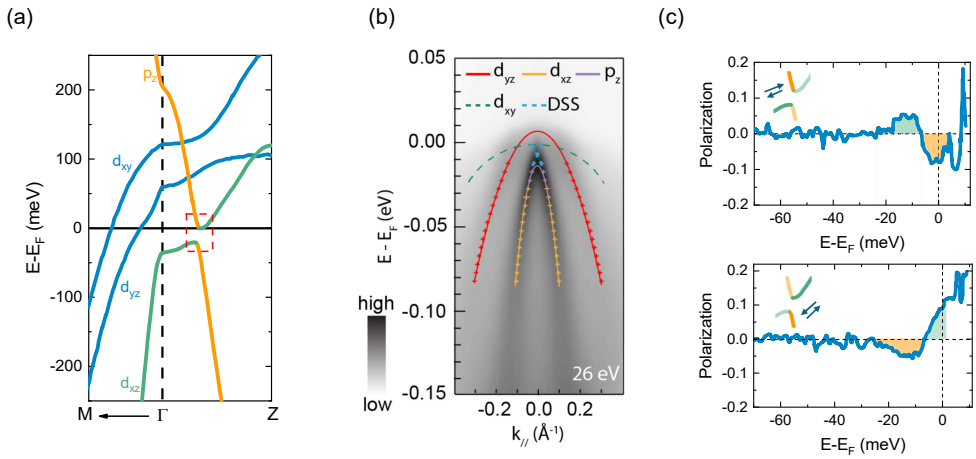

Figure 5.6: (a) First-principles calculations of the electronic dispersion along the Γ–M and Γ–Z directions of $FeSe_{0.45}Te_{0.55}$. The dashed rectangle marks the spin orbit coupling-induced gap associated with inverted bands. Data reprinted from Ref. [48]. (b) Representative angle-resolved photoemission spectrum (ARPES) along Γ–M measured at $h\nu = 26\,\mathrm{eV}$ with p polarization. Crosses correspond to the band dispersion extracted from momentum distribution curve analysis. Solid lines (red and purple–orange) correspond to parabolic fits for the d_{yz} and $p_z - d_{xz}$ states, while dashed curves (green and blue) highlight the d_{xy} band and the Dirac surface state (DSS) Reprinted from Ref. [258]. (c) Energy distribution curves obtained via spin-resolved ARPES, illustrating the spin-helical texture of the surface states. Data reprinted from Ref. [48]

An initial experimental evidence for this scenario was brought forward by Zhang et al. [48]: angle-resolved photoemission spectroscopy (ARPES) revealed the Dirac-cone–like surface states, spin-resolved ARPES verified their spin-helical texture, and energy distribution curve (EDC) analysis showed the opening of a superconducting gap at the surface (fig. 5.6b,c).

However, this interpretation has been challenged by more recent ARPES experiments. These studies reported that the Dirac cones in $FeSe_{1-x}Te_x$ become gapped below T_c not only at E_F [259]. Such behavior has been attributed to the onset of surface ferromagnetism, which, however, is expected to be detrimental to the topological insulator–based mechanism for topological superconductivity just described [260]. To address this issue, an alternative mechanism has been proposed [50]: topological superconductivity may instead emerge from the interplay of three ingredients – surface magnetism, Rashba SOC [261], and a hard superconducting gap with $s_\pm$-wave symmetry [262].

Regardless of the microscopic mechanism responsible for the emergence of surface p-wave topological superconductivity, theory predicts that such a state should host Majorana bound states at the boundary with a trivial topological phase. This expectation directly arises from the mismatch of the topological invariants characterizing the two phases. Given the relevance of Majorana bound states as fundamental building blocks for fault-tolerant quantum computation, considerable effort has been devoted to investigating their presence at the boundaries of the potential topological superconducting phase in $FeSe_{1-x}Te_x$. Such boundaries naturally emerge around defects. For instance, zero-bias conductance peaks –interpreted as Majorana bound states arising due to the bulk–boundary correspondence and called Majorana zero modes MZMs – have been observed on interstitial Fe atoms at the $FeSe_{1-x}Te_x$ surface [52] or at the ends of one-dimensional lines of missing Fe and/or Te atoms in a single-unit-cell-thick layer of $FeSe_{1-x}Te_x$ [53].

Defects, however, are not the only route to observe MZMs in $FeSe_{1-x}Te_x$. Boundaries capable of hosting MZMs can also appear in the vortex cores of a superconductor under an applied magnetic field [48, 50]. Indeed, in a p-wave topological superconductor, vortex cores are predicted to host vortex-bound states with energies following an integer sequence $E = \mu\Delta^2/E_F$, where $\mu = (0, \pm1, \pm2, \dots)$ [263]. In contrast, conventional s-wave superconductors exhibit vortex-bound states spaced according to half-odd-integer levels, $E = \mu\Delta^2/E_F$ where $\mu = (\pm1/2,\ \pm3/2,\ \pm5/2, \dots)$. These states, which notably lack a zero-energy mode, are known as Caroli-deGennes-Matricon (CdGM) states [141].

Unequivocally identifying a zero-energy peak as a MZM, however, is extremely challenging. Low-energy vortex-core states can be contaminated by impurities, bulk-state contributions, quasiparticle poisoning, and sample inhomogeneity [255]. Instrument sensitivity also plays a critical role: the measurement resolution must be sufficient to resolve individual vortex-bound states, otherwise a zero-bias peak could arise from the convolution of nearby finite-energy states rather than from a true MZM [51]. For $FeSe_{1-x}Te_x$, ARPES and scanning tunneling microscopy measurements estimate E_F to be 5–20 meV [264] and the smallest superconducting gap

Δ around 1.5 meV [262], implying that the lowest trivial CdGM states, given by ($E_{\mu=\pm1/2} = \pm\Delta^2/E_F$), are expected to occur in the range of roughly $\pm$(60–220) μeV. Distinguishing MZMs from these states therefore requires energy resolution of a few tens of μeV, achievable by operating at ultra-low temperatures to suppress thermal broadening and by minimizing instrumental noise sources such as electrical fluctuations and lock-in modulation. An illustrative example is provided by the work of Wang et al. [54], who performed scanning tunneling spectroscopy measurements in the vortex cores of $FeSe_{1-x}Te_x$ and reported the first observation of zero-energy peaks, which were attributed to potential MZMs. However, a subsequent study under similar conditions observed bound-state peaks only at finite energies, suggesting a trivial origin instead [55]. This discrepancy was attributed to sample inhomogeneity, which causes variations in the superconducting gap [265]. Supporting this view, another study [266] reported the coexistence of vortices exhibiting zero-bias peaks, interpreted as MZMs, and vortices without zero-bias peaks within the same sample, further indicating the role of inhomogeneity (see fig. 5.7). Addi-

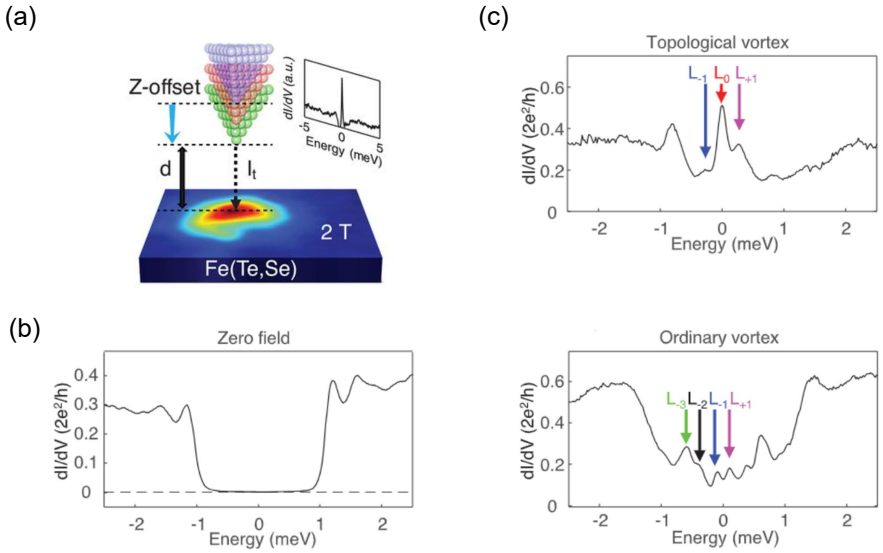

Figure 5.7: (a) Schematic of the scanning tunneling microscopy setup used to measure dI/dV spectra of vortex cores in $FeSe_{0.45}Te_{0.55}$. In the absence of a magnetic field, no vortices are observed and only the superconducting gap is detected, as shown in panel (b). When a magnetic field is applied, two types of vortices appear: topological and trivial. (c) Typical dI/dV spectrum taken at the center of a topological vortex (upper panel), showing a zero-bias in-gap state together with Caroli-de Gennes-Matricon (CdGM) states at integer multiples of Δ^2/E_F. In contrast, the spectrum at the center of a trivial vortex (lower panel) exhibits no zero-bias peak, with CdGM states instead occurring at half-integer multiples of Δ^2/E_F. Adapted from Ref. [266].

tionally, it was also noted that Wang et al. [54] conducted their measurements using a ^{3}He-refrigerator-based scanning tunnel microscope with an energy resolution of approximately 250 μeV – insufficient to resolve individual vortex-bound states [51]. In this context, H intercalation in $FeSe_{1-x}Te_x$ may provide significant advantages. Indeed, previous studies have shown that H doping (via gas absorption) in $FeSe_{1-x}Te_x$ – albeit at a x concentration different from 0.5 – results in an increase in T_c [56]. This increase likely corresponds to an enhancement of the superconducting gap(s), which can, in turn, increase the energy spacing between vortex-bound states, making non-trivial states potentially more distinguishable from trivial ones even at lower energy resolution. To explore this possibility, the present study applies IGP to $FeSe_{1-x}Te_x$, leveraging insights from earlier work in this thesis on parameter tuning to optimize H intercalation. The aim is to induce an increase in T_c and investigate the corresponding changes in the superconducting gap using PCARS.

5.2.2 Experimental methods: $FeSe_{1-x}Te_x$ samples

The measurements in this study are performed on $FeSe_{1-x}Te_x$ thin films grown by Prof. Iida's group (Nihon University, Tokyo). These films were specifically grown on CeO_2-coated yttria-stabilized zirconia substrates via pulsed laser deposition, with an ultraviolet KrF laser (wavelength: 248 nm) employed to ablate a $FeSe_{1-x}Te_x$ target. In this work, two batches prepared via this method, hereafter referred to as batch A and batch B, are examined.

Preliminary structural characterization of these batches was conducted by Prof. Iida's group immediately after fabrication via X-ray diffraction. The resulting diffraction patterns, shown in fig. 5.8a, display exclusively $(00l)$ reflections from both the film and substrate, demonstrating high phase purity and excellent c-axis orientation of the films. The c-axis lattice parameter, determined from the $00l$ peak positions, lies within the range 5.94 - 6.02 Å, consistent with the stoichiometry of $Fe_{1+\delta}Se_{1-x}Te_x$ with $x = 0.5$ [253, 267].
Subsequently, energy-dispersive X-ray spectroscopy (EDS) was performed by Dr. M. Bartoli at Politecnico di Torino to determine the film composition, focusing on iron excess and Te substitution. EDS analysis of two regions from a batch-A sample confirmed a Se:Te atomic ratio of 1:1 ($x = 0.5$), and revealed an iron content approximately 20% higher than the nominal stoichiometry (fig. 5.8b). Additionally, EDS mapping of a batch-B sample demonstrated a uniform spatial distribution of Fe, Se, and Te, with no indication of elemental clustering.
Final characterization included measuring the film thickness and evaluating surface morphology via atomic force microscopy (AFM). AFM scans were performed in tapping mode using a Bruker Innova microscope equipped with RTESPA-300 silicon tips. For batch A, the average thickness – determined from multiple edge profiles at different sample locations – was (205 ± 3) nm, while batch B exhibited a thickness

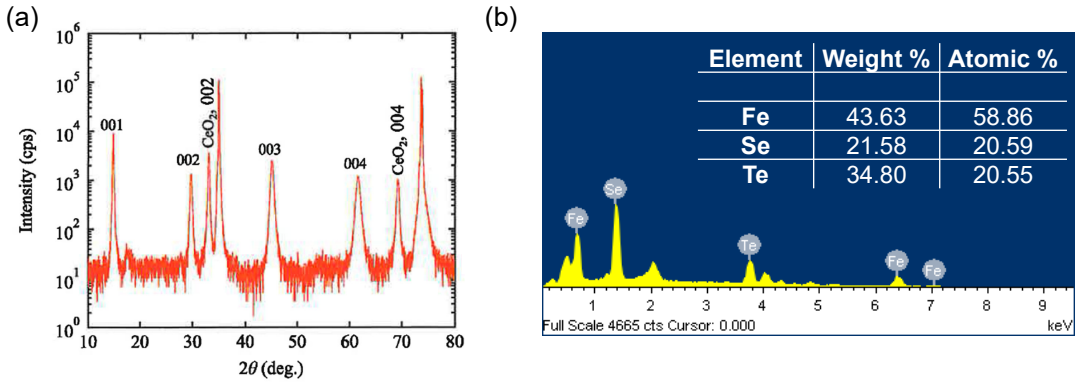

Figure 5.8: (a) Representative X-ray diffraction pattern from a batch-A sample, with the observed peaks identified and labeled as the $00l$ reflections of the $FeSe_{0.5}Te_{0.5}$ film and the CeO_2 coating on the substrate. (b) Representative energy-dispersive X-ray spectrum from a $200\times200\,\mu m^2$ scan of a batch-A sample. The inset displays the atomic and weight percentages of the detected elements.

of (198 ± 2) nm (fig. 5.9).

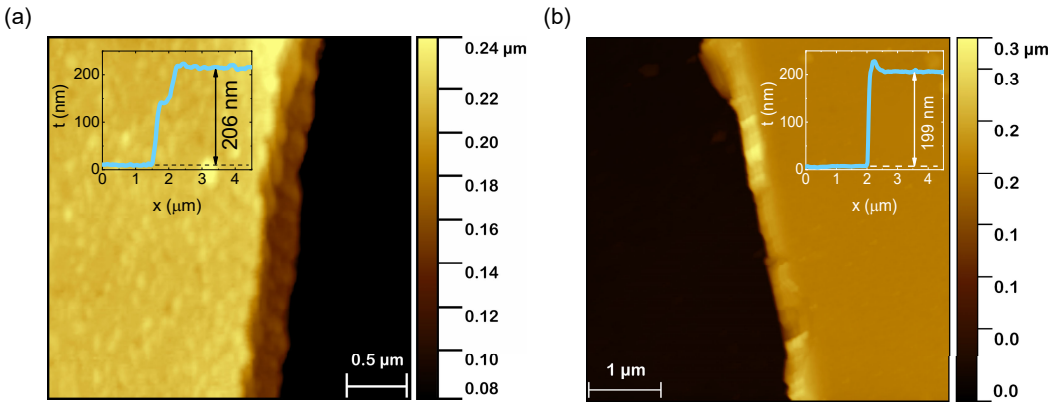

Figure 5.9: Representative topographic maps of $FeSe_{0.5}Te_{0.5}$ thin films from batch A (a) and batch B (b), showing the film edge relative to the substrate. Insets in each panel depict a representative height profile measured across the film edge.

High-resolution AFM scans over 1x1 μm^2 areas were acquired to investigate grain morphology. Representative high-resolution topographic maps from both batches are presented in fig. 5.10, clearly showing distinct granular features. Using ImageJ software, the perimeters of all visible grains were manually traced, and their enclosed areas were calculated. By approximating each grain as a circle, an effective radius (r_{eq}) was determined from these areas. The distribution of grain radii was

then plotted as a histogram and fitted with a Gaussian curve. The resulting best-fits reveal that batch A has larger grains with $r_{eq} = 68\,nm$ and a broader size distribution ($\sigma = 38\,nm$) compared to batch B, which exhibits an average radius of 38 nm with a narrower spread ($\sigma = 25\,nm$).

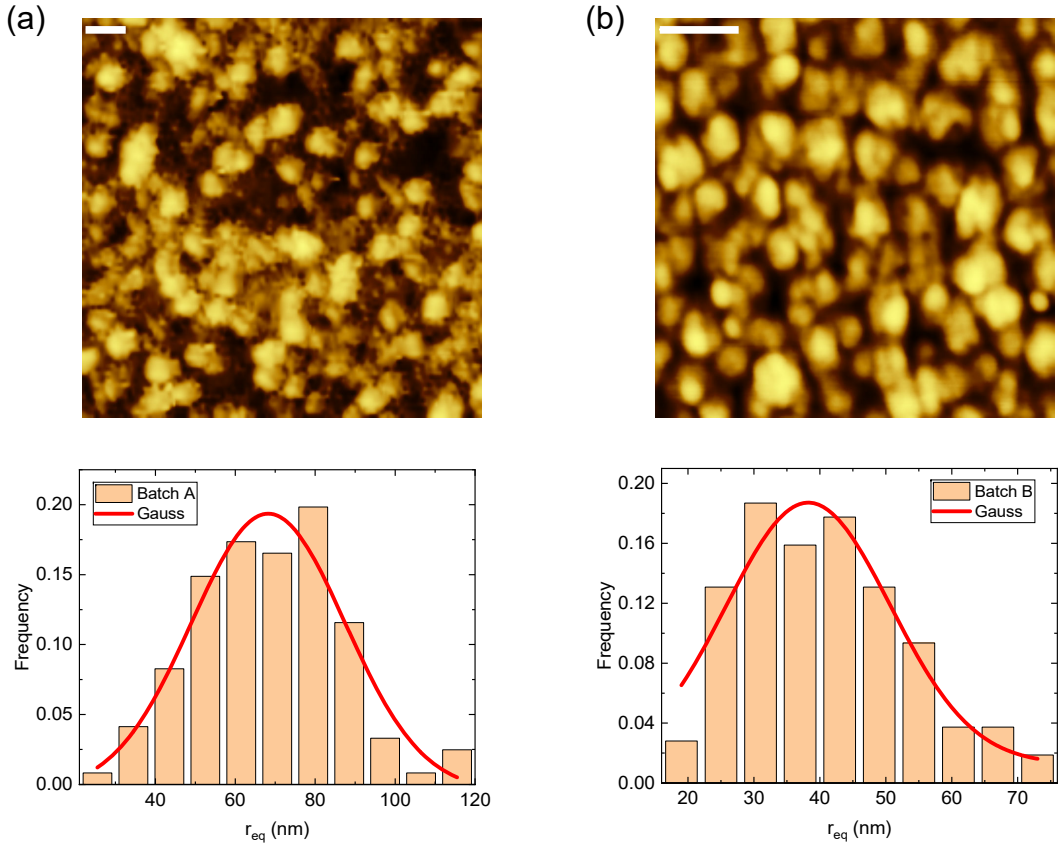

Figure 5.10: Representative topographic maps of $FeSe_{1-x}Te_x$ thin films from batch A (upper panel, a) and batch B (upper panel, b), illustrating the grain morphology. The white scale bar in each upper panel corresponds to 200 nm. The lower panels present histograms of the equivalent grain radius (r_{eq}) distributions, obtained by approximating the grains in the topographic maps as circles. Gaussian fits to the distributions are shown as red solid lines.

With the batches fully characterized, the study began by measuring their electric transport properties to identify the superconducting T_c. Directional PCARS was then performed to explore the superconducting gap structure and detect potential signs of unconventional superconductivity, possibly associated with surface topological states. Finally, *in-situ* IGP was performed on both batches with the goal of modifying the superconducting state. After IGP treatment, the samples were re-examined through electric transport measurements and PCARS.

5.2.3 Pristine $FeSe_{0.5}Te_{0.5}$: results

As an initial step, the superconducting properties of pristine batch-A and batch-B samples were characterized via electric transport and PCARS measurements. This provided a reference for comparison with IGP-treated $FeSe_{0.5}Te_{0.5}$ and for detecting possible treatment-induced modifications.

Electric transport characterization

The transport results are shown in fig. 5.11, where the $\rho(T)$ curves for both batches are displayed. In each case, the $\rho(T)$ curves exhibit metallic-like behavior ($d\rho/dT > 0$), consistent with previous reports on 200-nm-thick $FeSe_{0.5}Te_{0.5}$ films [268, 269], and show a superconducting transition reaching a zero-resistance state. A closer view of the transition region is shown in the right panel of fig. 5.11, where $\rho(T)$ is normalized to its value at 30 K and plotted over 0–30 K to highlight the differences between batches. Notably, the transition characteristics vary slightly: batch-A samples exhibit a $T_c = (16.1 \pm 1.1)$ K, determined from the maximum in the $d\rho/dT$ curve with the uncertainty given by the full FWHM of the peak, and an onset temperature $T^{on} \approx 16.9$ K, defined as the intersection of the linear extrapolation of the flux-flow regime with the normal-state curve. By contrast, batch-B samples display a sharper transition with $T_c = (17.4 \pm 0.2)$ K and $T^{on} \approx 17.8$ K. These distinctions are likely attributable to subtle differences in the growth process between the two batches.

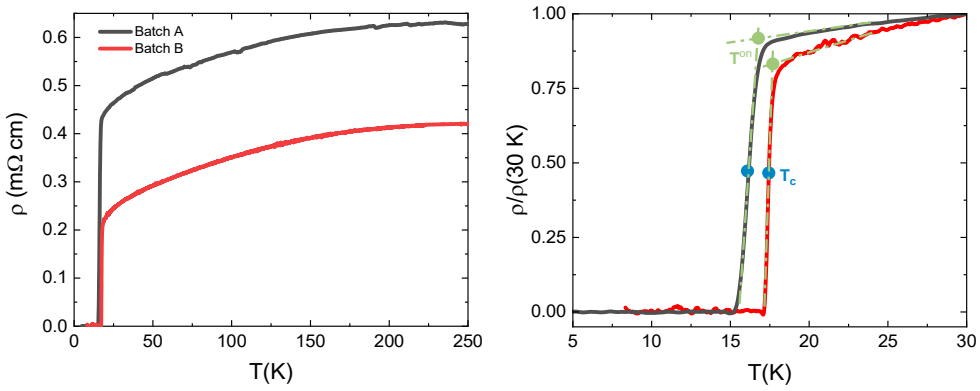

Figure 5.11: Left panel: temperature dependence of the resistivity of pristine $FeSe_{0.5}Te_{0.5}$ films from batch A (black line) and batch B (red line), which will subsequently undergo ionic gating-induced protonation. Right panel: a magnified view of the superconducting transition region, highlighting differences between the two batches. For easier comparison, each curve is normalized to its value at 30 K.

Point-contact Andreev reflection spectroscopy

After electrical transport measurements that determined the superconducting T_c of both batches, PCARS was conducted to probe their superconducting gap values. Initial measurements were carried out down to approximately 2 K. Representative spectra obtained at this base temperature are shown in fig. 5.12 for batch A (panel a and b) and for batch B (panel c).

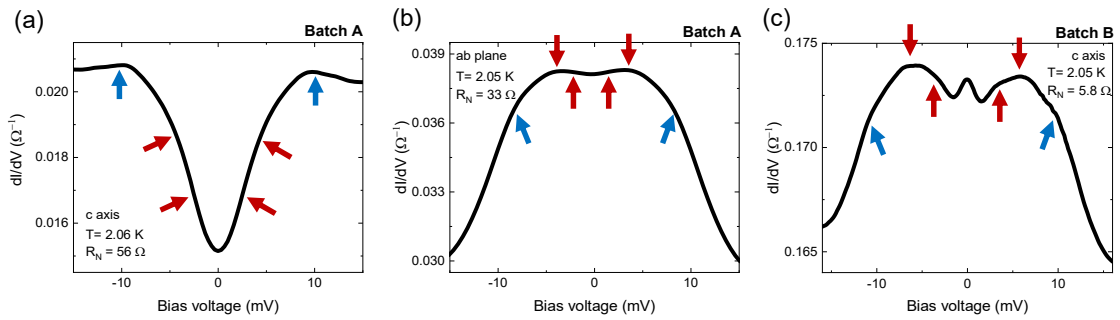

Figure 5.12: Representative point-contact Andreev reflection spectra (dI/dV vs. V) obtained from batch-A (panel a and b) and batch-B (panel c) $FeSe_{0.5}Te_{0.5}$. Each spectrum includes labels indicating the main current injection direction, the measurement temperature T and the normal-state contact resistance R_N. Spectral features associated with the superconducting gaps and the electron–boson interaction are indicated by red and blue arrows, respectively.

Notably, different contacts yielded distinct PCAR spectra, reflecting variations in barrier transparency at the superconductor/normal metal interface. Less transparent barriers produced tunneling-like spectra, in which non-idealities made the coherence peaks appear as two broad humps around a pronounced zero-bias dip (panel a). By contrast, more transparent barriers resulted in Andreev-like spectra, showing a conductance enhancement with two symmetric maxima (panel b and c). Despite these differences, recurring spectral features were consistently observed, as indicated by the colored arrows. Specifically, at energies of about ± 10 meV – provided the spectra were not strongly distorted by current dips due the contacts not being in the ideal ballistic regime – a shoulder appeared (blue arrows). This feature, previously observed in PCARS measurements on $FeSe_{1-x}Te_x$ [270], has been attributed to a strong electron–boson interaction (EBI), with spin fluctuations acting as the mediating boson [270]. Additional structures were observed around $\approx \pm 5$ meV: in tunneling-like spectra as shoulders within the dip, and in Andreev-like spectra as symmetric maxima (outer red arrows). These features, also observed in earlier PCARS works [270, 271, 121], are associated with an isotropic nodeless gap residing on the electronic pockets of the $FeSe_{0.5}Te_{0.5}$ Fermi surface, a sketch of which is shown in fig. 5.13. Much weaker features at lower energies were

also observed, corresponding to an average of the superconducting gaps residing on the hole pockets (inner red arrows). Unlike the other spectra, the one in panel c exhibits an unusual zero-bias peak, the origin of which will be addressed later in 5.2.5.

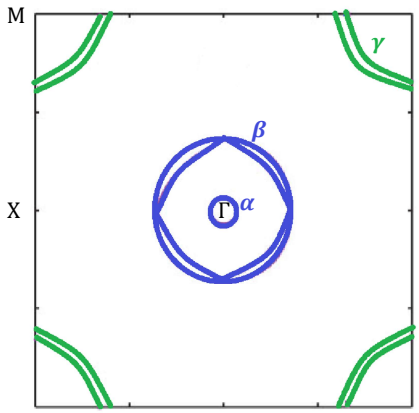

Figure 5.13: Sketch of the Fermi surface of $FeSe_{0.5}Te_{0.5}$, with the hole pockets around the Γ point shown in blue and the electron pockets around the M point in green [272]. The labels β and γ indicate collectively two Fermi sheets. This grouping is adopted because, in the context of superconducting gaps, previous angle-resolved photoemission spectroscopy measurements have resolved only three distinct gaps: one associated with the α sheet, one corresponding to the combined β sheets, and one to the combined γ sheets [273]. The finer internal structure of these sheets is therefore not considered.

Following the acquisition of the low-T spectra, the temperature was gradually increased: the evolution for the representative spectra shown in fig. 5.12 is displayed in fig. 5.14. For both tunneling-like and Andreev-like spectra, the amplitude of the features decreased with increasing temperature. In the tunneling-like case, the "coherence peaks" shifted to lower bias voltages, reducing the prominence of the zero-bias dip. Similarly, in the Andreev-like spectra, the conductance maxima shifted to lower bias, eventually merging into a broad zero-bias hump. These trends are consistent with the thermal suppression of the superconducting gap residing on the electron-like Fermi surface. Comparable trends were also observed for the weaker features associated with the gap opening on the hole-like Fermi surfaces and the EBI shoulder.
Additionally, a T-dependent downward shift of the conductance curves was noted. This effect arises from the portion of the $FeSe_{0.5}Te_{0.5}$ film between the point contact and the voltage electrode transitioning to the normal state under the combined influence of injected current and temperature, thereby introducing a series,

T-dependent spreading resistance. While negligible at low temperatures, this contribution becomes significant near T_c as the critical current decreases, resulting in a bending of the high-voltage tails, a downward shift of the curves, and an apparent stretching of the horizontal scale. At sufficiently high temperatures, all Andreev reflection features disappeared, and the spectra flattened into the featureless profile characteristic of the normal state.

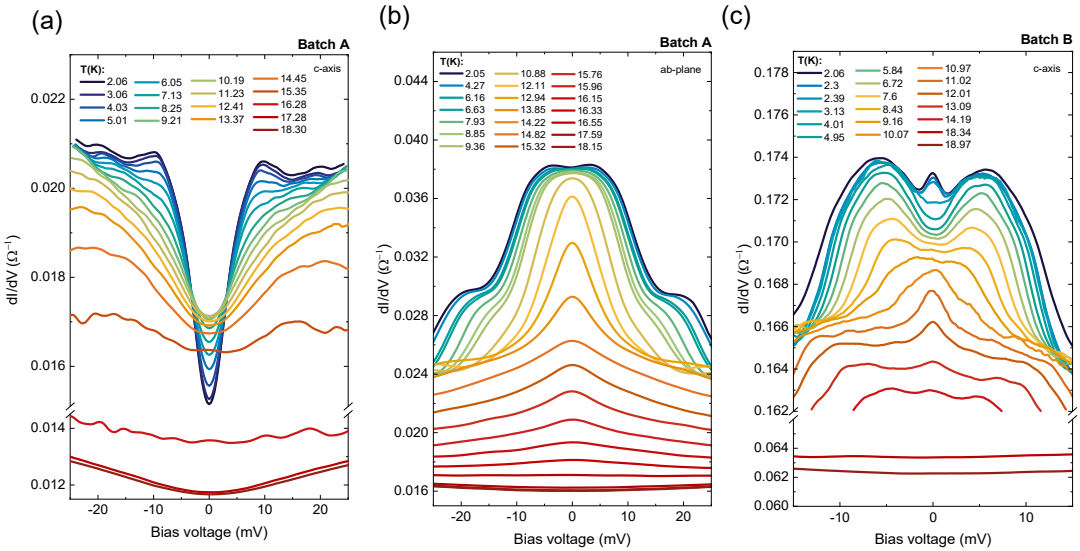

Figure 5.14: Temperature (T) dependence of the representative conductance spectra shown in fig. 5.12

After data acquisition, the experimental conductance spectra were analyzed to determine the energies corresponding to the superconducting gaps, providing a reference for comparison with protonated $FeSe_{0.5}Te_{0.5}$. This analysis involved several steps: symmetrizing the raw conductance spectra, normalizing them to the normal-state conductance measured just above T_c, correcting for the effects of spreading resistance, and finally fitting the resulting curves with an appropriate BTK model. Specifically, for each spectrum, the bias range below the EBI feature was initially selected and fitted using the 2D BTK model described in chapter 2, modified to include two distinct isotropic gaps, Δ_1 and Δ_2, corresponding to the gaps opening on the hole-like and electron-like Fermi surfaces, respectively. Following the procedure applied to H_xTiSe_2, the total conductance was expressed as a weighted sum of contributions from the electron and hole bands: $G = w_1G_1 + w_2G_2$ where each G_i is defined by eq. (2.8). This results in a 2D BTK model with seven free parameters: the gap amplitudes Δ_i, the broadening parameters Γ_i, the barrier strengths Z_i, and the spectral weights w_i, subject to the constraint $w_1 + w_2 = 1$. The best fits to the representative low-T curves from fig. 5.12a,b are shown in fig. 5.15 as solid red

lines, with the corresponding fitting parameters reported in the labels. For comparison, a single-band 2D BTK fit targeting Δ_2 was also performed (solid green line in fig. 5.15). The comparison clearly demonstrates that the two-gap BTK model provides significantly better agreement with the experimental data, supporting the validity of the two-gap approach.

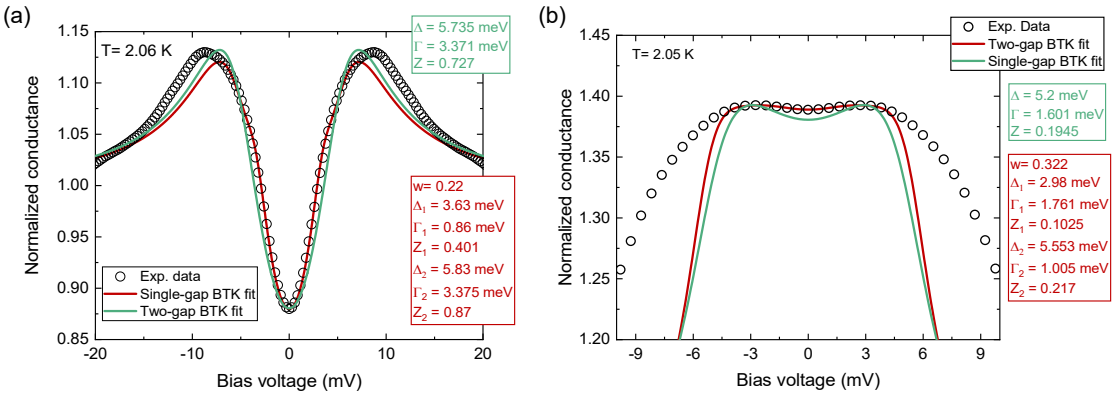

Figure 5.15: Comparison of the fits to the experimental normalized dI/dV spectra shown in fig. 5.12a,b (hollow black circles) using the two-gap BTK model (solid red lines) and the single-gap BTK model (solid green lines), demonstrating their respective agreements with the raw data. The fitting parameters for both the models are provided in the labels.

This two-gap BTK analysis was then applied to all spectra collected at different temperatures. Best fits to the representative spectra from fig. 5.14 are shown in fig. 5.16 (upper panels). Reliable fits could only be obtained up to about 10 K. At higher temperatures, pronounced current dips distorted the spectra, compromising the fitting procedure. The extracted gap amplitudes as a function of temperature are displayed in the lower panels, alongside BCS functions of the form $\Delta_i(T) = \Delta_i(0)\tanh\left(1.74\sqrt{T_c^A/T-1}\right)$, where T_c^A is defined as the temperature at which all Andreev reflection features vanish and the spectra assume the normal-state shape. Interestingly, in all cases, the ratios $2\Delta/k_BT_c$ exceed the BCS value of 3.53. In multiband systems, however, at least one gap is expected to have a ratio below this value. This can be explained by considering Δ_1 as the larger of the two gaps opening at the Γ point, arising from the crossing of the α and β sheets (fig. 5.13). Specifically, the β band generates a gap slightly larger than that associated with the α band. The second gap, associated with the α band and expected to have a ratio below the BCS value, is not directly observed here – likely because it is masked by the larger gap arising from the β band [273].
It should be noted that this analysis has so far neglected the influence of the EBI feature. Nevertheless, this structure – clearly visible as a shoulder around ± 10 meV – can have a non-trivial impact even on the lower-energy region where the two-gap

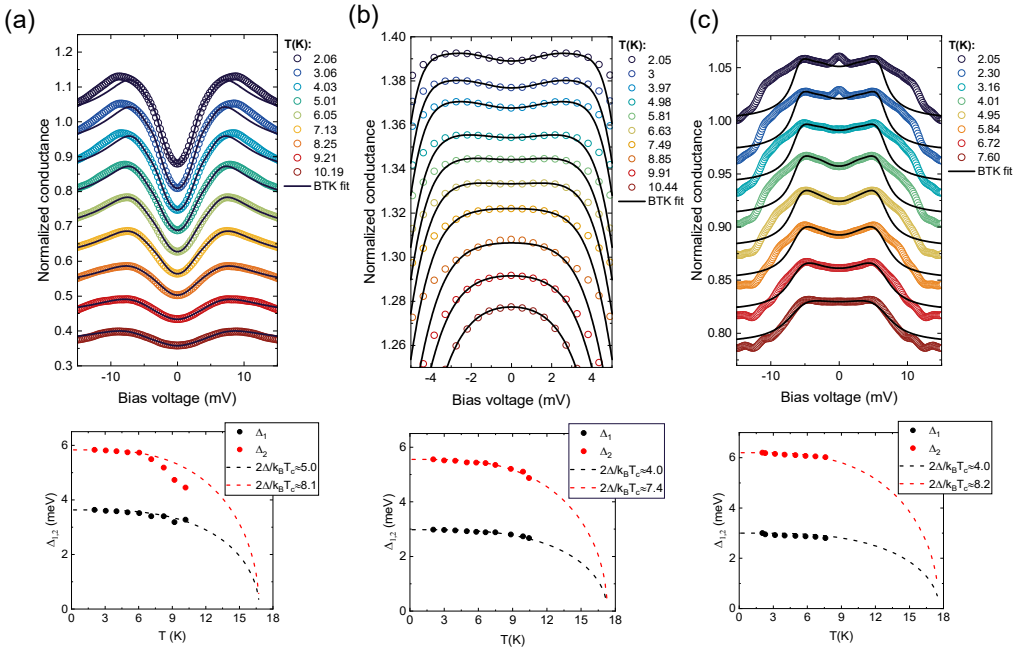

Figure 5.16: Upper panels: Representative two-band Δ_1-Δ_2 BTK fits (solid lines) to symmetrized and normalized spectra measured at various temperatures (symbols). The original experimental data prior to symmetrization and normalization correspond to the representative curves displayed in fig. 5.14. Note that in panel (c), the limited amplitude of the normalized signal requires introducing an additional free parameter, w_n, which is set to 0.9 in this case. This parameter represents the fraction of non-superconducting contacts and is discussed in section 5.2.5, where these spectra are analyzed again to propose an interpretation of the origin of the peak. Lower panels: T-dependence of Δ_1 (black circles) and Δ_2 (red circles) extracted from the fits in upper panels, respectively. Dashed lines are BCS functions of the form $\Delta_i(T) = \Delta_i(0)\tanh\left(1.74\sqrt{T_c^A/T-1}\right)$.

fitting is performed, potentially introducing systematic errors in the gap estimates. Previous work focusing on the EBI shoulder and the gap opening on the electron-like Fermi surface showed that accounting for this high-energy feature allows for a more accurate determination of the gap [270]. Specifically, it was found that fitting the spectra using a two-band BTK model – where one gap corresponds to the gap opening on the electron-like Fermi surface and the other represents the EBI shoulder (improperly treated as a gap) – yields a more reliable estimate of the gap itself than using a single-band model. Extending this approach to the present case, where both superconducting gaps are to be estimated, would require a three-band BTK model with nine free parameters, increasing the arbitrariness of the fitting procedure. An alternative strategy was therefore employed: the results from

fitting the low-energy part of the spectra to extract Δ_1 and Δ_2 were complemented by two-band BTK fits in which one gap corresponded to a physical one and the other to the EBI shoulder, denoted as Δ^* in analogy with previous work. This procedure allows the variability between the two approaches to be assessed and incorporated into the final values, yielding more robust estimates. In particular, for fits involving Δ^* and Δ_2, the extracted value of Δ_2 differed significantly from the previous analysis, confirming that the EBI feature – being close in energy to the gap opening on the electron-like Fermi surface – strongly affects its determination. Conversely, in fits involving Δ^* and Δ_1, the discrepancy in Δ_1 was comparable to the variation obtained by performing multiple Δ_1–Δ_2 fits on the same curve under slightly different normalizations. This behavior is therefore consistent with the expectation that the impact of the EBI feature diminishes as the energy separation increases.

The resulting T-dependence of the superconducting gaps for both batches are presented in fig. 5.17, with panel (a) corresponding to batch A and panel (b) to batch B. For both batches, the final values represent the average of two T-dependent trends obtained from different contacts. The uncertainties associated with these averages arise from different sources: for Δ_2, they are primarily due to the influence of the EBI structure on the determination of Δ_2 using the two-gap BTK fitting procedure, whereas for Δ_1, they reflect the intrinsic variability of this gap across different contacts. In line with the slightly different T_c values and superconducting transition shapes observed in transport measurements, the low-T gaps differ slightly between batches. Specifically, Δ_2 is consistent within uncertainties, whereas Δ_1 shows a larger discrepancy. Both gaps are well described by the BCS T dependence: $\Delta_i(T) = \Delta_i(0)\tanh\left(1.74\sqrt{T_c^A/T-1}\right)$, though the ratio $2\Delta/k_BT_c$ remains above the 3.53 BCS value.

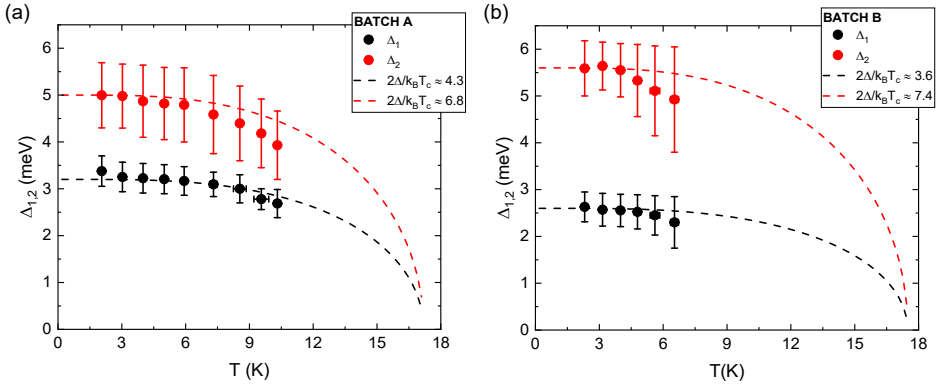

Figure 5.17: T-dependence of Δ_1 (black circles) and Δ_2 (red circles) obtained by averaging values from different contacts for batch A (panel a) and batch B (panel b). Dashed lines are BCS functions of the form $\Delta_i(T) = \Delta_i(0)\tanh\left(1.74\sqrt{T_c^A/T-1}\right)$.

As a final step in characterizing the pristine $FeSe_{0.5}Te_{0.5}$, the EBI feature present in the PCAR spectra was analyzed to estimate the characteristic energy of the boson spectrum, Ω_b. Indeed, for iron-based superconductors, previous studies have demonstrated that in the reversed-signed derivative of the conductance spectrum, the energy position of the first maximum (denoted as E_p) closely corresponds to the spin-fluctuation energy (Ω_b) obtained from neutron-scattering spin-resonance experiments, offset by the value of the larger superconducting gap [106]. Accordingly, the boson energy as a function of temperature can be estimated as $\Omega_b(T) = E_p(T) - \Delta_2(T)$. Consequently, the conductance spectra measured at different temperatures were differentiated to estimate E_p. Fig. 5.18 displays a representative set of $-dI^2/dV^2$ curves extracted from typical spectra for batch A (panel a) and batch B (panel b), with the first maxima marked, together with the corresponding conductance spectra from which the derivatives were obtained. For each spectrum, the position of the first maximum was taken as E_p, and an error bar was included to account for the uncertainty in locating the peak. This uncertainty

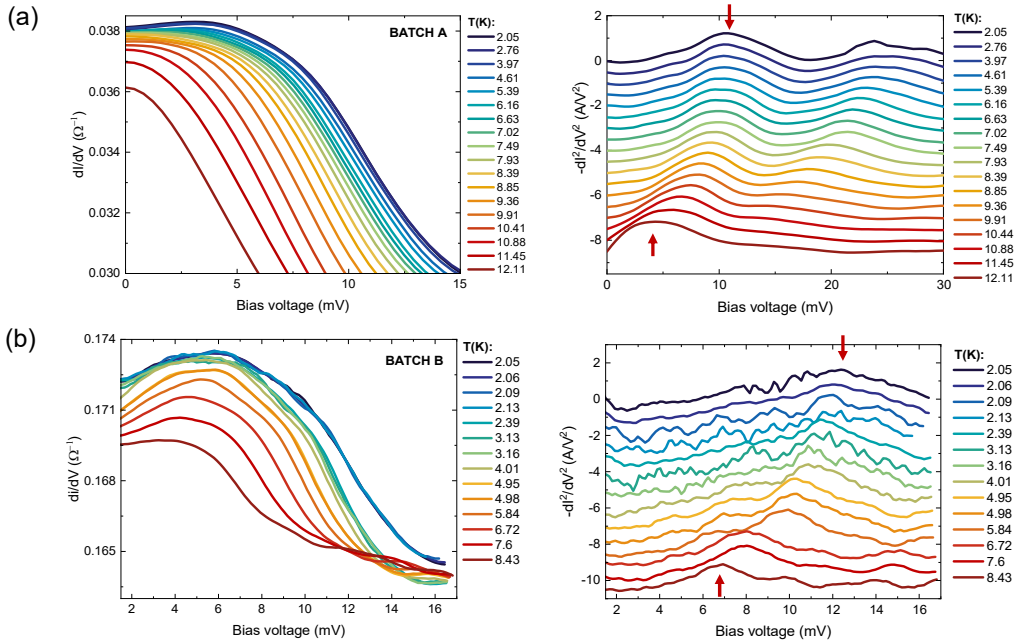

Figure 5.18: (a) Conductance spectra (dI/dV vs. V) from fig. 5.14a for batch A, displayed over the range 0–15 mV in the left panel, along with their corresponding derivatives ($-d^2I/dV^2$ vs. V) shown in the right panel. (b) Same as panel a, but for the spectra from fig. 5.14c for batch B. Red arrows highlight the temperature-dependent shift of the first peak, whose position, E_p, is used to estimate the characteristic boson energy, Ω_b. For clarity, the curves have been vertically offset.

is especially significant for noisy spectra or those measured near T_c^A, where the

signal amplitude decreases and tends to merge with the Δ_2 feature, making peak identification more challenging.

Once the energy E_p was extracted from the T-dependent spectra of the different contacts, the values were averaged for each batch at each temperature, as was done for the superconducting gaps. For batch A, the average reflects the mean of two distinct trends, corresponding to the spectra employed to estimate the average gaps for this batch. In contrast, for batch B, only a single trend is presented because the spectra from one of the two contacts used to determine the average gaps were too noisy to provide a reliable E_p estimate. In this averaging, the associated uncertainty was taken as the largest individual error among all contributing E_p. These results are presented in fig. 5.19, together with the averaged Δ_2 values for batch A (panel a) and batch B (panel b). From each pair (E_p, Δ_2), the bosonic energy Ω_b was calculated, with its uncertainty obtained as the quadratic sum of the errors in E_p and Δ_2.

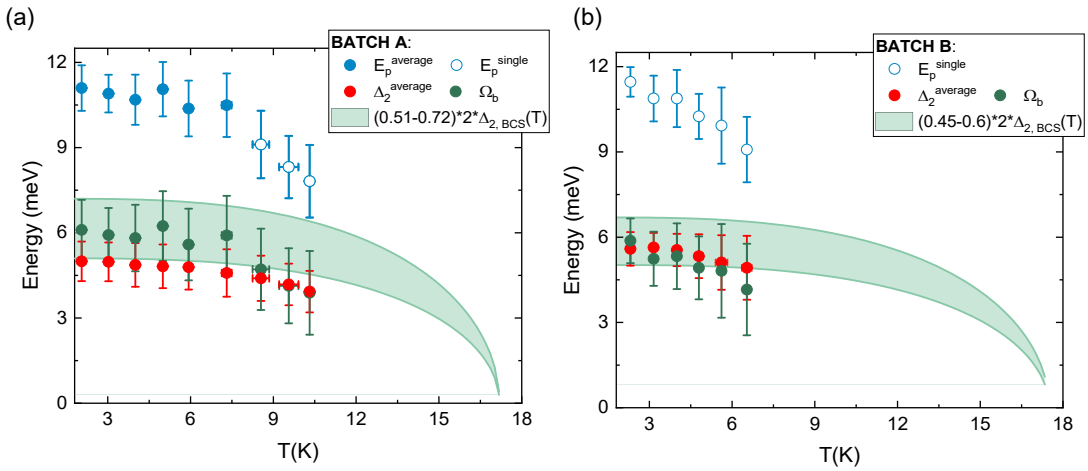

Figure 5.19: T-dependence of the peak energy E_p (blue circles), the gap opening on the electron-like Fermi surface Δ_2 (red circles, same as fig. 5.17), and the characteristic boson energy Ω_b (green circles), obtained as difference between E_p and Δ_2, for batch A (panel a) and batch B (panel b). The plotted values represent averages of two datasets obtained from different contacts; when only a single dataset was available, open symbols are used. The green shaded region is the convolution of curves of the type $k * \Delta_2(0) \tanh\left(1.74\sqrt{T_\mathrm{c}^\mathrm{A}/T - 1}\right)$.

Notably, Ω_b is expected to follow two empirical rules. First, its value at 0 K was empirically observed to relate to T_c through the expression $\Omega_\mathrm{b}(0) = 4.65 \cdot k_\mathrm{B} T_\mathrm{c}$, where k_B is the Boltzmann constant [274, 275]. Second, Ω_b has been observed to correlate with $2\Delta(T)$ through a proportionality constant k of approximately 0.64, a relationship observed across different classes of materials [276, 277].

Entering the Andreev-estimated critical temperatures, $T_c^A = (17.1 \pm 0.3)\,\mathrm{K}$ for batch A and $(17.5 \pm 0.3)\,\mathrm{K}$ for batch B, into the first empirical rule, $\Omega_b(0)$ is thus expected to be $(6.84 \pm 0.12)\,\mathrm{meV}$ for batch A and $(7.00 \pm 0.12)\,\mathrm{meV}$ for batch B. These empirically predicted values agree with the experimentally observed data within their uncertainties. Assuming a BCS-like temperature dependence for Δ_2 – previously shown to capture the data accurately (see fig. 5.17) – the proportionality constant k for batch A ranges from 0.51 (lower boundary of the shaded region) to 0.75 (upper boundary), giving an average $k = (0.63 \pm 0.11)$. For batch B, k ranges from 0.45 to 0.60, with an average $k = (0.53 \pm 0.08)$. Both averages are consistent, within uncertainties, with the empirical value of $k \approx 0.64$ observed in other materials.

5.2.4 Protonated $FeSe_{0.5}Te_{0.5}$: results

Ionic gating-induced protonation and electric transport measurements

Following the characterization of the pristine material, IGP was performed on $FeSe_{0.5}Te_{0.5}$ to evaluate whether this method can induce a measurable enhancement of its superconducting T_c and, consequently, of its energy gap(s), and to assess whether the process can be optimized to maximize these changes. Due to the lack of information regarding the tendency of $FeSe_{0.5}Te_{0.5}$ to release H once loaded, the IGP was carried out *in situ*. This configuration represents the most cautious approach, as the H intercalation can be stopped by quenching the sample into the cryostat, allowing direct measurement of transport properties without intermediate sample rinsing and contacting, as required in the *ex-situ* approach, which could potentially lead to deintercalation. As an additional precaution, the 1:3 choline chloride: glycerol deep eutectic solvent (1:3 ChCl:gly DES) described in chapter 3 was chosen as the electrolyte for IGP, based on prior observations with Pd indicating that this DES is less reactive than the conventionally used EMIM-BF_4.

Starting from pristine films, IGP treatments were conducted following the procedure established in the previous chapters, which had been shown to promote H^+ intercalation. V_G across the 1:3 ChCl:gly DES was ramped from 0 V to a final value – varied between processes in order to determine the threshold at which IGP induces modifications in the superconducting properties of $FeSe_{0.5}Te_{0.5}$ and to explore the possibility of optimizing this effect – at a rate of 1 mV/s. This ramping rate had previously been shown to allow the DES dynamics to follow the applied voltage reliably. Once the target voltage was reached, it was held for a duration of the order of 1 hour before the process was terminated by quenching the sample into the cryostat.
Monitoring the sample response during the IGP treatments revealed that for final V_G values exceeding 1.5 V – where the DES is expected to release H under

the applied bias – the resistivity of $FeSe_{0.5}Te_{0.5}$ generally decreases from its initial value, reaches a minimum, and then increases again. This trend is illustrated in fig. 5.20, which presents the time evolution of the resistitivity of a batch-A sample normalized to its pristine value for a representative IGP treatment, along with the corresponding applied V_G and gate current I_G. While the presence of the minimum in the resistivity is systematic, its occurrence does not correlate directly with V_G, appearing instead within the 2–2.7 V range depending on the specific IGP process, even among treatments nominally performed at the same final voltage. This variability is attributed to several factors, including intrinsic inhomogeneities within the $FeSe_{0.5}Te_{0.5}$ films and an effective V_G drop across the electric double layer that deviates from the nominal applied voltage, either due to an insufficiently large gate-to-sample surface ratio or to the intrinsic resistance of the DES (as discussed in chapter 2 [98]).

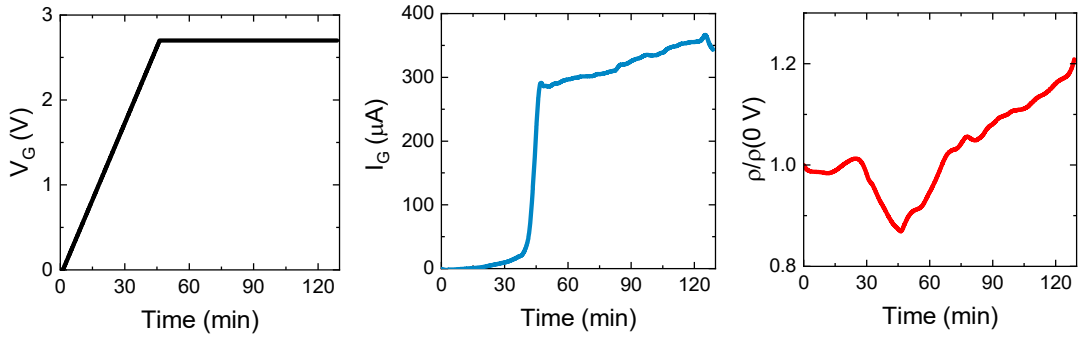

Figure 5.20: Representative example of an *in-situ* ionic gating-induced protonation process performed on a batch-A $FeSe_{0.5}Te_{0.5}$ film up to 2.7 V, with the response of the material monitored over time. The left panel shows the applied V_G as a function of time, the middle panel depicts the corresponding electrolyte response in terms of the gating current (I_G) flowing from the gate to the drain electrode placed on the sample, and the right panel presents the effective response of the material in terms of resistivity, measured in the four-probe configuration and normalized for simplicity to its value before the treatment.

Evidence that nominally identical films can exhibit different responses to IGP is provided by comparing the evolution of I_G as a function of V_G for batch-A and batch-B samples under equivalent treatments. As shown in fig. 5.21, the two batches exhibit distinctly different behaviors: the voltage at which I_G departs from zero – indicating the onset of electrochemical reactions – is lower for batch B than for batch A (deviation points indicated by dashed blue lines). This observation suggests that, although batch B appears physically similar to batch A in prior analyses, subtle differences – such as weaker substrate adhesion and smaller grain size, which increases the total grain-boundary length available for intercalation –

can cause H^+ insertion to begin at lower voltages. Consequently, at the same final V_G, batch B is likely to undergo more extensive H^+ intercalation.

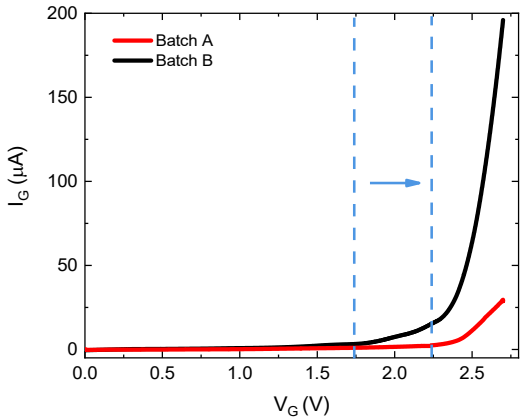

Figure 5.21: Comparison of representative gate current (I_G) vs. gate voltage (V_G) for batch-A (solid red line) and batch-B (solid black line) $FeSe_{0.5}Te_{0.5}$ samples subjected to ionic gating-induced protonation treatments with final applied $V_G = 2.7\,V$. The dashed blue lines indicate, for each batch, the voltage at which I_G deviates from zero, marking the onset of the electrochemical regime.

Transport measurements performed immediately after IGP revealed three distinct regimes depending on the final V_G. Focusing on batch A:

- For $V_G \leq 2.5\,V$, IGP has no detectable impact on the superconducting properties, with $\rho(T)$ remaining largely unchanged relative to the pristine batch-A $FeSe_{0.5}Te_{0.5}$.
- Around $V_G \approx 2.7\,V$, IGP effectively tunes the superconducting transition, shifting it to higher temperatures.
- For $V_G \geq 2.8\,V$, the injected H^+ ions likely introduce excessive disorder, leading to broadened transitions that, in some cases, fail to reach zero resistance or even show a suppressed T^{on} compared to the pristine reference.

These behaviors are illustrated in fig. 5.22a, which presents representative $\rho(T)$ curves normalized to the value at 35 K for each regime: colored lines correspond to the gated samples, while the black line represents pristine batch-A $FeSe_{0.5}Te_{0.5}$. Notably, the curve obtained after IGP at 2.55 V (blue line) closely follows the pristine behavior, with $T_c = (16.33 \pm 1.06)\,K$ and $T^{on} \approx 17\,K$, fully consistent with previously estimated values for batch A. The transition temperatures were determined as before: T_c via the derivative criterion, and T^{on} from the intersection of the linear extrapolation of the flux-flow regime with the normal-state curve.

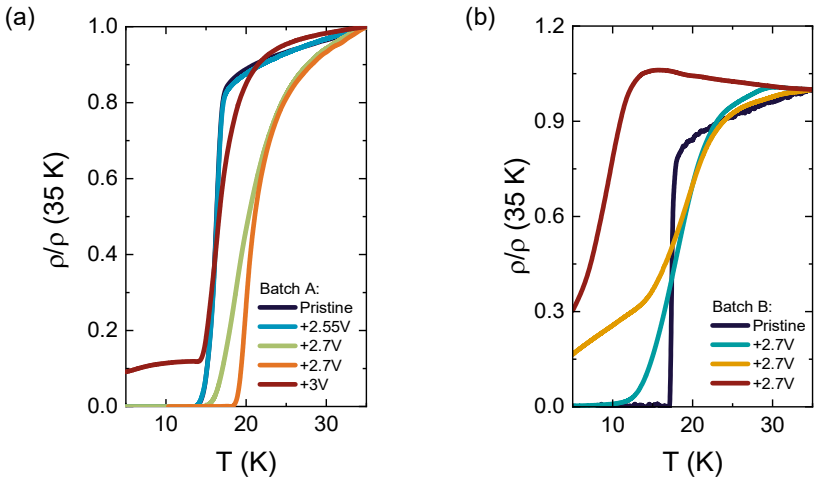

Figure 5.22: (a) Representative temperature dependence of the resistivity for films from batch-A $FeSe_{0.5}Te_{0.5}$ treated with ionic gating-induced protonation (IGP) at different final V_G values, as indicated in the legend. The black line corresponds to the pristine curve previously shown in fig. 5.11, included here for reference. (b) Representative temperature dependence of the resistivity for films from batch-B $FeSe_{0.5}Te_{0.5}$ treated with IGP at a final $V_G = 2.7\,V$. The black and blue curves were measured in a four-probe configuration, while all other curves were measured in a three-probe configuration.

The green and orange curves, corresponding to IGP at 2.7 V, both show an enhancement of the superconducting transition, with T_c increased by about 3-4 K and T^{on} by about 5 K. However, the exact degree of enhancement proved highly process-dependent: even for nominally identical final V_G, the resulting $\rho(T)$ curves exhibited different shapes. In the example shown, the green curve features a broader transition with its low-T foot aligned to the pristine case, whereas the orange curve shifts more uniformly to higher temperature. This variation, reflecting the process-dependent variability previously observed in the time evolution of resistivity during IGP, leads to corresponding differences in the extracted transition parameters: the green curve yields $T_c = (19 \pm 6)\,K$ and $T^{on} \approx 22.4\,K$, while the orange curve gives $T_c = (19.9 \pm 1.9)\,K$ and $T^{on} \approx 21.8\,K$. It should be noted that, since IGP alters the curve shape, the choice of criterion for determining T_c can affect the results. For instance, defining T_c as the temperature at which the resistivity reaches 50% of its normal-state value yields results roughly 0.7 K higher than the derivative criterion, corresponding to shifts of 4–5 K relative to the pristine sample instead of 3–4 K. Finally, the red curve corresponds to one of the scenarios resulting from IGP at $V_G > 2.7\,V$, where disorder likely prevents the superconducting transition from reaching a zero-resistance state, indicating that a fully connected superconducting

path was not established. The broadness of the curve also complicates the interpretation of the effect of IGP on the superconducting properties. As a matter of fact, the resulting $T_c = (16 \pm 3)\,\mathrm{K}$ remains consistent with the pristine sample, while T^{on} of $\approx 18.7\,\mathrm{K}$ is higher than that of the pristine reference but lower than the values obtained at $V_G = 2.7\,\mathrm{V}$. Since IGP performed at voltages above 2.7 V does not clearly outperform the results obtained at 2.7 V, in this study, $V_G = 2.7\,\mathrm{V}$ is considered the optimized voltage for achieving the maximum enhancement of superconducting properties in batch-A $FeSe_{0.5}Te_{0.5}$ films.

When the optimized protocol developed for batch A is applied to batch B, strong reactions were observed, consistent with the previously noted higher reactivity of this batch to V_G. In several cases, portions of the films detached from the substrate. For samples where detachment was limited, resistivity was measured using the four-probe configuration (blue line in fig. 5.22b); when film adhesion compromised contact integrity, the three-probe configuration was used instead (yellow and red lines in fig. 5.22b). These measurements generally exhibit broad superconducting transitions that do not reach the zero-resistance state. The onset temperature T^{on} varied significantly, sometimes exceeding that of the pristine reference (black line) or dropping well below it in cases dominated by disorder, in agreement with prior observations of $FeSe_{0.5}Te_{0.5}$ exposed to H from the gas phase [56]. Since batch B is expected to undergo more extensive intercalation than batch A at the same final V_G, these findings confirm that the observed behavior – already apparent in the third regime for batch A – originates from excessive disorder induced by excessive H^+ intercalation.

Point-contact Andreev reflection spectroscopy

Following IGP and electrical transport measurements, PCARS was performed to probe the superconducting gap function of the modified superconducting phase. Since electrical transport measurements were conducted *in situ* immediately after IGP – with the sample still covered by the electrolyte and the V_G applied – the same *in-situ* approach was used for PCARS. This strategy ensured an accurate characterization of the IGP-induced phase while minimizing the risk of deintercalation, considering that the tendency of $FeSe_{0.5}Te_{0.5}$ to release H is not well established. Electrical contacts suitable for soft PCARS were therefore placed on the sample prior to IGP. After gating, the doped state was characterized via transport measurements, and PCARS was performed upon reaching the base temperature. This *in-situ* soft PCARS configuration had not been previously explored, as the frozen electrolyte under an applied V_G was assumed to prevent access to the spectroscopic regime. In this work, soft contacts exhibiting clear spectroscopic features, or soft contacts that could be tuned to the spectroscopic regime via voltage pulses, were successfully obtained for the first time under gating.

Representative spectra recorded at a base temperature of approximately 2 K for samples exhibiting enhanced superconductivity, as determined from transport measurements, are shown in fig. 5.23. The spectrum in panel a corresponds to batch-A $FeSe_{0.5}Te_{0.5}$ and represents an IGP-enhanced state, where T^{on} is increased by 1.3 K relative to the pristine value. The spectrum in panel b, obtained from batch-B $FeSe_{0.5}Te_{0.5}$, also corresponds to an IGP-enhanced state, with T^{on} increased by 5.2 K. In both cases, the current was predominantly injected along the c axis. Similar to the pristine case, the point contacts exhibited different regimes depending on the barrier transparency, ranging from Andreev-like behavior (panel a) to tunnel-like behavior (panel b). Despite differences in transparency, the characteristic spectral features observed in the pristine state were still present after IGP treatment, although the EBI structures were on average less pronounced. A comparable behavior was found in samples with suppressed superconductivity.

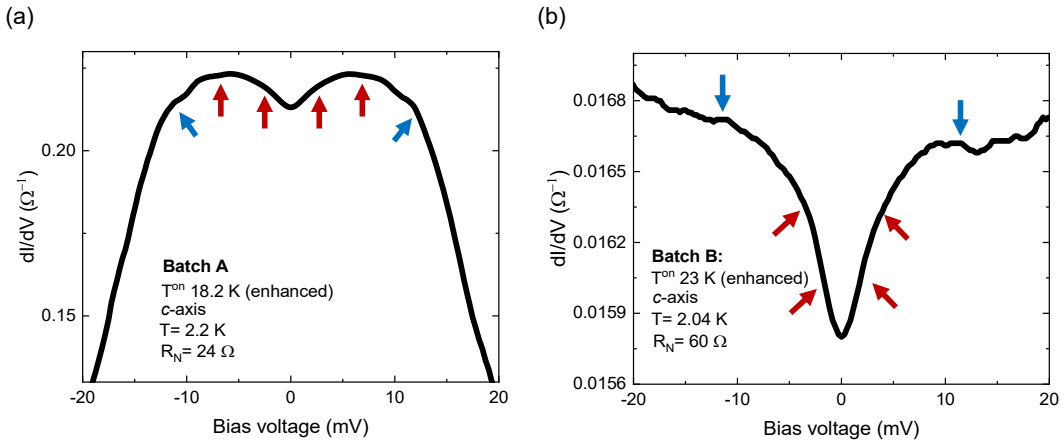

Figure 5.23: Representative point-contact Andreev reflection spectra (dI/dV vs. V) of IGP-treated $FeSe_{0.5}Te_{0.5}$ for two samples: one from batch A (panel a) and one from batch B (panel b). Previous transport measurements on these samples indicated enhanced superconductivity following IGP treatment. Each spectrum is labeled with the batch type, the onset temperature T^{on} from transport data, the primary current injection direction, the measurement temperature T, and the normal-state contact resistance R_N. Features corresponding to the superconducting gaps and electron–boson interaction are marked by red and blue arrows, respectively.

The T evolution of the PCAR spectra was also monitored by gradually increasing the temperature and acquiring a spectrum at each step. The evolution for the representative spectra shown in fig. 5.23 is displayed in fig. 5.24. As for pristine $FeSe_{0.5}Te_{0.5}$, the amplitude of the spectral features decreased with increasing temperature, while their positions shifted toward lower energy. A T-dependent downward shift of the conductance curves, along with bending of the high-voltage

tails due to the spreading resistance of the film, was also observed. At sufficiently high temperatures, all Andreev reflection features disappeared, and the spectra flattened to the featureless profile characteristic of the normal state. These observations motivate a quantitative analysis of whether the IGP induces measurable shifts in the energy positions of the superconducting gap features and the EBI structures.

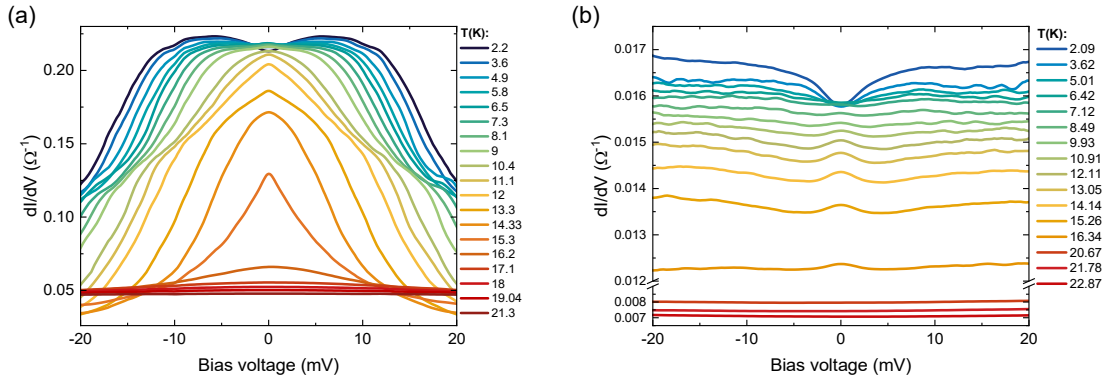

Figure 5.24: Temperature (T) dependence of the representative conductance spectra shown in fig. 5.23.

Consequently, the experimental conductance spectra were analyzed to extract the superconducting gap energies and compare them with the pristine values. As in the previous case, the raw conductance spectra were first symmetrized, normalized to the normal-state conductance measured just above T_c, corrected for the influence of spreading resistance, and finally fitted using the appropriate BTK model. In particular, each spectrum was fitted below the EBI feature using a 2D BTK model with two isotropic gaps, Δ_1 and Δ_2, associated with the hole-like and electron-like bands, respectively, as in the pristine case. Best fits to the representative spectra of fig. 5.24b are shown in fig. 5.25a. No fitting results are reported for spectra above 5 K, as the occurrence of non-ideal current dips distorts the signal, making the determination of the gaps unreliable. The corresponding T dependence of the extracted gaps is reported in panel b, together with BCS-like functions with $T_c^A = 19.6$ K. Interestingly, the extracted values of Δ_1 and Δ_2 yield $2\Delta/k_BT_c$ ratios that are respectively smaller and larger than the BCS value.

Unlike in pristine $FeSe_{0.5}Te_{0.5}$, estimating gap variability by directly considering the influence of the EBI structure on the spectra is unsuitable due to the EBI structures being on average less pronounced. A more reliable approach is to evaluate the gap variability through Δ_1–Δ_2 fitting on normalized spectra derived by dividing the raw data for slightly different normalization curves. Averaging the results from multiple normalization choices for the spectrum in fig. 5.24a at 2 K, and taking half the resulting spread as the uncertainty, yields gap values of $\Delta_1 = (2.1 \pm 0.3)$ meV

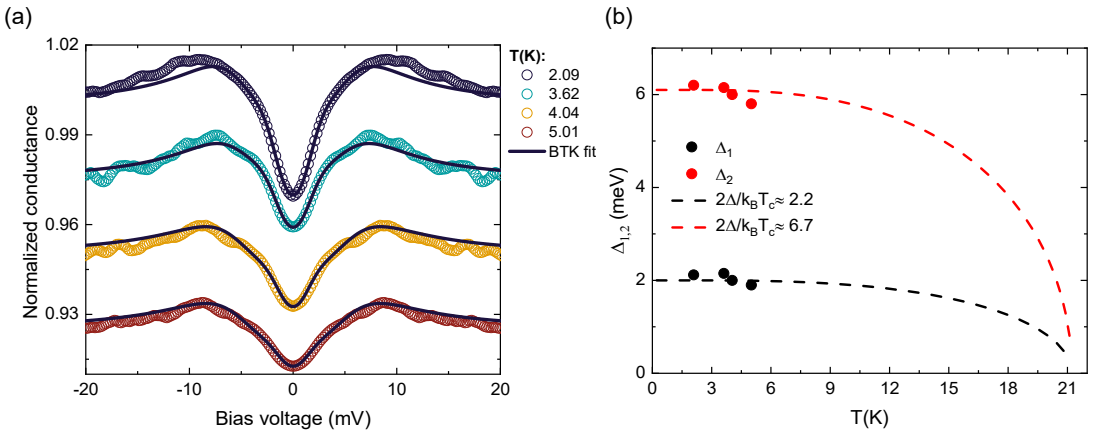

Figure 5.25: (a) Representative two-band Δ_1-Δ_2 BTK fits (solid lines) to symmetrized and normalized spectra measured at various temperatures (symbols). The original experimental data prior to symmetrization and normalization correspond to the representative curves displayed in fig. 5.24b. (b) T-dependence of Δ_1 (black circles) and Δ_2 (red circles) extracted from the fits in panel a. Dashed lines are BCS functions of the form $\Delta_i(T) = \Delta_i(0)\tanh\left(1.74\sqrt{T_c^A/T - 1}\right)$.

and $\Delta_2 = (6.8 \pm 0.9)$ meV (fig. 5.26a,b). The smaller gap is notably lower than that of the pristine reference, while the larger gap is significantly higher, consistent with the behavior observed in fig. 5.25, providing quantitative evidence that IGP effectively tunes the superconducting gaps of $FeSe_{0.5}Te_{0.5}$. Specifically, it is likely that the intercalated H, acting not only as a charge dopant and shifting the Fermi level, could also lead to a nontrivial modification of the hole-like bands at the Γ point (fig. 5.13). In particular, the β band – previously responsible for the larger gap at Γ – may no longer cross the Fermi level after H intercalation, effectively closing that gap. Consequently, the smaller gap associated with the α band at Γ, which was previously obscured by the nearby β band and may also experience a slight modification due to H, becomes observable.
The same limitation regarding the EBI feature visibility applies to estimating the characteristic boson energy, Ω_b, and assessing its consistency with previously discussed empirical rules. This analysis was feasible only for spectra in which these features were clearly resolved, such as those in fig. 5.24a. Indeed, the sign-reversed derivative of these spectra (fig. 5.26c) displays a well-defined first maximum corresponding to the E_p feature, which correlates directly with Ω_b. As the temperature increases, this maximum gradually shifts from ± 15 meV at 2.2 K – a value higher than that observed in the corresponding pristine reference – to lower energies.
To extract Ω_b, E_p must be corrected by subtracting the corresponding Δ_2, whose T dependence was determined using the procedure described above. For completeness, panels a and b in fig. 5.26 summarize the main results of this determination.

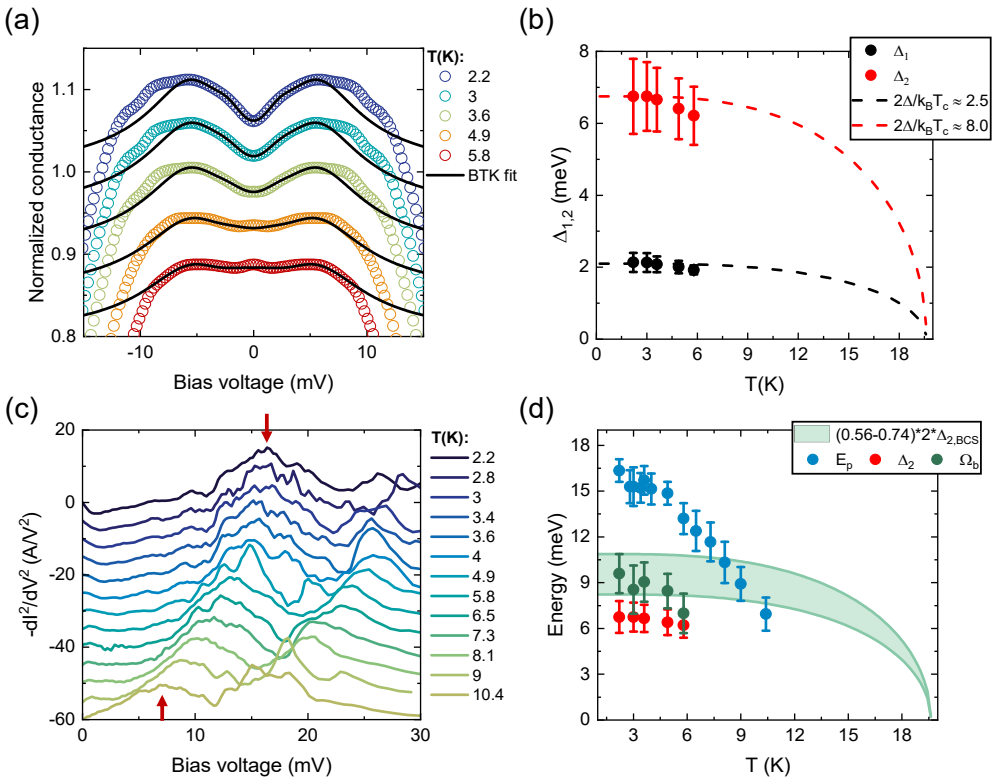

Figure 5.26: (a) Representative two-gap Δ_1–Δ_2 BTK fits (solid lines) applied to symmetrized and normalized spectra measured at various temperatures T (symbols). The original raw data, prior to symmetrization and normalization, correspond to the curves shown in fig. 5.24a. (b) T dependence of Δ_1 (black circles) and Δ_2 (red circles), obtained by averaging values from two-gap BTK fits of spectra derived by dividing the raw data by slightly different normalization curve. One dataset included in this average corresponds to the fits shown in panel (a). Error bars indicate the maximum variation among values from different normalizations. Dashed lines are BCS functions of the form $\Delta_i(T) = \Delta_i(0)\tanh\left(1.74\sqrt{T_c^A/T-1}\right)$. (c) Derivative of the conductance spectra ($-d^2I/dV^2$ vs. V) from fig. 5.24a. Red arrows indicate the T-dependent shift of the first peak, whose position E_p is used to estimate the characteristic boson energy Ω_b. For clarity, the curves are vertically offset. (d) T dependence of the peak energy E_p (blue circles), the electron-like gap Δ_2 (red circles, same as panel b), and the characteristic boson energy Ω_b (green circles), defined as $E_p - \Delta_2$. Error bars are calculated as the quadratic sum of the uncertainties in E_p and Δ_2. The green shaded area represents the convolution of curves of the form $k * \Delta_2(0)\tanh\left(1.74\sqrt{T_c^A/T-1}\right)$ with k spanning from 0.55 to 0.74.

Specifically, panel a shows the best-fit curves of the raw spectra from fig. 5.24a, divided by the normal state adjusted to intersect the raw data at an appropriate dI/dV value. Panel b reports the average values of Δ_1 and Δ_2 obtained by performing two-gap BTK fitting on spectra normalized at slightly different intersection points; one of these datasets corresponds to the fits shown in panel a. Ω_b was eventually calculated by subtracting the average Δ_2 from E_p, and the resulting T dependence of all three quantities is shown in fig. 5.26d.
As in the pristine case, the experimentally determined Ω_b was compared with the two empirical rules governing its behavior: the first relates its zero-T value to the critical temperature, $\Omega_b(0) = 4.65 \cdot k_B T_c$ [274, 275], and the second describes its T dependence, expected to follow twice that of Δ_2, scaled by a proportionality constant k [276, 277]. Using the Andreev-estimated critical temperature, $T_c^A = (19.6 \pm 0.6)\,\mathrm{K}$, the first rule predicts $\Omega_b(0) = (7.9 \pm 0.2)\,\mathrm{meV}$, in agreement with the experimentally observed value. Assuming a BCS-like T dependence for Δ_2 – which accurately captures the data (see fig. 5.26b) – the proportionality constant k ranges from 0.55 (lower boundary of the shaded region) to 0.74 (upper boundary), yielding an average value $k = (0.65 \pm 0.10)$. This result is consistent both with the "universal" value of 0.64 reported for other materials and with the value obtained in the pristine sample [276, 277].

5.2.5 Discussion

In fig. 5.27, the outcomes of various IGP processes that either enhanced or suppressed superconductivity are presented in terms of their superconducting gap values, extracted from Δ_1–Δ_2 BTK fits of the spectra acquired at the lowest temperature, and plotted as a function of the Andreev critical temperature T_c^A. Since this temperature closely matches the onset temperature obtained from transport measurements, it serves as a reliable indicator of superconductivity enhancement or suppression relative to the pristine sample. This approach enables a direct visualization of how the superconducting gaps evolve after the IGP processes, providing a more robust confirmation of the trends identified in specific cases discussed in the previous results section.
For instance, this suggests that H intercalation, besides acting as a charge dopant and thereby shifting the Fermi level, also induces a nontrivial modification of the bands at the Γ point-bands that, in the pristine material, give rise to two gaps detected via ARPES. Specifically, it is plausible that the band responsible for the larger gap no longer intersects the Fermi level upon H intercalation, resulting in the closure of that gap. As a result, the smaller gap – previously obscured by the proximity in energy of the larger one and likely unaffected by H intercalation – becomes discernible.
As evident from the plot, the gap opening on the electron-like Fermi surface Δ_2 follows a clear trend: the gap increases with increasing T_c^A, with a ratio $2\Delta/k_B T_c \approx$

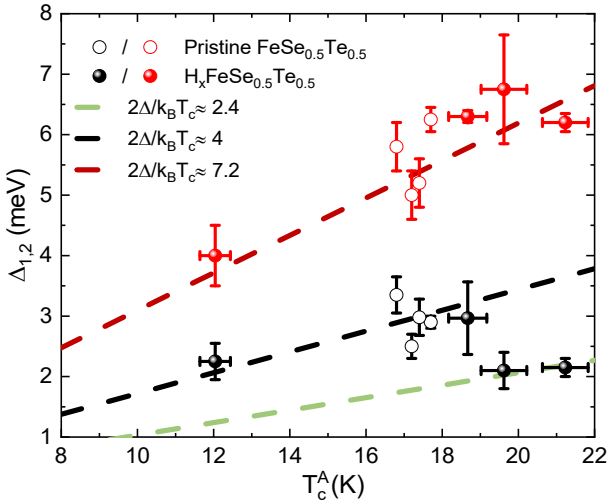

Figure 5.27: Superconducting gap values extracted from Δ_1–Δ_2 BTK fits of low-temperature spectra after various IGP treatments, plotted versus the Andreev critical temperature T_c^A (filled circles). For comparison, gaps from pristine samples are shown as hollow circles.

7.2, in agreement with previous observations for this gap [273]. Consequently, samples exhibiting an enhanced onset temperature also show an increased Δ_2, while those with a suppressed onset temperature display a reduced Δ_2 compared to the pristine case.
The behavior of Δ_1, identified as the convolution of two gaps opening on the hole-like pockets at the Γ point, is more complex. In the pristine sample and in samples with suppressed onset temperatures, Δ_1 follows a linear trend with a slope corresponding to $2\Delta/k_BT_c \approx 4$, consistent with the gap associated with the β band at the Γ point [273]. The smaller gap associated with the α band – expected to have a ratio below the BCS limit in multigap systems – is likely unobservable due to its close proximity to the larger gap, which masks its spectral features. Conversely, in samples showing enhanced onset temperatures, the β-band-related gap is no longer detectable, while the smaller gap becomes apparent. This observation strongly suggests that H intercalation may close the β-band gap, slightly modify the α-band gap, and render the latter discernible. The newly visible gap follows a trend with T_c^A corresponding to $2\Delta/k_BT_c \approx 2.4$, in agreement with expectations for the α-band gap [273].
This nontrivial behavior, together with the fact that the enhancement of Δ_2 in the sample showing a 5 K increase in onset temperature is only a few percent compared to the pristine case, indicates that such modifications are unlikely to significantly improve the distinguishability of Majorana bound states inside the vortex cores

from other trivial effects, thus allowing more definitive conclusions regarding the origin of the observed zero-bias peak in the vortex cores.

Signatures of unconventional superconductivity

Interestingly, in a few rare instances, zero-bias peaks were detected in the low-T spectra for both pristine and IGP-treated samples, across both batches. Representative examples are shown in fig. 5.28. The case presented in panel a, corresponding to pristine $FeSe_{0.5}Te_{0.5}$ shown already in fig. 5.12c, is the most complete example: within an Andreev-like signal, all previously observed features are present – namely, the symmetric maxima and the inner shoulders associated with the gaps opening on the electron-like and hole-like bands (red arrows), as well as the outer shoulders related to the EBI structures (blue arrows) – together with the additional appearance of a zero-bias peak (green arrow). In panel b, the tunnel-like spectrum from an IGP-treated sample with enhanced T_c (as determined from transport measurements) appears less ideal, showing predominantly the feature associated with Δ_2 and the zero-bias conductance peak, while the Δ_1 feature is not clearly visible, likely due to strong convolution with the zero-bias peak.

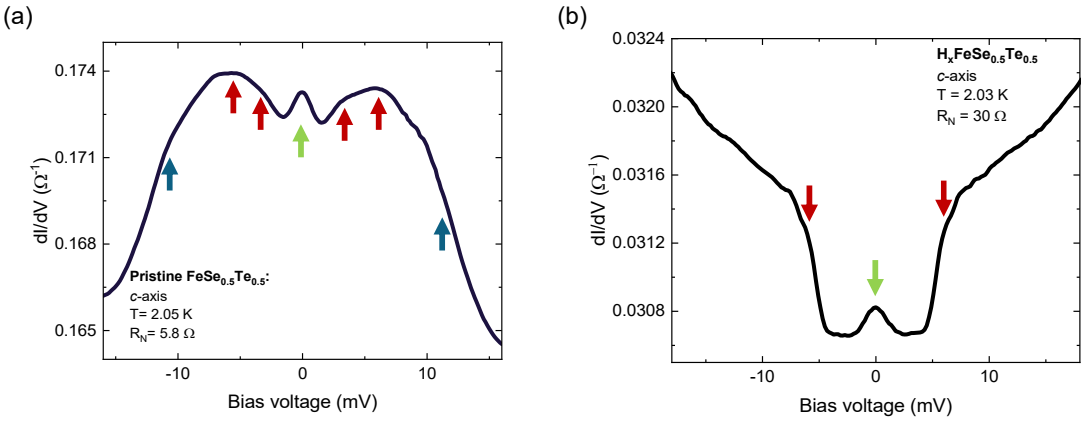

Figure 5.28: Representative point-contact Andreev reflection spectra (dI/dV vs. V) of pristine $FeSe_{0.5}Te_{0.5}$ (a) and $H_xFeSe_{0.5}Te_{0.5}$ obtained via ionic-gating-induced protonation (b). Each spectrum is labeled with the main current injection direction, the measurement temperature T, and the normal-state contact resistance R_N. Spectral features associated with the superconducting gaps, the electron–boson interaction structure, and the anomalous zero-bias peak are indicated by red, blue, and green arrows, respectively.

To further investigate the origin of the zero-bias peak, its evolution was studied as a function of both temperature and magnetic field (B). Regarding the temperature dependence, a representative example is shown in fig. 5.29a, depicting the

evolution of the spectrum from fig. 5.28b. The zero-bias peak is clearly visible at the lowest temperature ($\approx 2\,\mathrm{K}$) but disappears by approximately 3.13 K, where the spectrum near zero bias instead exhibits a dip arising from the gap features. Panel b illustrates the effect of an applied magnetic field on the zero-bias peak, focusing on the spectral region near zero bias. As B increases, the peak diminishes in both amplitude and width (estimated in terms of the full-width half maximum of the peak), indicating its suppression under magnetic field.

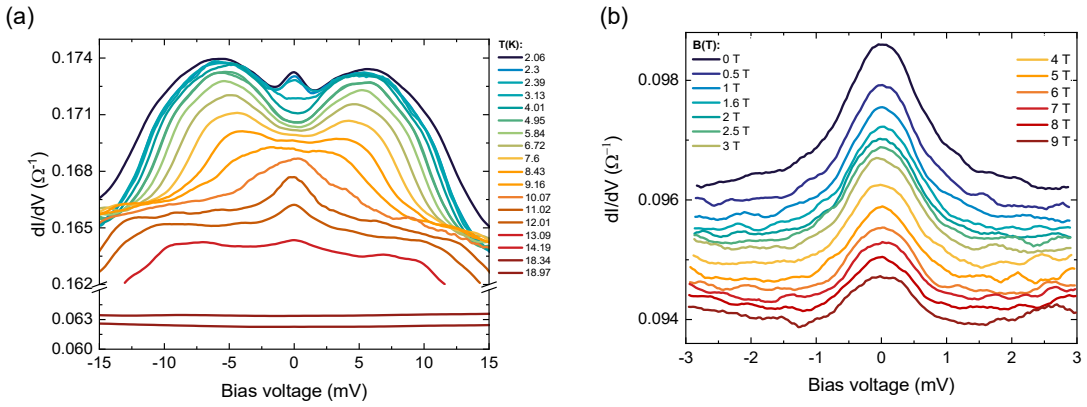

Figure 5.29: Representative conductance spectra (dI/dV vs. V) showing the evolution of the zero-bias peak with temperature (T) (panel a) and magnetic field (B) (panel b). Both sets of data are from pristine $FeSe_{0.5}Te_{0.5}$.

A possible origin of this peak could be the potential presence of the $p_x \pm ip_y$ surface topological superconducting pairing proposed by Fu and Kane [34]. Notably, the peak is observed in both pristine and IGP-treated $FeSe_{0.5}Te_{0.5}$, suggesting that introducing H via IGP – in the amounts that enhanced T^{on} by 1.8 K and increased the superconducting gaps – does not compromise the topological surface state, if this is indeed the origin of the peak. If this interpretation holds, it is likely that this p-wave signal appears alongside the s-wave pairing present in the bulk of $FeSe_{0.5}Te_{0.5}$, since PCARS probes the material to a depth on the order of the coherence length. As a result, the measurement can detect contributions from both the surface and the bulk, producing spectra that effectively represent a convolution of the two signals. Similar behavior has been observed in heterojunctions formed between the dual topological insulator BiSe and the conventional superconductor $NbSe_2$ [278].

To test the hypothesis of a convolution between bulk and surface states, the raw spectra were symmetrized, normalized to the normal-state conductance measured just above T_c, corrected for the effects of spreading resistance, and finally fitted using a two-gap 2D BTK model, where one gap corresponds to the p-wave state and the other to the s-wave state. In this framework, only the s-wave gap Δ_2, corresponding to the dominant contribution observed in the PCARS spectra, was

included, whereas Δ_1 was neglected. This approach avoids the need for a three-gap model, which would introduce additional free parameters and increase the risk of overfitting. Within this two-gap BTK model, the total conductance is expressed as: $G = w_s G_s + w_p G_p$ where G_s and G_p are the conductances associated with the s- and p-wave components, respectively, each defined by eq. (2.8). In particular, in eq. (2.8), the s-wave gap Δ_s is taken as isotropic (constant in momentum space), while the p-wave gap is parameterized as $\Delta_p[\cos(k_x) + \sin(k_y)]$, thereby implementing the $p_x \pm ip_y$ symmetry. This approach yields a 2D BTK model with seven free parameters: the gap amplitudes $\Delta_{s,p}$, the broadening parameters $\Gamma_{s,p}$, the barrier strengths $Z_{s,p}$, and the spectral weights $w_{s,p}$, subject to the normalization constraint $w_s + w_p = 1$. Due to the limited amplitude of the normalized signal, fitting the BTK model requires an additional free parameter, w_n, which acts as a multiplicative factor on the theoretical BTK curve to rescale it vertically to match the experimental spectra. Physically, w_n represents the fraction of non-superconducting nanojunctions in the micron-sized soft point contact, meaning that only a fraction $1 - w_n$ of the total nanojunctions actually contributes to the measured Andreev or tunnel signal.

The results of this fitting procedure for the spectra in fig. 5.28 are shown in fig. 5.30 (solid red lines). In both cases, the BTK model reproduces the experimental data with overall good agreement, though a noticeable discrepancy appears around $2 - 3\,\text{meV}$ due to the absence of the Δ_1 contribution in the model. As indicated by the labels showing the best-fit parameters, the extracted p-wave gap values are similar, and the Δ_2 values are consistent with those obtained using the two-gap Δ_1–Δ_2 analysis described earlier. Minor variations in other parameters, such as Z_s and Z_p, can be ascribed to the distinct spectral character: panel (a) shows an Andreev-like spectrum, while panel (b) is more tunnel-like. For completeness, the best fits from the Δ_1–Δ_2 analysis are also included in fig. 5.30 (solid blue lines).

Finally, given that the T dependence shown in fig. 5.29a exhibits a peak that disappears just 1 K above the base temperature, it is challenging to extract a reliable T-dependent trend for the potential p-wave feature from the available curves. Consequently, the analysis is instead focused on the magnetic-field dependence shown in fig. 5.29b. In this case, since the spectra were measured within a narrow range around zero bias and no signatures attributable to the bulk s-wave component are observed, a single-gap BTK model is applied, retaining only the p-wave component. This is achieved by using the total conductance previously employed and setting $w_p = 1$. This procedure is applied to the raw conductance spectra shown in fig. 5.29b, after symmetrization and normalization. The normal state for each curve is approximated by fitting an even-order polynomial to the spectral tails, since the magnetic field required to completely suppress superconductivity and access the true normal state ($\sim 50\,\text{T}$ [279]) lies beyond the experimental range. The resulting best fits, up to 6 T, are shown in fig. 5.31a, while fig. 5.31b displays the

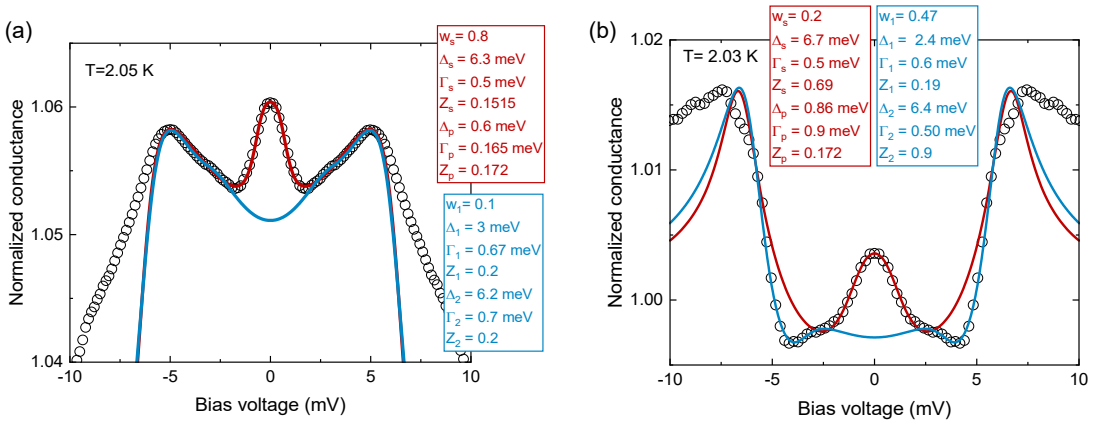

Figure 5.30: Comparison of the best-fit curves obtained by fitting the experimental spectra shown in fig. 5.28 implementing either a conventional s+s-wave BTK model, which accounts for the features associated with gaps Δ_1 and Δ_2 (solid blue lines), or an s+p-wave BTK model, which captures the dominant s-wave gap Δ_2 and the zero-bias peak (solid red lines), assuming that the zero-bias peak originates from surface topological superconductivity. The fitting parameters for both the models are provided in the labels. In both cases, the fraction of normal contacts w_n was fixed at 0.9.

B dependence of the extracted p-wave gap. Notably, this quantity exhibits an approximately linear decrease with increasing magnetic field over the explored range, consistent with the behavior expected for a superconducting gap feature and supporting the association of the observed peak with a gap.

Nevertheless, more definitive evidence regarding the origin of the peak is still lacking and is required before making claims about its possible topological nature. In particular, it is important to understand the specific conditions that, in rare cases, led to the observation of this peak. Notably, the peak has been detected regardless of whether the contact was placed on the surface – injecting current along the c-axis – or on the edge – injecting current within the ab-plane. It has also been observed independently of the type of conductive paste used, whether gold or silver, despite their different grain sizes that could influence the probing length. Its possible connection to topological surface states, however, highlights the potential of PCARS as a tool for detecting surface signatures of topological superconductivity.

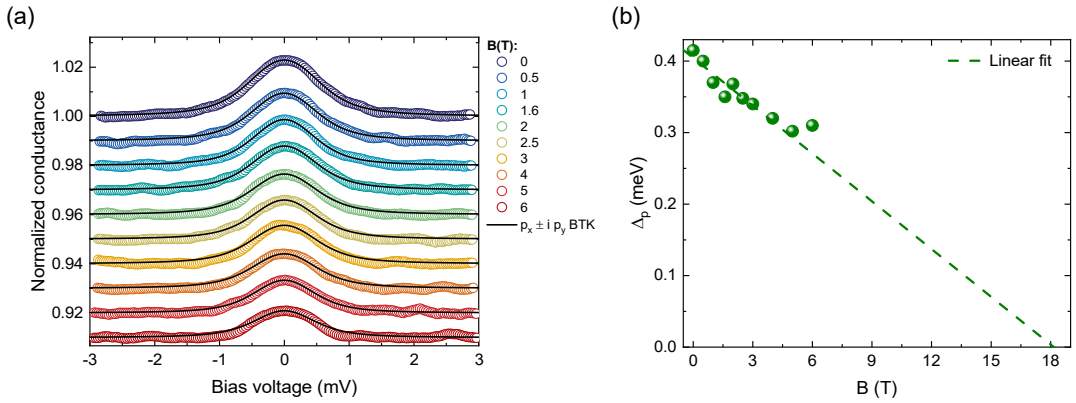

Figure 5.31: (a) Representative $p_x \pm ip_y$ BTK fits (solid lines) to symmetrized and normalized spectra measured at various magnetic fields B (symbols). The original experimental data prior to symmetrization and normalization correspond to the representative curves displayed in fig. 5.29b. (b) B-dependence of the p-wave gap (Δ_p, green symbols) extracted from the fits in panel a. The dashed line represents a linear fit to the extracted values.

5.3 Conclusions

In this final chapter, the study applied the two techniques in which expertise had been developed in the previous chapters – IGP and PCARS – to investigate topological superconductors, the ultimate focus of this thesis, owing to the strong interest in this phase of matter and its potential for enabling fault-tolerant quantum computation. Two candidate topological superconductors were specifically addressed: electron-doped Bi_2Se_3 and $FeSe_{0.5}Te_{0.5}$. For Bi_2Se_3, H intercalation was induced via IGP to attain the electron-doped phase previously claimed to be superconducting. The aim was first to verify the existence of this superconducting phase and, if successful, to investigate its superconducting order parameter using PCARS to determine whether it would be compatible with a topological state. In the case of $FeSe_{0.5}Te_{0.5}$, H intercalation was instead used to enhance its critical temperature and superconducting gaps, aiming at obtaining a functionalized material where a zero-bias peak observed in the vortex cores can be more confidently attributed to Majorana bound states, rather than to a convolution of finite-bias states characteristic of a trivial, non-topological superconductor.

Regarding Bi_2Se_3, despite leveraging the expertise gained from previous IGP studies described in this thesis, H intercalation did not result in the emergence of a superconducting transition detectable via electrical transport measurements, even when replicating the exact conditions under which superconductivity in $H_xBi_2Se_3$

was previously claimed. This discrepancy may be attributed to differences in characterization techniques, as resistivity measurements were used here, whereas the original claim relied on susceptibility measurements. This might suggest that, if a superconducting phase does form, the superconducting volume fraction may be too small to produce a detectable signal under present conditions – an issue that could be mitigated in susceptibility-based measurements.
Nevertheless, significant variability in the temperature dependence of the resistivity of Bi_2Se_3 was observed across different IGP processes, where parameters such as working temperature, gate voltage and time, and electrolyte type were tuned to explore different levels of H intercalation. These observations motivate, as a future perspective, a more systematic and detailed study of Bi_2Se_3 under varying intercalation levels, with quantitative estimation of H content in each treatment. Such an approach would enable a more rigorous understanding of the response of the material and, ideally, help identify the concentration range where superconductivity emerges, if it indeed develops.

In contrast, for $FeSe_{0.5}Te_{0.5}$, H intercalation via IGP effectively tuned the superconducting phase, both in terms of critical temperature and superconducting gaps. Specifically, an enhancement of the gap opening on the electron-like Fermi surface was observed in H-intercalated $FeSe_{0.5}Te_{0.5}$ relative to the pristine material, although modest. In addition, a nontrivial behavior was observed for the two gaps opening at the hole-like Fermi surfaces at the Γ point. Specifically, the larger of the two gaps observable in the pristine sample appeared to vanish upon H-induced T_c enhancement, while the smaller gap became detectable. This behavior requires further investigation, including scanning tunneling microscopy studies of vortex cores, to understand its impact on the identification of Majorana bound states and the distinction from trivial superconducting signatures. Additionally, in rare cases, PCARS revealed a zero-bias peak in both pristine and intercalated $FeSe_{0.5}Te_{0.5}$, interpreted as a potential signature of an unconventional, topological, superconducting state at the surface, with the bulk remaining trivial. If confirmed, the presence of this peak in both pristine and intercalated samples suggests that the intercalation levels achieved do not disrupt the superficial topological state of the pristine material. This finding thus potentially opens a pathway for using PCARS not only to probe bulk topological superconductivity but also to investigate surface states, while employing IGP to functionalize the material and tune the superconducting properties in ways advantageous for detecting topological superconducting phases.

Conclusions and future perspectives

This thesis has explored hydrogen intercalation via ionic gating-induced protonation as a versatile approach to induce or tune superconductivity in thin films and layered materials, with the ultimate goal of addressing candidate topological superconductors – a research area of considerable interest due to their potential as platforms for intrinsically fault-tolerant quantum computation. A multi-step approach was adopted to achieve this ultimate goal, beginning with the development of expertise in ionic gating-induced protonation for attaining controlled hydrogen intercalation, and in point-contact Andreev reflection spectroscopy to probe the superconducting gap function and detect possible signatures of unconventional (potentially topological) superconductivity. These techniques were then applied to the study of candidate topological superconductors.

Along this pathway, the first major outcome obtained is the *development of guidelines to maximize hydrogen loading* in palladium via ionic gating-induced protonation using a deep eutectic solvent – an electrolyte class not previously explored for this purpose. Palladium was chosen as a model system due to its high hydrogen absorption capacity and well-characterized transport properties as a function of hydrogen content, though the guidelines outlined here *can be adapted to optimize hydrogen insertion in other materials* with minimal modification. Following this rationale, a 1:3 choline chloride:glycerol deep eutectic solvent, which is in principle optimized for enhanced hydrogen doping, was employed. Electrical resistivity measurements revealed a strong positive correlation between applied gate voltage and hydrogen uptake, yielding hydrogen concentrations up to 37% higher than those obtained using the conventional ionic liquid EMIM-BF_4. Compared to previously reported hydrogenation levels in materials other than palladium, the hydrogen content achieved here on averaged exceeded them by 91%.
However, despite promising results, hydrogen doping exhibited notable spatial inhomogeneity, leading to broadened and incomplete superconducting transitions in PdH_x. This observation underscores the necessity of optimizing ion transport and

diffusion, both within the host lattice and across the electrolyte interface. Future efforts should focus on designing deep eutectic solvents with lower viscosity, higher proton availability, broader electrochemical windows, and extended operational temperature ranges to achieve more uniform hydrogen distributions. Such improvements would not only enhance the applicability of ionic gating-induced protonation in fundamental research but also broaden its utility for hydrogen storage, superconductivity studies, and spintronic applications.

Building on the expertise gained in performing and controlling ionic gating-induced protonation, the second stage of this work focused on 1T-$TiSe_2$, a layered transition metal dichalcogenide exhibiting charge-density-wave order in its pristine state. Ionic gating-induced protonation was employed to synthesize H_xTiSe_2, recently shown to be superconducting and preliminarily suggested to host a nontrivial superconducting order parameter. This system was investigated using three complementary techniques: magnetotransport measurements, soft point-contact Andreev reflection spectroscopy, and tunneling spectroscopy. Experimental evidence consistently revealed a *non-trivial superconducting order parameter characterized by two nodeless gaps*, whose temperature dependence is in agreement with both Baredeen-Cooper-Schrieffer theory and Eliashberg models for two-band superconductivity. Although variations in gap amplitudes were observed across different Andreev reflection spectroscopy contacts – suggesting a spatial modulation of the order parameter – tunneling spectroscopy measurements confirmed that two-gap superconductivity occurs at the local, atomic level. This finding ruled out the possibility of phase-separated single-gap regions that, when probed by a less spatially resolved technique such as soft point-contact Andreev reflection spectroscopy, could mimic an apparent two-gap behavior. When interpreted alongside previous *ab-initio* calculations, *these results suggest that H_xTiSe_2 exhibits multigap superconductivity arising from an unconventional multi-orbital single-band mechanism*, rather than from a conventional multi-band Fermi surface.
Beyond its intrinsic scientific significance, this study also offered valuable hands-on experience with soft point-contact Andreev reflection spectroscopy on layered materials, experience that later proved crucial for investigating the candidate topological superconductors discussed in this thesis.

Indeed, exploiting the proficiency developed in both ionic gating-induced protonation and soft point-contact Andreev reflection spectroscopy during the earlier stages of this work, the final part of the thesis focused on applying these techniques to two candidate topological superconducting systems: Bi_2Se_3 and $FeSe_{0.5}Te_{0.5}$. In the case of Bi_2Se_3, ionic gating-induced protonation was employed to test the previously reported superconducting hydrogen-doped phase. Despite an extensive exploration of gating parameters, *no superconducting transition was observed via resistivity measurements*, even under conditions nominally identical to those described in the

earlier study. However, the variability in the resistive behavior observed across multiple protonation configurations suggests that hydrogen incorporation does indeed alter the electronic properties of Bi_2Se_3. This finding raises questions regarding the robustness and reproducibility of the previously claimed hydrogen-induced superconducting phase, suggesting that the superconducting volume fraction may be too small to be observed in transport measurements, though it might still be detectable in susceptibility experiments as previously claimed. A more systematic investigation of hydrogen-doped Bi_2Se_3 – including precise quantification of the incorporated hydrogen content – is therefore recommended to determine the precise conditions under which superconductivity, if present, emerges.
In contrast, *$FeSe_{0.5}Te_{0.5}$ displayed clear tunability of its superconducting phase via H intercalation*, both in the critical temperature observed through electrical transport and in the superconducting gaps measured via soft point-contact Andreev reflection spectroscopy – *successfully performed for the first time under ionic gating*. A modest enhancement of the gap opening on the electron-like Fermi surface was observed, while the gaps opening on the hole-like Fermi surfaces at the Γ point exhibited complex, nontrivial evolution: the larger of the two gaps, dominant in the pristine material, appeared to vanish in compounds where hydrogen-doping significantly enhanced their critical temperature, allowing the smaller gap, previously obscured, to become detectable. This behavior is consistent with the disappearance of one of the hole-like Fermi surfaces following the intercalation of hydrogen ions. These observations thus point to complex modifications of the superconducting state induced by hydrogen and underscore the need for complementary investigations, including scanning tunneling microscopy of vortex cores, to fully understand the impact on the identification of Majorana bound states. Remarkably, rare *zero-bias peaks were observed in point-contact Andreev reflection spectra* both for pristine and intercalated samples, *consistent with the potential presence of topological surface superconductivity*. The persistence of this feature under hydrogen intercalation suggests that moderate hydrogen doping can tune bulk superconducting properties without disrupting superficial topological states, offering a pathway to functionalize materials for enhanced detection of Majorana bound states and highlighting point-contact Andreev reflection spectroscopy as a valuable tool for exploring superficial topological superconducting phases.

Appendix A

Supporting material for chapter 3

This appendix reports the full details of the study whose main motivations and results were briefly introduced in chapter 3. Although the work offered useful guidance on ionic gating-induced protonation (IGP) for subsequent work in this thesis, its primary focus was on the hydrogen (H) insertion technique itself, rather than on tuning the superconducting properties of materials via H insertion – the central theme of this dissertation. For this reason, only a summary appeared in the main text, whereas the full study is provided here.

The appendix is organized as follows: it first reviews the properties of palladium that motivated its choice as the experimental platform, then outlines the experimental methods, and finally presents and discusses the measurement results.

A.1 Test material: palladium

As highlighted in the main text, palladium (Pd) was chosen as the most suitable material for this study due to its well-characterized response to increasing H doping levels.

Pd is a transition metal with a face-centered cubic crystal structure and is well known to readily absorb H [280]. Remarkably, the H content (x) in PdH_x directly correlates with its electrical resistivity at 295 K. This correlation is commonly studied in terms of a normalized quantity $\chi_R = \rho(x)/\rho(0)$, where $\rho(x)$ is the resistivity of PdH_x, while $\rho(0)$ is the resistivity of pristine Pd. As shown in fig. A.1a, the χ_R ratio increases steadily with increasing H content, reaching a maximum near $x \approx 0.7$, before gradually decreasing back to unity when x approaches 1 [281, 164, 166, 163]. This distinctive feature makes Pd a strategic choice for this study, as it enables the indirect estimation of H uptake via resistivity measurements, effectively addressing the difficulty of directly quantifying x with the available experimental

setup as explained below.

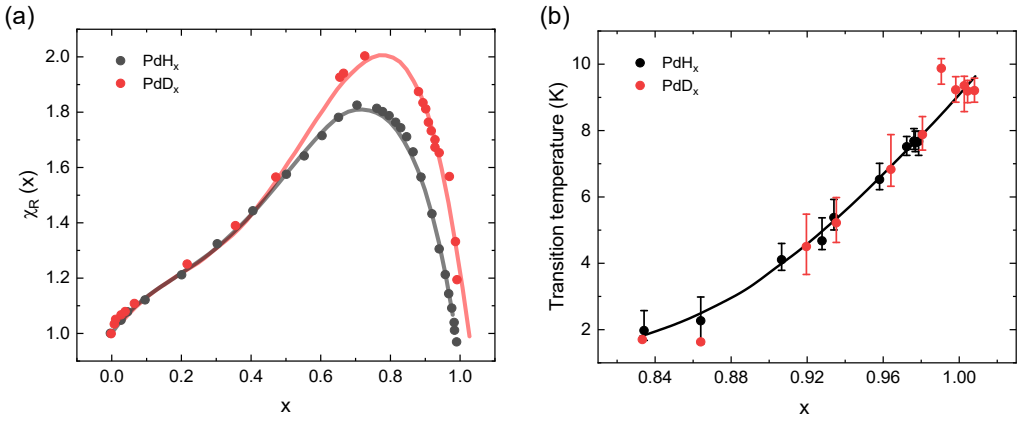

Figure A.1: (a) Empirical correlation between the χ_R resistivity ratio and the hydrogen/deuterium (H/D) content x. Data taken from Ref. [281]. (b) Empirical relationship between the superconducting critical temperature of PdH(D)$_x$ and the H/D concentration. For PdD$_x$, the data points are shifted horizontally by 0.04 to facilitate comparison with the PdH$_x$ trend. Data taken from Ref. [282]

Beyond resistivity at 295 K, further insight into the H content can be obtained by examining the temperature dependence of resistivity (ρ–T curves). These curves reveal a distinct anomaly around 50 K, appearing as a pronounced peak. The temperature at which this anomaly occurs (T_a) systematically shifts with varying H concentration. For $x > 0.6$, T_a increases with increasing x, while the peak simultaneously decreases and ultimately disappears at higher H concentrations ($x \geq 0.8$) [283, 284]. This feature appears consistently across multiple physical properties of PdH$_x$, including specific heat [285, 286], internal friction [287], and thermal relaxation [288]. Initially, this anomaly was attributed to an order–disorder phase transition [280, 289], but more recent investigations indicate that it is primarily caused by kinetic effects associated with changes in the short-range ordering of H [290, 291].

At high H concentrations ($0.8 \lesssim x \leq 1$), where the anomaly disappears and no further insights on the H content can be drawn from it, PdH$_x$ undergoes a superconducting transition at ambient pressure, with T_c reaching up to 9 K depending on x (see fig. A.1b) [292, 293, 165, 294, 295, 296, 283, 297]. Detecting superconductivity in PdH$_x$ synthesized through the deep eutectic solvent (DES)-based IGP method examined in this work would thus provide direct evidence of substantial H incorporation into the Pd lattice. Such a finding would be particularly noteworthy given the well-known tendency of Pd to release H as readily as it absorbs it [298]. Thus, demonstrating that DES gating facilitates H intercalation even in materials

with low H retention would indicate that this approach could have wide-ranging applications.
Additionally, Pd-based noble metal alloys are known to exhibit superconductivity when loaded with H [299], and theoretical studies have predicted the possibility of high-temperature superconducting phases in $PdCuH_x$ [300]. Therefore, successfully achieving substantial H intercalation in pure Pd via this simple DES gating technique would also introduce a new approach for exploring its alloys as potential superconductors under ambient pressure conditions and relatively high temperatures.

A.2 Experimental methods

Pd samples. The measurements in this study were performed on Pd samples, either as bulk foils or thin films, with the goal of exploring different sample thicknesses to determine whether higher H concentrations could be achieved by reducing the sample volume (so as to increase the surface-to-volume ratio).
Focusing on the materials used, bulk Pd foils, purchased from Sigma Aldrich with a purity of 99.9%, were used as received after a 15-minute sonication in ethanol. The actual thickness of these commercial foils was measured with a micrometer and found to be $(25 \pm 1)\,\mu m$. Surface morphology was analyzed via atomic force miscorscopy (AFM) in tapping mode under ambient conditions, employing a Bruker Innova microscope equipped with RTESPA-300 silicon tips. The AFM images obtained (fig. A.2a) displayed a surface predominantly marked by an oriented scratch pattern, likely a result of the polishing process. The root mean square (RMS) roughness and average roughness of the bulk foil was found to be approximately 14 nm and 11 nm, respectively.

In contrast, the thin Pd films were fabricated in a Hall bar pattern by Dr. D. De Fazio at the Institut de Ciencies Fotoniques-ICFO (Barcelona) using standard microfabrication techniques. These films were grown on sapphire substrates through photolithography, followed by thermal evaporation of a nominally 2 nm thick titanium layer, and then a nominally 35 nm thick Pd layer. AFM characterization showed a smooth, featureless surface with no visible granular structure (see fig. A.2b). The measured RMS and mean roughness values of 0.8 nm and 0.5 nm, respectively, confirmed a high-quality deposition. The actual film thickness was determined to be (34 ± 7) nm, based on an average of multiple step edge measurements, one of which is shown in the inset of fig. A.2b.

Electrolyte. In this study, a 1:3 choline chloride: glycerol DES, hereafter referred to as 1:3 ChCl:gly DES, was used as the electrolyte for IGP. This composition was selected for its high ionic conductivity, primarily due to the choline chloride salt,

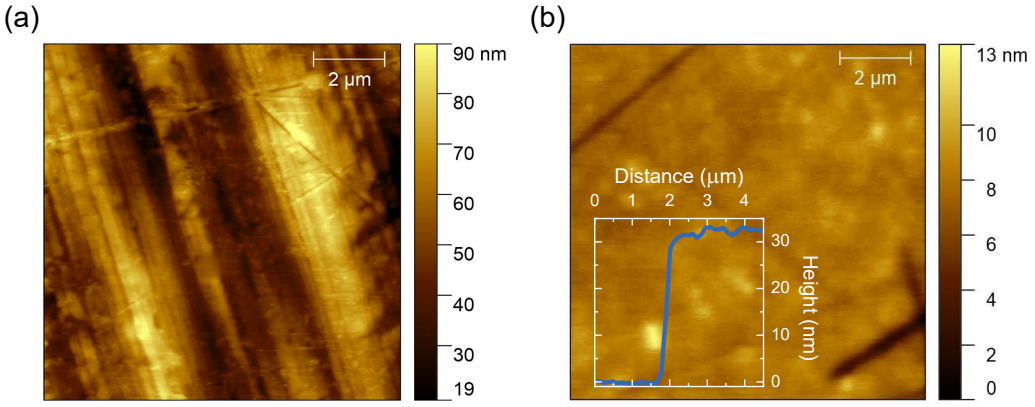

Figure A.2: (a) Representative atomic force micorscopy (AFM) topography map of a Pd foil sample. (b) Representative AFM topography map of a Pd thin film sample, with the inset displaying the height profile measured across the film edge. Adapted from Ref. [105].

which facilitates the formation of a strong electric field at the DES/sample interface. Additionally, glycerol can release protons at relatively low voltages, making it an ideal choice for this application [158, 159, 160]. The 1:3 molar ratio also reduces viscosity, promoting better conductivity and more uniform H^+ uptake [161]. This 1:3 ChCl:gly DES was prepared by Dr. G. Tofani at the University of Pisa, following the procedure described in [167], and its water content was measured to be 520 ppm.

A.3 Results

A.3.1 Ionic gating-induced protonation: methods and results

In-situ IGP was performed on Pd films and foils under ambient condition, as described in section 2.2.2, implementing the appropriate configuration based on the selected cooling system for subsequent ρ-T measurements. *In-situ* protonation was preferred over *ex-situ* because Pd readily releases H.

During a typical IGP procedure, the gate voltage (V_G) was gradually increased from 0 V to a value beyond the cathodic stability limit of the 1:3 ChCl:gly DES, thereby initiating the release of free H^+ ions [158, 301, 302], as anticipated in section 2.2.3. A sweep rate of 1 mV/s was used to allow the ionic dynamics within the 1:3 ChCl:gly DES to properly follow the changing voltage. To prevent device degradation caused by the enhanced reactivity of the DES at high voltages, V_G was

carefully maintained below 12 V. Once the final V_G was reached, it was held constant for a specific duration, which was determined as explained below. Finally, the process was stopped by rapidly cooling the system, as discussed in section 2.2.3. Gate current (I_G) was monitored alongside voltage application to study the 1:3 ChCl:gly DES response to voltage changes and gating time. Representative time evolutions of V_G and I_G are shown in fig. A.3 for bulk foils (fig. A.3a) and thin films (fig. A.3b). All I_G profiles showed low values (a few nA) for $V_G \lesssim 1.9$ V, indicating

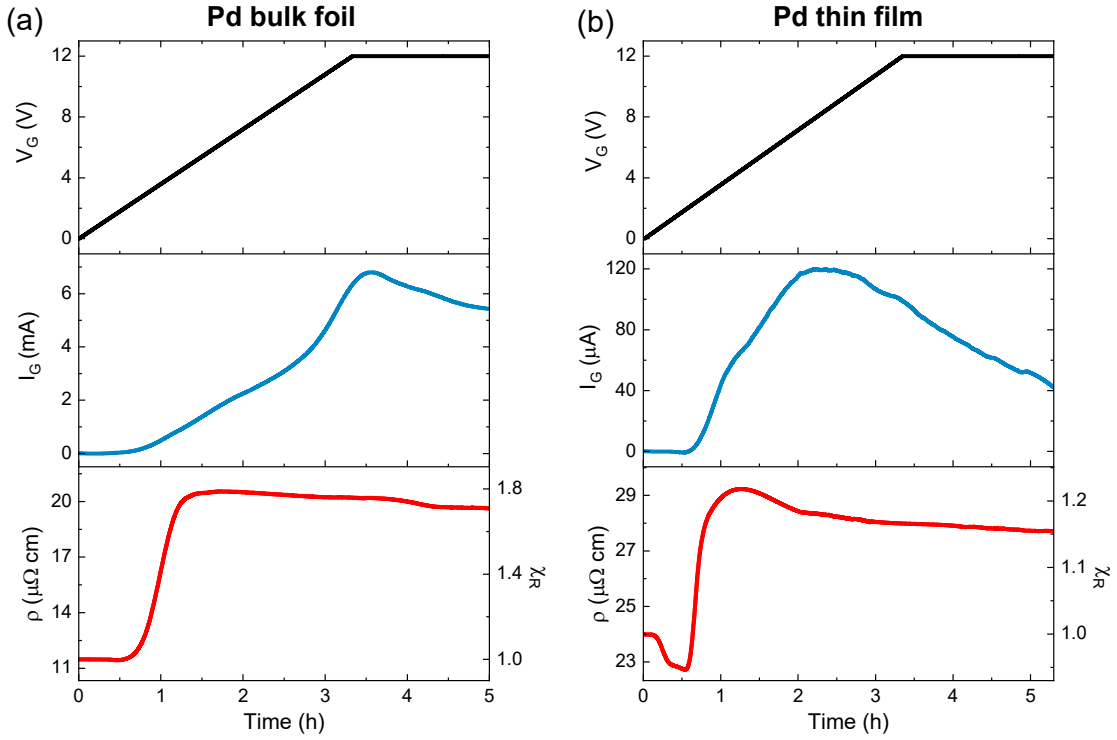

Figure A.3: Representative examples of the dynamics that occurred during ionic gating-induced protonation of a Pd bulk foil (a) and of a Pd thin film (b) under ambient condition. For each process shown, the *in-situ* applied gate voltage V_G, gate current I_G, and electrical resistivity ρ are displayed in the top, middle, and bottom panels, respectively. The ρ values are displayed both in absolute units (left axis) and normalized to the pristine resistivity ($\chi_R = \rho(x)/\rho(0)$) (right axis). Typical values for I_{DS} used to measure ρ are approximately 10 µA for films and 1 mA for foils. Reprinted from Ref. [105].

that H^+ production was inactive in this range. When V_G exceeded this threshold, I_G increased, marking the onset of electrochemical processes. As V_G increased further, I_G continued to rise due to the enhanced release of H^+ ions, reached a peak, and then gradually decreased. This decrease could be partially ascribed to the pseudocapacitive behavior of the polarized DES, as it began roughly when the

voltage ramp reached its final value [303]. However, another contributing factor was likely the gradual degradation of the DES under voltages beyond its stability window, which compromised its ability to sustain a stable production of free H^+ ion over time. The 1.9 V threshold was notably higher than the cathodic stability limit of 1.38 V previously reported for this 1:3 ChCl:gly DES on glassy carbon electrodes [158, 301, 302]. However, the oxidation potential of glycerol varies significantly with electrode material and can even drop below 1 V under certain conditions.

Since not all detected H^+ ions contributing to I_G are necessarily involved in protonation (some may participate in side reactions, such as H evolution [97]), the I_G measurement alone cannot confirm successful protonation. Therefore, to directly assess the impact of protonation on the sample, its resistivity was monitored throughout the treatment. This approach was particularly relevant for PdH_x, given the established correlation between its ρ and H concentration. Representative examples of the time evolution of ρ and its derived χ_R are presented in fig. A.3 for gated bulk foils (fig. A.3a) and thin films (fig. A.3b), complementing the information from V_G and I_G. Both Pd foils and Pd films displayed comparable overall χ_R profiles over time, characterized by an initial increase to a peak followed by a gradual decrease to a stable value. This pattern mirrors the trend observed in fig. A.1a, which illustrates the relationship between χ_R and H content. This suggests a direct correlation between gating time and H uptake, with the eventual stabilization likely resulting from a dynamic equilibrium between H intrinsically desorbed by Pd and H injected from the DES. Once stabilization was reached, or if a change in slope occured – potentially because the DES no longer sustained H^+ pumping, allowing H^+ release from the sample – the system was then cooled down.
Closer examination of the curves reveals that gated Pd films exhibited distinct characteristics compared to bulk foils, likely due to their lower thickness. First, the overall variation in χ_R was significantly smaller for Pd films (with a maximum χ_R of ≈ 1.4) compared to foils (with a maximum χ_R of ≈ 1.8). This observation is consistent with previous studies on Pd thin films [304, 305] and is primarily attributed to a stress-dependent reduction in H solubility [304]. Second, at voltages $V_G \lesssim 1.9$ V, the films exhibited a localized reduction in ρ, which consequently led to a decrease in χ_R (fig. A.3b). Since electrochemical processes for H production were inactive in this region, this distinctive feature was likely the result of electrostatic gating. This effect caused charge carriers to accumulate at the surface, increasing the local carrier concentration and thereby decreasing ρ. Notably, while this phenomenon occurred in both Pd foils and films, it produced a measurable signal only in the films. This discrepancy was attributed to the significantly smaller thickness of the films (34 nm compared to 25 µm for the foils), which makes their electronic properties more sensitive to surface charge accumulation [306, 307, 308, 309].

Final values of χ_R after gating of both Pd bulk foils (hollow circles) and Pd thin

films (filled circles) are summarized in fig. A.4. The observed trend mirrors the time evolution of χ_R shown in fig. A.3 and is similarly attributed to an increasing H content with higher V_G.

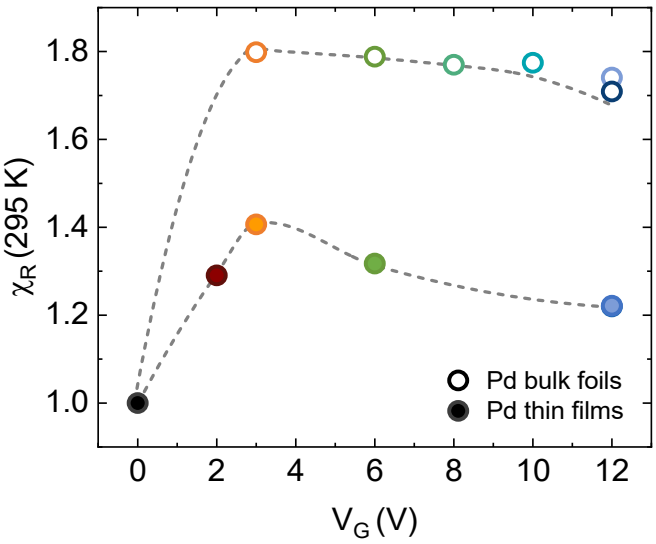

Figure A.4: Resistivity ratio χ_R plotted against the final applied gate voltage V_G for both bulk foils (represented by hollow circles) and thin films (represented by filled circles) following each ionic gating-induced protonation process. The gray dashed lines are added as guides to the eye. Reprinted from Ref. [105].

A.3.2 Temperature-dependent resistivity characterization

T-dependent resistivity measurements were carried out before and after the IGP treatment, as outlined in section 2.1.1, to verify that the observed changes in χ_R for $V_G \gtrsim 1.9\,\mathrm{V}$ resulted from successful protonation. The resulting $\rho - T$ curves are shown in fig. A.5 for both bulk foils (panel a) and thin films (panel b), alongside the corresponding pristine data. To facilitate better comparison, each curve is normalized to its value at 295 K.

For bulk Pd foils, post-gating $\rho - T$ curves (colored lines, fig. A.5a) deviated significantly from the pristine behavior (black line, fig. A.5a). As expected for metals, the pristine resistivity $\rho(0)$ decreased with temperature, eventually saturating below $T \lesssim 5\,\mathrm{K}$. Its initial value of $11.5\,\mu\Omega\,\mathrm{cm}$ at 295 K (see fig. A.3a) was consistent with literature values [310, 311]. In contrast, gated samples exhibited the characteristic anomaly near 50 K, as described in section A.1, which is typical of PdH_x and thus provides strong evidence for the successful incorporation of H into the

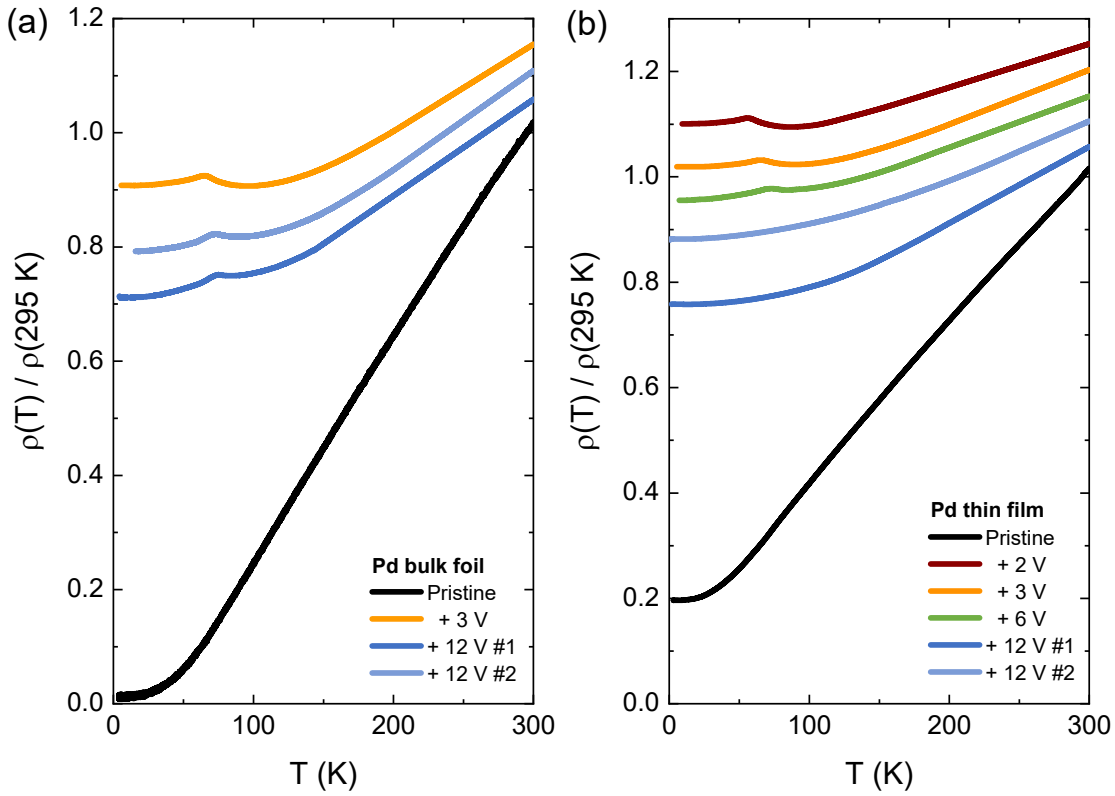

Figure A.5: Temperature dependence of the resistivity (ρ) of Pd bulk foils (a) and Pd thin films (b) before and after ionic gating-induced protonation. Each curve is normalized to its value at $T = 295\,K$ and labeled based on the final applied gate voltage V_G. For clarity, curves with $V_G > 0$ are vertically shifted by 0.05. The color code for the gated curves is consistent with that in fig. A.4, preserving the same color mapping for the applied V_G. Reprinted from Ref. [105].

Pd lattice. Its occurrence temperature T_a, defined as the local maximum of the $\rho - T$ curve within the 0–100 K range, is expected to increase with increasing x for $x > 0.6$, while the peak amplitude simultaneously decreases [283, 284]. This behavior was clearly reflected in the ρ–T curves of gated foils as V_G increased from 3 to 12 V (orange and blue lines in fig. A.5a, respectively), corroborating that the decrease in χ_R observed in fig. A.4 for $V_G \gtrsim 5\,V$ primarily resulted from further H uptake rather than desorption. However, the persistence of the anomaly, even at $V_G = 12\,V$, suggested that the H concentration in this case likely remained below the threshold required to induce a detectable superconducting transition. In fact, previous studies have shown that in superconducting PdH_x samples, the peak height is so diminished that the resistivity anomaly becomes undetectable [293, 162].

In thin films, the pristine ρ–T behavior was also metallic (black line in fig. A.5b),

with a 295 K resistivity of 24 μΩ cm (fig. A.3b), in agreement with typical values for 35 nm-thick Pd films [312, 313]. As with foils, applying a gate voltage $V_G \gtrsim 1.9$ V led to a clear deviation of the ρ–T curves from the pristine curve, indicating successful H incorporation into the Pd lattice. In this case, the resistivity anomaly appeared only for final V_G values between 2 V and 6 V, with the anomaly shifting to higher temperatures as V_G increased. This behavior supported the interpretation that the observed reduction in χ_R (fig. A.3b) was again due to further H uptake rather than desorption.

Unlike the behavior observed in bulk foils, the resistivity anomaly in thin films vanished at $V_G = 12$ V, and the ρ–T curves (solid blue lines in fig. A.5b) reverted to a metallic-like profile, although with a much higher residual resistivity compared to the pristine case. This suggested that, in thin films, the H concentration had exceeded the threshold value ($x \sim 0.85$) beyond which the resistivity anomaly disappears [280]. Although the precise origin of this difference remained unclear, a plausible explanation is that the higher surface-to-volume ratio of thin films relative to those of foils could increase the likelihood of attaining a higher H content under comparable gating conditions. In this high-H regime, where the peak disappears, a non-zero superconducting critical temperature is expected to emerge, as previously mentioned. Indeed, $\rho - T$ measurements on thin films gated at 12 V revealed slight drops for $T \lesssim 2$ K, indicative of incipient superconducting transitions [162, 294, 283, 297, 296, 295, 292]. A magnified view of the 12 V gated curves shown in fig. A.5b is provided in fig. A.6.

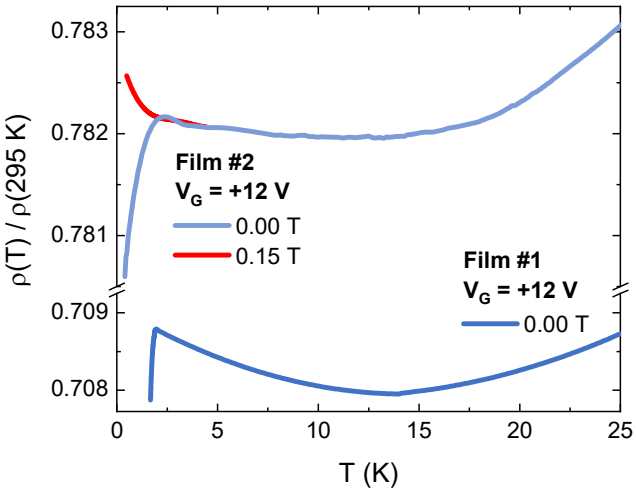

Figure A.6: Magnified view of the resistivity vs. temperature (ρ-T) curves from fig. A.5 for the 12 V-gated thin films, measured at a magnetic field of 0 T. The additional red curve, measured under the same conditions as the light blue curve but at a magnetic field of 0.15 T, emphasizes the superconducting nature of the drop in the ρ-T curves. Reprinted from Ref. [105].

The superconducting origin of these drops was corroborated by their suppression under a magnetic field of 150 mT, a field strength selected to exceed the zero-temperature upper critical field of PdH_1 ($H_{c2}(0) \approx 110$ mT [292, 313, 314]), and thus sufficient to quench superconductivity in any Pd hydride phase. An example of this suppression is shown by the solid red line in fig. A.6. However, the observation of only a partial transition down to 0.35 K suggested that a qualitative assessment of H content was inadequate. A quantitative analysis was required to determine whether this incomplete transition arises from insufficient overall H concentration or from inhomogeneities in its spatial distribution within the film.

A.4 Determination of the hydrogen content

Direct quantitative assessment of H concentration for each IGP process could not be achieved using *ex-situ* techniques. This limitation arose because protonated Pd samples would have rapidly released H between the end of the IGP process and the time of measurement, making any estimation of the H concentration reached unreliable. *In-situ* methods, such as ^{1}H nuclear magnetic resonance [42, 8, 146], were also impractical because they require specialized equipment and bulk samples, making them suitable for Pd foils but not for thin films. As a result, *in-situ* methods would have provided only partial solutions to the problem. Consequently, instead of directly measuring the H content, an indirect estimation approach was employed. This method relied on the established correlation between the H concentration and the χ_R ratio [281, 163, 164, 166]. Specifically, it exploited previous studies that independently measured the final χ_R ratio and the corresponding attained H content. By interpolating these datasets, an empirical function was developed that takes the experimental χ_R values as input and estimates the corresponding x concentrations as output.

A summary of the relevant studies used to derive this empirical relationship is shown in fig. A.7a (symbols). Notably, the dataset from Smith et al. [166] is not shown in its original form. Instead, it has been adjusted to align with the other datasets, which were measured at 295 K, whereas the original data from ref. [166] were collected at 273 K. This adjustment assumes a linear dependence of ρ on T within the relevant temperature range. Based on this assumption, the value of χ_R as a function of x at 295 K was obtained from the original 273 K data using the following relation:

$$\chi_R(x,295\,K) = \frac{\rho(x,273\,K)\,[1+\alpha_{PdH_x}(295\,K-273\,K)]}{\rho(0,273\,K)\,[1+\alpha_{Pd}(295\,K-273\,K)]} \tag{A.1}$$

where α_{PdH_x} and α_{Pd} are the temperature coefficients of the resistivity for PdH_x and Pd, respectively. According to ref. [166], α_{PdH_x} is linear in x. Thus, by linearly

interpolating the data presented in their work, the following expression for $\alpha_{PdH_x}(x)$ was derived: $\alpha_{PdH_x}(x) = (43 - 37x) \times 10^{-4}\,\mathrm{K}^{-1}$. By substituting this into eq. (A.1) and assuming $\alpha_{\mathrm{Pd}} = \alpha_{\mathrm{PdH_x}}(0)$, data from ref. [166] were extrapolated to 295 K.

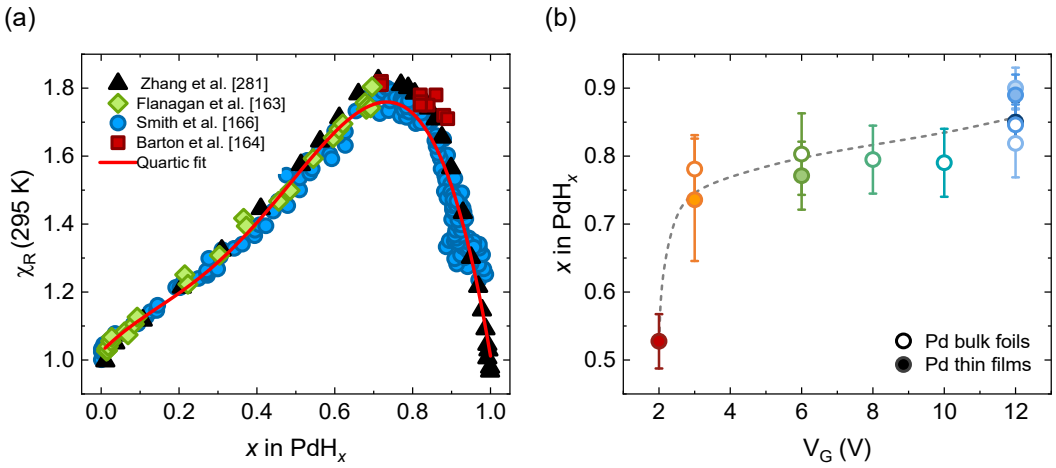

Figure A.7: (a) Empirical relationship relating χ_{R} to the hydrogen content x in $\mathrm{PdH_x}$, based on selected significant studies in the literature. Symbols indicate data adapted from references [281, 163, 166, 164], while the solid red curve represents their best fit according to eq. (A.2). (b) Gate voltage (V_{G}) dependence of the x concentrations, indirectly derived from the χ_{R} values shown in panel (a), for gated bulk foils (hollow circles) and thin films (filled circles). The color code is consistent with that in fig. A.4, preserving the same color mapping for the applied V_{G}. The gray dashed line serves again solely as a visual guide. Adapted from Ref. [105].

Once all data had been adjusted to the same temperature, the empirical relationship between χ_{R} and x was established using an approach similar to that outlined by Zhang *et al.* in [281]. Specifically, the data from fig. A.7a were fitted with a fourth-order polynomial, yielding the following empirical formula:

$$\chi_{\mathrm{R}} = a + bx + cx^2 + dx^3 + ex^4 \tag{A.2}$$

with $a = (1.023 \pm 0.015)$, $b = (1.2 \pm 0.3)$, $c = (-3.3 \pm 1.1)$, $d = (9.9 \pm 1.7)$, and $e = (-7.7 \pm 0.8)$. The solid red curve in fig. A.7a represents this equation.

This empirical relationship, derived from bulk Pd datasets, is effective for determining H content in Pd foils. However, for thin films, the $\chi_{\mathrm{R}} - x$ relationship deviates from the bulk behavior due to the reduced thickness (as shown by the filled circles in fig. A.4). As a result, an adjustment was necessary when dealing with thin films; otherwise, directly calculating χ_{R} would have yielded inaccurate estimates

of H concentration. A practical adjustment involved mapping the measured $\chi_{\mathrm{R,film}}$ to an effective $\chi_{\mathrm{R,bulk}}$ value using a linear transformation. The choice of a linear transformation was supported by previous studies [304, 305], which showed that the reduced thickness of Pd thin films causes a uniform suppression of the $\chi_{\mathrm{R}} - x$ relationship compared to bulk samples, without altering the overall shape of the curve. Specifically, this transformation can be expressed as follows:

$$\chi_{\mathrm{R,\,bulk}}(x) = m \cdot \chi_{\mathrm{R,\,film}}(x) + q \tag{A.3}$$

with m and q fulfilling two conditions that ensure the intrinsic shape of the curve is preserved. Specifically, the first condition, based on the definition of χ_{R}, requires that at the pristine state ($x = 0$), the χ_{R} values for both Pd bulk and films are equal to unity. This results in the constraint: $m + q = 1$. The second condition requires that the peak position remains unchanged under the transformation, resulting in the constraint:

$$\chi_{\mathrm{R,\,bulk,\,max}} = m \cdot \chi_{\mathrm{R,\,film,\,max}} + q$$

where $\chi_{\mathrm{R,\,bulk,\,max}}$ is the maximum value obtained from eq. (A.2) and $\chi_{\mathrm{R,\,film,\,max}}$ is the maximum χ_{R} value derived from each specific IGP process (see fig. A.3b). Combining these two constraints yields the following expressions for m and q:

$$m = \frac{1 - \chi_{\mathrm{R,\,bulk,\,max}}}{1 - \chi_{\mathrm{R,\,film,\,max}}} \quad \text{and} \quad q = 1 - m \tag{A.4}$$

With this correction applied to Pd films, the empirical relationship could be reliably used to estimate H concentrations. However, eq. (A.2) does not provide a unique value of x for a given χ_{R}. Instead, two distinct real solutions are obtained for each χ_{R} value, except at the maximum of the curve. Consequently, a method was required to distinguish between these two solutions and accurately select the correct one for the experiment, ensuring a unique mapping between χ_{R} and x. This was achieved by analyzing the time evolution of ρ during each IGP process (fig. A.3), in order to determine whether the final χ_{R} value was approached along the rising or falling branch of the χ_{R} vs. time curve. Identifying the branch allows for the exclusion of one of the two possible solutions, thus establishing a unique correspondence between χ_{R} and x. The uncertainty associated with this approach arises from the inherent variability in the literature data used to derive the empirical relation between χ_{R} and x (fig. A.7a). Thus, for each χ_{R} value, half of the spread in the x data shown in fig. A.7a was assigned as the uncertainty of the x value obtained by solving eq. (A.2).

The H concentrations estimated applying this indirect method to the raw data in fig. A.4 are shown in fig. A.7b. As before, the results are plotted as a function of the final V_{G} value attained during each IGP procedure.

A.5 Validation of the indirect hydrogen-content estimation

Before interpreting the results shown in fig. A.7, it was essential to evaluate the accuracy of the χ_R–x association obtained through the indirect method outlined above, as well as its susceptibility to potential systematic errors. This assessment was based on a physical parameter that was independent of χ_R but still correlated with the value of x, thereby avoiding circular reasoning. A suitable choice was the temperature T_a of the anomaly observed in the ρ–T curves of PdH_x. It is well established that T_a increases monotonically with H concentration for $x > 0.6$ and is independent of $\rho(295\,K)$, the quantity on which χ_R depends [283, 165, 284, 280]. Consequently, T_a provided a robust, independent benchmark for validating the indirect determination of x.
For each measured ρ–T curve, the H concentration x was first estimated using the method based on χ_R. Then, T_a was determined by identifying the local maximum in the ρ–T curve within the temperature range 40–100 K, using a parabolic fitting procedure. In samples with $0.5 \leq x \leq 0.8$, the ρ–T curves exhibited a well-defined local maximum, allowing for direct fitting of a parabolic function of the form $\rho(T) = a + b \cdot (T - T_{max})^2$, around the peak region. For samples with H concentrations outside this range ($x < 0.5$ or $x > 0.8$), a distinct anomaly remained present, but appeared as a pronounced shoulder, rather than a sharp peak, superimposed on the underlying metallic behavior of the ρ–T curve. In these cases, the metallic contribution was subtracted to isolate the anomaly, making it more prominent and suitable for parabolic fitting.

Regardless of the form of the anomaly, the parameter T_{max} extracted from the fit – along with its associated uncertainty – was taken as the estimate of T_a. The resulting $T_a - x$ data pairs for each measured curve are shown in fig. A.8 (filled red circles) and compared with data from Araki *et al.* [165] (hollow black circles), where both T_a and H content were experimentally determined.
Qualitatively, the results exhibit strong agreement with those reported in ref. [165], which showed that T_a remains constant with increasing x up to the phase boundary between the $\alpha + \beta$ and pure β phases of PdH_x [280]. Beyond this boundary, T_a increases linearly within the pure β phase. To quantify this agreement, both the present data and those from ref. [165] were fitted using a constant-plus-linear model, and the resulting parameters were compared. The fit to the data from ref. [165] (dashed black lines in fig. A.8) yielded a constant temperature of (53.8 ± 1.2) K up to $x = 0.65$, followed by a linear dependence $T_a = [(-22 \pm 6) + x \cdot (116 \pm 7)]$ K for $x > 0.66$. Applying the same model to the present data (dashed red lines in fig. A.8) resulted in $T_a = (53.8 \pm 1.6)$ K up to $x = 0.69$, with a subsequent linear trend given by $T_a = [(-23 \pm 10) + x \cdot (116 \pm 14)]$ K for $x > 0.69$. The fitted parameters are in

agreement within the respective uncertainties, thereby validating the accuracy of the adopted indirect method for determining H concentrations in gated Pd samples.

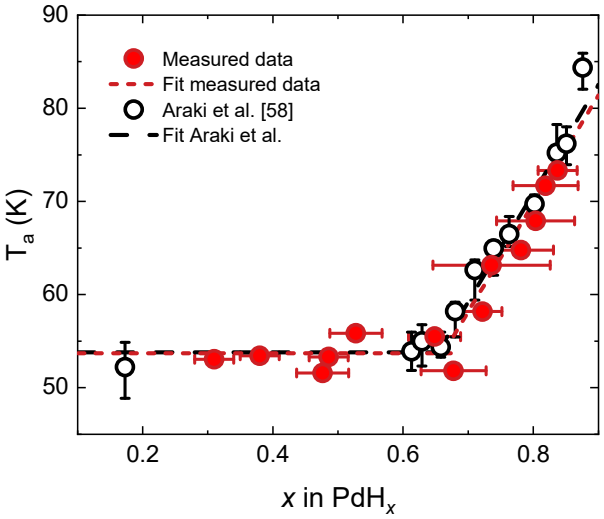

Figure A.8: Dependence of the anomaly temperature T_a in the resistivity vs. temperature curves of PdH_x on hydrogen concentration (x). The filled red circles represent our data, while the hollow black circles are data taken from ref. [165]. The dashed lines correspond to a constant-plus-linear fits for both data sets, as explained in the text. Adapted from Ref. [105].

A.6 Discussion

A.6.1 Evaluation of the performance of the deep eutectic solvent

The confirmed reliability of the indirect method for estimating H concentration in gated Pd samples allowed for a confident interpretation of the data shown in fig. A.7b. As discussed in the main text, these data revealed a positive correlation between H uptake and gate voltage exceeding the cathodic limit of the 1:3 ChCl:gly DES, identified at $V_G = 1.9\,V$. Notably, maintaining a final applied $V_G = 12\,V$ until χ_R stabilized (≈ 2 hours) led to a maximum x of (0.85 ± 0.03) in bulk Pd foils and of (0.89 ± 0.03) in thin films.

With the intrinsic capacity of the 1:3 ChCL:gly DES to promote H uptake established, its performance was directly compared to that of the widely used EMIM-BF_4 to assess the potential of DESs as viable alternatives to ionic liquids for inducing

IGP. As discussed in the main text, the experiment was thus repeated with EMIM-BF_4 and the maximum H concentration was achieved in Pd thin films by applying a final V_G of +3.0 V for 3 hours, yielding $x = (0.65 \pm 0.04)$ as determined by the same indirect method used earlier. This corresponded to an H density of approximately 3.9×10^{22} cm^{-3}. This result was further corroborated by the observed anomaly in the ρ-T dependence at (55.5 ± 0.05) K, consistent with prior findings for a H content of 0.65 [165].

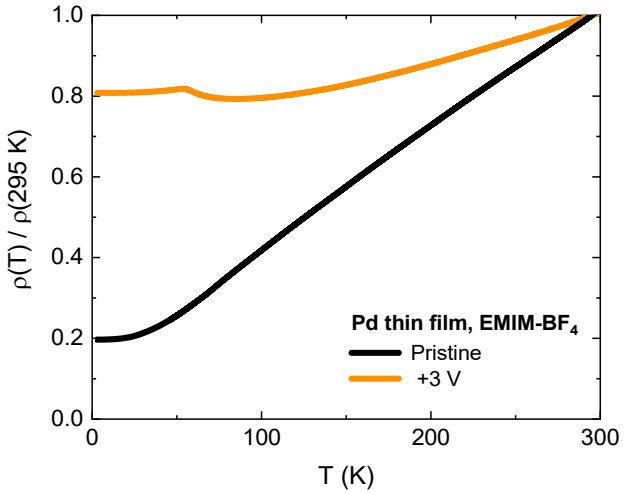

Figure A.9: Representative temperature-dependent resistivity (ρ) of a Pd thin film measured after ionic gating protonation, with a final gate voltage of 3 V applied for 3 h across EMIM-BF_4 (orange line). The pristine behavior is shown for comparison (black curve). Each curve is normalized to its value at $T = 295$ K.

Comparing the performance of 1:3 ChCl:gly DES and EMIM-BF_4, it become thus evident that the deep eutectic solvent outperformed the more conventional ionic liquid.
Overall, the H density achieved in Pd via IGP using the 1:3 ChCl:gly DES represents the highest reported for this method to date. This outstanding performance stemmed from the inherently high solubility of H in Pd combined with the advantageous properties of the 1:3 ChCl:gly DES, highlighting the strong potential of this class of electrolyte for future IGP applications. Table 3.1 and A.1 summarize this result alongside previous studies in which IGP was performed using ionic liquids on a variety of materials, including transition metal dichalcogenides and oxides.

A.6.2 Inhomogeneity

As anticipated in the main text and expanded here, although this DES-based IGP method proved to enable impressively high H loading, the resulting H distribution

Compound	Electrolyte	Stoichiometry	Cell volume Å^3	H density 10^{22} cm^{-3}	Ref.
Pd	1:3 ChCl:gly DES	$PdH_{0.89}$	16.85 [162]	5.3	[105]
Pd	EMIM-BF_4	$PdH_{0.65}$	16.69 [162]	3.9	-
WO_3	DEME-TFSI	$H_{0.35}WO_3$	110 [82]	0.3	[82]
$SrRuO_3$	N/S ionic liquid	H_1SrRuO_3	62.5 [315]	1.6	[315]
$SrFeO_{2.5}$	HMIM-TFSI	$H_1SrFeO_{2.5}$	60.3 [145]	1.7	[145]
$SrCoO_{2.5}$	DEME-TFSI	$H_{2.2}SrCoO_{2.5}$	65.1 [83]	3.1	[83]
$NiCo_2O_4$	DEME-TFSI	$H_{1.86}NiCo_2O_4$	71.4 [101]	2.6	[101]
$TiSe_2$	EMIM-BF_4	H_2TiSe_2	65.7 [8]	3.0	[8]

Table A.1: Overview of the highest hydrogen (H) concentrations achieved in various compounds through electrochemical loading. For studies where H densities are not explicitly reported, these values are estimated by dividing the reported stoichiometries by the corresponding unit-cell volumes. Note that all unit-cell volumes are given per formula unit.

was likely to be highly inhomogeneous. Evidence for this came from the observation that insufficient overall H uptake could be confidently ruled out in samples exhibiting only partial superconducting transitions in this study. For instance, the sample with the highest attained H content ($PdH_{0.89\pm0.03}$) was expected – based on earlier studies [293] discussed in section A.1 – to exhibit a superconducting transition with a mid-point T_c between 1.9 K and 4.3 K. However, the temperature dependence of this $PdH_{0.89\pm0.03}$ sample revealed only the onset of a superconducting transition at 1.9 K (fig. A.6), where the onset was defined as the temperature at which the zero-field ρ-T curve significantly deviates from that measured at $B = 150$ mT. Despite this onset, no clear mid-point of the transition was observed, even down to 0.35 K. Given the reliable determination of the H content, this discrepancy was attributed to pronounced inhomogeneity in H distribution within the Pd sample, leading to a broadened and incomplete transition. This explanation is supported by previous secondary ion mass spectrometry studies on protonated oxide films [82, 84], which showed that the gate-induced H concentration tends to peak at the surface and gradually decreases toward the bulk. Consequently, in the gated Pd samples studied here, the superconducting state could be limited to a thin surface layer, potentially non-percolating, which may lead to the observed incomplete resistive transition. Therefore, enhancing the uniformity of H concentration is critical for advancing the synthesis of high-quality H-loaded samples via IGP. Future work should therefore focus on improving ionic transport and achieving more uniform H diffusion within the host material to fully realize the potential of DES-based IGP.

Bibliography

[1] N. W. Ashcroft. «Metallic hydrogen: a high-temperature superconductor?» In: *Phys. Rev. Lett.* 21.26 (1968), p. 1748. DOI: 10.1103/PhysRevLett.21.1748.

[2] N. W. Ashcroft. «Hydrogen dominant metallic alloys: high temperature superconductors?» In: *Phys. Rev. Lett.* 92.18 (2004), p. 187002. DOI: 10.1103/PhysRevLett.92.187002.

[3] Y. Li et al. «The metallization and superconductivity of dense hydrogen sulfide». In: *J. Chem. Phys.* 140.17 (2014). DOI: 10.1063/1.4874158.

[4] D. Duan et al. «Pressure-induced metallization of dense $(H_2S)_2H_2$ with high-T_c superconductivity». In: *Sci. rep.* 4.1 (2014), p. 6968. DOI: 10.1038/srep06968.

[5] A. P. Drozdov et al. «Conventional superconductivity at 203 kelvin at high pressures in the sulfur hydride system». In: *Nature* 525.7567 (2015), pp. 73–76. DOI: 10.1038/nature14964.

[6] A. P. Drozdov et al. «Superconductivity at 250 K in lanthanum hydride under high pressures». In: *Nature* 569 (2019), pp. 528–531. DOI: 10.1038/s41586-019-1201-8.

[7] L. Boeri et al. «The 2021 room-temperature superconductivity roadmap». In: *J. Phys.: Condens. Matter* 34.18 (2022), p. 183002. DOI: 10.1088/1361-648X/ac2864.

[8] E. Piatti et al. «Superconductivity induced by gate-driven hydrogen intercalation in the charge-density-wave compound 1 T-$TiSe_2$». In: *Commun. Phys.* 6.1 (2023), p. 202. DOI: 10.1038/s42005-023-01330-w.

[9] Y. Meng et al. «Significant enhancement of critical current density in H^+-intercalated FeSe single crystal». In: *Supercond. Sci. Technol.* 35.7 (2022), p. 075012. DOI: 10.1088/1361-6668/ac72cd.

[10] Z. Liu et al. «Protonation enhanced superconductivity in PdTe2». In: *J. Phys. Condens. Matter* 34.33 (2022), p. 335603. DOI: 10.1088/1361-648X/ac7767.

[11] Y. Meng et al. «Protonation-induced discrete superconducting phases in bulk FeSe single crystals». In: *Phys. Rev. B* 105.13 (2022), p. 134506. DOI: 10.1103/PhysRevB.105.134506.

[12] S. Liu et al. «Superconductivity and Charge-density-wave-like Transition in $Th_2Cu_4As_5$». In: *J. Am. Chem. Soc.* 146.12 (2024), pp. 8260–8268. DOI: 10.1021/jacs.3c13257.

[13] G. Venditti and S. Caprara. «Charge-density waves vs. superconductivity: Some results and future perspectives». In: *Condens. Matter.* 8.3 (2023), p. 54. DOI: 10.3390/condmat8030054.

[14] M. Yi et al. «Dynamic competition between spin-density wave order and superconductivity in underdoped $Ba_{1-x}K_xFe_2As_2$». In: *Nat. commun.* 5.1 (2014), p. 3711. DOI: 10.1038/ncomms4711.

[15] E. Morosan et al. «Superconductivity in Cu_xTiSe_2». In: *Nat. Phys.* 2.8 (2006), pp. 544–550. DOI: 10.1038/nphys360.

[16] E. Morosan et al. «Multiple electronic transitions and superconductivity in Pd_xTiSe_2». In: *Phys. Rev. B* 81.9 (2010), p. 094524. DOI: 10.1103/PhysRevB.81.094524.

[17] L. J. Li et al. «Controlling many-body states by the electric-field effect in a two-dimensional material». In: *Nature* 529 (2016), pp. 185–189. DOI: 10.1038/nature16175.

[18] M. Liao et al. «Coexistence of resistance oscillations and the anomalous metal phase in a lithium intercalated $TiSe_2$ superconductor». In: *Nat. Commun.* 12.1 (2021), p. 5342. DOI: 10.1038/s41467-021-25671-8.

[19] J.-Y. Ji et al. «Superconducting Gap and Its Little-Parks-like Oscillations with High-Order Harmonics in Lithium Intercalated 1T-$TiSe_2$». In: *Nano Lett.* (2025). DOI: 10.1021/acs.nanolett.5c02401.

[20] S. Y. Li et al. «Single-gap s-wave superconductivity near the charge-density-wave quantum critical point in Cu_xTiSe_2». In: *Phys. Rev. Lett.* 99.10 (2007), p. 107001. DOI: 10.1103/PhysRevLett.99.107001.

[21] A. D. Hillier et al. «Probing the superconducting ground state near the charge density wave phase transition in $Cu_{0.06}TiSe_2$». In: *Phys. Rev. B* 81.9 (2010), p. 092507. DOI: 10.1103/PhysRevB.81.092507.

[22] J. Kačmarčík et al. «Heat capacity of single-crystal Cu_xTiSe_2 superconductors». In: *Phys. Rev. B* 88.2 (2013), p. 020507. DOI: 10.1103/PhysRevB.88.020507.

[23] M. Zaberchik et al. «Possible evidence of a two-gap structure for the Cu_xTiSe_2 superconductor». In: *Phys. Rev. B* 81.22 (2010), p. 220505. DOI: 10.1103/PhysRevB.81.220505.

[24] R. D. H. Hinlopen et al. «Lifshitz transition enabling superconducting dome around a charge-order critical point». In: *Sci. Adv.* 10.27 (2024), eadl3921. DOI: 10.1126/sciadv.adl3921.

[25] A. Stern and N. H. Lindner. «Topological quantum computation—from basic concepts to first experiments». In: *Science* 339.6124 (2013), pp. 1179–1184. DOI: 10.1126/science.1231473.

[26] X.-L. Qi and S.-C. Zhang. «Topological insulators and superconductors». In: *Rev. Mod. Phys.* 83.4 (2011), pp. 1057–1110. DOI: 10.1103/RevModPhys.83.1057.

[27] M. Sato and Y. Ando. «Topological superconductors: a review». In: *Rep. Prog. Phys.* 80.7 (2017), p. 076501. DOI: 10.1088/1361-6633/aa6ac7.

[28] M. Leijnse and K. Flensberg. «Introduction to topological superconductivity and Majorana fermions». In: *Semicond. Sci. Technol.* 27.12 (2012), p. 124003. DOI: 10.1088/0268-1242/27/12/124003.

[29] M. Mandal et al. «Topological superconductors from a materials perspective». In: *Chem. Mater.* 35.16 (2023), pp. 6184–6200. DOI: 10.1021/acs.chemmater.3c00713.

[30] Y. Li and Z.-A. Xu. «Exploring topological superconductivity in topological materials». In: *Adv. Quantum Technol.* 2.9 (2019), p. 1800112. DOI: 10.1002/qute.201800112.

[31] V. Mourik et al. «Signatures of Majorana fermions in hybrid superconductor-semiconductor nanowire devices». In: *Science* 336.6084 (2012), pp. 1003–1007. DOI: 10.1126/science.1222360.

[32] A. Das et al. «Zero-bias peaks and splitting in an Al–InAs nanowire topological superconductor as a signature of Majorana fermions». In: *Nature Phys* 8 (2012), pp. 887–895. DOI: 10.1126/science.1222360.

[33] R. Von and Fabian O. «Chemical principles of intrinsic topological superconductors». In: *Chem. Mat.* 35.22 (2023), pp. 9455–9472. DOI: 10.1021/acs.chemmater.3c00760.

[34] L. Fu and C. L. Kane. «Superconducting proximity effect and majorana fermions at the surface of a topological insulator». In: *Phys. Rev. Lett.* 100.9 (2008), p. 096407. DOI: 10.1103/PhysRevLett.100.096407.

[35] M. Wang et al. «A combined method for synthesis of superconducting Cu doped Bi_2Se_3». In: *Sci. Rep.* 6.1 (2016), p. 22713. DOI: 10.1038/srep22713.

[36] S. Sasaki et al. «Topological superconductivity in $Cu_xBi_2Se_3$». In: *Phys. Rev. Lett.* 107.21 (2011), p. 217001. DOI: 10.1103/PhysRevLett.107.217001.

[37] L. Fu and E. Berg. «Odd-parity topological superconductors: theory and application to $Cu_xBi_2Se_3$». In: *Phys. Rev. Lett.* 105.9 (2010), p. 097001. DOI: 10.1103/PhysRevLett.105.097001.

[38] Z. Liu et al. «Superconductivity with topological surface state in $Sr_xBi_2Se_3$». In: *J. Am. Chem. Soc.* 137.33 (2015), pp. 10512–10515. DOI: 10.1021/jacs.5b06815.

[39] Shruti et al. «Superconductivity by Sr intercalation in the layered topological insulator Bi_2Se_3». In: *Phys. Rev. B* 92.2 (2015), p. 020506. DOI: 10.1103/PhysRevB.92.020506.

[40] J. Shen et al. «Nematic topological superconducting phase in Nb-doped Bi_2Se_3». In: *npj Quantum Mater.* 2.1 (2017), p. 59. DOI: 10.1038/s41535-017-0064-1.

[41] T. Asaba et al. «Rotational symmetry breaking in a trigonal superconductor Nb-doped Bi_2Se_3». In: *Phys. Rev. X* 7.1 (2017), p. 011009. DOI: 10.1103/PhysRevX.7.011009.

[42] Y. Cui et al. «Ionic-liquid-gating induced protonation and superconductivity in FeSe, $FeSe_{0.93}S_{0.07}$, ZrNCl, 1T-TaS_2 and Bi_2Se_3». In: *Chin. Phys. Lett.* 36.7 (2019), p. 077401. DOI: 10.1088/0256-307X/36/7/077401.

[43] K. Matano et al. «Spin-rotation symmetry breaking in the superconducting state of $Cu_xBi_2Se_3$». In: *Nat. Phys.* 12.9 (2016), pp. 852–854. DOI: 10.1038/nphys3781.

[44] S. Yonezawa et al. «Thermodynamic evidence for nematic superconductivity in $Cu_xBi_2Se_3$». In: *Nat. Phys.* 13.2 (2017), pp. 123–126. DOI: 10.1038/nphys3907.

[45] Y. Pan et al. «Rotational symmetry breaking in the topological superconductor $Sr_xBi_2Se_3$ probed by upper-critical field experiments». In: *Sci. Rep.* 6.1 (2016), pp. 1–7. DOI: 10.1038/srep28632.

[46] G. Du et al. «Superconductivity with two-fold symmetry in topological superconductor $Sr_xBi_2Se_3$». In: *Sci. China-Phys. Mech. Astron.* 60.3 (2017), p. 037411. DOI: 10.1007/s11433-016-0499-x.

[47] Z. Wang et al. «Topological nature of the $FeSe_{0.5}Te_{0.5}$superconductor». In: *Phys. Rev. B* 92.11 (2015), p. 115119. DOI: 10.1103/PhysRevB.92.115119.

[48] P. Zhang et al. «Observation of topological superconductivity on the surface of an iron-based superconductor». In: *Science* 360.6385 (2018), pp. 182–186. DOI: 10.1126/science.aan4596.

[49] T. Shibauchi, T. Hanaguri, and Y. Matsuda. «Exotic superconducting states in FeSe-based materials». In: *J. Phys. Soc. Jpn.* 89.10 (2020), p. 102002. DOI: 10.7566/JPSJ.89.102002.

[50] E. Mascot et al. «Topological surface superconductivity in $FeSe_{0.45}Te_{0.55}$». In: *Commun. Phys.* 5.1 (2022), p. 188. DOI: 10.1038/s42005-022-00943-x.

[51] T. Machida et al. «Zero-energy vortex bound state in the superconducting topological surface state of Fe(Se,Te)». In: *Nat. Mater.* 18.8 (2019), pp. 811–815. DOI: 10.1038/s41563-019-0397-1.

[52] J.-X. Yin et al. «Observation of a robust zero-energy bound state in iron-based superconductor Fe(Te, Se)». In: *Nat. Phys.* 11.7 (2015), pp. 543–546. DOI: 10.1038/nphys3371.

[53] C. Chen et al. «Atomic line defects and zero-energy end states in monolayer Fe (Te, Se) high-temperature superconductors». In: *Nat. Phys.* 16.5 (2020), pp. 536–540. DOI: 10.1038/s41567-020-0813-0.

[54] D. Wang et al. «Evidence for Majorana bound states in an iron-based superconductor». In: *Science* 362.6412 (2018), pp. 333–335. DOI: 10.1126/science.aao1797.

[55] M. Chen et al. «Discrete energy levels of Caroli-de Gennes-Matricon states in quantum limit in $FeTe_{0.55}Se_{0.45}$». In: *Nat. commun.* 9.1 (2018), p. 970. DOI: 10.1038/s41467-018-03404-8.

[56] S. I. Bondarenko et al. «The Impact of Hydrogenation on Structural and Superconducting Properties of $FeTe_{0.65}Se_{0.35}$ Single Crystals». In: *Materials* 14.24 (2021), p. 7900. DOI: 10.3390/ma14247900.

[57] H. M. Syed, C. J. Webb, and E. MacA. Gray. «Hydrogen-modified superconductors: A review». In: *Prog. Solid State Ch.* 44.1 (2016), pp. 20–34. DOI: 10.1016/j.progsolidstchem.2016.02.001.

[58] D. Qiu et al. «Recent advances in 2D superconductors». In: *Adva. Mat.* 33.18 (2021), p. 2006124. DOI: 10.1002/adma.202006124.

[59] H.-T. Zhang et al. «Beyond electrostatic modification: design and discovery of functional oxide phases via ionic-electronic doping». In: *Adv Phys-X* 4.1 (2019), p. 1523686. DOI: 10.1002/adma.202006124.

[60] K. Ueno et al. «Field-Induced Superconductivity in Electric Double Layer Transistors». In: *J. Phys. Soc. Jpn.* 83.3 (2014), p. 032001. DOI: 10.7566/JPSJ.83.032001.

[61] P. Simon and Y. Gogotsi. «Materials for electrochemical capacitors». In: *Nat. mater.* 7.11 (2008), pp. 845–854. DOI: 10.1038/nmat2297.

[62] T. Sato, G. Masuda, and K. Takagi. «Electrochemical properties of novel ionic liquids for electric double layer capacitor applications». In: *Electrochim. Acta* 49.21 (2004), pp. 3603–3611. DOI: 10.1016/j.electacta.2004.03.030.

[63] A. T. Bollinger et al. «Superconductor–insulator transition in $La_{2-x}Sr_xCuO_4$ at the pair quantum resistance». In: *Nature* 472.7344 (2011), pp. 458–460. DOI: 10.1038/nature09998.

[64] J. Garcia-Barriocanal et al. «Electronically driven superconductor-insulator transition in electrostatically doped $La_2CuO_{4+\delta}$ thin films». In: *Phys. Rev. B* 87.2 (2013), p. 024509. DOI: 10.1103/PhysRevB.87.024509.

[65] K. Hanzawa et al. «Key factors for insulator-superconductor transition in FeSe thin films by electric field». In: *IEEE Trans. Appl. Supercond.* 27.4 (2016), pp. 1–5. DOI: 10.1109/TASC.2016.2639738.

[66] K. Ueno et al. «Electric-field-induced superconductivity in an insulator». In: *Nat. Mat.* 7.11 (2008), pp. 855–858. DOI: 10.1038/nmat2298.

[67] Y. Saito et al. «Metallic ground state in an ion-gated two-dimensional superconductor». In: *Science* 350.6259 (2015), pp. 409–413. DOI: 10.1126/science.1259440.

[68] J. T. Ye et al. «Superconducting dome in a gate-tuned band insulator». In: *Science* 338.6111 (2012), pp. 1193–1196. DOI: 10.1126/science.1228006.

[69] K. Ueno et al. «Discovery of superconductivity in $KTaO_3$ by electrostatic carrier doping». In: *Nat. nanotechnol.* 6.7 (2011), pp. 408–412. DOI: 10.1038/nnano.2011.78.

[70] P. A. Lee, N. Nagaosa, and X.-G. Wen. «Doping a Mott insulator: Physics of high-temperature superconductivity». In: *Rev. Mod. Phys.* 78.1 (2006), pp. 17–85. DOI: 10.1103/RevModPhys.78.17.

[71] A. Sakai et al. «Thermoelectric properties of electron-doped $KTaO_3$». In: *Jpn. J. Appl. Phys.* 48.9R (2009), p. 097002. DOI: 10.1143/JJAP.48.097002.

[72] J. T. Ye et al. «Liquid-gated interface superconductivity on an atomically flat film». In: *Nat. Mater.* 9.2 (2010), pp. 125–128. DOI: 10.1038/nmat2587.

[73] J. Jeong et al. «Suppression of metal-insulator transition in VO_2 by electric field-induced oxygen vacancy formation». In: *science* 339.6126 (2013), pp. 1402–1405. DOI: 10.1126/science.1230512.

[74] K. Shibuya and A. Sawa. «Modulation of Metal-Insulator Transition in VO_2 by Electrolyte Gating-Induced Protonation». In: *Adv. Electron. Mater.* 2.2 (2016), p. 1500131. DOI: 10.1002/aelm.201500131.

[75] E. Piatti, J. Montagna Bozzone, and D. Daghero. «Anomalous metallic phase in molybdenum disulphide induced via gate-driven organic ion intercalation». In: *Nanomat.* 12.11 (2022), p. 1842. DOI: 10.3390/nano12111842.

[76] J. Wang et al. «Superconductivity at 44.4 K achieved by intercalating $EMIM^+$ into FeSe». In: *Chin. Phys. B* 30.10 (2021), p. 107402. DOI: 10.1088/1674-1056/ac1f09.

[77] J. Fan et al. «Reversible Intercalation of 1-Ethyl-3-methylimidazolium Cations into MoS_2 from a Pure Ionic Liquid Electrolyte for Dual-Ion Cells». In: *ChemElectroChem* 6.3 (2019), pp. 676–683. DOI: 10.1002/celc.201801583.

[78] F. Xiong et al. «Li intercalation in MoS_2: in situ observation of its dynamics and tuning optical and electrical properties». In: *Nano letters* 15.10 (2015), pp. 6777–6784. DOI: 10.1021/acs.nanolett.5b02619.

[79] Y. Wu et al. «Dimensional reduction and ionic gating induced enhancement of superconductivity in atomically thin crystals of $2H$-$TaSe_2$». In: *Nanotechnology* 30.3 (2018), p. 035702. DOI: 10.1088/1361-6528/aaea3b.

[80] W. Shi et al. «Superconductivity series in transition metal dichalcogenides by ionic gating». In: *Sci. Rep.* 5.1 (2015), p. 12534. DOI: 10.1038/srep12534.

[81] N. Lu et al. «Electric-field control of tri-state phase transformation with a selective dual-ion switch». In: *Nat.* 546.7656 (2017), pp. 124–128. DOI: 10.1038/nature22389.

[82] M. Wang et al. «Electric-field-controlled phase transformation in WO_3 thin films through hydrogen evolution». In: *Adv. Mater.* 29.46 (2017), p. 1703628. DOI: 10.1002/adma.201703628.

[83] H. Li et al. «Electric field–controlled multistep proton evolution in $H_xSrCoO_{2.5}$ with formation of H-H dimer». In: *Adv. Sci.* 6.20 (2019), p. 1901432. DOI: 10.1002/advs.201901432.

[84] M. Rafique et al. «Ionic Liquid Gating Induced Protonation of Electron-Doped Cuprate Superconductors». In: *Nano Lett.* 19.11 (2019), pp. 7775–7780. DOI: 10.1021/acs.nanolett.9b02776.

[85] H. Yuan et al. «High-density carrier accumulation in ZnO field-effect transistors gated by electric double layers of ionic liquids». In: *Adv. Funct. Mater.* 19.7 (2009), pp. 1046–1053. DOI: 10.1002/adfm.200801633.

[86] L. Zhang et al. «The mechanism of electrolyte gating on high-T_c cuprates: The role of oxygen migration and electrostatics». In: *ACS nano* 11.10 (2017), pp. 9950–9956. DOI: 10.1021/acsnano.7b03978.

[87] G. V. S. Rao et al. «Superconductivity in alkaline earth metal and Yb intercalated group VI layered dichalcogenides». In: *J. Solid State Chem.* 9.4 (1974), pp. 323–329. DOI: 10.1016/0022-4596(74)90090-5.

[88] S. Jo et al. «Electrostatically induced superconductivity at the surface of WS_2». In: *Nano lett.* 15.2 (2015), pp. 1197–1202. DOI: 10.1021/nl504314c.

[89] P. Cavaliere. «Fundamentals of water electrolysis». In: *Water Electrolysis for Hydrogen Production*. Springer, 2023, pp. 1–60.

[90] H. Ji, J. Wei, and D. Natelson. «Modulation of the Electrical Properties of VO_2 Nanobeams Using an Ionic Liquid as a Gating Medium». In: *Nano Lett.* 12.6 (2012), pp. 2988–2992. DOI: 10.1021/nl300741h.

[91] S. Chen et al. «Gate-controlled VO_2 phase transition for high-performance smart windows». In: *Sci. Adv.* 5.3 (2019), eaav6815. DOI: 10.1126/sciadv.aav6815.

[92] S. Kouno et al. «Superconductivity at 38 K at an electrochemical interface between an ionic liquid and $FeSe_{0.8}Te_{0.2}$ on various substrates». In: *Sci. rep.* 8.1 (2018), p. 14731. DOI: 10.1038/s41598-018-33121-7.

[93] *Low Level Measurements Handbook - 7th Edition*. Keithley Instruments, Inc.

[94] L. J. van der Pauw. «A method of measuring specific resistivity and Hall effect of discs of arbitrary shape». In: *Philips Res. Repts.* 13.1 (1958). DOI: 10.1142/9789814503464_0017.

[95] Y. Cui et al. «Protonation induced high-T_c phases in iron-based superconductors evidenced by NMR and magnetization measurements». In: *Sci. Bull.* 63.1 (2018), pp. 11–16. DOI: 10.1016/j.scib.2017.12.009.

[96] T. Katase et al. «Room-Temperature-Protonation-Driven On-Demand Metal-Insulator Conversion of a Transition Metal Oxide». In: *Adv. Electron. Mater* 1.7 (2015), p. 1500063. DOI: 10.1002/aelm.201500063.

[97] S. Sarkar and S. C. Peter. «An overview on Pd-based electrocatalysts for the hydrogen evolution reaction». In: *Inorg. Chem. Front.* 5.9 (2018), pp. 2060–2080. DOI: 10.1039/C8QI00042E.

[98] I. Gutiérrez-Lezama et al. «Ionic gate spectroscopy of 2D semiconductors». In: *Nat. Rev. Phys.* 3.7 (2021), pp. 508–519. DOI: 10.1038/s42254-021-00317-2.

[99] H. Yuan et al. «Hydrogenation-induced surface polarity recognition and proton memory behavior at protic-ionic-liquid/oxide electric-double-layer interfaces». In: *J. Am. Chem. Soc.* 132.19 (2010), pp. 6672–6678. DOI: 10.1021/ja909110s.

[100] A. J. Bard, L. R. Faulkner, and H. S. White. *Electrochemical methods: fundamentals and applications*. John Wiley & Sons, 2022.

[101] M. Wang et al. «Manipulate the electronic and magnetic states in $NiCo_2O_4$ films through electric-field-induced protonation at elevated temperature». In: *Adv. Mat.* 31.16 (2019), p. 1900458. DOI: 10.1002/adma.201900458.

[102] M. Wu et al. «Ferromagnetic Insulating Ground-State Resolved in Mixed Protons and Oxygen Vacancies-Doped $La_{0.67}Sr_{0.33}CoO_3$ Thin Films via Ionic Liquid Gating». In: *ACS Appl. Mater. Interfaces* 16.16 (2024), pp. 20767–20775. DOI: 10.1021/acsami.4c00724.

[103] M. Wu et al. «Influences of cation distribution on proton insertion dynamics in complex spinel $NiCo_2O_4$ thin films via ionic liquid gating». In: *Phys. Rev. Mat.* 7.7 (2023), p. 075001. DOI: 10.1103/PhysRevMaterials.7.075001.

[104] E. Piatti et al. «Possible charge-density-wave signatures in the anomalous resistivity of Li-intercalated multilayer MoS_2». In: *Appl. Surf. Sci.* 461 (2018), pp. 269–275. DOI: 10.1016/j.apsusc.2018.05.232.

[105] G. Gavello et al. «Facile synthesis of palladium hydride via ionic gate-driven protonation using a deep eutectic solvent». In: *J, Mol. Liq.* 420 (2025), p. 126826. DOI: 10.1016/j.molliq.2024.126826.

[106] D. Daghero and R.S. Gonnelli. «Probing multiband superconductivity by point-contact spectroscopy». In: *Supercond. Sci. Technol.* 23.4 (2010), p. 043001. DOI: 10.1088/0953-2048/23/4/043001.

[107] S. Sasaki et al. «Odd-Parity Pairing and Topological Superconductivity in a Strongly Spin-Orbit Coupled Semiconductor». In: *Phys. Rev. Lett.* 109.21 (2012), p. 217004. DOI: 10.1103/PhysRevLett.109.217004.

[108] P.-G. De Gennes. *Superconductivity of metals and alloys*. CRC press, 2018.

[109] G.E. Blonder and M. Tinkham. «Metallic to tunneling transition in Cu-Nb point contacts». In: *Phys. Rev. B* 27.1 (1983), p. 112. DOI: 10.1103/PhysRevB.27.112.

[110] D. Daghero et al. «Point-contact spectroscopy in neutron-irradiated $Mg^{11}B_2$». In: *Phys. Rev. B* 74.17 (2006), p. 174519. DOI: 10.1103/PhysRevB.74.174519.

[111] G. Deutscher. «Andreev-Saint-James reflections: A probe of cuprate superconductors». In: *Rev. Mod. Phys.* 77.1 (2005), pp. 109–135. DOI: 10.1103/RevModPhys.77.109.

[112] V. Baltz et al. «Conductance features in point contact Andreev reflection spectra». In: *J. Phys. Condens. Matter.* 21.9 (2009), p. 095701. DOI: 10.1088/0953-8984/21/9/095701.

[113] A. M. Duif, A. G. M. Jansen, and P. Wyder. «Point-contact spectroscopy». In: *J. Phys. Condens. Matter* 1.3157 (1989). DOI: 10.1088/0953-8984/1/20/001.

[114] B. Nikolić and P. B. Allen. «Electron transport through a circular constriction». In: *Phys. Rev. B* 60.6 (1999), p. 3963. DOI: 10.1103/PhysRevB.60.3963.

[115] G Wexler. «The size effect and the non-local Boltzmann transport equation in orifice and disk geometry». In: *Proc. Phys. Soc.* 89.4 (1966), p. 927. DOI: 10.1088/0370-1328/89/4/316.

[116] G. Sheet, S. Mukhopadhyay, and P. Raychaudhuri. «Role of critical current on the point-contact Andreev reflection spectra between a normal metal and a superconductor». In: *Phys. Rev. B* 69.13 (2004), p. 134507. DOI: 10.1103/PhysRevB.69.134507.

[117] P. Samuely et al. «Point contact Andreev reflection spectroscopy of superconducting energy gaps in 122-type family of iron pnictides». In: *Phys. C* 469.9-12 (2009), pp. 507–511. DOI: 10.1016/j.physc.2009.03.037.

[118] P. Szabó et al. «Evidence for two-gap superconductivity in $Ba_{0.55}$ $K_{0.45}Fe_2As_2$ from directional point-contact Andreev-reflection spectroscopy». In: *Phys. Rev. B* 79.1 (2009), p. 012503. DOI: 10.1103/PhysRevB.79.012503.

[119] X. Lu et al. «Superconducting order parameter in nonmagnetic borocarbides $R$$Ni_2B_2C$ (R= Y, Lu) probed by point-contact Andreev reflection spectroscopy». In: *Phys. Rev. B* 83.10 (2011), p. 104519. DOI: 10.1103/PhysRevB.83.104519.

[120] R. S. Gonnelli et al. «Point-contact Andreev-reflection spectroscopy in $ReFeAsO_{1-x}F_x$ (Re= La, Sm): Possible evidence for two nodeless gaps». In: *Phys. C* 469.9-12 (2009), pp. 512–520. DOI: 10.1016/j.physc.2009.03.039.

[121] D. Daghero et al. «Directional point-contact Andreev-reflection spectroscopy of Fe-based superconductors: Fermi surface topology, gap symmetry, and electron–boson interaction». In: *Rep. Prog. Phys.* 74.12 (2011), p. 124509. DOI: 10.1088/0034-4885/74/12/124509.

[122] Y. G. Naidyuk et al. «Superconducting gaps in FeSe studied by soft point-contact Andreev reflection spectroscopy». In: *Phys. Rev. B* 96.9 (2017), p. 094517. DOI: 10.1103/PhysRevB.96.094517.

[123] R. Holm. *Electric contacts: theory and application*. Springer Science & Business Media, 2013.

[124] P. Parab et al. «Critical analysis of soft point contact Andreev reflection spectra between superconducting films and pressed In». In: *J. Phys. Condens. Matter* 29.13 (2017), p. 135901. DOI: 10.1088/1361-648X/aa5bfb.

[125] R. S. Gonnelli et al. «Evidence for gap anisotropy in CaC_6 from directional point-contact spectroscopy». In: *Phys. Rev. Lett.* 100.20 (2008), p. 207004. DOI: 10.1103/PhysRevLett.100.207004.

[126] R. S. Gonnelli et al. «Direct Evidence for Two-Band Superconductivity in MgB_2 Single Crystals from Directional Point-Contact Spectroscopy in Magnetic Fields». In: *Phys. Rev. Lett.* 89.24 (2002), p. 247004. DOI: 10.1103/PhysRevLett.89.247004.

[127] G. E. Blonder, M. Tinkham, and T. M. Klapwijk. «Transition from metallic to tunneling regimes in superconducting microconstrictions: Excess current, charge imbalance, and supercurrent conversion». In: *Phys. Rev. B* 25.7 (1982), p. 4515. DOI: 10.1103/PhysRevB.25.4515.

[128] S. Kashiwaya et al. «Theory for tunneling spectroscopy of anisotropic superconductors». In: *Phys. Rev. B* 53.5 (1996), p. 2667. DOI: 10.1103/PhysRevB.53.2667.

[129] R. C. Dynes, V. Narayanamurti, and J. Garno. «Direct measurement of quasiparticle-lifetime broadening in a strong-coupled superconductor». In: *Phys. Rev. Lett.* 41.21 (1978), p. 1509. DOI: 10.1103/PhysRevLett.41.1509.

[130] A. Plecenik et al. «Finite-quasiparticle-lifetime effects in the differential conductance of $Bi_2Sr_2CaCu_2O_y$/Au junctions». In: *Phys. Rev. B* 49.14 (1994), p. 10016. DOI: 10.1103/PhysRevB.49.10016.

[131] H. Srikanth and A. K. Raychaudhuri. «Modeling tunneling data of normal metal-oxide superconductor point contact junctions». In: *Phys. C: Superconductivity* 190.3 (1992), pp. 229–233. DOI: 10.1016/0921-4534(92)90600-H.

[132] Y. Tanaka, S. Tamura, and J. Cayao. «Theory of Majorana zero modes in unconventional superconductors». In: *Prog. Theor. Exp. Phys.* 2024.8 (2024), p. 08C105. DOI: 10.1093/ptep/ptae065.

[133] H. Pan and S. Das Sarma. «Majorana nanowires, Kitaev chains, and spin models». In: *Phys. Rev. B* 107.3 (2023), p. 035440. DOI: 10.1103/PhysRevB.107.035440.

[134] K. Jiang, X. Dai, and Z. Wang. «Quantum anomalous vortex and Majorana zero mode in iron-based superconductor Fe(Te, Se)». In: *Phys. Rev. X* 9.1 (2019), p. 011033. DOI: 10.1103/PhysRevX.9.011033.

[135] L. Kong et al. «Majorana zero modes in impurity-assisted vortex of LiFeAs superconductor». In: *Nat. Commun.* 12.1 (2021), p. 4146. DOI: 10.1038/s41467-021-24372-6.

[136] K. T. Law, P. A. Lee, and T. K. Ng. «Majorana fermion induced resonant Andreev reflection». In: *Phys. Rev. Lett.* 103.23 (2009), p. 237001. DOI: 10.1103/PhysRevLett.103.237001.

[137] C.-K. Chiu et al. «Scalable Majorana vortex modes in iron-based superconductors». In: *Sci. Adv.* 6.9 (2020), eaay0443. DOI: 10.1126/sciadv.aay0443.

[138] E. J. H. Lee et al. «Zero-bias anomaly in a nanowire quantum dot coupled to superconductors». In: *Phys. Rev. Lett.* 109.18 (2012), p. 186802. DOI: 10.1103/PhysRevLett.109.186802.

[139] M. Ternes et al. «Subgap structure in asymmetric superconducting tunnel junctions». In: *Phys. Rev. B* 74.13 (2006), p. 132501. DOI: 10.1103/PhysRevB.74.132501.

[140] D. I. Pikulin et al. «A zero-voltage conductance peak from weak antilocalization in a Majorana nanowire». In: *New J. Phys.* 14.12 (2012), p. 125011. DOI: 10.1088/1367-2630/14/12/125011.

[141] C. Caroli, P. G. De Gennes, and J. Matricon. «Bound fermion states on a vortex line in a type II superconductor». In: *Phys. Lett.* 9.4 (1964), pp. 307–309. DOI: 10.1016/0031-9163(64)90375-0.

[142] L. Y. L. Shen and J. M. Rowell. «Zero-bias tunneling anomalies—temperature, voltage, and magnetic field dependence». In: *Phys. Rev.* 165.2 (1968), p. 566. DOI: 10.1103/PhysRev.165.566.

[143] C. Chen et al. «Observation of discrete conventional Caroli–de Gennes–Matricon states in the vortex core of single-layer FeSe/$SrTiO_3$». In: *Phys. Rev. Lett.* 124.9 (2020), p. 097001. DOI: 10.1103/PhysRevLett.124.097001.

[144] T. H. Hsieh and L. Fu. «Majorana fermions and exotic surface andreev bound states in topological superconductors: Application to $Cu_xBi_2Se_3$». In: *Phys. Rev. Lett.* 108.10 (2012), p. 107005. DOI: 10.1103/PhysRevLett.108.107005.

[145] F. Yan et al. «Ionic-Liquid-Gating-Induced Hydrogenation in Epitaxial Strontium Ferrite». In: *Adv. Funct. Mater.* (2024), p. 2316608. DOI: 10.1002/adfm.202316608.

[146] G. Prando et al. «Cluster charge-density-wave glass in hydrogen-intercalated $TiSe_2$». In: *Phys. Rev. Materials* 7.9 (2023), p. 094002. DOI: 10.1103/PhysRevMaterials.7.094002.

[147] R. Chu et al. «Electrical control of spin Hall effect in Pt by hydrogen ion adsorption and desorption». In: *ACS nano* 16.10 (2022), pp. 16077–16084. DOI: 10.1021/acsnano.2c04297.

[148] W. Guo et al. «Nonvolatile n-type doping and metallic state in multilayer-MoS_2 induced by hydrogenation using ionic-liquid gating». In: *Nano Letters* 22.22 (2022), pp. 8957–8965. DOI: 10.1021/acs.nanolett.2c03159.

[149] E. Piatti et al. «Ionic liquids for electrochemical applications: Correlation between molecular structure and electrochemical stability window». In: *J. Mol. Liq.* 364 (2022), p. 120001. DOI: 10.1016/j.molliq.2022.120001.

[150] S. S. de Jesus and R. Maciel Filho. «Are ionic liquids eco-friendly?» In: *Renew. Sust. Energ.* 157 (2022), p. 112039. DOI: 10.1016/j.rser.2021.112039.

[151] M. Amde, J.-F. Liu, and L. Pang. «Environmental application, fate, effects, and concerns of ionic liquids: a review». In: *Environ. Sci. Technol.* 49.21 (2015), pp. 12611–12627. DOI: 10.1021/acs.est.5b03123.

[152] S. K. Singh and A. W. Savoy. «Ionic liquids synthesis and applications: An overview». In: *J. Mol. Liq.* 297 (2020), p. 112038. DOI: 10.1016/j.molliq.2019.112038.

[153] M.G. Freire et al. «Hydrolysis of Tetrafluoroborate and Hexafluorophosphate Counter Ions in Imidazolium-Based Ionic Liquids». In: *J. Phys. Chem. A* 114.11 (2010), pp. 3744–3749. DOI: 10.1021/jp903292n.

[154] B. B. Hansen et al. «Deep Eutectic Solvents: A Review of Fundamentals and Applications». In: *Chem. Rev.* 121.3 (2020), pp. 1232–1285. DOI: 10.1021/acs.chemrev.0c00385.

[155] J. Płotka-Wasylka et al. «Deep eutectic solvents *vs* ionic liquids: Similarities and differences». In: *Microchem. J.* 159 (2020), p. 105539. DOI: j.microc.2020.105539.

[156] K. Radošević et al. «Evaluation of toxicity and biodegradability of choline chloride Based deep eutectic solvents». In: *Ecotoxicol. Environ. Saf.* 112 (2015), pp. 46–53. DOI: 10.1016/j.ecoenv.2014.09.034.

[157] S. Khandelwal, Y. K. Tailor, and M. Kumar. «Deep eutectic solvents (DESs) as eco-friendly and sustainable solvent/catalyst systems in organic transformations». In: *J. Mol. Liq.* 215 (2016), pp. 345–386. DOI: 10.1016/j.molliq.2015.12.015.

[158] W. Wang et al. «Choline chloride-based deep eutectic solvents as electrolytes for wide temperature range supercapacitors». In: *J. Energy Storage* 71 (2023), p. 108141. DOI: 10.1016/j.est.2023.108141.

[159] Y. Huang et al. «Synthesis of GO-modified Cu_2O nanosphere and the photocatalytic mechanism of water splitting for hydrogen production». In: *Int. J. Hydrogen Energy* 42.7 (2017), pp. 4007–4016. DOI: 10.1016/j.ijhydene.2016.10.011.

[160] S. Lee et al. «Highly selective transformation of glycerol to dihydroxyacetone without using oxidants by a PtSb/C-catalyzed electrooxidation process». In: *Green Chem.* 18.9 (2016), pp. 2877–2887. DOI: 10.1039/C5GC02865E.

[161] A. Mero et al. «Comparison of physicochemical and thermal properties of choline chloride and betaine-based deep eutectic solvents: The influence of hydrogen bond acceptor and hydrogen bond donor nature and their molar ratios». In: *J. Mol. Liq.* 377 (2023), p. 121563. DOI: 10.1016/j.molliq.2023.121563.

[162] J. E. Schirber and B. Morosin. «Lattice constants of β-PdH_x and β-PdD_x with x near 1.0». In: *Phys. Rev. B* 12.1 (1975), p. 117. DOI: 10.1103/PhysRevB.12.117.

[163] T. B. Flanagan and F. A. Lewis. «Relationships between Electrical Resistance and the Hydrogen Content of Palladium». In: *Z. Phys. Chem.* 27 (1961), pp. 104–111. DOI: 10.1524/zpch.1961.27.1_2.104.

[164] J. C. Barton and F. A. Lewis. «Overvoltage and the Hydrogen Content of Palladium Cathodes». In: *Z. Phys. Chem.* 33 (1962), pp. 99–110. DOI: 10.1524/zpch.1962.33.1_4.099.

[165] H. Araki et al. «Phase diagram of hydrogen in palladium». In: *J. Low Temp. Phys.* 134 (5 2004), pp. 1145–1151. DOI: 10.1023/B:JOLT.0000016734.40467.28.

[166] R. J. Smith and D. A. Otterson. «Electrical resistivity of PdH_x system for H/Pd atom ratios to $0 \cdot 97$». In: *J. Phys. Chem. Solids* 31 (1 1970), pp. 187–189. DOI: 10.1016/0022-3697(70)90300-8.

[167] A. Mero et al. «Sustainable valorization of cherry (*Prunus avium L.*) pomace waste via the combined use of (NA) DESs and bio-ILs». In: *Green Chem.* 26.10 (2024), pp. 6109–6123. DOI: 10.1039/D4GC00526K.

[168] J. A. Wilson and A. D. Yoffe. «The transition metal dichalcogenides discussion and interpretation of the observed optical, electrical and structural properties». In: *Adv. Phys.* 18.73 (1969), pp. 193–335. DOI: 10.1080/00018736900101307.

[169] S. Manzeli et al. «2D transition metal dichalcogenides». In: *Nat. Rev. Mater.* 2.8 (2017), p. 17033. DOI: 10.1038/natrevmats.2017.33.

[170] W. Choi et al. «Recent development of two-dimensional transition metal dichalcogenides and their applications». In: *Mater. Today* 20.3 (2017), pp. 116–130. DOI: 10.1016/j.mattod.2016.10.002.

[171] Y. W. Li et al. «Observation of topological superconductivity in a stoichiometric transition metal dichalcogenide $2M$-WS_2». In: *Nat. Commun.* 12.1 (2021), p. 2874. DOI: 10.1038/s41467-021-23076-1.

[172] A. F. Kusmartseva et al. «Pressure Induced Superconductivity in Pristine $1T$-$TiSe_2$». In: *Phys. Rev. Lett.* 103.23 (2009), p. 236401. DOI: 10.1103/PhysRevLett.103.236401.

[173] K. Sato et al. «New Lithium- and Diamines-Intercalated Superconductors $Li_x(C_2H_8N_2)_yTiSe_2$ and $Li_x(C_6H_{16}N_2)_yTiSe_2$». In: *J. Phys. Soc. Jpn.* 86.10 (2017), p. 104701. DOI: https://doi.org/10.7566/JPSJ.86.104701.

[174] C. Heil et al. «Origin of superconductivity and latent charge density wave in NbS_2». In: *Phys. Rev. Lett.* 119.8 (2017), p. 087003. DOI: 10.1103/PhysRevLett.119.087003.

[175] A. Sanna et al. «Real-space anisotropy of the superconducting gap in the charge-density wave material 2*H*-$NbSe_2$». In: *npj Quantum Mater.* 7.1 (2022), p. 6. DOI: 10.1038/s41535-021-00412-8.

[176] I. Guillamón et al. «Superconducting density of states and vortex cores of 2*H*-NbS_2». In: *Phys. Rev. Lett.* 101.16 (2008), p. 166407. DOI: 10.1103/PhysRevLett.101.166407.

[177] J. Kačmarčík et al. «Studies on two-gap superconductivity in 2*H*-NbS_2». In: *Phys. C: Supercond. Appl.* 470 (2010), S719–S720. DOI: 10.1016/j.physc.2009.10.131.

[178] T. Yokoya et al. «Fermi surface sheet-dependent superconductivity in 2*H*-$NbSe_2$». In: *Science* 294.5551 (2001), pp. 2518–2520. DOI: 10.1126/science.1065068.

[179] E. Boaknin et al. «Heat Conduction in the Vortex State of $NbSe_2$: Evidence for Multiband Superconductivity». In: *Phys. Rev. Lett.* 90.11 (2003), p. 117003. DOI: 10.1103/PhysRevLett.90.117003.

[180] I. Guillamon et al. «Intrinsic atomic-scale modulations of the superconducting gap of 2*H*-$NbSe_2$». In: *Phys. Rev. B* 77.13 (2008), p. 134505. DOI: 10.1103/PhysRevB.77.134505.

[181] D. J. Rahn et al. «Gaps and kinks in the electronic structure of the superconductor 2*H*-$NbSe_2$ from angle-resolved photoemission at 1 K». In: *Phys. Rev. B* 85.22 (2012), p. 224532. DOI: 10.1103/PhysRevB.85.224532.

[182] Y. Noat et al. «Quasiparticle spectra of 2*H*-$NbSe_2$: Two-band superconductivity and the role of tunneling selectivity». In: *Phys. Rev. B* 92.13 (2015), p. 134510. DOI: 10.1103/PhysRevB.92.134510.

[183] E. Piatti et al. «Direct evidence for two-gap superconductivity in hydrogen-intercalated titanium diselenide». In: *Mater. Today Phys.* 95 (2025), p. 101883. DOI: 10.1016/j.mtphys.2025.101883.

[184] Y. Saito, T. Nojima, and Y. Iwasa. «Quantum phase transitions in highly crystalline two-dimensional superconductors». In: *Nat. Commun.* 9.1 (2018), p. 778. DOI: 10.1038/s41467-018-03275-z.

[185] L. Li et al. «Anomalous quantum metal in a 2D crystalline superconductor with electronic phase nonuniformity». In: *Nano Lett.* 19.6 (2019), pp. 4126–4133. DOI: 10.1021/acs.nanolett.9b01574.

[186] B. L. Altshuler, A. G. Aronov, and P. A. Lee. «Interaction effects in disordered Fermi systems in two dimensions». In: *Phys. Rev. Lett.* 44.19 (1980), p. 1288. DOI: 10.1103/PhysRevLett.44.1288.

[187] H. Fukuyama. *Electron–Electron Interactions in Disordered Systems*. Ed. by A. L. Efros and M. Pollak. Amsterdam: North Holland, 1985.

[188] R. Bianco, M. Calandra, and F. Mauri. «Electronic and vibrational properties of $TiSe_2$ in the charge-density-wave phase from first principles». In: *Phys. Rev. B* 92.9 (2015), p. 094107. DOI: 10.1103/PhysRevB.92.094107.

[189] T. Rohwer et al. «Collapse of long-range charge order tracked by time-resolved photoemission at high momenta». In: *Nature* 471.7339 (2011), pp. 490–493. DOI: 10.1038/nature09829.

[190] G. Blatter et al. «Vortices in high-temperature superconductors». In: *Rev. Mod. Phys.* 66.4 (1994), p. 1125. DOI: 10.1103/RevModPhys.66.1125.

[191] N. A. Lewellyn et al. «Infinite-randomness fixed point of the quantum superconductor-metal transitions in amorphous thin films». In: *Phys. Rev. B* 99.5 (2019), p. 054515. DOI: 10.1103/PhysRevB.99.054515.

[192] X. Wang et al. «Robust quantum Griffiths singularity above 1.5 K in nitride thin films». In: *Phys. Rev. B* 107 (2023), p. 094509. DOI: 10.1103/PhysRevB.107.094509.

[193] P. Berghuis and P. H. Kes. «Two-dimensional collective pinning and vortex-lattice melting in a-$Nb_{1-x}Ge_x$ films». In: *Phys. Rev. B* 47.1 (1993), p. 262. DOI: 10.1103/PhysRevB.47.262.

[194] M. H. Theunissen and P. H. Kes. «Resistive transitions of thin film superconductors in a magnetic field». In: *Phys. Rev. B* 55.22 (1997), p. 15183. DOI: 10.1103/PhysRevB.55.15183.

[195] S. Ullah and A. T. Dorsey. «Critical fluctuations in high-temperature superconductors and the Ettingshausen effect». In: *Phys. Rev. Lett.* 65.16 (1990), p. 2066. DOI: 10.1103/PhysRevLett.65.2066.

[196] M. Tinkham. «Effect of fluxoid quantization on transitions of superconducting films». In: *Phys. Rev.* 129.6 (1963), p. 2413. DOI: 10.1103/PhysRev.129.2413.

[197] G. Dezi et al. «Negative electronic compressibility and nanoscale inhomogeneity in ionic-liquid gated two-dimensional superconductors». In: *Phys. Rev. B* 98.21 (2018), p. 214507. DOI: 10.1103/PhysRevB.98.214507.

[198] G. Venditti et al. «Nonlinear I-V characteristics of two-dimensional superconductors: Berezinskii-Kosterlitz-Thouless physics versus inhomogeneity». In: *Phys. Rev. B* 100.6 (2019), p. 064506. DOI: 10.1103/PhysRevB.100.064506.

[199] Y. Xing et al. «Extrinsic and intrinsic anomalous metallic states in transition metal dichalcogenide Ising superconductors». In: *Nano Lett.* 21.18 (2021), pp. 7486–7494. DOI: 10.1021/acs.nanolett.1c01426.

[200] A. Gurevich. «Enhancement of the upper critical field by nonmagnetic impurities in dirty two-gap superconductors». In: *Phys. Rev. B* 67.18 (2003), p. 184515. DOI: 10.1103/PhysRevB.67.184515.

[201] X. Xing et al. «Two-band and Pauli-limiting effects on the upper critical field of 112-type iron pnictide superconductors». In: *Sci. Rep.* 7.1 (2017), p. 45943. DOI: 10.1038/srep45943.

[202] D. Ding et al. «Multivalley Superconductivity in Monolayer Transition Metal Dichalcogenides». In: *Nano Lett.* 22 (2022), pp. 7919–7926. DOI: 10.1021/acs.nanolett.2c02947.

[203] R. S. Gonnelli et al. «Magnetic-field dependence of the gaps in a two-band superconductor: A point-contact study of MgB_2 single crystals». In: *Phys. Rev. B* 69.10 (2004), 100504(R). DOI: 10.1103/PhysRevB.69.100504.

[204] D. Daghero et al. «Superconductivity of underdoped PrFeAs(O,F) investigated via point-contact spectroscopy and nuclear magnetic resonance». In: *Phys. Rev. B* 102.10 (2020), p. 104513. DOI: 10.1103/PhysRevB.102.104513.

[205] D. Torsello et al. «Nodal multigap superconductivity in the anisotropic iron-based compound $RbCa_2Fe_4As_4F_2$». In: *npj Quantum Materials* 7.1 (2022), pp. 1–7. DOI: 10.1038/s41535-021-00419-1.

[206] T. Y. Chen, S. X. Huang, and C. L. Chien. «Pronounced effects of additional resistance in Andreev reflection spectroscopy». In: *Phys. Rev. B* 81 (21 2010), p. 214444. DOI: 10.1103/PhysRevB.81.214444.

[207] S. Döring et al. «Influence of the spreading resistance on the conductance spectrum of planar hybrid thin film SNS' junctions based on iron pnictides». In: *J. Phys. Conf. Ser.* 507.1 (2014), p. 012008. DOI: 10.1088/1742-6596/507/1/012008.

[208] D. Daghero et al. «A model for critical current effects in point-contact Andreev-reflection spectroscopy». In: *Low Temp. Phys.* 49 (2023), pp. 886–892. DOI: 10.1063/10.0019702.

[209] K. Zhao et al. «Disorder-induced multifractal superconductivity in monolayer niobium dichalcogenides». In: *Nat. Phys.* 15.9 (2019), pp. 904–910. DOI: 10.1038/s41567-019-0570-0.

[210] H. Suhl, B.T. Matthias, and L. R. Walker. «Bardeen-Cooper-Schrieffer theory of superconductivity in the case of overlapping bands». In: *Phys. Rev. Lett.* 3.12 (1959), p. 552. DOI: 10.1103/PhysRevLett.3.552.

[211] G. A. Ummarino et al. «Three-band s±Eliashberg theory and the superconducting gaps of iron pnictides». In: *Phys. Rev. B* 80.17 (2009), p. 172503. DOI: 10.1103/PhysRevB.80.172503.

[212] G. A. Ummarino et al. «Two-band Eliashberg equations and the experimental T_c of the diboride $Mg_{1-x}Al_xB_2$». In: *Phys. C: Supercond. Appl.* 407 (2004), pp. 121–127. DOI: 10.1016/j.physc.2004.05.009.

[213] D. Torsello et al. «Analysis of the London penetration depth in Ni-doped $CaKFe_4As_4$». In: *Phys. Rev. B* 100.9 (2019), p. 094513. DOI: 10.1103/PhysRevB.100.094513.

[214] N.V. Baranov et al. «Ni intercalation of titanium diselenide: effect on the lattice, specific heat and magnetic properties». In: *J. Condens. Matter Phys.* 16.50 (2004), p. 9243. DOI: 10.1088/0953-8984/16/50/014.

[215] R.C. Dynes. «McMillan's equation and the T_c of superconductors». In: *Solid State Commun.* 10.7 (1972), pp. 615–618. DOI: 10.1016/0038-1098(72)90603-5.

[216] J.P. Carbotte. «Properties of boson-exchange superconductors». In: *Rev. Mod. Phys.* 62.4 (1990), p. 1027. DOI: 10.1103/RevModPhys.62.1027.

[217] G. Ghigo et al. «Penetration depth of $Ba_{1-x}K_xFe_2As_2$ single crystals explained within a multiband Eliashberg s±approach». In: *Phys. Rev. B* 96.1 (2017), p. 014501. DOI: 10.1103/PhysRevB.96.014501.

[218] G.A. Ummarino and R.S. Gonnelli. «Breakdown of Migdal's theorem and intensity of electron-phonon coupling in high-T_c superconductors». In: *Phys. Rev. B* 56.22 (1997), R14279. DOI: 10.1103/PhysRevB.56.R14279.

[219] M Mansor and J P Carbotte. «Upper critical field in two-band superconductivity». In: *Phys. Rev. B* 72.2 (2005), p. 024538. DOI: 10.1103/PhysRevB.72.024538.

[220] G. A. Ummarino et al. «Predictions of multiband s±strong-coupling Eliashberg theory compared to experimental data in iron pnictides». In: *J. Supecond. Novel Magn.* 24 (2011), pp. 247–253. DOI: 10.1007/s10948-010-1006-3.

[221] P. Knowles et al. «Fermi surface reconstruction and electron dynamics at the charge-density-wave transition in $TiSe_2$». In: *Phys. Rev. Lett.* 124.16 (2020), p. 167602. DOI: 10.1103/PhysRevLett.124.167602.

[222] M. D. Watson et al. «Orbital-and k_z-selective hybridization of Se 4p and Ti 3d states in the charge density wave phase of $TiSe_2$». In: *Phys. Rev. Lett.* 122.7 (2019), p. 076404. DOI: 10.1103/PhysRevLett.122.076404.

[223] J. Jeong et al. «Electronic structure study of Cu-doped 1T-$TiSe_2$ by angle-resolved photoemission spectroscopy». In: *Phys. C: Supercond. Appl.* 470 (2010), S648–S650. DOI: 10.1016/j.physc.2009.11.123.

[224] E. Piatti et al. «Multi-valley superconductivity in ion-gated MoS_2 layers». In: *Nano Lett.* 18.8 (2018), pp. 4821–4830. DOI: 10.1021/acs.nanolett.8b01390.

[225] H. Zhang et al. «Band filling and cross quantum capacitance in ion-gated semiconducting transition metal dichalcogenide monolayers». In: *Nano Lett.* 19.12 (2019), pp. 8836–8845. DOI: 10.1021/acs.nanolett.9b03667.

[226] E. Piatti, D. Romanin, and R. S. Gonnelli. «Mapping multi-valley Lifshitz transitions induced by field-effect doping in strained MoS_2 nanolayers». In: *J. Phys. Condens. Matter* 31.11 (2019), p. 114002. DOI: 10.1088/1361-648X/aaf981.

[227] H. Lind and S. Lidin. «A general structure model for Bi-Se phases using a superspace formalism». In: *Solid State Sci.* 5.1 (2003), pp. 47–57. DOI: 10.1016/S1293-2558(02)00080-8.

[228] Y. S. Hor et al. «Superconductivity in $Cu_xBi_2Se_3$ and its Implications for Pairing in the Undoped Topological Insulator». In: *Phys. Rev. Lett.* (2010). DOI: 10.1103/PhysRevLett.104.057001.

[229] L. A. Wray et al. «Observation of topological order in a superconducting doped topological insulator». In: *Nat. Phys.s* 6.11 (2010), pp. 855–859. DOI: 10.1038/nphys1762.

[230] M. Wang et al. «A combined method for synthesis of superconducting Cu doped Bi_2Se_3». In: *Sci. Rep.* 6.1 (2016), p. 22713. DOI: 10.1038/srep22713.

[231] Y. Fang, W.-L. You, and M. Li. «Unconventional superconductivity in $Cu_xBi_2Se_3$ from magnetic susceptibility and electrical transport». In: *New J. Phys.* 22.5 (2020), p. 053026. DOI: 10.1088/1367-2630/ab7fca.

[232] S. Yonezawa. «Nematic superconductivity in doped Bi_2Se_3 topological superconductors». In: *Condensed Matter* 4.1 (2018), p. 2. DOI: 10.3390/condmat4010002.

[233] M. Kriener et al. «Electrochemical synthesis and superconducting phase diagram of $Cu_xBi_2Se_3$». In: *Phys. Rev. B.* 84.5 (2011), p. 054513. DOI: 10.1103/PhysRevB.84.054513.

[234] M. Kriener et al. «Bulk Superconducting Phase with a Full Energy Gap in the Doped Topological Insulator $Cu_xBi_2Se_3$». In: *Phys. Rev. Lett.* 106.12 (2011), p. 127004. DOI: 10.1103/PhysRevLett.106.127004.

[235] M. Bagchi, J. Brede, and Y. Ando. «Observability of superconductivity in Sr-doped Bi_2Se_3 at the surface using scanning tunneling microscope». In: *Phys. Rev. Mat.* 6.3 (2022), p. 034201. DOI: 10.1103/PhysRevMaterials.6.034201.

[236] Y.-R. Lin et al. «Vertical position of Sr dopants in the $Sr_xBi_2Se_3$ superconductor». In: *Phys. Rev. B* 104.5 (2021), p. 054506. DOI: 10.1103/PhysRevB.104.054506.

[237] Y. Qiu et al. «Time reversal symmetry breaking superconductivity in topological materials». In: *arXiv preprint arXiv:1512.03519* (2015).

[238] D. Das et al. «Time-reversal invariant and fully gapped unconventional superconducting state in the bulk of the topological compound $Nb_{0.25}Bi_2Se_3$». In: *Phys. Rev. B* 102.13 (2020), p. 134514. DOI: 10.1103/PhysRevB.102.134514.

[239] S. M. Kevy et al. «Structural and electronic inhomogeneity of superconducting Nb-doped Bi_2Se_3». In: *Phys. Rev. B* 103.8 (2021), p. 085107.

[240] G. Du et al. «Superconductivity with two-fold symmetry in topological superconductor $Sr_xBi_2Se_3$». In: *Sci. China Physics Mech. Astronomy.* 60.3 (2017), p. 037411. DOI: 10.1007/s11433-016-0499-x.

[241] W. H. Jiao et al. «Growth and characterization of Bi_2Se_3 crystals by chemical vapor transport». In: *AIP Adv.* 2.2 (2012). DOI: 10.1063/1.4727957.

[242] Y. S. Hor et al. «p-type Bi_2Se_3 for topological insulator and low-temperature thermoelectric applications». In: *Phys. Rev. B* 79.19 (2009), p. 195208. DOI: 10.1103/PhysRevB.79.195208.

[243] T. Plecháček, J. Navratil, and J. Horak. «Free current carrier concentration and point defects in $Bi_{2-x}Sb_xSe_3$ crystals». In: *J. Solid State Chem.* 165.1 (2002), pp. 35–41. DOI: 10.1006/jssc.2001.9486.

[244] M. Busch et al. «High-temperature quantum oscillations of the Hall resistance in bulk Bi_2Se_3». In: *Sci. Rep.* 8.1 (2018), p. 485. DOI: 10.1038/s41598-017-18960-0.

[245] R. T. Paulino and M. A. Avila. «Bulk conducting states of intrinsically doped Bi_2Se_3». In: *J. Phys. Chem. C* 128.9 (2024), pp. 3885–3893. DOI: 10.1021/acs.jpcc.3c05533.

[246] O. Chiatti et al. «2D layered transport properties from topological insulator Bi2Se3 single crystals and micro flakes». In: *Sci. Rep.* 6.1 (2016), pp. 1–11. DOI: 10.1038/srep27483.

[247] H. Cao et al. «Structural and electronic properties of highly doped topological insulator Bi_2Se_3 crystals». In: *Phys. Status Solidi RRL* 7.1-2 (2013), pp. 133–135. DOI: 10.1002/pssr.201206457.

[248] J. Shiogai et al. «Electric-field-induced superconductivity in electrochemically etched ultrathin FeSe films on $SrTiO_3$ and MgO». In: *Nature Phys.* 12.1 (2016), pp. 42–46. DOI: 10.1038/nphys3530.

[249] F. B. Meng et al. «Metal-insulator transition in organic ion intercalated VSe_2 induced by dimensional crossover». In: *Phys. Rev. B* 102.16 (2020), p. 165410. DOI: 10.1103/PhysRevB.102.165410.

[250] C. Wang et al. «Thorium-doping–induced superconductivity up to 56 K in $Gd_{1-x}Th_xFeAsO$». In: *Europhys. Lett.* 83.6 (2008), p. 67006. DOI: 10.1209/0295-5075/83/67006.

[251] F.-C. Hsu et al. «Superconductivity in the PbO-type structure α-FeSe». In: *PNAS* 105.38 (2008), pp. 14262–14264. DOI: 10.1073/pnas.0807325105.

[252] S. Medvedev et al. «Electronic and magnetic phase diagram of β-$Fe_{1.01}Se$ with superconductivity at 36.7 K under pressure». In: *Nat. Mater* 8.8 (2009), pp. 630–633. DOI: 10.1038/nmat2491.

[253] J. Zhuang et al. «Unabridged phase diagram for single-phased $FeSe_xTe_{1-x}$ thin films». In: *Sci. Rep.* 4.1 (2014), p. 7273. DOI: 10.1038/srep07273.

[254] M. Z. Shi et al. «FeSe-based superconductors with a superconducting transition temperature of 50 K». In: *New J. Phys.* 20.12 (2018), p. 123007. DOI: 10.1088/1367-2630/aaf312.

[255] A. Kreisel, P. J. Hirschfeld, and B. M. Andersen. «On the remarkable superconductivity of FeSe and its close cousins». In: *Symmetry* 12.9 (2020), p. 1402. DOI: 10.3390/sym12091402.

[256] X. Liu et al. «Electronic structure and superconductivity of FeSe-related superconductors». In: *J. Condens. Matter Phys.* 27.18 (2015), p. 183201. DOI: 10.1088/0953-8984/27/18/183201.

[257] P. D. Johnson et al. «Spin-orbit interactions and the nematicity observed in the Fe-based superconductors». In: *Phys. Rev. Lett.* 114.16 (2015), p. 167001. DOI: 10.1103/PhysRevLett.114.167001.

[258] Y.-F. Li et al. «Orbital ingredients and persistent Dirac surface state for the topological band structure in $FeTe_{0.55}Se_{0.45}$». In: *Phys. Rev. X* 14.2 (2024), p. 021043. DOI: 10.1103/PhysRevX.14.021043.

[259] N. Zaki et al. «Time-reversal symmetry breaking in the Fe-chalcogenide superconductors». In: *PNAS* 118.3 (2021), e2007241118. DOI: 10.1073/pnas.2007241118.

[260] X. Wu et al. «Topological orders competing for the Dirac surface state in FeSeTe surfaces». In: *Phys. Rev. Research* 3.1 (2021), p. 013066. DOI: 10.1103/PhysRevResearch.3.013066.

[261] S. V. Borisenko et al. «Direct observation of spin-orbit coupling in iron-based superconductors». In: *Nature Phys.* 12.4 (2016), pp. 311–317. DOI: 10.1038/nphys3594.

[262] T. Hanaguri et al. «Unconventional s-wave superconductivity in Fe(Se, Te)». In: *Science* 328.5977 (2010), pp. 474–476. DOI: 10.1126/science.1187399.

[263] G. E. Volovik. «Fermion zero modes on vortices in chiral superconductors». In: *JETP Letters* 70.9 (1999), pp. 609–614. DOI: 10.3390/sym12091402.

[264] S. Rinott et al. «Tuning across the BCS-BEC crossover in the multiband superconductor $Fe_{1+y}Se_xTe_{1-x}$: An angle-resolved photoemission study». In: *Sci. Adv.* 3.4 (2017), e1602372. DOI: 10.1126/sciadv.1602372.

[265] T. Machida and T. Hanaguri. «Searching for Majorana quasiparticles at vortex cores in iron-based superconductors». In: *Prog. Theor. Exp. Phys.* 2024.8 (2024), p. 08C103. DOI: 10.1093/ptep/ptad084.

[266] S. Zhu et al. «Nearly quantized conductance plateau of vortex zero mode in an iron-based superconductor». In: *Science* 367.6474 (2020), pp. 189–192. DOI: 10.1126/science.aax0274.

[267] E. Bellingeri et al. «High quality epitaxial $FeSe_{0.5}Te_{0.5}$ thin films grown on $SrTiO_3$ substrates by pulsed laser deposition». In: *Supercond. Sci. Technol.* 22.10 (2009), p. 105007. DOI: 10.1088/0953-2048/22/10/105007.

[268] E. Bellingeri et al. «T_c= 21 K in epitaxial $FeSe_{0.5}Te_{0.5}$ thin films with biaxial compressive strain». In: *Appl. Phys. Lett.* 96.10 (2010). DOI: 10.1063/1.3358148.

[269] P. Yuan et al. «High performance $FeSe_{0.5}Te_{0.5}$ thin films grown at low temperature by pulsed laser deposition». In: *Supercond. Sci. Technol.* 28.6 (2015), p. 065009. DOI: 10.1088/0953-2048/28/6/065009.

[270] D. Daghero et al. «Point-contact Andreev-reflection spectroscopy in Fe(Te, Se) films: multiband superconductivity and electron-boson coupling». In: *Supercond. Sci. Technol.* 27.124014 (2014). DOI: 10.1088/0953-2048/27/12/124014.

[271] M. Tortello et al. «Multigap superconductivity and strong electron-boson coupling in Fe-based superconductors: a point-contact Andreev-reflection study of $Ba(Fe_{1-x}Co_x)_2As_2$ single crystals». In: *Phys. Rev. Lett.* 105.23 (2010), p. 237002. DOI: 10.1103/PhysRevLett.105.237002.

[272] Y. Yang et al. «Comparison of band structure and superconductivity in $FeSe_{0.5}Te_{0.5}$ and FeS». In: *Chin. Phys. B* 26.12 (2017), p. 127401. DOI: 10.1088/1674-1056/26/12/127401.

[273] H. Miao et al. «Isotropic superconducting gaps with enhanced pairing on electron Fermi surfaces in $FeTe_{0.55}Se_{0.45}$». In: *Phys. Rev. B Condens.* 85.9 (2012), p. 094506. DOI: 10.1103/PhysRevB.85.094506.

[274] J. Paglione and R. L. Greene. «High-temperature superconductivity in iron-based materials». In: *Nat. Phys.* 6.9 (2010), pp. 645–658. DOI: 10.1038/nphys1759.

[275] Y. Qiu et al. «Spin gap and resonance at the nesting wave vector in superconducting $FeSe_{0.4}Te_{0.6}$». In: *Phys. Rev. Lett.* 103.6 (2009), p. 067008. DOI: 10.1103/PhysRevLett.103.067008.

[276] D. S. Inosov et al. «Normal-state spin dynamics and temperature-dependent spin-resonance energy in optimally doped $BaFe_{1.85}Co_{0.15}As_2$». In: *Nat. Phys.* 6.3 (2010), pp. 178–181. DOI: 10.1038/nphys1483.

[277] G. Yu et al. «Universal relation between magnetic resonance and superconducting gap in unconventional superconductors». In: *Nat. Phys.* 5 (2009), pp. 873–875. DOI: 10.1038/nphys1426.

[278] G. Rastogi et al. «Emergent *p*-Wave Superconductivity in a Dual Topological Insulator BiSe via Superconducting Proximity Effect». In: *ACS Appl. Mater. Interfaces* 17.5 (2025), pp. 8456–8463. DOI: 10.1021/acsami.4c15770.

[279] C. Tarantini et al. «Significant enhancement of upper critical fields by doping and strain in iron-based superconductors». In: *Phys. Rev. B— Cond. Matter.* 84.18 (2011), p. 184522. DOI: 10.1103/PhysRevB.84.184522.

[280] F. D. Manchester, A. San-Martin, and J. M. Pitre. «The H-Pd (hydrogen-palladium) system». In: *JPE* 15.1 (1994), pp. 62–83. DOI: 10.1007/BF02667685.

[281] W.-S. Zhang, Z.-F. Zhang, and Z.-L. Zhang. «Some problems on the resistance method in the in situ measurement of hydrogen content in palladium electrode». In: *J. Electroanal. Chem.* 528.1 (2002), pp. 1–17. DOI: 10.1016/S0022-0728(02)00845-8.

[282] R.J. Miller and C.B. Satterthwaite. «Electronic model for the reverse isotope effect in superconducting Pd-H (D)». In: *Phys. Rev. Lett.* 34.3 (1975), p. 144. DOI: 10.1103/PhysRevLett.34.144.

[283] J. M. E. Harper. «Effect of hydrogen concentration on superconductivity and clustering in palladium hydride». In: *Phys. Lett. A* 47.1 (1974), pp. 69–70. DOI: 10.1016/0375-9601(74)90110-8.

[284] N. S. Ho and F. D. Manchester. «The electrical resistivity of palladium–hydrogen and palladium–deuterium alloys between 4 and 300 K». In: *Can. J. Phys.* 46.11 (1968), pp. 1341–1345. DOI: 10.1139/p68-454.

[285] P. Mitacek and John G. Aston. «The Thermodynamic Properties of Pure Palladium and its Alloys with Hydrogen between 30 and 300°K.» In: *J. Am. Chem. Soc.* 85.2 (1963), pp. 137–141. DOI: 10.1021/ja00885a005.

[286] D. M. Nace and J. G. Aston. «Palladium Hydride. III. Thermodynamic Study of Pd_2D from 15 to 303° K. Evidence for the Tetrahedral PdH_4 Structure in Palladium Hydride». In: *J. Am. Chem. Soc.* 79.14 (1957), pp. 3627–3633. ISSN: 0002-7863. DOI: 10.1021/ja01571a003.

[287] J. K. Jacobs et al. «The '50 K' transition in palladium-hydrogen alloys. I. Internal friction». In: *J. Phys. F Met. Phys.* 6.12 (1976), p. 2219. DOI: 10.1088/0305-4608/6/12/008.

[288] J. K. Jacobs and F. D. Manchester. «The '50 K' transition in palladium hydrogen alloys. II. Specific heat and thermal relaxation». In: *J. Phys. F Met. Phys.* 7.1 (1977), p. 23. DOI: 10.1088/0305-4608/7/1/013.

[289] O. Blaschko. «Fermi-surface imaging effect in the D short-range order of PdD_x». In: *Phys. Rev. B* 29 (9 1984), pp. 5187–5189. DOI: 10.1103/PhysRevB.29.5187.

[290] S. S. Setayandeh, C. J. Webb, and E. MacA. Gray. «Electron and phonon band structures of palladium and palladium hydride: A review». In: *Prog. Solid State Chem.* 60 (2020), p. 100285. ISSN: 0079-6786. DOI: 10.1016/j.progsolidstchem.2020.100285.

[291] H. Akiba et al. «Glass transition and positional ordering of hydrogen in bulk and nanocrystalline palladium». In: *Phys. Rev. B* 92 (6 2015), p. 064202. DOI: 10.1103/PhysRevB.92.064202.

[292] T. Skośkiewicz. «Superconductivity in the palladium-hydrogen system». In: *Phys. Status Solidi B.* 59.1 (1973), pp. 329–334. DOI: 10.1002/pssb.2220590133.

[293] R. W. Standley, M. Steinback, and C. B. Satterthwaite. «Superconductivity in $PdH_x(D_x)$ from 0.2 K to 4 K». In: *Solid State Commun.* 31.11 (1979), pp. 801–804. DOI: 10.1016/0038-1098(79)90391-0.

[294] T. Skoskiewicz. «Superconductivity in the palladium-hydrogen and palladium-nickel-hydrogen systems». In: *Phys. Status Solidi A.* 11.2 (1972), K123–K126. DOI: 10.1002/pssa.2210110253.

[295] F. Ochmann and B. Stritzker. «Superconductivity of simple metal-hydrogen systems produced by ion implantation». In: *NIM* 209 (1983), pp. 831–834. DOI: 10.1016/0167-5087(83)90887-6.

[296] B. Stritzker and W. Buckel. «Superconductivity in the palladium-hydrogen and the palladium-deuterium systems». In: *Z. Phys. A* 257.1 (1972), pp. 1–8. DOI: 10.1007/BF01398191.

[297] D. R. Krahn et al. «The critical fields of superconducting palladium hydride». In: *Phys. Status Solidi A.* 46.1 (1978), pp. 209–212. DOI: 10.1002/pssa.2210460125.

[298] A. Stern, A. Resnik, and D. Shaltiel. «Thermal desorption spectra of the PdH_x system in a powder form». In: *J. Phys. F: Met. Phys.* 14.7 (1984), p. 1625. DOI: 10.1088/0305-4608/14/7/012.

[299] B. Stritzker. «High superconducting transition temperatures in the palladium-noble metal-hydrogen system». In: *Z. Phys.* 268.2 (1974), pp. 261–264. DOI: 10.1007/BF01669889.

[300] R. Vocaturo et al. «Prediction of ambient-pressure superconductivity in ternary hydride $PdCuH_x$». In: *J. Appl. Phys.* 131.3 (2022). DOI: 10.1063/5.0076728.

[301] Q. Li et al. «The electrochemical stability of ionic liquids and deep eutectic solvents». In: *Sci. China Chem.* 59.5 (2016), pp. 571–577. DOI: 10.1007/s11426-016-5566-3.

[302] N. S. Sinclair et al. «Electrochemical decomposition of primary alcohol groups in deep eutectic solvents». In: *J. Electrochem. Soc.* 168.10 (2021), p. 106506. DOI: 10.1149/1945-7111/ac2d14.

[303] Scholtz F. *Electroanalytical Methods.* Springer-Verlag, Berlin Heidelberg, 2010.

[304] S. Wagner and A. Pundt. «Electrical resistivity and hydrogen solubility of PdH_c thin films». In: *Acta Mater.* 58.4 (2010), pp. 1387–1394. DOI: 10.1016/j.actamat.2009.10.045.

[305] M. Lee and R. Glosser. «Resistivity of Thin Films of the Palladium-Hydrogen System as a Function of Film Thickness». In: *Z. Phys. Chem.* 147 (1986), pp. 27–32. DOI: 10.1524/zpch.1986.147.1_2.027.

[306] D. Daghero et al. «Large conductance modulation of gold thin films by huge charge injection via electrochemical gating». In: *Phys. Rev. Lett.* 108.6 (2012), p. 066807. DOI: 10.1103/PhysRevLett.108.066807.

[307] E. Piatti. «Ionic gating in metallic superconductors: A brief review». In: *Nano Express* 2.2 (2021), p. 024003. DOI: 10.1088/2632-959X/ac011d.

[308] E. Piatti et al. «Reversible tuning of superconductivity in ion-gated NbN ultrathin films by self-encapsulation with a high-κ dielectric layer». In: *Phys. Rev. Appl.* 18.5 (2022), p. 054023. DOI: 10.1103/PhysRevApplied.18.054023.

[309] E. Piatti et al. «Control of bulk superconductivity in a BCS superconductor by surface charge doping via electrochemical gating». In: *Phys. Rev. B* 95.14 (2017), p. 140501. DOI: 10.1103/PhysRevB.95.140501.

[310] R. A. Matula. «Electrical resistivity of copper, gold, palladium, and silver». In: *J. Phys. Chem. Ref. Data* 8.4 (1979), pp. 1147–1298. DOI: 10.1103/PhysRevB.95.140501.

[311] K. Baba et al. «Electrical resistivity changes due to interstitial hydrogen in palladium-rich substitutional alloys». In: *J. Mater. Sci.* 25.9 (1990), pp. 3910–3916. DOI: 10.1103/PhysRevB.95.140501.

[312] A. Satrapinski et al. «Temperature dependence of Pd thin-film cryoresistors». In: *IEEE Trans. Instrum. Meas.* 60.7 (2011), pp. 2469–2474. DOI: 10.1109/TIM.2011.2139290.

[313] M. Horobiowski, T. Skośkiewicz, and E. Trojnar. «Magnetization of the superconducting palladium hydrides». In: *Phys. Status Solidi B* 79.2 (1977), K147–K150. DOI: 10.1002/pssb.2220790260.

[314] L. E. Sansores, J. Tagüeña-Martínez, and A. M. Sanchez. «The specific heat and critical magnetic field of superconducting PdH(D)». In: *J. Low Temp. Phys.* 43.3 (1981), pp. 205–215. DOI: 10.1007/BF00116151.

[315] Z. Li et al. «Reversible manipulation of the magnetic state in $SrRuO_3$ through electric-field controlled proton evolution». In: *Nat. Commun.* 11.1 (2020), p. 184. DOI: 10.1038/s41467-019-13999-1.

List of publications

- Piatti E., Torsello D., Gavello G., Ghigo G., Gerbaldo R., Bartoli M. and Duraccio D.: *"Tailoring the Magnetic and Electrical Properties of Epoxy Composites Containing Olive-Derived Biochar through Iron Modification"*, Nanomaterials **13**, 2326 (2023).

- Gavello G., Tofani G., De Fazio D., Lettieri S., Mezzetta A., Guazzelli L., Pomelli C.S., Gonnelli R.S and Daghero D.: *"Facile synthesis of palladium hydride via ionic gate-driven protonation using a deep eutectic solvent"*, Journal of Molecular Liquids **420**, 126826 (2025).

- Pugliese V., Gavello G., Nieto Hernández E., Redolfi E., Scattolo E., Cian A., Missale E., Bortone A., Dell'Anna R., Ditalia Tchernij S., Giubertoni D. and Forneris J.: *"Formation yield of germanium-vacancy centers in diamond upon keV ion nano-implantation and thermal annealing"*, Journal of Applied Physics **138**, 044401 (2025).

- Piatti E., Gavello G., Ummarino G. A., Košuth F., Szabó P., Samuely P., Gonnelli R.S. and Daghero D.: *"Direct evidence for two-gap superconductivity in hydrogen-intercalated titanium diselenide"*, Materials Today Physics **95**, 101883 (2025)